Hard X-ray Observations

of

Sco X-1 and GX 1+4

A thesis submitted for the
Degree Doctor of Philosophy

by

William Boyd
Stefan W.B. Dieters

Department of Physics
University of Tasmania

December 1990

This thesis contains no material submitted for any other degree. The work presented herein is that of the author, except where duely acknowledged.

Stefan W.B. Dieters Date:

To my parents.

The waves have a story to tell me,
As I lie on the lonely beach;
Chanting aloft in the pine tops,
The wind has a lesson to teach;
But the stars sing an anthem of glory,
I cannot put into speech.

Robert Service "The Three Voices"

Acknowledgements

Like any large project the preparation and launch of an X-ray balloon payload is a group effort. The people who have assisted in the work presented in this thesis are spread in both time and space.

Firstly I'd like to thank all those who were involved in the 1983 Brazil campaign, particularly Dr. K. Harper of Imperial College who provided the 3-axis magnetometer data from the 1983 Brazil flight. The initial data decoding for this flight was done by Dr. A. B. Giles. My immediate predecessor Dr. D. J. Watts who wrote the initial version of the non-linear least squares fitting program which was used extensively by the author.

The success of the Alice Springs 1986 balloon flight was the result of the hard work of many. To all those involved, my thanks for a great working environment. Special mention goes to Dr. R. Sood (University College ADFA) for overseeing the preparation, launch and recovery of the payload. Initial data decoding and editing was done by L. Waldron (University College ADFA) and Dr. A. B. Giles. The collaborating teams form Germany and Italy were led by Dr. R. Staubert and Dr. P. Ubertini.

At the University of Tasmania I would like to thank Dr. D. P. Sharma for his encouragement and help. The initial idea for observing Sco X-1 with the Mt. Canopus telescope is due to Dr. A. B. Giles. I would like to thank Dr. R. Watson and Dr. K. Hill for their help on various observing projects. Dr. Hill provided a great deal of assistance with 'things FORTRAN'.

My supervisor Dr. J. Greenhill has always provided encouragement, a good sounding board for ideas and good suggestions for further work.. This thesis was written on a Macintosh PC provided by Kym Hill. Typing was done by L. Compalina, L. Paine, P. Coleman and Meggan Rose and my brother Mark.

I acknowledge the receipt of a Commonwealth Post-graduate Award for the year 1987 and a University of Tasmania grant for three months in 1985/86.

My thanks go to the other post-graduate students for their help and company. I am grateful to my friends both in Hobart and in Melbourne for all their support especially to Kym Hill and Co. for the many trips to the beach. I cannot express my gratitude to Meggan for being who she is: - a very special person who can remind all, that life is wonderful.

Finally, this thesis would not have been possible without the financial and more importantly, moral support of my parents.

TABLE OF CONTENTS

Chapter 1

Introduction

Come let us on the the sea-shore stand
And wonder at a grain of sand;
And then into the meadow pass
And marvel at a blade of grass;
Or cast our vision high and far
And thrill with wonder at a star;

Robert Service "The Wonder"

They are ill discoverers that think there is no land
when they can see nothing but sea

Francis Bacon,
"Advancement of Learning", Book II 1605

1.1 Introduction

Extra-solar X-ray astronomy started in 1962 with the detection of Sco X-1 and the galactic center during a rocket flight designed to find lunar X-rays. Since then, mainly as a result of a series of dedicated satellite missions the number of known (until 1984) X-ray sources had increased to about 1000. This number is comparable to the number stars brighter than 4th magnitude. The X-ray sky at this sensitivity appears as crowded as a moonlit night. The most comprehensive catalogue is that from the HEAO-1 satellite (1977/1978). This catalogue (Wood et al. 1984) lists 842 sources at energies below 20 keV. Unlike optical wavelengths about half the brightest soft to medium energy X-ray sources are associated with extra-galactic objects which are either galaxy groups or active galactic nuclei (AGN eg. Quasars, Seyfert, BL Lac). Fainter AGN may make up the bulk of the diffuse X-ray background. The galactic objects are mainly binary stars containing either a white dwarf or neutron star. The rest are stars with enhanced solar-like activity. The number of known X-ray sources is set to increase to about 100,000 (much the same as number of stars visible with binoculars) with the completion of the present ROSAT survey. In a twist of history, one of the early ROSAT images actuality showed the moon.

However at energies above 40 keV only about 100 sources are known. The HEAO-A-4 catalogue (Levine et al. 1984) contains 84 sources, most of which are neutron star binaries. The number of detected sources is low because of the low effective area of the detector and the intrinsic rarity of neutron star binaries.

X-ray observations probe the environment close to the neutron star. The inner accretion disk makes a significant contribution to the flux below 20 keV. Hard X-ray wavelengths are primarily produced in the accretion column above the poles of X-ray pulsars or in the boundary region between the disk and neutron star of the non-pulsing systems. Cyclotron line emission or absorption, resulting from the strong magnetic field of X-ray pulsars is observable. For strong ($>10^{12}$ G) magnetic fields these lines fall in the hard X-ray regime. The recently discovered quasi periodic oscillations (QPO) have not yet been detected at energies above about 20 keV. Since they are believed to originate just above the surface of the neutron star a determination of their spectrum and behaviour at higher energies would provide a useful probe particularly for the bright galactic bulge sources such as Sco X-1. At lower energies these sources show no direct sign of the neutron star because of the surrounding scattering cloud. They are expected to show weak

beaming at higher energies and hence reveal the rotation period of the neutron star. Another problem which requires hard X-ray observations is the source of the hard component of the diffuse cosmic X-ray background. Chapter 2 contains a brief overview of the various types of X-ray sources with a particular emphasis upon their hard X-ray properties. The low mass X-ray binaries and X-ray pulsars are considered in detail. Sco X-1 and GX 1+4 are reviewed separately.

Hard X-ray satellite observations have been limited by mass and volume constraints on the detectors. At present there are two satellite experiments sensitive to 20-100 keV photons (MIR-HEXE and GRANAT). Balloon flights allow large area detectors to be used. Although limited in duration compared to potential satellite observations, balloon borne detectors can still make significant discoveries. A prime example is the discovery of a cyclotron resonance line in the spectrum of Her X-1. Proportional counters and phoswich detectors have been used. Proportional counters provide potentially better resolution and lower backgrounds than phoswich detectors. In collaboration with Imperial College the University of Tasmania X-ray group has flown a 5000 cm^2 proportional counter detector, on several occasions between 1976 and 1983. A new detector with far better background rejection including using escape gating was flown from Alice Springs, Australia in 1986. This flight was made in collaboration with University College (ADFA) Canberra, Australia , Astronomisches Institüt Tübingen, Germany and Astrofisica Spaziale Frascati, Italy. This detector has an effective area of ~2000 cm^2. Observation from the 1983 and 1986 flights provide the bulk of the data presented within this thesis.

In Chapter 3 the detection process in xenon proportional counters is examined. The application of escape gating is discussed. Because of the complicated spectral response of proportional counters the methods used to find the source X-ray spectrum require explanation. Also discussed are the temporal analysis methods used to search for QPO and coherent pulsations. This material is also relevant to searches, conducted using the University of Tasmania's 1 metre telescope, for optical pulsars within the SN1987A supernova remnant and the X-ray binary, Wackerling 2134. This work is not presented within this thesis since it is not directly related to the bulk of the work undertaken and because of time constraints.

The two balloon payloads (flown in 1983 and 1986) are described in Chapter 4. Details are given of both University of Tasmania proportional counters as well as the detectors supplied by Imperial College (1983) and Astrofisica Spaziale

Frascati, Italy (1986). The Astronomisches Institüt Tübingen, Germany supplied a rotation modulation collimator for the Italian detector during the 1986 campaign. The various navigation sensors and the aspect servo system are detailed. The performance of the UT detectors and servo system is evaluated. Initial test results of the escape gating method are also included.

Finding the pointing direction of a balloon borne detector is explained in Chapter 5. In particular the effects of tilting upon the output of the navigation sensors is considered. Calculation of the final aspect solution for the 1983 flight was made more difficult because one of the two inclinometers was inoperative. By matching the azimuth as measured using the sun-sensor and 3-axis magnetometer, a pointing history could be found. This process was hampered by the inability to check the 1983 platform for possible misalignments. The 1983 payload was flown before the author joined the X-ray group. A balloon failure led to the destruction of the payload. The results from observations of Sco X-1, SS433, the QSO MR2251-178 and the SMC region are also presented in Chapter 5.

The 1986 flight observations of Sco X-1 are presented in Chapter 6. These data were searched for the presence of hard X-ray QPO and Low Frequency Noise (LFN). This analysis was severely limited by a number of on board timing problems. Much time was spent in understanding and correcting these errors. Standard temporal analysis methods (eg the FFT) could not be directly employed. Upper limits to any QPO's were set using methods explained within Chapter 3. The spectrum and its variability are also discussed. The possible appearance of a hard tail in the energy spectrum is examined critically.

Fast photometric observations designed to search for optical QPO and low frequency optical noise in Sco X-1 are presented in Chapter 7. Unlike previous optical searches, comparison stars were also monitored enabling an absolute red noise level to be found. The state of Sco X-1 is known from simultaneous X-ray observations made by the EXOSAT satellite. Many of the methods presented in Chapter 3 and used in Chapter 6 were applied to the photometry. The results are discussed in terms of the Z source scheme (van der Klis 1989) for QPO sources.

The penultimate chapter considers the GX 1+4 observations made during the 1986 Alice Springs flight. The pulse period is found using epoch folding techniques. Simulations yielded the probable error in the period. Using this period the variation in pulse profile with energy is examined. Similarly pulse phase spectroscopy was

undertaken. The results are discussed in terms of present pulsar accretion theory. Particular emphasis is placed upon the two photon emission model of Kirk, Nagel, and Storey (1986). The data only has been fully analyzed recently, so the discussion in relation to the theory is limited by time constraints on the author.

Finally the conclusions reached during this thesis are summarized in Chapter 9.

The χ^2 minimization program used to find the best fit source spectrum was initially written by Dr. Watts. It has been modified extensively by Dr. Sharma and the author. The initial decoding of the 1983 flight data was done using programs written by Dr. Giles and Dr. Duldig. Apart from this the analysis presented in Chapter 5 is solely the author's work. The initial impetus for the Sco X-1 optical observations (Chapter 7) was provided by Dr. Giles. In the initial data reduction the author was greatly assisted by Dr. K. Hill. The 1986 flight data was initially decoded by Dr. Giles and L. Waldron. The 1986 pointing system solution was undertaken by Dr. Sharma. The production of the escape gated spectrum for GX 1+4 and Sco X-1 is the work of the author. The period search and phase folding was undertaken independently Dr. Sharma and the author: There were only minor differences in the final outcomes, in terms of the derived period and pulse shape.

Much of the author's knowledge of the Kirk, Nagel and Storey (1986) model comes from correspondence between Drs. M. Storey and J. Greenhill. The initial resonant absorption model is due to Dr. M. Storey. The re-evaluation of this model, to include an emission line near 97 keV, are the concepts of the author.

1.2 Publication List

The following list contains all published papers to which the author has contributed. The earlier papers (pre. 1984) are the results of work conducted prior to the when the author commenced this Ph.D. The Pluto observations are an extension of the author's use of the Mt. Canopus telescope. Initial reports of the work within this thesis are presented mainly in Greenhill et al. (1989) and Dieters et al. (1991).

Dieters S. W.B. and Cornelliius W. A. Health Dept. Report (1982).

Coates D.W., Dieters S.W.B., Innis J.L., Moon T.L. and Tompson K. Int. Bull. Var. Stars, No. 2233 (1982).

Innis J.L., Coates D.W., Dieters S.W.B., Moon T.T.and Thompson K. Int. Bull.-Var. Stars, No. 2386 (1983).

Giles A.B., Dieters S.W.B., Emery M.W., Fenton K.B., Greenhill J.G., Sharma D.P., Warren D.M., Sprent A., Sood R.K., Thomas J.A., Mace O.B., Denehy B.V. and Waldron L. Proc. 3rd National Space Engineering Symposium, Canberra pp. 255-259 (1988).

Sharma D.P., Dieters S.W.B., Emery M.W., Fenton K.B., Giles A.B, Greenhill J.G., Sprent A., Warren D.M., Salmon G.L., Sood R. K. and Thomas J. A. Proc. 20th Intternational Cosmic Ray Conf., Moscow **2** pp. 285-288 (1987).

Hill K.M., Dieters S.W.B. and Watson R.D. IAU Circ. 4612 (1988)

Hubbard W.B., Hunten D.M., Dieters S.W.B., Hill K.M. and Watson R.D. Nature **336** pp. 452-454 (1988).

Hunten D.M., Hubbard W.B., Dieters S.W.B., Hill K.M. and Watson R.D. Abstract in Bull. Amer. Astron. Soc. **20** p. 805 (1988).

Dieters S.W.B., Green P.M., Hill K.M.and Watson R.D. IAU Circ. 4773 (1989).

Greenhill J.G., Giles A.B., Sharma D.P., Dieters S.W.B., Sood R.K., Thomas J. A., Waldron L., Manchanda R.K., Carli R., Hammer P., Kendziorra E., Staubert R., Bazzano A., Ubertini P. and La Padula C. Astron. Astrophys. **208** pp. L1-L4 (1989).

Greenhill J.G., Giles A.B., Sharma D.P., Warren D.M., Sprent A., Emery M.W., Dieters S.W.B., Fenton K.B., Sood R.K., Waldron L.M., Thomas J.A., Mace O. and Manchanda R.K. Proc. Astron. Soc. Aust. **8** pp.166-168 (1989).

Dieters S.W.B., Greenhill J.G., Sharma D.P., Sood R.K., Waldron L. and Storey M. C. Adv. Spa. Res. **11** 35 (1991).

Dieters S. W.B., Hill K. M. and Watson R. D. Int. Bull. Var. Stars, No.3500 (1990).

Greenhill J.G., Giles A.B., Salmon G.L., Sharma D.P. and Dieters S.W.B. Accepted Adv. Spa. Res. (1990).

Greenhill J.G., Sharma D. P, Dieters S.W.B., Fenton K.B., Sood R.K. and Waldron L. Proc. 21st Inter. Cosmic Ray Conf., Adelaide **1** pp.29-31 (1990).

Millis R.L., Wassermann I.H., Franz O.G., Nye R.A., Gilmore A.C., Kilmartin P.M., Allen W.H., Watson R.D., Dieters S.W.B., Hill K.M., Giles A.B., Blow G., Priestley J., Walker W.S.G., Marino B.F., Dix D.G., Page A., Kennedy H.D., Elliot J.L., Dunham E., Bosh A.S., Young L.A., Silvan S.M. and Klemola A R. Icarus, in press (1990).

Sharma D.P., Greenhill J.G., Dieters S.W.B., Emery M.W., Fenton K.B., Giles A.B., Manchanda R.K., Sood R.K., Sprent A., Thomas J.A., Waldron L. and Warren D.M. Proc. 21st Inter.Cosmic Ray Conf., Adelaide **1** pp. 32-35 (1990).

Chapter 2

Review : Galactic X-Ray Sources

Although the myriad things are many, their order is one.

Chuang Tzu

The Heavens .... are now seen to resemble a luxuriant garden, which contains the greatest variety of productions, in different flourishing beds; and one advantage we may at least reap from it is that we can, as it were, extend the range of our experience to an immense duration. For, to continue the simile I have borrowed from the vegetable kingdom, it is not almost the same thing, whether we live successively to witness the germination, blooming foliage, fecundity, fading, withering, and conception of a plant, or whether a vast number of specimens, selected from every change through which the plant passes in the course of its existence be brought at once to our view?

William Hershel

2.1 Introduction

The aim of this review is to provide the background and context to the analysis of the hard X-ray observations presented within this thesis. Following this aim, only a brief outline is given for objects not directly related to Sco X-1 and GX 1+4 which are the main subjects of this thesis. These sources are a low mass X-ray binary and a X-ray pulsar respectively.

The properties of various galactic X-ray sources are introduced. These include supernova remnants and associated single pulsars, the corona-spheric stellar sources and the cataclysmic variables.

The low mass X-ray binaries (LMXB) are discussed in detail. The understanding of LMXB has been enhanced recently by the discovery of quasi periodic oscillations (QPO) in their X-ray flux. A summary of the current observations and theories of QPO's is given. Using the 1986 flight data a search was made for 20-40keV QPO from Sco X-1. Sco X-1 is discussed in detail.

In contrast to the LMXB most of the X-ray pulsars are in high mass X-ray binary systems (HMXB). These systems are briefly introduced. The topic of accretion torques is discussed in detail. In Chapter 8 of this thesis a pulse period determination of GX 1+4 is made using data taken during a balloon flight on the 26th of November 1986.

The current and theoretical status of cyclotron line and X-ray continuum emission is summarized. This theory is used in the discussion of the energy dependence of the pulse profiles of GX 1+4 as observed in 1986. Finally models of GX 1+4 are discussed.

Within this review the emphasis is on hard or balloon energy X-ray observations. The term hard and balloon energy X-rays will be reserved for X-rays with energies greater than 20 keV. X-rays with energies below 20 keV and above about 2 keV are termed as being medium energy. The lowest energy X-rays, i.e. <2 keV, are called soft.

2.2 Galactic X-Ray Sources.

Within the galaxy there is a wide variety of X-ray sources. These can be broken up into three broad categories ; supernova remnants, normal stars and collapsed objects.

Supernova remnants can be split into two groups; shell like and the rarer Crab like or plerion type. The X-ray (at soft and medium energies) spectrum of the shell like remnants is dominated by line emission from the shocked gas at a temperature of kT≈10 keV. The line species are not in ionization equilibrium making modelling of the spectra very difficult. Even the underlying continuum is uncertain. However, at higher energies the spectrum is thermal. The plerion sources are dominated by synchrotron emission and the emission of the central pulsar. They have power law X-ray spectra.

Stars from practically every section of the Hertzsprung-Russell diagram are found to be soft to medium energy X-ray emitters. See Rosser, Golub and Vaina (1985) for a review. The sun with $L_x=8x10^{26}$ erg s^{-1} is at the lower level of observed X-ray activity. By analogy with solar activity the X-ray emission of late type stars comes from coronal holes. The measured temperature is 10^7 to 10^8 K. The combination of rapid rotation and deep convective layers, greatly enhances the efficiency of the dynamo mechanism and hence solar type activity in late type stars. Luminosities up to 10^{31} erg s^{-1} are observed from the red giant components of RS CVn binaries. Solar like flares are seen at optical and radio wavelengths from many M type dwarfs. By the solar analogy, soft to hard X-ray flares are also expected. So far none has been detected because of the low fluxes involved.

Early O-F type stars seem to produce X-rays within their strong slow moving stellar winds. Apparently instabilities develop, creating local density enhancements and consequent shocks within the wind. Luminosities of up to $L_x = 10^{34}$ erg s^{-1} and a thermal bremsstrahlung spectrum with temperatures of $3x10^6$ K are observed from the bright O stars.

As a class the cataclysmic variables (CV's) are the next most numerous X-ray sources within the galaxy. Nearly all involve a white dwarf within a binary system. The optical properties of CV's are dominated by an accretion disk. Strong Balmer lines, a blue continuum and rapid flickering are the major optical characteristics. The CV's in general consist of an approximately normal star, white

dwarf and/or an accretion disk or stream. There is often a bright hot spot on the disk where matter from the companion strikes the disk. The majority have orbital periods between 82 min and 17.5 hours. There is a well defined gap in periods between 2 and 3 hours. Am CVn, consisting of two degenerate stars has an orbital period of 17 minutes. Most symbiotic stars and some recurrent novae contain a giant companion and hence have long, days to weeks orbital periods (Hoffmeister et al. 1985 and references therein).

There are numerous sub-groups within the cataclysmic variables. There are two ways of making the sub-classifications; one based upon their outburst behaviour and the other upon the role of the magnetic field of the white dwarf.

The novae and recurrent novae have large outburst amplitudes, 8-15 magnitudes and ≈6 magnitudes respectively.. The rise to maximum takes a day or two while the fall can last months to years. The outbursts of recurrent novae are shorter in duration (a week). During a nova outburst a 10^{-8} - 10^{-6} Mʘ shell of matter is ejected. The total luminosity of a nova outburst is 10^{41} ergs. It is most probably the result of a thermonuclear explosion at the base of material accreted onto the white dwarf. Other mechanisms such as enhanced mass transfer may be responsible for some outbursts of the recurrent novae which include many types of companion stars.

Many years after an outburst novae show both CIII/NIII blend and HeII emission lines in addition to Balmer lines. A large number of CV's have a similar optical spectrum and flickering behaviour but have not been observed to outburst. These are labelled the nova like systems.

Dwarf novae have lower amplitudes (<6m) and total outburst energies of 10^{35} - 10^{39} ergs. A rapid <1 day rise is followed by a more gradual decay (≈3 day). These recur on time scales ≈10 days to a year. The outbursts are thought to be due to a temperature-viscosity instability within the accretion disk. The trigger is probably an enhancement in the accretion rate. Several sub-groups of the dwarf novae exist. At approximately regular intervals the SU UMa have longer (≈7 day) bright super outbursts. In outburst a second period slightly longer than the orbital period is found. The Z Cam stars occasionally pause for days or months on the decline from an outburst.

The symbiotic stars (very slow novae, e.g. Z And) consist of a giant and a hot dwarf (possibly a white dwarf) embedded within a common envelope. Some have long (months) low amplitude (<4 mag) outbursts. All are soft X-ray sources. The X-ray s presumably originate from matter accreting onto the hot star.

The other more physically relevant method of classifying CV's is by the effect the white dwarf's magnetic field has on the accretion process. The polar or AM Her stars have the strongest magnetic fields. No accretion disk forms but matter is funnelled directly from the inner Lagrangian point to the poles of the white dwarf. Here a shock forms above the poles. Half the free fall energy is radiated directly away from the white dwarf giving rise to a hard, ≤50 keV blackbody spectrum. The other half of the energy is propagated downward and re-radiated from the white dwarf's surface producing a 0.1 keV blackbody spectrum. At higher accretion rates the accretion column becomes optically thick and the hard spectral component is softened by Compton scattering.

When the magnetic field is lower, a disk can form, but is disrupted at some distance from the white dwarf. Material is channelled over a wide azimuth onto the poles. A hard spectrum is produced within the shock above the poles. X-rays are also produced at the boundary layer between the magnetosphere and disk. These are the intermediate polars or DQ Her stars. At optical wavelengths their main distinguishing feature is the presence of two periods (orbital and white dwarf rotation) and their beats. Only the white dwarf rotation period is seen at X-ray wavelengths.

If the magnetic field is weak the accretion disk extends to near the surface of the white dwarf. Here a boundary layer is formed which gives rise to a thermal bremsstrahlung spectrum with a high temperature (kT≈5-50 keV). The disk blocks and re-radiates some of the radiation. A blackbody, kT=20-30 keV, spectrum is produced on the surface.

Polars, DQ Her and non-polars are not confined to any particular class of CV e.g. Nova V1500 Cyg is also an Am Her star and the dwarf nova EX Hya is an intermediate polar. A division based upon the role of the magnetic field can also be applied to binary systems containing neutron stars.

Within the galaxy there is a total of ≈100 luminous neutron star, X–ray binaries as compared to the approximately ~10^4 CV's. These neutron star binaries emit up to

10^{38} erg s^{-1} at X-ray wavelengths. They are split into two broad groups depending upon the mass of the normal star. The high mass X-ray binaries (HMXB) generally have O or B type companions and usually emit regular pulses at the neutron star's spin period. The ratio of L_X/L_{opt} is low ($\leq$10). The low mass X-ray binaries (LMXB) have faint companions. The optical flux is dominated by the accretion disk and so the L_X/L_{opt} ratio is high (10^2 - 10^3). Most do not pulse. They are concentrated within the galactic bulge and globular clusters and as such are Population II objects.

Most of the black hole candidates have properties similar to the LMXB. The prototype black hole, Cyg X-1, has a high mass blue super-giant companion.

2.3 The Low Mass X-ray Binaries.

Historically, the low mass X-ray binaries (LMXB) have been split into five subgroups: bright galactic bulge sources, those in globular clusters, X-ray bursters, X-ray novae and pulsating sources. Most of the globular cluster sources have been found to exhibit X-ray bursts. They are preferentially located in the cores of the most centrally condensed clusters. Many may be formed by capture. The system masses can be estimated from their radial distances from the cluster centres. The total average system (neutron star + companion) mass is ~1.5 M$\odot$ (Charles 1989 and references therein).

A typical X-ray burst is a sudden, ~1 sec rise in X-ray brightness followed by a 3-100 sec. decline. Two types of X-ray bursts are observed. Type II bursts are only observed from MXB1730-335 or "The Rapid Burster". The time interval between successive bursts is seconds to minutes. The X-ray spectrum remains at a constant temperature (T~10^7 K) throughout the burst. The intensity of the burst is related to the waiting time prior to the burst. At present there is no accepted theory for the origin of type II burst, although it is generally agreed that the energy source is unstable accretion.

Type I bursts are observed from all burst sources including the rapid burster. The recurrence time is hours to days. Their spectra are thermal with a peak temperature of ~3×10^7K. The temperature decreases during the burst. At maximum brightness the equivalent blackbody radius is ≈7km. Concurrent optical bursts are delayed (1-2 sec.) and smoothed with respect to the X-ray burst. This can be explained by

the optical burst arising from X-ray reprocessing within a disk about 1-2 light seconds in radius (Lewin and Joss 1983)

The persistent flux is a factor of 100 times larger than the average burst flux. This is about the ratio of the available accretion and nuclear energies for a neutron star. The small blackbody radius and the above energy ratio argument suggest that the Type I bursts are produced by a thermonuclear run away on a neutron star.

Because of the high density and temperature gradients in the outer regions of a neutron star, any nuclear reactions can only occur within thin shells. The outermost hydrogen burning shell is stable but helium burning is unstable whenever greater than ~10^{21} g of matter has been accreted by the neutron star. Numerical simulations show bursts that reproduce the main characteristics of the observed bursts. At high (>10^{18} g s^{-1}) (Section 2.6.1.2 of Lewin and Joss 1983) accretion rates, bursts are suppressed. Above this accretion rate continuous nuclear burning occurs.

The optical flux of burst sources and LMXB in general is dominated by the accretion disk. When an optical counterpart is found the spectrum shows a blue continuum with the absorption lines being weak or absent . Only a few emission lines are visible, principally HeII λ4686, CIII/NIII λλ4630-4650 and sometimes Balmer lines. The continuum colour indicates a disk temperature of >15,000 K. In the cases where stellar absorption lines are visible (e.g. the X-ray novae: A0620-00, Cen X-4, Aql X-1 , 1743-28) they are of a mid K dwarf. Otherwise, line strength limits also indicate a late dwarf secondary (Canizares, McClintock, Grindlay 1979).

The X-ray novae have a sharp 2-5 magnitude rise in brightness followed by a more gradual decline over an interval of days to weeks. Some are associated with Be secondaries and as such are massive X-ray binaries. Others, which generally show a soft X-ray spectrum are associated with G or K type main sequence dwarves. When the companion's optical spectrum is not visible minimum line limits suggest a faint main sequence star. One X-ray nova (A0620-00) is considered a black hole candidate.

Table 2.1

Source		Type	Phenomenology	Porb	P+G	P	W+M
Sco X-1	1617-155	Z	QPO	19.2	I		2
GX5-1	1758-250	Z	QPO		I	*	
SCO X-2	GX349+2	Z	QPO		I	*	2
GX17+2	1813-140	Z	QPO (bu)	19.8?	I	*	2
GX9+1	1758-205	A			I	*?	2
GX340+0	1642-455	Z	QPO		(I)		
GX3+1	1744-265	A	QPO (Bu)		I	*	
GygX-2	2142+380	Z	QPO (bu) Mo	235.2	(I)		
GX13+1	1811-171	A			I	*	
GX9+9	1738-169	A	Mo	4.2	I	X?	
4U1820-30	NGC6624	A	QPO Bu Mo	0.2	II	X	
4U1705-44		A	Bu			X	2
4U1636-53		A	Bu	3.8	II	X	1
Ser X-1	1837-049		Bu		II	X	1
GC X-1	1742-294		Bu?				
GX354-0	4U1728-33	A	Bu		II	X	1
4U1735-44		A	Bu	4.6	II	X	1
GX339-4	1659-487		QPO BH	14.8?	II	X	

All LMXB are intrinsically faint (M_V ~+1). Their faintness and lack of spectral lines has made orbital radial velocity variations difficult to detect. Until recently very few systems were found to exhibit any orbital modulation at either X-ray or optical wavelengths. The lack of eclipses can be explained by a thick accretion disk shielding the secondary from a direct view of the central X-ray source. Fortunately this situation is partially circumvented. Observations of the bursters and globular cluster sources by EXOSAT have found several sources which have orbital modulations.

Some sources have partial or total eclipses while others show periodic, irregularly shaped dips, and a few have approximately sinusoidal variations. Optical photometry has added to the list of LMXB with known orbital periods. These are summarized in Table 2.1. Most of the sources that show an orbital modulation are globular cluster or burst sources. All the bursters have orbital periods less than seven hours indicating that the companion is a low mass main sequence star.

Two circumstances allow orbital effects to be observed. Firstly the X-ray radiation illuminates and heats the inner face of the accretion disk. Material is evaporated off the disk forming an accretion disk corona (ADC). Even though the central source may be completely obscured by the disk, the ADC scatters X-rays into our line of sight. Secondly the outer rim thus varies substantially (0·1-0·2 $R_\odot$) in height, modulating the flux observed from the ADC and central source. The impact of the gas stream originating at the inner Lagrangian point causes a bulge in the outer rim of the disk. The X-ray source can be seen directly when the low section of the rim is toward us. Detailed modelling of the X-ray and optical modulation of 1822-37 indicates that the ADC is about half the radius of the disk (White 1989 and references therein).

There is strong evidence that ADC are a common feature of LMXB. Broadened Fe XXVI (6.7 keV) fluorescence lines are observed from most LMXB. The width of these lines is best explained by Compton scattering within a hot corona around a central source.

Many LMXB sources show a positive intensity temperature correlation, when the spectra are fitted by a thermal bremsstrahlung model. Higher quality X-ray spectra (in the < 30 keV band) can be best fitted by a two component spectrum. One component is a constant soft spectrum variously modelled as a multicolour black

body or a Comptonized thermal spectrum. The other component is a variable, blackbody spectrum with kT~2 keV. The relative contribution of this harder component increases with increasing source brightness. This will cause an apparent rise in temperature when a single thermal bremsstrahlung spectrum is used to model the data. There seems to be a correlation between the strength of this hard component and source luminosity (Mitsuda and Tanaka 1985). The hard component is associated with the magnetic field boundary layer while the soft component is associated with the inner accretion disk. The Comptonization of the soft component is due to an overlying coronae.

Most balloon energy (>20keV) spectra can be fitted by a thermal bremsstrahlung spectrum with kT~5 keV. When this is done several LMXB show an intensity temperature correlation as at lower energies (<20 keV).

Comptonization naturally explains the temperature intensity correlation as an increase in optical depth with increasing intensity. As the optical depth increases more soft photons are scattered to higher energies and so the spectrum hardens. An increase in optical depth can be achieved by either a contraction of the scattering cloud while conserving its mass or an increase in the number of atoms in the cloud. An increase in accretion rate would lead to an increase in both luminosity and mass of the cloud while the temperature remains constant (Lamb and Sanford 1979, White, Peacock, Taylor 1985). The Comptonization model generally used is the analytic approximation of Chapline and Stevens (1973) to the more general theory (e.g. Sunyaev and Titarchuck 1980). Typical optical depths are τ=2-12.

The most popular theory to explain QPO requires the neutron star to have a significant (~10^{12} G) magnetic field. No neutron star rotational pulsations have been observed from any LMXB (a possible exception is GX 339-4 Imamura et al. 1987 and Steiman-Cameron et al. 1990). A surrounding corona is a very effective means of suppressing any beaming from the neutron star (Kylafis and Klimis 1987, Brainard and Lamb 1987, Wang and Schlickeiser 1987). Accretion disk coronae are expected on the grounds of eclipse modelling (particularly 1822-37), the width of iron fluorescence lines, X-ray spectra and the lack of neutron star pulsations.

Based upon their behaviour on X-ray colour-colour diagrams the LMXB have been divided into "Z" and "Atoll" sources. On a colour-colour diagram the "Z" sources trace out a three branched "Z" shaped pattern. The colour - colour diagrams for the

"Atoll" sources are characterized by a series of disconnected states ("islands"). Quasi periodic oscillations (broad 4-30 Hz peaks in the power spectra) are found predominantly amongst the "Z" sources. This division breaks the LMXB along the same lines as previous classifications. (Parsignault and Grindlay 1978, Pomman 1982, White and Mason 1984). The concordance of these earlier classifications was first pointed out by van Paradijs and Lewin (1985).

Table 2.1 is a compilation of the data presented by van Paradijs and Lewin (1985) and van der Klis (1989). From this table it can be seen that the bulge sources generally have two component medium energy spectra, show a positive intensity-temperature correlation and are QPO and Z sources with bursting being rare or non-existent. The burst sources tend to show a single power law spectrum with no intensity-hardness relation. They are mainly Atoll sources with no QPO. The orbital periods tend to be shorter than for the bulge sources.

Earlier classifications were based on variability and spectral characteristics. Parsignault and Grindlay (1978) used the presence of an intensity-temperature relation and short term flaring as the criteria to divide the LMXB. As discussed previously the temperature-intensity correlation is a consequence of the two component spectral characteristic. The existence of a two component or a single power law spectrum was used by White and Mason (1984) to categorize the LMXB. However, more recent measurements (Mitsuda and Tanaka 1985) showed that the two component spectra are universal amongst LMXB and so earlier spectral classification schemes are possibly invalid.

The underlying cause of the distinction between the two groups of LMXB is uncertain. Burst and "Z" type spectral behaviour are not mutually exclusive e.g. GX 17+2. It is not clear that luminosity is the distinguishing feature since some bright non-bursters have been classed as Atoll sources (e.g. GX 9+1 and GX 13+1). One clue is that of the Atoll sources 4 have short periods (< 5 hours) in contrast to the 2 bulge sources (Sco X-1, Cyg X-2) which have long (>15 hours) periods. This reflects a difference in the companion stars. The burst sources and X-ray novae all have main sequence late type companions while Sco X-1 and Cyg X-2 probably have evolved counterparts. Main sequence companions will result in the mass transfer rate being driven by gravitational radiation and/or magnetic braking and so provide lower accretion rates. The nuclear evolution of giant companions would generate higher mass transfer rates. It has also been suggested that the difference between the two groups is due to

different evolutionary histories. In systems containing giants the neutron stars maybe formed primarily by accretion induced collapse of a white dwarf. The systems with main sequences are thought to have gone through a more normal evolutionary sequence, possibly including a common envelope phase (van der Klis 1989 and references therein).

The origin and subsequent evolution of LMXB is still highly speculative. The LMXB particularly those with evolved secondaries have been considered as progenitors for the millisecond binary pulsars. The neutron star is spun up to millisecond periods by accretion and the companion evolves into a degenerate object. There are, however, major problems with this scenario (Ray and Kluzniak 1990).

2.3.1 Black Hole Candidates

Except for Cyg X-1 the black hole candidates all have properties indicating that the normal star is of low mass. The X-ray properties of black hole candidates are similar, but not identical to those of the LMXB. There are several properties which are supposed to indicate the presence of a black hole rather than a neutron star. These discriminators are based upon the features of Cyg X-1 the best studied and most widely accepted black hole candidate. The upper limit for the mass of a neutron star is about 3M⊙. Cyg X-1 is thought to be a black hole because of the high mass (9M⊙) of the compact object. A high mass estimate is the only reliable signature of a black hole. On this basis LMC X-3, A0620-00, LMC X-1 and SS433 are considered firm black hole candidates (Tanaka 1989). In all cases there are, however, some doubts based upon the difficulties of the methods used to obtain the masses.

Rapid (millisecond timescale) flickering at X-ray wavelengths was long considered a good marker of a black hole. However both the burst source Cir X-1 and the X-ray pulsar X0331 + 53 show flickering. Dual spectral behaviour is common amongst the firm black hole candidates. In the high state the spectrum has an ultra soft (<1 keV) and a harder power law component. In the low state a single power law is a good representation of the spectrum. Based upon this criterion and the presence of flickering, GX 339-4 and more recently GS2000+25, GS2023+23 and GS1826-24 are considered black hole candidates (Tanaka 1989).

Both LMC X-1 and GX339-4 have shown QPO. In the case of LMC X-1 the QPO are at different frequencies from those seen in LMXB. GX339-4 displays 6Hz mode QPO similar to the LMXB (Kitamoto 1989). The present knowledge of the production of QPO's is insufficient to use their presence as a discriminator against a black hole. Imamura et al. (1987) have reported a 1·13 msec periodicity in GX339-4. This period was not confirmed but a 190 sec period has been found (Steiman-Cameron 1990). Either period would be proof of a neutron star in the GX 339-4 system.

2.3.2 Quasi-Periodic Oscillations.

The discovery of quasi-periodic oscillations (QPO) during high time resolution X-ray studies of several LMXB has allowed the direct probing of the environment close to the neutron star. Observationally QPO appear as a broad peak in the power spectrum. The central frequency is between 0·1 and 55Hz and the width is typically 20 to 60% of the central frequency. The width of the peak implies that the signal is coherent over about 10^5 cycles (Lewin, Paradijs and van der Klis 1987). The underlying signal is not strictly coherent with either the period amplitude and/or phase varying erratically. The QPO peaks are in contrast to the sharp power spectral peak expected from the coherent signal from the rotation of a neutron star.

Associated with the QPO are three noise components. These appear as extra power above that expected from counting statistics. Very Low Frequency noise (VLFN), usually dominates the power spectra below 0·01 to 0·1 Hz with a total strength of a few percent. Its shape is generally fitted by a power law with an index between 1·2 and 2·3. VLFN may be related to the variability of LMXB on time scales of hours to days. However it has not been well studied at frequencies below 1mHz. Low Frequency noise (LFN) is mostly a monotonically decreasing or "red" noise component. The shape has been fitted with an exponential, a Lorentzian centred at zero frequency, or a cutoff power law (α -1 to +0·3) extending to 5 to 15 Hz. Occasionally it has a peak. Typically LFN, amounts to a signal of 3-4% rms. LFN can sometimes have a broad peak. High Frequency Noise (HFN) is a more or less flat continuum, power law shape, up to a cutoff frequency (25 to >100 Hz). Strengths between 1·6 - 8% have been reported from bulge LMXB. A summary of the various noise components is given by van der Klis (1989).

Quasi-periodic oscillations have been observed from the LMXB Cyg X-2, Sco X-1, GX 340+0, GX 17+2 (Sco X-2), GX 5-1, GX 3+1, GX 349+2, the

rapid burster, (MXB 1730-335), 4U1820-30 and Cir X-1 . The black hole candidates GX-339-4 and LMC X-1 both show QPO, as do the X-ray pulsars Cen X-3, EXO 2030+375 and 4U1626-67. VLFN and HFN but no QPO have been observed from 4U1636-53, 4U1705-44, 4U1735-44, GX9+9, GX9+1, 4U1728-34 and 4U1608-52. Only VLFN has been detected from GX13+1. The above list contains every category of X-ray binary.

Historically, QPO were first detected during bursts of the rapid burster but were taken as being 'just' another unusual property of this source. The first LMXB found to exhibit QPO was GX 5-1. The sources GX 5-1, Cyg X-2 and Sco X-1 have played an important role in the development of the understanding of the QPO phenomena.

During the initial observations of GX 5-1 the central frequency (20-50Hz) was strongly dependent upon the source intensity. The strength of the QPO and LFN were also directly correlated to the intensity. Two similar models were advanced. In both the neutron star has a moderate strength magnetic field ($B \sim 10^8$-10^9G). This is strong enough to disrupt the accretion disk some distance from the neutron star's surface. The situation is analogous to that of the intermediate polars amongst the cataclysmic variables. The QPO frequency was identified with either the frequency of the innermost Keplerian orbit in the disk or the beat between the neutron star's rotation and the inner edge of the disk. Both models owe their origin to similar models attempting to explain optical, longer period, quasi-periodic oscillations from cataclysmic variables.

The intensity dependence of the QPO frequency is explained by an increase in accretion rate which causes extra pressure upon the magnetosphere. The magnetosphere shrinks and the inner edge of the disk moves inward increasing the observed frequency. The QPO and LFN are considered to be produced by many individual oscillating shots. (Lamb et al. 1985, Lamb 1986). The LFN are a consequence of the average shot flux being positive. In this model the strength of the LFN and QPO must be positively correlated.

The beat frequency model specifically predicts that the neutron star should be rotating at near the Keplerian frequency of the inner disk, i.e. hundreds of hertz. Despite sensitive searches (<1%) no definite coherent signal has been found. This can be explained by a combination of several factors. At weaker magnetic fields the beam should be broader and the field may be multi-polar (Wang and Schlickeiser

1987). A surrounding hot cloud would effectively smear any pulsations. This cloud can be identified with the ADC. Initially it was thought that the observed millisec. time lags between hard and soft QPO photons could be explained solely by Compton scattering within an ADC. However the cloud radius (>1000km) determined from the time lag is much larger than that of the ADC found from eclipse modelling (White 1988, van der Klis 1989). Recent models of the 6Hz QPO suggest that a time lag is intrinsic to the oscillation mechanism.

Initially it seemed that a relatively simple model could explain the observed QPO/red noise properties. Subsequently, analysis of Sco X-1 data revealed intensity dependent 10-20 Hz QPO and 6-15 Hz QPO with an erratic frequency-intensity relation. Also found were ~6Hz QPO with the central frequency weakly anticorrelated with source intensity. The strengths of the QPO and LFN were anticorrelated. Similarly intensity independent 25-55 Hz QPO were observed from Cyg X-2.

Observations of other sources continued to add to the array of different QPO/LFN behaviours. Quasi periodic oscillations near 6Hz were found to be common. The picture became clearer when it was realized that the QPO/LFN properties of Sco X-1 strictly correspond to its state (active/quiescent). The 6Hz QPO were only found in the quiescent state and the 10-20 Hz QPO were found during the flaring state. This two state scheme is only part of the overall behaviour which is most clearly seen in Cyg X-2.

When a hardness intensity diagram (HID) is formed for Cyg X-2 a "Z" shape is seen. The pattern is clearer if a plot of soft energy range hardness (colour) versus a harder energy colour is created. Such a diagram is called a colour-colour plot (CCP). See Figure 2.1. The top branch where the hardness is roughly independent of intensity is called the horizontal branch (HB). The down stroke is where Cyg X-2 spends most of its time and is called the normal branch (NB). By analogy with Sco X-1 the slightly rising, lowest, branch is called the flaring branch (FB). These names are purely historical, the horizontal branch is not necessarily horizontal, some sources spend little of their time on the normal branch and only a few show Sco X-1 type flaring at any stage. The various properties of the QPO are summarized in the schematic colour-colour diagram at Figure 2.1 and in Table 2.2.

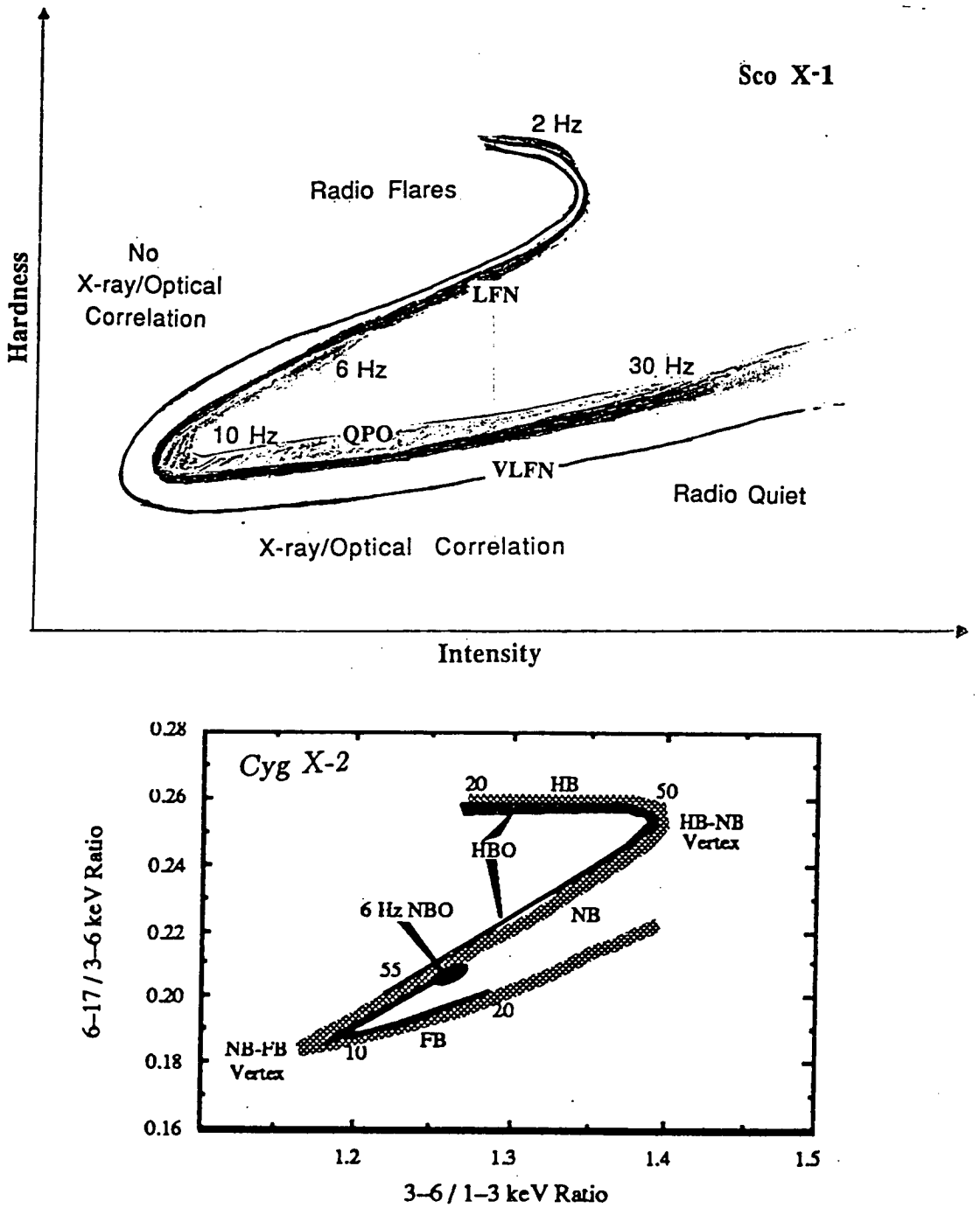

Fig 2.1 A schematic representation of the Hardness-Intensity and Colour-Colour properties of the Z sources. The lower diagram is taken from figure 1 of Lamb (1989). In the hardness-intensity diagram for Sco X-1 the width of the three bands is an indication of the strength of the various power components (QPO, LFN, VLFN). The two main differences between Sco X-1 and the majority of Z sources (Cyg X-2 etc) is the presence of a flaring branch and the appearance of a 2Hz feature in the Horizontal Branch (HB) instead of 20 - 50 Hz QPO. The majority of Z sources LFN is strongest in the HB. Sco X-1 follows a similar pattern especially if the 2Hz feature is accepted as a LFN component. For Sco X-1 the LFN is weakest when the 6Hz QPO is strongest which is contrary to the behaviour of Cyg X-2. During the Flaring Branch (FB) the red noise of Sco X-1 extends over a wider than average frequency range and so LFN can be considered as present. The radio behaviour of Sco X-1 is general to the Z sources.

Table 2.2

Component	Shape[A]	Strength (rms) 2-20 keV	Other Properties		Time Lags
All Branches					
VLFN	PL	0.5 - 3%	α	1.5-2.	
HFN	Cut PL	1.5 - 4%	ν_{cut}	40 - 80 Hz	
HB					
LFN	Cut PL	3-4%	α	-1 - +0.3[B]	
			ν_{cut}	5 - 10 Hz	10 msec soft lags
QPO	Lorentz	2 - 7%	ν_{QPO}	15 - 55 Hz	4msec hard lags
			$\Delta\nu/\nu$	0.2 - 0.4	
NB					
QPO	Lorentz	1 - 5%	ν_{QPO}	5 - 7 Hz[C]	150° hard lags
				Dn/n	0.2 -1.5
FB					
QPO	Lorentz	5-10%[D]	ν_{QPO}	10 - 20 Hz[E]	

This table is based on table 3 of van der Klis 1989 and the infomation in table 3.1 of Lewin, van Paradijs and van der Klis (1987).

A : PL= Power Law $\nu^{-\alpha}$, Cut PL = Cutoff Power Law $\nu^{-\alpha}e^{-\nu/\nu_{cut}}$

B : If $\alpha < 0$·1-2 Hz peak eg Sco X-1, Sco X-2

C : Approximatlly constant. Weakly related to intensity

D : Only Sco X-1 and Sco X-2 show FB behaviour (Shultz, Hasinger and Trümper 1989). Strength in the 5-35 keV range for Sco X-1.

E : Strong positive correlation with intensity.

In the HB the frequency of the 2-6% rms (20-50 Hz) QPO is positively correlated with source intensity for all objects except Sco X-1 and GX17+2 (Sco X-2). Occasionally a weak 2nd harmonic is seen. The spectrum of both QPO and LFN is harder than the overall source spectrum. For most sources the LFN is strongest on the horizontal branch. The high frequency QPO can persist as the source moves from the HB into the upper part of the NB. Simultaneously the LFN rapidly decreases in strength. Low frequency (~6 Hz) QPO appear in the lower sections of the normal branch. The strength and central frequency of the 6Hz QPO are only slightly dependent upon the intensity. Similar 4-8 Hz QPO have been observed from the non- "Z" LMXB. These may not be related to the 6Hz mode QPO of the "Z" sources. The spectrum of the 6Hz QPO has a minimum fractional amplitude near 6 keV. There is a smooth transition between the NB and the FB with the QPO frequency slowly increasing from 6-10 Hz. Thus the NB and FB seem to be the same phenomena while the HB QPO are distinct. Flaring QPO's have only been observed from Sco X-1 and Sco X-2. As the intensity increases the central frequency increases from ~10 Hz to ~25 Hz. The QPO peak broadens and eventually dissolves into a flat excess noise continuum. At the highest intensities, during flares, there are no QPO but very strong (≈8% rms) VLFN. The spectrum of the QPO and red noise is harder than the overall source spectrum.

A second group of "Atoll" sources can be identified (van der Klis 1989 and Schultz, Hasinger and Trümper 1989) using X-ray colour-colour diagrams. Instead of a "Z" pattern the colour-colour plot is broken up into isolated 'banana' and 'island' states. The 'banana' states are characterized by slightly curved fuzzy areas while the 'island' states are isolated patches upon the colour-colour diagram. The states are broader than expected from Poisson statistics. When a string of these banana and island states is found they look like the broken rim of an atoll. Movement between and within states is much more gradual than with the "Z" sources. More regular bursting behaviour is seen during island states which tend to be fainter than the banana states.

Both VLFN and HFN components have been found. The VLFN is strongest (2-3% rms) in banana states and <1% in the island states. Conversely HFN dominates the island states with strengths up to 20% rms. Its shape can either be "red" or with a broad peak. Additional structure is often seen in both noise components, including peaks similar to those seen as QPO in Z sources.

Included within the initial list of QPO sources are the two peculiar burst sources (Cir X-1 and the rapid burster MXB1730-335). Cir X-1, a recurrent X-ray transient, has displayed 5-17Hz QPO and a sharp 1.4Hz QPO during two separate outbursts. A HFN, 30-300 Hz, component was seen on one occasion and very strong >0.05Hz red noise at another. At present no behavioural pattern is apparent. Three different types of QPO's have been observed from the rapid burster. During long flat topped bursts 2-5 Hz narrow ($\Delta\nu/\nu = 0.05$) QPO and weak red noise has been observed. These QPO have been identified with HB QPO because of their similarity in frequency and a slight anticorrelation of frequency with intensity. Strong (<3.5% rms) 2-4.5 Hz QPO sometimes appear in the non-bursting flux after short Type II bursts. 0.4-1 Hz QPO also occur in the persistent flux. Smooth transitions from one QPO type to another have been observed. The frequencies are not the same as the Z source QPO and so it is uncertain whether the rapid burster QPO are directly related.

Narrow ($\Delta\nu/\nu = 0.11$) low frequency (0.0751 Hz), 3% rms strength, QPO have been observed from the black hole candidate LMC-X-1 (Kitamoto 1989). This QPO peak is transient.

A similar (0.05Hz, 20 sec) QPO has been observed from GX339-4 during a high, active state. More remarkable is the discovery of intensity dependent ~6Hz QPO from this black hole candidate with occasionally a strong 2nd harmonic. Three types of VLFN, which are dependent upon GX339-4's position on a colour-colour diagram, are observed (Kitamoto 1989). The black hole candidature of GX339-4 is based upon its ultra soft spectrum, two state behaviour and rapid variability. These properties are similar to Cyg X-1 . However, the reported discovery of a 1·13 msec periodicity would imply the presence of a neutron star within the system (Imamura et al. 1987). This detection has not been confirmed but a 190 sec periodicity has been found which could be the rotation period of a neutron star.(Steinman-Cameron et al. 1990).

A natural testing ground for the beat frequency model are the X-ray pulsars. Here the neutron star's rotation is clearly discernible. The analysis problem is to separate any QPO/noise signal from the pulse period. This has been done for the X-ray pulsars, Cen X-3, EXO2020+37, and 4U1626-27 (Nagase 1989, Agellini 1989). The observed QPO frequencies are consistent with either the beat frequency or Keplerian frequency models. However, the implied rotation frequency of the inner

edge of the disk is inconsistent with accretion torque theory used to successfully explain the spin up/down behaviour of the X-ray pulsars.

2.3.3 QPO Models

Numerous models have been proposed to explain the "Z" source QPO. (see Lewin, van Paradijs, van der Klis 1988 for a review). Only one model has been definitely excluded by the available observations. If the QPO's are produced by non-radial g mode vibrations of the neutron star the 2nd harmonic should be at a frequency $\sqrt{3}$ greater than the fundamental. Second harmonics are observed at double the QPO frequency.

Other models include photon reflection off the inside of an accretion disk funnel, transient hot spots within the magnetosphere/disk boundary layer, occultation models, and general relativistic instabilities. Reflection and hot spot models have difficulty explaining the 5% rms strength of the QPO. Occultation models are still viable. There is considerable evidence for structure in the rim of accretion disks (i.e. partial eclipses of burst sources). A general relativistic instability at about 3 times the Schwarzschild radius can explain the 6Hz mode QPO. Such a model would be applicable to both neutron stars, with and without magnetic fields, and to black holes. The most detailed and strongest model is still the beat frequency model originally proposed by Alphar and Shahan (1985) and recently updated (Lamb 1989) to present a unified model of the accretion flow, spectral changes and the QPO's in the Z sources.

In this model the relatively weak (B ~10^8-10^9G) magnetic field of the neutron star disrupts the accretion disk 10-15 km above its surface. Inside the magnetosphere the flow is slowed by outward radiation pressure. The inflow is nearly radial and relatively cool (i.e.≈1 keV).

Surrounding this region is a hot (i.e. 10-20 keV) less dense inner disk corona. At accretion rates near the Eddington luminosity (>0.9 L_E) this region is overlaid by a cooler (i.e. ≈1 keV) disk corona. The hot inner corona Comptonizes the outward moving photons producing the harder (2 keV) component in the medium energy spectrum and the millisecond delays between the hard and soft photons seen in QPOs.

The horizontal branch QPOs correspond to the lowest accretion rates (L_X ~0.5-0.9 L_E). Here the beat frequency model is operative. At higher accretion rates (L_X ~0.9 - 0.95 L_E) opacity/luminosity instabilities in the radial inflow region produce the ~6 Hz mode QPO. The frequency of the oscillations is approximately twice the settling time-scale of the radial inflow. The settling time-scale depends upon the inflow velocity and the radius of the inflow region which both depend upon how close the source is to the Eddington limit. This explains the dependence of central frequency on source intensity. Also explained is the spectrum of the 6Hz QPO. The opacity variations cause the spectrum to rock about the electron temperature (~5 keV). This temperature corresponds to the energy at which the 6Hz QPO has the lowest strength (Lamb 1989 and references therein).

At $L_X > L_E$ the radial inflow becomes broken up into dense inward moving plasma and outward bound photon/hot plasma bubbles. The flow becomes unstable and photon hydrodynamic (PHD) oscillations can be set-up. When the luminosity increases the photon bubbles expand compressing the incoming plasma causing the frequency and amplitude of the PHD oscillations to increase. At a sufficiently high luminosity a wide range of PHD modes will be excited. The PHD oscillations are used to explain the FB QPO, which dissolve into a broad noise continuum at high L_X.

2.4 Sco X-1

Sco X-1 was the first extra solar X-ray source discovered and subsequently identified with an optical counterpart. It is one of the brightest X-ray objects in the sky. Since discovery it has been extensively studied at many wavelengths. In many ways it is considered as the prototype of the high luminosity, low mass or "bulge" X-ray binaries. However, Sco X-1 has features that set it apart.

The optical counterpart is a relatively bright, 13th magnitude, blue (B-V=0.2) star. It has been found to be variable on time-scales from seconds to days. The historical range is m_b=11.8 to 13.7. Night to night variations are about one magnitude. Smooth brightness changes of about half a magnitude occur in hours and there are flares with rise times ≥ 20 sec (Petro et al.1981). There is also 0.2 mag. flickering. These variations should be compared with an orbital modulation of only 0·22 magnitudes.

The photometric period of 0·787313±0·000001 day (Gottlieb, Wright and Liller 1975) is confirmed as being the orbital period by radical velocity measurements (La Sala, Thorstensen 1985 and references therein). The orbital elements of Crampton, Cowley, Hutchings and Kaat (1976), hereafter CCHK, yield a velocity amplitude of ~60kms which implies a mass function 0·016M⊙ and $a_x \sin i = 6 \times 10^{10}$ cm. A low inclination (~30°)is considered to be most likely because there is little or no orbital variation in the weak emission lines (CCHK), at X-ray wavelengths (Priedhorsky Holt 1987) or in the optical (Gottlieb, Wright and Liller 1975, Wright et al. 1975). Assuming an X-ray object mass $m_x = 1{\cdot}3 M_\odot$ then i is 25°-30° and the companion mass is 0·8-1·2M⊙. This is consistent with upper limits set by the lack of any absorption lines in the spectrum. In order to power the X-ray emission the companion must be undergoing Roche lobe overflow. Given the above $a_x \sin i$ the companion must be slightly evolved (Cowley and Crampton 1975).

The distance to Sco X-1 is rather uncertain because of the variable interstellar extinction in the region. The most comprehensive analysis of the reddening in the region was carried out by Kunde (1987) who found a distance of ~250pc. Such a distance is consistent with the reddening of the stars closest to Sco X-1, IRAS 100μm measurements and soft X-ray hydrogen column densities. This contrasts strongly with the often used distance of ~700pc (Bradt and McClintock 1983).

There are two possible origins for the emission lines (HeII, H Balmer, CIII/NIII), the disk near the compact object, or the heated face of the star (Milgrom 1976). CCHK argue that the latter option would lead to an unreasonably large mass for the companion. Observations of simultaneous X-ray and optical flares (Petro et al. 1981) indicate that the reprocessing site is much nearer to the compact object.

During the numerous multi-wavelength observing campaigns (Mook et al. 1975, Bradt et al.1975, Canizares et al. 1975, White et al. 1976, Ilovaisky et al. 1980, Willis et al. 1980, Petro et al. 1981, Wood et al. 1989). Sco X-1 has been seen to have two distinct states, a bright active state and a faint quiescent state. The threshold brightness is about $m_B = 12.7$

In the active state Sco X-1 exhibits rapid flickering and flaring at both optical and X-ray (<30 keV) wavelengths. Generally the optical/X-ray correlation is good. However X-ray flares have been observed without any optical counterparts and vice versa. In the X-ray region flares have short (<3 sec) rise times (Petro et al.

1981) while at optical wavelengths the flares are smeared on a timescale of up to 20 seconds. At higher energies (>20 keV) the fastest timescale variations seen are ~10sec (Jain et al. 1984), but this may be due to statistical limitations on the detectability of faster variations.

2.4.1 Site for Optical Smearing

The optical smearing suggests that most of the optical flux is due to reprocessed X-ray radiation. The site of the optical smearing is somewhat of a mystery. The obvious site for the optical flux is the X-ray illuminated face of the companion star. Observations by Petro et al. (1981) show that there is no delay greater than 3sec between the optical and X-ray flares. At the time of these observations, given the orbital elements of CCHK, the projected X-ray source to companion distance was 8-9 lts. Therefore the companion can not be the reprocessing site.

Reprocessing can also occur within the accretion disk. Since the disk is symmetrical about the X-ray source the difference in light travel time between the near and far edges of the disk will be zero and so there will be no measured time lag between the X-ray and optical flares. Even if the disk extends all the way to the inner Lagrangian point it would be only 4.4 lt.sec. across. Thus geometrical smearing caused by the light travel time across the disk could not account for the 20sec optical smearing time-scale. Another source of smearing is the time it takes to reprocess the X-rays (Illarionov and Sunyaev 1972). At energies below 8keV both Chester (1979) and Pederson et al. (1982) agree that reprocessing will be prompt; taking the X-rays less than a second to penetrate the disk and be re-radiated as optical photons. However at energies above 8keV (Chester) or >15keV (Pederson) the reprocessing time is of the order of 10sec. There is evidence that Sco X-1 does flare at these energies (e.g. Jain et al. 1984). The combined effect of slow reprocessing of hard X-rays and geometrical smearing could produce optical smearing on time-scales close to 20sec. In this picture there is still no delay between the softer X-ray s (as observed by Petro et al. (1981)) and optical flares because these X-rays would be re-processed promptly. There should be a delay, due to reprocessing, between a coincident hard (>20keV) flare and the corresponding soft X-ray or optical flare.

Another possible site for the optical smearing is in a surrounding corona. The optical depth needs to be greater at optical wavelengths than in the X-ray region. Just such an increase in optical depth at lower frequencies is required to match the

optical/infra-red flux with the 5 keV thermal bremsstrahlung spectrum at X-ray energies (Chodil et al. 1968, Mark et al..1969, Neugebauer et al. 1969) . In this model (Felten and Rees 1972) the infra-red to X-ray spectrum can be reproduced by considering the effects of both Thompson/Compton scattering and free-free absorption upon a thermal bremsstrahlung source buried inside a uniform spherical corona.

The absorption coefficient for free-free transitions with respect to frequency ν is given by

$$\kappa_{ff}(\nu) = 0.01778 \frac{N_e^2}{T^{3/2}\nu^2} G(\nu,T)$$

The Gaunt factor $G(\nu,T) = \frac{\sqrt{3}}{\pi} \ln\Lambda$

where $$\Lambda = \frac{4kT}{\gamma h\nu} \approx 4.7\text{x}10^{10}\, T/\nu \qquad 2.1$$

where N_e is the number density of electrons, ν is the frequency, T the temperature. The Gaunt factor $G(\nu,T)$ with $\gamma=1.781$ is a good appropriation when the temperature is $>3.6\text{x}10^5$K and for frequencies greater than the plasma frequency. The resulting optical depth $\tau_{ff}(\nu) = \kappa_{ff}(\nu)*R$ (κ_{ff} is the free-free cross section and R is the radius of the absorbing cloud). The Thompson scattering optical depth (τ_{sc}) is

$$\tau_{sc} = \kappa_{sc}*R = \sigma_T N_e = 6.65\text{x}10^{25}\, N_e\, R \qquad 2.2$$

where and σ_T is the Thompson scattering cross section for electrons and κ_{sc} is the scattering cross section. At low frequencies where the optical depth due to free-free absorption dominates that due to Thompson scattering the emergent spectrum follows the Rayleigh-Jeans law i.e. flux $\propto \nu^2$.

At the highest frequencies (X-rays) Thompson/Compton scattering dominates and the resulting flux falls rapidly. The exact shape of the X-ray spectrum depends upon τ_{sc} and energy redistribution effects of Compton scattering (e.g. Felten and Rees (1972), Sunyaev and Titarchuck 1980). At these energies the cloud is optically thick and so the photons must random walk their way out of the scattering

medium. Calculations based upon pure Thompson scattering by Sunyaev and Titarchuck show that the majority of photons escape after

$$\tau_{escape} \approx 0.3\tau_{sc}R/C \qquad 2.3$$

seconds (C is the speed of light).

At intermediate frequencies where κ_{ff} and κ_{sc} are comparable the final spectral flux is proportional to frequency. In the case of Sco X-1 this occurs at optical and ultraviolet wavelengths. As in the case when free-free absorption dominates the absorption mean free path is $S=1/\kappa_{ff}$, and the photons undergo scattering and so they random walk through the cloud. The mean depth of penetration is $x_1 = 1/\kappa_{sc}*\sqrt{N}$ where N is the number of steps of length S. Therefore since $N=\kappa_{sc}/\kappa_{ff}$ then $x_1 \approx \sqrt{\kappa_{sc}*\kappa_{ff}}$. The number of steps required to leave the cloud is $N_{cloud} = R^2/x_1^2$ and so the escape time is

$$T_{escape} \approx \left(\frac{R^2}{x_1^2}\right)\left(\frac{x_1}{C}\right) = \frac{R^2}{(x_1 C)} \qquad 2.4$$

When typical values of cloud radius and electron number density, as derived for low (~250pc rather than 1kpc) source distances by Chodil et al. the escape times are less than one second. This estimate is similar to that made by Pederson et al..(1982) and is not surprising since the value of τ_{ff} require to match the optical flux is only ~0.6.

Of the three possible smearing sites considered only a combination of both geometrical and radiative reprocessing timescales can give rise to optical smearing timescales of the order of 20 seconds. More exotic sites such as an extended cloud ejected by Sco X-1 have been suggested Petro et al. (1981).

2.4.2 Tri-modal Behaviour.

During the quiescent state the correlation between optical and X-ray (<20keV) flux changes is less definite. The optical flux can change by 0.5 mag. without any noticeable difference in the X-ray flux. The reverse has also been observed. While no X-ray or optical flares occur during the quiet state, Sco X-1 does flare at radio wavelengths. Flux changes from ≤20mJy to 250 mJy in an hour have been observed. Radio flares occur about 15% of all observations. At most times Sco X-1 undergoes erratic radio flux fluctuations that bear no apparent relation to

optical or X-ray variations (Wade and Hjellming 1971). A modern appraisal (Pennix 1989) of this radio behaviour in terms of the "Z" source model confirms that Sco X-1 only flares when in the horizontal branch. This is similar to the radio performance of Cyg X-2 and GX17+2 (Sco X-2).

A systematic study of optical spectral changes with state has not been undertaken. During various radial velocity studies it was noted that the Balmer lines are strongest when Sco X-1 is optically faintest and the reverse is true for the HeII lines (Cowley and Crampton 1975, Crampton, Cowley, Hutchings and Kaat 1976, Willis et al. 1980) The HeI lines also show similar changes with brightness (Edwards-Chesley 1975). All the optical emission lines have been noted to undergo rapid (~5 minute) timescale variations in profile (Willis et al. 1980). In the UV, the continuum and emission line intensities are found to be state dependent, both being fainter in the NB (quiescent state) than in the flaring branch (Willis et al. 1980, Vrtilek 1989).

Long period (20-120sec) quasi periods have been noted during optical photometry of Sco X-1 (see Frohlich 1973 for a summary). These are not to be confused with the fast (6-30 Hz) X-ray quasi-period oscillations (QPO's) discovered by Middleditch and Priedhorsky (1986). The first indications of X-ray QPO are in the observations of Angel, Kesterbaum and Novick (1971). Further analysis, (Priedhorsky et al. 1986, and van der Klis et al. 1987) showed that the properties of the X-ray QPO and red noise components were dependent upon the state of Sco X-1 .

A plot of X-ray hardness v intensity clearly displays two branches connected at low intensities. These branches correspond to the quiescent and flaring states. When faintest 5.9-7.9 Hz , 1Hz FWHM, 4.2-6.6%rms QPO's are observed. In this 6Hz mode the centroid frequency is only weakly correlated with intensity ($f_c \propto I^{-0.52\pm0.06}$). In contrast to GX1-5 the associated red noise is weak, being $\leq$3% rms in the quiescent state of Sco X-1. The 6Hz QPO are only observed at the lowest flux levels. When the source brightens, while remaining inactive, the QPO slowly disappear while the red noise becomes stronger. The quiescent state is identified with normal branch of the "Z" source LMXB.

The transition to the flaring branch can be rapid (~100sec). During this period the QPO frequency increases from 7Hz to 18Hz, and the width increases from ~3.5 to

7 Hz without any obvious correlation with intensity. The red noise remains below 3% in amplitude.

In the active state 10-20Hz QPO are observed with the central frequency strongly correlated with intensity (i.e. $f_c \propto I^{\alpha}$ where $\alpha=3{\cdot}15\pm0{\cdot}2$). As Sco X-1 increases in brightness during flares, the QPO increase in central frequency, broaden and decrease in amplitude. At the highest intensities the QPO dissolve into a broad continuum of excess power.

Recently a horizontal branch has been observed in Sco X-1 (Hasinger, Priedhorsky, Middleditch 1989). In this state the hardness remained constant as the intensity varied. At this time a 2Hz feature was observed. This can be described as either a peak or a broad continuum that has been cut off. GX17+2 also shows a 2Hz feature in the horizontal branch (Langmeier et al. 1985). In all states VLFN is observed varying from <0·1% in the horizontal branch, 1.3%-1.6% while 6Hz QPO were present through to 3.6% in the flaring branch. Also apparent is a high frequency noise (HFN) component. This is a flat noise continuum (3%-6% rms) with a cut off at ~60Hz.

The tri-modal hardness intensity behaviour of Sco X-1 place it firmly amongst the "Z" sources. The flaring branch, with its large ~10min long, flares, has no exact counterpart amongst the other bright LMXB except for GX17+2 (Sco X-2). These two sources are the only LMXB to show flaring branch QPO's (Pennix et al. 1989). In the horizontal branch, other Z sources have QPO's whose frequency (20-50Hz) are strongly connected with source intensity.

As with other Z sources no sudden changes in state have been observed. There have only been smooth transitions between adjacent states i.e. HB-NB and NB-FB apex.

2.4.3 Coherent Periods?

Early optical searches for coherent signals from Sco X-1 were unsuccessful. See Frohlich (1962) for a summary. In the 100 to 500 Hz range, Frohlich found a 3% p-p upper limit.

Similar searches in the X-ray region have found no pulsations. An upper limit of about 1% rms was set over the 3-330 Hz range by Boldt, Holt and Serlemitsos

(1971). In the 1-12 keV band Friedman et al. (1969) set a similar upper limit over the 0.25-14 Hz range.

The conjecture that the neutron star in bright LMXB should have millisecond rotation periods (Alphar and Shaham 1985) prompted more sensitive searches. Middleditch and Priedhorsky (1986) set upper limits of 0.8% rms over the 0-250 Hz range. They found a candidate period at 270.73383(±2)Hz (4·53 msec) which they rejected because it showed no orbital Doppler shifting. A 2.93 msec (341 Hz) period was reported by Damle et al. (1987,1989). When folded at this period, the resulting, 18-40 keV pulse profile was a broad sinusoid. However using March 12, 1986, 5-35 keV, EXOSAT data Hasinger and van der Klis (1987) set stringent (99% confidence) upper limits of 0.4% for any coherent signal in the 338-344 Hz range. With the same data more general upper limits (with 95% confidence) of 0.3% (1-200 Hz), 0.5% (200-1000 Hz), and 0.7% (1000-2000 Hz) were set by Hasinger, Priedhorsky and Middleditch (1989). Neither of the two reported periods has been detected (3σ level) in 200 GeV γ-ray data (Brazier et al. 1990). The same authors set a 2.5% limit to any pulsed emission with periods greater than 2 msec.

2.4.4 X-ray spectrum.

The X-ray spectrum of Sco X-1 can be split into two regions; above and below 20 keV. This break is partially due to differences in behaviour in the two energy bands. The distinction is mainly made because all balloon observations are limited by atmospheric absorption to energies greater than 20 keV. Most satellite experiments have been insensitive above 20 keV. At soft energies (<2 keV) interstellar absorption becomes important. This spectral region is also where abundant, atomic species have lines and absorption edges.

Initially the X-ray to infra-red spectrum was fitted by a thermal bremsstrahlung model with a single temperature of ≈5 keV (Chodil et al. 1968). In the medium energy (>2 keV) X-ray band the plasma cloud was considered optically thin while toward longer wavelengths the cloud becomes progressively more optically thick. Thus at optical and infra-red wavelengths the flux is significantly suppressed by free-free absorption (e.g. Chodil et al. 1968). Most of the early X-ray observations (2-40 keV) could be fitted with a thermal bremsstrahlung spectrum with a temperature between 2 and 8 keV. A positive correlation between X-ray brightness and apparent temperature became well established. This correlation was

dubbed Sco X-1 behaviour and so Sco X-1 became the prototype for the bright galactic bulge sources (Mason et al. 1976). Comptonization naturally explains the temperature intensity correlation as an increase in optical depth. Later higher quality medium energy (<20 keV) observations required some Comptonization to successfully model the spectra (Lamb and Sanford, 1979; White, Peacock and Taylor 1985).

For Sco X-1 the equivalent width of the iron line has been measured as 25-50 keV by White Peacock and Taylor (1985) and as ~40 ev by Suzuki et al. (1984). Comptonization provides the most plausible explanation for the broadness of the line. The line energy of 6.7 keV and equivalent width implies that the Comptonizing cloud has a temperature $2\text{-}4\text{x}10^7$ K.

A single emission region model even with Compton scattering and free-free absorption at optical wavelengths , does not however explain the optical colour changes. The optical emission lines must originate in a cooler ($T \sim 10^5$K) region than the X-rays. This second region is probably a hot spot where the matter stream from the companion impacts the disk (Crampton and Cowley 1975), rather than the X-ray heated face of the companion star (Milgrom 1976). There is both correlated and uncorrelated X-ray/optical behaviour, once again suggesting two distinct emission regions (Canizares et al. 1975, Ilovaisky et al. 1980). The Comptonizing region must also be distinct from the X-ray source since there is no modulation in iron line properties with the orbital period. During flares the iron line remains unchanged while the X-ray continuum brightens and hardens. If the continuum and iron line were produced in the same site the line would be expected to widen during a flare (White and Mason 1985). The site of the flares is either near the neutron star or, at the hot spot. The Compton scattering is thought to originate in a corona surrounding the neutron star and inner disk (White, Peacock and Taylor, 1985).

This picture is supported by more recent medium energy spectra that are be best fitted with two components. One component is a ~2 keV blackbody while the other is variously considered as a multicolour blackbody (Mitsuda et al. 1984), an unsaturated Comptonized spectrum (White, Peacock and Taylor 1985) or thermal bremsstrahlung (Vacca et al. 1987). In all two component models the blackbody component increases in temperature and intensity during flares. A similar result is derived from X-ray colour-colour diagrams of numerous LMXB (Shultz, Hasinger and Trümper 1989). The range in temperature is 1-2 keV while the black body

intensity increases from 20 to 40% of the total 5-35 keV flux. The other softer component of the spectrum remains constant in temperature (~1 keV) and intensity. The blackbody component has been identified with the inner accretion disk or boundary layer between the neutron star's magnetosphere and the inner disk. The multicolour or Comptonized component is associated with the accretion disk and overlying corona.

At high energies (>20 keV) the spectrum of Sco X-1 can be adequately modelled using a thermal bremsstrahlung spectrum including an energy dependent Gaunt factor. Such a spectrum is equivalent to the unsaturated Compton component used at lower energies by (White, Peacock Taylor 1985). Their spectral model is of the form

$$I(E) = E^{\Gamma} \exp(-E/kT) \qquad 2.4$$

which is just a generalization of a thermal bremsstrahlung spectrum. The E^{Γ} term can represent either Comptonization or an energy dependent Gaunt factor. The temperature is generally determined as being between 2 and 10 keV, with the majority about 5 keV. The intensity at 30 keV varies from ~5×10^{-4} to 2×10^{-3} photons $sec^{-1} cm^{-2} keV^{-1}$.

At balloon energies (E>20 keV) Sco X-1 displays similar time variability as at lower energies. The bright active state and quiescent state are still evident. Presumably the hard and medium energy fluxes act in tandem but there are very few observations that cover the entire X-ray region. At hard energies the fastest time scale for flux variations is about 10 sec. Unlike at medium energies, there is no strong evidence for a positive correlation between temperature and the intensity above 20 keV (see Jain et al. 1984 and references therein).

Occasionally a hard, flat tail (E>40 keV) has been reported (e.g. Duldig et al. 1983). However, other observations have set upper limits orders of magnitude lower than the observed hard tail flux (Jain et al. 1984 and references therein.) The reality of the hard tail is a strongly debated issue. The major objections stem from the difficulty in determining an accurate background at balloon altitudes. There is also no satisfactory model to explain any hard tail. The hard tail and the intensity-temperature correlation is discussed in more detail in relation to the 1986 observations of Sco X-1 . Note that a hard tail is well established in some sources.

2.4.5 Radio Morphology

Radio maps of the Sco X-1 region show three co-aligned sources. (Hjellming and Wade 1971). The SW and NE components are 2' and 1·3' away from the central source which is coincident with the optical counterpart of Sco X-1 . All three radio sources share the same proper motion (0.03" yr^{-1} at PA 180°) as the optical object, and hence are physically related (Geldzahler, Fomalont and Cohen 1989). The NE component is moving radially away from the core (0.015±0.013"yr^{-1}) with a projected velocity of 35±3km s^{-1}, assuming a distance of 500 pc. The SW component is moving at less than 0.030" yr^{-1}.

The central core and NE lobe are not resolved being respectively <0.01" and <0.07" in angular size (Geldzahler, Fomalont and Cohen, GFC, 1989 and Geldzahler as quoted by Velusamy and Subrahmanya 1989). The SW lobe is resolved into a hot spot and tail by VLA (Geldzahler et al. 1981) and VLBI measurements (GFC 1989). The triple structure of Sco X-1 is typical of many AGN's particularly the hot spot tail morphology of the SW lobe. Two other sources, 1617-153 and 1616-160 are also co-aligned within 3° of the central source (Velusamy et al. 1985, Velusamy & Subrahmanya 1989).

The radio spectrum of the central source was suggested as being non-thermal because of its high surface brightness temperature during radio flares (Hjellming and Wade 1971). A subsequent search for linear or circular polarization set upper limits of 10% and 20% respectively. Both the central source and NE lobe have turnovers at low frequencies (~1·5 GHz) in their radio spectra. The SW component has a power law spectrum with α ~0·75 over the range 0.3-5 GHz (Velusamy and Subrahmanya 1989). If the central source is thermal the ~1GHz turnover and small angular size require a temperature $>10^7$K (Velusamy et al. 1985).

The triple radio source of Sco X-1 is often regarded as a stellar analogue of the similar AGN radio sources. As such a study of Sco X-1 should provide clues to the nature of these extra-galactic sources. However, the properties of Sco X-1 provide several puzzles which have not been resolved.

If the NE component, and to a lesser extent the SW component, are ejected plasmons it is difficult to explain why such small bright sources are moving so slowly and also not rapidly dissipating. Self gravitation requires a mass of

$>10^{-3}M_{\odot}$ which would be seen on photographs. Ram pressure is inoperative because of the low velocity. Confinement by a hot external gas, such as that of a young (4000 year old) supernova remnant (Kundt, Gopal-Krishna 1984) is ruled out since no accompanying X-ray (Geldzahler and Hertz 1987) or extended radio emission (Geldzahler et al. 1981) has been detected.

In the magnetic focussing model (Achterberg, Blanford and Goldrich 1983) the central core generates a strong toroidal magnetic field about the beam, focussing it at the hot spots, i.e. the NE and SW components. At the hot spots the beam becomes dissipative because of internal shocks. After the hot spot the beam spreads and is eventually stopped by ram pressure of the ambient medium. Since the beam is not stopped at the hot spots there is little outward pressure and so the spots do not move rapidly. In this model the end points of the beams correspond to the co-aligned sources 1617-153 and 1616-160. Since these outrigger sources are 31.6' and 18.3' away from the Sco X-1 the implied expansion velocities are 600 and 1000 km s^{-1} respectively. In this case both out-rigger sources can be confined by ram pressure. This model predicts a conical shape for the hot spots, with the apex pointing towards the central source. The SW component is resolved and has a conical shape but with the apex away from Sco X-1 .

Although other X-ray binaries are variable radio sources only two others have similar morphology i.e. SS433 and Cyg X-3. A map of Cyg X-3 is given in Figure 9.19 of Hjellming 1988 (contains a review of LMXB radio emission). Also note that both Sco X-1 and Cyg X-3 have been detected at γ-ray energies. The mechanism producing the collimated jets is highly speculative. Achterberg, Blanford and Goldrich (1983) pointed out that the calculated base radius of the jets of Sco X-1 is comparable to the size of the accretion disk. The disk probably provides the collimation mechanism. The thick disk model of Shakura and Sunyaev (1973) is compatible with similar models used to explain the X-ray spectrum and QPO (Lamb 1986). This model includes the presence of a geometrically thick accretion disk corona with a central channel. Such a channel could conceivably collimate outflowing material. Along similar lines, Bell (1990) has suggested that anisotropic inverse synchrotron absorption collimates the outgoing radiation in AGN. The jet material is then radiatively accelerated along the central funnel in the thick disk. Alternate models are discussed by Begelman and Rees (1984).

2.5 X-ray Pulsars

The X-ray pulsars are a marked contrast to their radio counterparts. Radio pulsars have spin periods of between a few milliseconds and about 3 seconds and all have generally lengthening periods. Most are single. There are only four X-ray pulsars with properties similar to radio pulsars, i.e. Crab, Vela, MSH 15-82 (=PSR 1509-58) and PSR 0540-69. All are associated with supernovae remnants. Only the Crab and Vela pulsars have been extensively studied at X-ray wavelengths. The Crab pulsar has a doubled peaked pulse profile at all wavelengths. The Vela pulsar shows no X-ray pulsations but emits pulsed radiation at radio, optical and γ-ray wavelengths. Non-pulsing point like X-ray sources are associated with a few other supernovae remnants. The X-ray spectrum of the Crab pulsar/nebula is a power law with index α=-2. The spectrum is produced by synchrotron radiation. All the single X-ray pulsars are considered young compared to the bulk of the radio pulsars.

In contrast the ~30 known X-ray pulsars are all in binary systems and are powered by accretion onto the neutron star via either Roche Lobe overflow or a strong stellar wind. They have periods, uniformly distributed between 69ms (A053-668) and 835 sec (X Per). Orbital periods range from 0.0228 days (4U1626-27) to 537 days (X Per). The pulsars that have been regularly monitored, have shown a wide variety of spin period histories: including spin downs and sustained spin up. Rates of period change range from $-\dot{P}/P$ 10^{-2} to 10^{-6} yr^{-1}. The pulse is usually very broad having a duty cycle near 50% as compared to ~3% for the radio pulsars. The difference in spin histories, period distribution and radiation emission are all due to the difference in power source.

2.5.1 Low Mass X-ray Pulsars

One group of X-ray pulsars have low mass companions e.g. Her X-1, 4U1626-67, GX 1+4 and possibly 1E2259+583 and OAO1657-415. Like other LMXB the optical flux is dominated by the accretion disk. The companions have absolute magnitudes of $M_V > 3$. Her X-1 has a companion mass of $1.99 \, ^{+0.12}_{-0.14} \, M_\odot$ and as such is sometimes considered as a borderline case between the high mass X-ray binaries (HMXB) and LMXB. The pulse period of 1.24 sec is seen at both X-ray and optical wavelengths. The optical pulsations appear to come from X-ray reprocessing within the atmosphere of the companion. The system also shows a 35 day on/off cycle which is accompanied by pulse profile changes. One suggested

explanation is precession of the neutron star. The compact binary pulsar 4U1626-67 also has both optical and X-ray pulsations with a period of 7.68 sec. The optical pulses, from the faint (v=18.7) counterpart, have two periods separated by 4 mHz presumably due to beating with the orbital period. This indicates an orbital period near 2491 sec. The orbital radius is thus implied to be ≈1Lt s. and the companion mass is <0.5 Mʘ. Pulse timing analysis of 1E2259+583 and OAO 1657-415 have set upper limits of 0.2 Lt s. and 2 Lt s. respectively for the values of $a_x$sini. Both systems are thus considered LMXB. The mass of the optical counterpart of GX 1+4 has not been directly measured but it is expected to be low because the orbital period is long (>20 days).

2.5.2 The High Mass X-Ray Binaries

Most of the X-ray pulsars have massive, luminous, companions which dominate the optical properties of the system. The overall L_x/L_{opt} ratio is less than ten which is far less than for the LMXB. These optically bright high mass X-ray binaries (HMXB) are divided into two broad groups based upon the nature of their companions. One group have supergiant O-B type companions and can be split into two sub-groups. One sub-group have short pulse periods and because of their high X-ray luminosity (L_x 10^{37}-10^{38} erg s^{-1}) are thought to be powered by Roche lobe overflow (e.g. Cen X-3, SMC X-1). The orbital periods tend to be <10 days. The other subgroup have longer pulse periods (>100 sec) and larger orbits (P_{orb} up to 41 days) e.g. GX 304-1, X Per. They are thought to be powered by accretion from the strong, 10^{-6}-10^{-10} Mʘ y^{-1}, stellar wind of the companion which nearly fills its critical potential lobe. The supergiant companions show ellipsoidal light variations of 5-10% amplitude.

The other major group of HMXB are those with Be type companions (e.g. 4U0115+45, GX301-1). The Be stars are rotating near their break up velocity and may shed equatorial rings of matter. Orbital periods of between 16 and 188 days have been found. Most of these systems are hard X-ray transients. Several have elliptical orbits and exhibit regular outbursts. The outbursts cannot be explained solely by the increase in accretion rate as the neutron star approaches the companion and thus probing the denser regions of the stellar wind. To produce the large observed luminosity ranges some enhancing process must be occurring. The high accretion rates at periastron could be caused by crossings of a dense equatorial ring or by intermittent Roche lobe overflow. The irregular transients would be powered by ejections from the Be star.

Significant progress has been made in determining the orbits of many X-ray pulsars. X-ray pulse arrival time analysis yields the radial velocity of the compact object and absorption line radial velocities are available from bright companions. Many of the massive systems have eclipses. These measurement yield estimates of the mass of the neutron star. At present all masses measured are statistically consistent with the canonical mass of 1.4M⊙, although the Her X-1 appears to be lower in mass while Vela X-1 is slightly higher. See Nagase (1989) for a recent compilation.

Generally the pulse profiles are asymmetric sinusoids with an amplitude of 10-90% of the mean flux level. Most have an ≈50% duty cycle. There is a trend of pulse shape with luminosity (White, Swank and Holt 1983, Collmar and Gruber 1989, Nagase 1989 references therein). At low luminosities, 10^{36} erg s^{-1}, the pulse shape is a simple single peaked sinusoid with little or no dependence in shape upon energy. At modest luminosities, $L_X=10^{36}$ to ~10^{37} erg s^{-1}, the low energy pulse profile becomes complex with double or multiple peaks/dips. There is a strong dependence of pulse morphology with energy. Phase shifts of 180° are sometimes observed. At higher energies, (>20 keV), the pulse profile tends to be simple in form with single or double peaked sinusoids. At the highest luminosities, L_X~10^{38} erg s^{-1}, the pulse profile is again simple at all energies. The morphology is usually a double peaked sinusoid. Individual sources, most notably EXO 2030+375, show pulse profile changes, concurrently with brightness changes. Several individual sources are examined by Collmar and Gruber (1989).

2.5.3 Spin Up/Down.

A wide range of spin period histories are observed. These range from no average period change (4U0115+63, 1E2259+586, 4U1145-619, 1E1145·1-614, 4U1538-53) to spin down (Vela X-1) or spin up (SMC X-1 , 4U1626-67) (Nagase 1990 and references therein). Alternate episodes of period decrease and constant period are evident in the timing data for Her X-1, Cen X-3. Recently, GX 1+4 has shown change from sustained period decrease to spin down. Some sources such as Vela X-1, A0535+76, GX 301-2 have random short term (<10 day) fluctuations in pulse period. The latter are all long orbital period systems. The rapid pulse period changes are probably caused by variations in accretion rate from the unsteady wind. Detailed studies of Vela X-1 show that the period variations are consistent with a random walk process in both amplitude and sign in the accretion torques (Boyton et al. 1986).

Amongst the 5 X-ray pulsars that have shown extended periods of continuous spin up (SMC X-1, Her X-1, Cen X-3, 4U1626-67, GX 1+4), there is definite evidence for an accretion disk in four systems. There is no direct evidence for a disk in the GX 1+4 system. However, a disk is required to explain its rapid period change during the 1970's. During the 1970's GX 1+4 had the shortest spin up time scale ($P/\dot{P}$ ~50yr) of any X-ray pulsar. Generally the timescale $P/\dot{P}$ is $2\text{-}6\text{x}10^3$ yr.

Any theory of the accretion process must explain the size and behaviour of the pulse period changes as well as the high luminosity of some sources.

2.5.4 Accretion Torques

The presence of a strong magnetic field will disrupt the accretion disk a distance r_m from the neutron star's centre. At this magnetospheric radius the magnetic pressure is balanced by the inward ram pressure of the disk. Within this radius the flow is dominated by the magnetic field. In the simplest case there is no magnetic threading of the disk, i.e. the velocity at the inner edge of the disk is Keplerian. Also ignored are any other non-material torques. With the above assumptions and in the case where the magnetic axis is coaligned with the rotation axis and both are perpendicular to the disk plane, the spin up rate is given by:

$$\dot{P}/P \approx -3\text{x}10^{-5}\left(\frac{\zeta V_r}{V_{ff}}\right)^{1/7} M_x^{-10/7} R_6^{6/7} I_{45}^{-1} \mu_{30}^{2/7} L_{37}^{6/7} P \ \text{yr}^{-1} \qquad 2.5$$

Here, M_x is the mass of the X-ray emitter is solar masses, R_6 is in units of 10^6cm (10km), I_{45} is the moment of inertia for the compact object in units of 10^{45} g cm^{-2}, μ_{30} is the magnetic moment in units of 10^{30} gauss cm^3, the X-ray luminosity L_{37} is in units of 10^{37} erg s^{-1} and the pulse period P is in seconds. The radial velocity is V_r which is generally assumed to be equal to the free-fall velocity, V_{ff}. The factor ζ represents the fractional solid angle subtended by the in-falling matter at the magnetosphere of the compact star. It is thought to be near unity. Also assumed is that the luminosity is directly proportional to the mass accretion rate. The above equation can be simplified to:

$$\dot{P}/P = -1\text{x}10^{-5} f P L_{37}^{6/7} \ \text{yr}^{-1} \qquad 2.6$$

where f is expected to be ~1 for a neutron star and 0.003 for a white dwarf. A plot of observed $\dot{P}/P$ versus log ($PL_{37}^{6/7}$), e.g. Joss and Rappaport (1984), shows the X-ray pulsars clustered about the trend expected for neutron stars.

In the case where the magnetic axis is perpendicular to the rotation axis, i.e. in the plane of the disk, the spin up rate is given by (Börner as referenced by Nagase 1989):

$$\dot{P}/P = -7{\cdot}9\ \alpha\ M_X^{2/3}\ I_{45}^{-1}\ L_{37}\ P^{4/3}\ yr^{-1} \qquad 2.7$$

In this case, α is the factor expressing the uncertainty of the accretion flow. It can take either sign.

Within the simplified model, where the magnetic and rotational axes are parallel (i.e. equation 2.6), there is no place for spin down episodes. Spin up and spin down do occur and have even been noted in the same system. Thus any complete theory must provide for a change in sign of the accretion torque.

The above theory assumed an infinitely thin boundary layer between an unperturbed disk and the magnetic field dominated region. In the theory of Gosh and Lamb (1979), the disk is threaded by the magnetic field out to a radius r_s. This is generally larger than the co-rotation radius (r_{co}) where the centrifugal forces are balanced by local gravity, i.e.

$$r_{co} = \left(\frac{GM_x}{\Omega^2}\right)^{1/3} \approx 1.5\text{x}10^8\ M_x^{1/3} P^{2/3}\ cm \qquad 2.8$$

where Ω is the angular frequency of the neutron star rotation. This radius can be larger or smaller than the radius of the magnetosphere (r_m). In the case of spherical accretion the magnetosphere boundary is set by the distance where magnetic pressure balances the ram pressure of the infalling material at

$$r_m^0 \approx 2.9\text{x}10^8\ \mu_{30}^{4/7} M_x^{-1/7} R_6^{-2/7} L_{37}^{-2/7}\ cm \qquad 2.9$$

The latter equation is valid if all the kinetic energy of the in-falling material is converted to observable radiation (X-rays). In the case of disk accretion, the pressure balance is replaced by the balance of the pressure gradient against the

gravitational force. For disk accretion the calculated values of inner boundary are $r_m \approx r_m^0$. Note that for a given neutron star the position of the inner edge of the disk is determined only by the accretion rate.

The disk is split into three regions, the outer unperturbed disk ($r > r_s$), the outer transition region ($r_{co} < r < r_s$) and the inner boundary layer ($r_m < r < r_{co}$). See Figure 2.2 reproduced from Gosh and Lamb (1979). If $r_s < r_{co}$, the disk is rotating faster than the neutron star and its magnetosphere and so there is a spin-up torque. This is the slow rotator case which applies to most X-ray pulsars. In the converse case where $r_s > r_{co}$, the magnetosphere is moving faster than the disk and so the star is spun down. In intermediate cases, either spin up or spin down can occur depending upon the relative torque contributions of the inner (spin up) and outer (spin down) boundary transition zones.

Detailed models of the torque accretion are best described in terms of the fastness parameter,

$$\omega_s = \frac{\Omega}{\Omega_k(r_m)} = \left(\frac{r_m}{r_{co}} \right)^{3/2} \qquad 2.10$$

which is defined as the ratio of the angular frequency of the neutron star to that of the matter at the magnetospheric boundary. There is a critical fastness at which neither spin up nor spin down occurs, i.e. $\omega_c = 0.35$. This occurs when $r_m = 0.5\, r_{co}$ i.e. when the transition region is evenly divided between the outer and inner regions.

Considering the extended boundary layer the change in period becomes

$$-\dot{P} = 5{\cdot}0 \times 10^{-5}\, n(\omega_s)\, R_6^{6/7}\, \mu_{30}^{2/7}\, I_{45}^{-1}\, M_x^{-3/7} \left(P L_{37}^{3/7} \right) \quad \text{s yr}^{-1} \qquad 2.11$$

where the numerical value of $n(\omega_s)$ is given approximately by Gosh and Lamb (1979) and is plotted in Henrichs (1983) as figure 11.5.

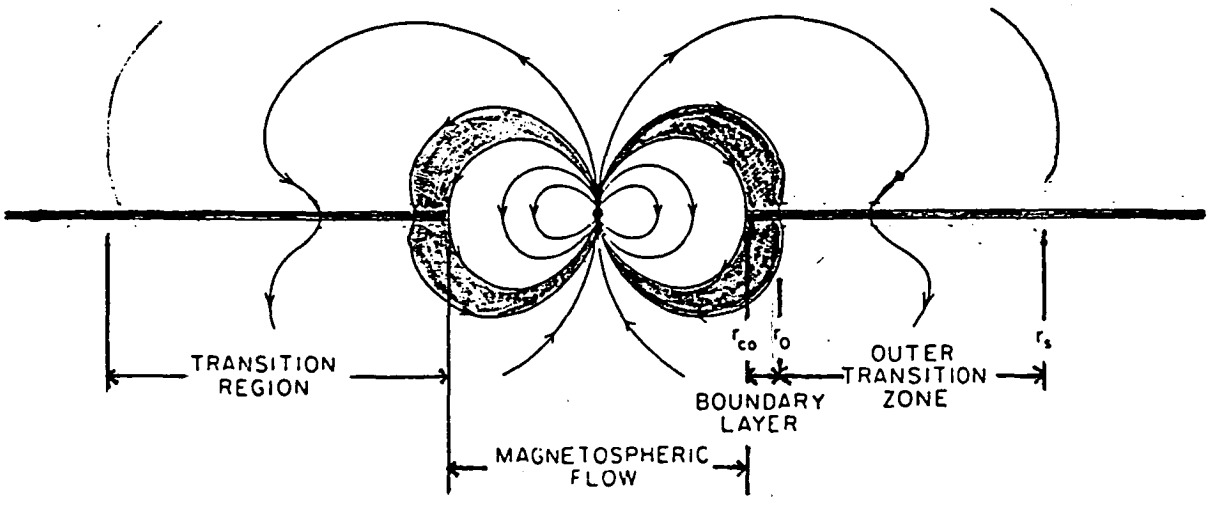

Fig 2.2 A representation of the inner magnetosphere and disk region of an accreting neutron star. Within the corotation radius r_{co} no disk is formed. Between the radii r_{co} and r_o matter is drawn from the disk and funnelled onto the magnetic poles. In the outer transition the magnetic field continues to thread the disk. Outside r_s the disk is unperturbed. This diagram is a slightly modified version of figure 1 of Gosh and Lamb (1979).

In the slow rotator case ($\omega_s << 1$) the period derivative becomes directly proportional to $PL^{3/7}$. When $\omega_s = \omega_c$ the value of $n(\omega_s)$ is more dependent upon $\mu_{30}^{6/7}$ and so $-\dot{P}$ drops below the P v $PL^{3/7}$ extrapolation. When various pulsars are plotted on a log $(-\dot{P})$ versus log $(PL^{3/7})$ graph most fall on curves corresponding to $0{\cdot}48 < M_{30} < 4{\cdot}5$ and with a mass near $1{\cdot}3\ M\odot$. See Figure 11.6 of Henrichs (1983).

With the Gosh and Lamb model there is an equilibrium period where no net spin-up or spin-down is expected. This occurs when $\omega_s = \omega_c = 0.35$ and for a particular neutron star is given by

$$P_{eq} = 3.9\, R_6^{-3/7}\, \mu_{30}^{6/7}\, M_x^{-2/7}\, L_{37}^{-3/7} \quad \text{sec} \qquad 2.12$$

If the magnetospheric radius exceeds the co-rotation radius centrifugal forces expel the incoming material. No accretion takes place and the pulsar switches off. This is called the "propeller" effect. In terms of luminosity no further accretion takes place when the luminosity falls below

$$L_{min} = 2 \times 10^{37}\, R_6^{-1}\, \mu_{30}^{2}\, M_{1.4M\odot}^{-2/3}\, P^{-7/3} \quad \text{erg s}^{-1} \qquad 2.13$$

The mass is in units of $1.4M\odot$ and the period is in seconds. The large range of the outbursts at the recurrent Be transients can be explained by the propeller effect. If the critical accretion rate is reached only near periastron passage, the pulsar will suddenly be turned on and then off as it moves away from the companion star. This causes a large short-duration brightness increase without the need for a large density gradient within the companions stellar wind. The higher luminosity persistent Be star binaries have higher overall accretion rates and so are on for most, if not all ,.of their orbit.

2.5.5 Wind Accretion

Accretion on to the neutron star can take place directly from the wind of the companion without formation of a disc. The early type companion stars of HMXB lose $\dot{M}_c < 10^{-6}\ M\odot\ yr^{-1}$ (Hutchings 1982). Matter is swept up over a cylindrical volume with a radius larger than the neutron star magnetosphere. The accretion radius depends upon the relative speed of the neutron star with respect to the stellar wind. As a fraction of the orbital separation, a, the accretion radius is given by:

$$\frac{r_{acc}}{a} = \frac{2}{1+M_c/M_x} \frac{1}{(1+V_w/V_{orb})^2} << 1 \qquad 2.14$$

where V_w is the wind velocity from the companion of mass M_c. If the companion mass loss rate is $\dot{M}_c$ in a steady spherically symmetric wind only a fraction will be accreted by the neutron star, i.e.

$$\dot{M}/\dot{M}_C = \frac{1}{1+M_c/M_x}\left(\frac{V_{orb}}{V_w}\right)^4 \frac{1}{\left[1+\beta(V_{orb}/V_w)^2\right]^{2/3}} \qquad 2.15$$

where $$\beta = \left[1-\lambda(R_c/a)^2\right]^2 \qquad 2.16$$

is a factor accounting for the effects of the companion star rotation.

Here R_c is the companion star's radius and λ is the ratio of the rotational angular momentum of the companion to the orbital angular momentum of the neutron star.

The target or leading face of the accretion cylinder captures more matter than the trailing side because there is a non-zero angle between the relative velocity (of the companion star's wind with respect to the neutron star's orbital velocity) and the motion of the neutron star. A density gradient is created across the accretion cylinder. The angular momentum accretion rate, per unit mass of infalling material is given by:

$$\ell = \frac{1}{2}\frac{V_{orb}}{a} r_{acc}^2 \eta \qquad 2.17$$

where η is a numerical parameter which is unity for a uniform radial win (Shapiro and Lightman as quoted by Nagase 1989). Accretion is enhanced if there are radial and azimuthal density gradients within the wind. Using a standard radiatively driven wind velocity law (equation 2.17 is a simplification of equation 19 of Nagase (1989)):

$$\eta = 1 + \frac{7}{4}\left[\frac{a}{r_c} - 1\right] \qquad 2.18$$

There is no azimuthal component involved in this estimate of η. For Vela X-1 , η has been estimated as ~3·4 (Nagase 1989).

The maximum possible change in pulse period for direct wind accretion is given by :

$$\dot{P}/P = 1.3\text{x}10^{-6}\,\eta\,\dot{M}_{16}\,I_{45}^{-1}\,V_{rel.8}^{-4}\,P_{orb}^{-1}\,P_s \qquad 2.19$$

The orbital period (P_{orb}) is in units of days, the relative wind velocity is in units of 10^8 cm s^{-1} and the spin period (P_s) is in seconds. Using Vela X-1 as an example the maximum possible $|\dot{P}/P| \approx 5 \times 10^{-3}$ yr^{-1} which is sufficient to explain the observed period changes (Nagase 1989). This estimate is comparable to the torques possible via disk accretion.

The above calculation assumes that all the angular momentum accreted at the accretion radius is transferred to the neutron star. Numerical simulations indicate that only a small fraction of the angular momentum is actually accreted by the neutron star. Direct wind accretion is therefore insufficient to explain the large spin up/down changes seen in wind fed pulsars.

A disk can form within the stellar wind. The standard criterion for disk formations is that the inner Keplerian orbit is greater than the magnetospheric radius i.e.

$$r_k = \frac{\ell^2}{GM_x} > r_m \qquad 2.20$$

Here ℓ is the specific angular momentum of matter in the Keplerian orbit about the neutron star. This restriction can be translated into a constraint on the relative velocity of the neutron star.

$$V_{rel} < 33\,P_{orb}^{-1/4}\,\xi^{1/4}\,M_X^{5/14}\,\mu_{30}^{-1/14}\,I_{45}^{-1}\,R_6^{5/28}\,L_{37}^{1/28}\ \text{km s}^{-1} \qquad 2.21$$

where the orbital period is in days. The numerical factor, ξ, is near unity. Because of the high wind velocity of early type stars a disk is not expected to form using this criterion.

Börner et al. (1987) have suggested that a disk is formed by the inevitable drag at the magnetosphere/wind boundary. In this model, the neutron star of Vela X-1 is rotating near its equilibrium period ($r_m = r_{co}$), thus a small change in accretion rate (~1%) can cause a change in torque direction. The estimated magnetic moment of

the neutron star is about $\mu_{30}=10^{32}$ g cm^{-3} which corresponds to a surface magnetic field strength of a few times 10^{13} G. This is high compared to those inferred from radio pulsars and other X-ray pulsars. Recent evidence of a 70-96 keV line like excess suggests a strong magnetic field ~7×10^{12} G (Kendziorra et al. 1989).

The wind environment of the companion is variable. The presence of a strong X-ray source also modifies the wind significantly. The X-rays can ionize a substantial fraction of the wind visible to the pulsar (Nagase 1989 p42). Within this ionized region the UV line acceleration mechanism stops and the wind becomes stagnant. Collision between the stagnated region and the radiatively driven wind creates a strong leading shock and dense trailing sheets behind the neutron star. A disk can now form because of the low velocity of the matter near the neutron star. Such a situation explains several observations. Rapid changes in the X-ray absorption column density are thought to arise from the trailing sheets. Iron line emission would arise from the X-ray heated disk. Occultations of the neutron star by the disk can explain occasions when, out of eclipse, no pulses are seen.

More recent 2D numerical calculations by Matsuda et al. (1987) indicate that the disk is not steady. Either a prograde or retrograde disk can form depending upon the exact nature of the stellar wind. Thus, spin reversals can be explained in terms of different rotation senses of a disk formed by a bow shock. In this model a weak ($\leq10^{12}$G) magnetic field is adequate since there is no need to have $r_m \approx r_{co}$.

2.5.6 Continuum Energy Spectrum

The energy spectrum is generally described as a power low (spectral index mostly $0.8 < \alpha < 1.5$) with a high energy cutoff. The cutoff energy, E_{cut}, is usually between 20 and 100 keV and the folding energy (E_f) of the spectrum above the cutoff is 10-30 keV. At low energies an iron line of energy 6.4 keV is observed. The equivalent width is > 100 keV while the intrinsic width is < 0.5 keV. The iron line arises from fluorescence in cool extended circumstellar material. Variable low energy absorption is observed on time-scales ranging from a fraction of the orbital period to years. The strong magnetic field manifests itself as cyclotron lines in the X-ray spectra of Her X-1, 4U0115+63 and possibly 1E2259+586 and 4U1538-52. Results for GX 1+4 are discussed within Chapter 8 of this thesis.

2.5.7 Cyclotron Lines : Observations

Discoveries of cyclotron lines have been made in X-ray spectra in Her X-1 (Trümper et al. 1978), 4U0115+63 (Wheaton et al. 1979) and 4U1538-52 (Clark et al. 1989). Line like features have been reported for 4U1626-67 (Pravdo et al. 1979) Vela X-1 (Kendziorra et al. 1989), X2259+586 (Koyama et al. 1989), GX-1+4 (Maurer et al. 1982) and the Crab Nebula (Ling et al. 1979). Cyclotron lines in the 10-100 keV range have been reported from γ-ray bursters. See Kirk and Trümper (1983) for a review. Any doubts about their reality have been settled by recent observations using the GINGA satellite. Clear cyclotron features have been observed from the γ ray bursters GB880205, GB870303 and possibly GB890929 (Murakami 1989). Also observed from gamma ray bursts are 400 keV, broad emission lines. These are thought to be ~20% red-shifted 511 keV annihilation.

The Her X-1 cyclotron line is the best studied. The line feature can be represented as either an absorption line at ~34 keV or an emission line at ~50 keV. A possible second harmonic at ~110 keV (Trümper et al. 1978) has not been confirmed (e.g. Soong et al. 1990). The central energy varies as a function of pulse phase ranging from 30-37 keV as an absorption line or from 34 to 50 keV as an emission line. The line is strongest near the peak of the pulse (Soong et al. 1990). Recent observations by Mihara et al. (1990) support the absorption line model.

The line feature of 4U0115+63 can be modelled as either an emission line at 11.75±0.75 or a line in absorption at 11.3±0.9 keV. An alternative model is that of a pair of absorption lines: a line at ~11 keV and its second harmonic at ~23 keV. The line at ~11 keV is <5 keV FWHM in breadth. (White Swank and Holt 1983).

Only an absorption line at 21.5±0.51 keV could be fitted to the spectrum of 4U1538-52 (Clark et al. 1990).

The 19 keV hump in the spectrum of 4U1626-67 was found to be phase dependent (Pravdo et al. 1979). However Kii et al. (1986) considered this feature as being produced by Comptonization. After modelling the 0.6-30 keV pulse profiles, they suggested that the cyclotron energy is actually 80 keV.

A marginal emission feature at 7.1±0.1 was found in the general and pulsed spectrum of X2259+586 (Koyama et al, 1989). This is not an iron line feature

which have energies between 6.4 and 6.7 keV. There was no strong pulse phase modulation in the 6.9-11.6 keV band.

Recent HEXE measurements of Vela X-1 show a broad, 70 to 96keV, excess in the spectrum. Above 96 keV the flux is consistent with being zero. During the same observation, a spin period modulation was apparent at all energies observed (28-96 keV) (Kendziorra et al. 1989).

Maurer et al. (1982) reported a broad emission feature at ~42 keV in the spectrum of GX 1+4. It was modulated in strength at the pulse period. A similar feature was found by Beurle et al. (1983).

The Crab Nebula pulsar shows a line at near 70 - 80 keV. This can be interpreted as either as a cyclotron line or Kα emission from lead in the detector (Ling et al. 1979). It has been found to be transient on time scales of 25 min. It appears to be modulated at the 33ms period of the Crab pulsar (Strickman, Kurfess and Johnson 1982).

A pair of cyclotron absorption lines at 19.3±0.7 keV and 38.6±0.7 keV with widths of 4.1±2.2 keV and 14.4±4.6 FWHM have been measured from the gamma ray burster GB 880205. A similar pair of lines were found at 20.4±0.7 keV (3.5±2.7 FWHM) and 40.6±2.6 keV (12.3±6.3 FWHM) from GB 870303 (Murakami 1989).

The cyclotron line spectral shape from X-ray binaries can be represented by a gaussian profile with a width (FWHM) between ~1 keV (4U0115+63) and ~20 keV (Her X-1). The line strength and centroid energy vary systematically during the pulse. The line is only prominent over a limited phase range.

2.5.8 Cyclotron Lines: Theory

In the very strong magnetic field of a neutron star electrons can only move freely along the field lines. Circular movement about the field lines is quantized into the Landau levels. In the relativistic case the spectrum eigen-values are given by:

$$E_{js} = m_e c^2 \left[1 + \left\{ \frac{P_z}{m_e c} \right\}^2 + (2j + S + 1) \frac{B}{B_c} \right]^{1/2} - m_e c^2 \qquad 2.22$$

where P_z is the electron momentum along the field lines, and j = 0,1,2,3 ···· and $s = \pm 1$ are the angular momentum and spin quantum numbers respectively (Trümper 1982). The spin and angular momentum transitions have approximately the same energy. The energy levels are approximately evenly spaced when the transition energy is small compared to the rest energy of the electron. At a critical magnetic field strength, $B_c = 4{\cdot}14 \times 10^{14}$G, the cyclotron energy levels are separated by the annihilation energy of electron/position pairs. In this case electrons and positions are spontaneously created and then annihilate.

In the non-relatavistic limit the energy levels are given by:

$$E_n = n\,\hbar\omega_{cyc} = \frac{n\hbar eB}{m_e c} \approx 11.6\, B_{12}\, E_{cyc}\ \text{keV} \qquad 2.23$$

where B_{12} is the magnetic field strength in units of 10^{12} G, ω_{cyc} is the cyclotron frequency and E_{cyc} is the cyclotron energy in keV. The energy levels must be corrected for the effects of gravitational red-shift which are of the order 20-40% for a neutron star.

Using the above approximation (without red-shift correction) the magnetic field strengths implied by the cyclotron features range from $0.6B_{12}$ (7.1 keV, X2259+589) to 7.3 B_{12} (85 keV, Vela X-1). The second and higher harmonics are potentially very useful. The ratio of the line energies depends mainly upon the magnetic field strength. Once this is determined the actual line energies can be used to find the gravitational red shift. A measure of the red-shift would constrain models of neutron star internal structure. Such an analysis has not been successfully attempted.

Beside cyclotron lines, theoretical studies of the continuum spectrum and the energy dependence of the pulse profile suggest other observable quantities related to the field strength. The spectrum is found to become harder and hence the cutoff energy increases with higher field strengths. The pulse profiles apparently change from a doubled peak to a single peak at about ~1/4 - 1/3 E_{cyc} (Harding et al. 1983, Mézàros et al. 1986). These studies assume that bremsstrahlung radiation is the dominant emission mechanism..

2.5.9 Accretion Cup Theory

After passing into the magnetosphere, probably via Kelvin-Helmholtz instabilities, the accreted material free falls along the magnetic field lines. The strong magnetic dipole field guides the material into two small ($\lesssim$1km) polar caps. Here the plasma is decelerated and the X-ray radiation emitted. Two basic approaches have been taken to model the spectrum and pulse profiles of the outgoing radiation.

One is to consider the flow of the material making simplifications to the radiation transfer process. Conversely the micro-physics is considered and assumptions made about the geometry and conditions within the polar caps. Further, the models can be divided into those where either radiation or gas pressure is considered to be dominant. In high luminosity sources, radiation pressure should be dominant while at low luminosities gas pressure will have a major influence upon the dynamics of the accretion cap. The existence of a shock is uncertain.

The reviews of Kirk and Trümper (1982), Mézàros (1984), Frank, King and Raine (1985) and Storey (1986) have been used as the basis of the following discussion of the theory of neutron star polar cap accretion.

When the luminosity is greater than about $(A/4\pi R^2)\, L_E$, (A is the area of the polar cap, R is the radius of the neutron star and L_E is the Eddington limiting luminosity), the accretion region becomes optically thick, and a radiative shock forms. A two dimensional study of the hydrodynamics of this case is made by Wang and Frank (1981). These authors took approximate account of the magnetic effects upon the Thompson scattering opacities. Behind the shock a dense (~5g cm^{-3}) mound shaped atmosphere of slowly settling gas forms. The gas in this region is in thermodynamic equilibrium. The radiation diffuses sideways, escaping near the base of the column producing a fan beam. If viewed from near the neutron star the emission region would appear as a thin ring about the base of the accretion column. A similar situation was also found in simulations by Kraus et al. (1989) which include a comprehensive treatment of both the dynamics and radiation transfer. A significant amount of radiation can also escape along the axis of the column. The height of the column increases, as the luminosity increases, becoming comparable to the neutron star's radius near the Eddington luminosity.

At low luminosities ($<10^{37}$ erg/s) it is uncertain whether or not a shock develops above the pole cap. Without a shock the incoming protons and electrons are

decelerated by either inelastic nuclear collisions or Coulomb encounters. Because of the high free fall velocity (~c/2) the plasma will be stopped, via Coulomb interactions at densities of 20-50 g cm^{-3}. At these densities the optical depth is high (τ~8). Only at the highest densities do nuclear collisions contribute significantly to the deceleration. The energy is thus released within a very thin (~10-200 cm) thick layer. Very little radiation is expected to emerge from the sides of the 'slab' like emitting region, because of the very high transverse opacity. A narrow or pencil beam radiation pattern emerges.

Such 'slab' emitting regions are the starting point of many models that consider the details of the radiation processes. (e.g. Nagel 1981). The strong magnetic field modifies the micro-physics of the accreting plasma. The cross-sections of both Compton scattering and bremsstrahlung have strong anisotropies. Both are resonant at the cyclotron frequency. In magnetic fields near the critical strength there are a large number of virtual electron-position pairs, which cause the plasma to be birefringent (vacuum polarization). Each polarization has different angular resonance emission properties. Most studies only include a subset of the possible effects. A summary of the properties of various early models is given by Wang, Wasserman and Salpeter (1988).

In the low luminosity, gas pressure dominated case a shock can form via Coulomb collisions or the two stream instability. When a shock does form (say via Coulomb collisions), the structure of the emitting region is a column rather than a slab. As in the radiation pressure dominated models most of the radiation escapes out the sides of the column producing a fan beam. Likewise the height of the accretion column increases with both accretion rate and magnetic field strength (Langer and Rappaport 1982).

In a high column the local magnetic field strength will vary significantly over the emitting region. Thus cyclotron absorption will occur over a wide range of frequencies. The output spectrum will drop rapidly up to the cyclotron frequency at the surface. In a short column, the cyclotron frequency is more or less constant over the emission region and so a 'line' feature may be present in the source spectrum.

Even at low luminosities radiation pressure may play an important role. Kirk (1985) proposed a hybrid model where a shock is supported by a thin gas pressure dominated layer. Below the shock in the settling region, radiation pressure

dominates the flow. In this model the inflowing material is supersonic and optically thin above the shock while in the post shock region the plasma is optically thick, in thermodynamic equilibrium and moving subsonically. In the mound shaped atmosphere the velocity is greatest just behind the shock and along the axis of the column. The temperature decreases with distance above the neutron star and radial distance from the magnetic axis. In the shock the temperature approaches $\sim 10^{11}$ K for the ions and $>5 \times 10^9$ K for the electrons. At these temperatures the electrons occupy many Landau levels. This models applies to flows where the luminosity L is in the range $(\Omega/4\pi) < L/L_E < (\Omega/4\pi)^2$ (Kirk 1985). Here Ω is the solid angle subtended by the column.

In most models the dominant emission mechanism has been taken as being bremsstrahlung radiation. However, it has been shown that two photon cyclotron emission dominates both the cyclotron and continuum emission in most X-ray pulsars. In this mechanism the electron excited into the first Landau level decays emitting two photons. Several other two photon transitions are also possible. These cyclotron photons pass through the medium by the process of resonant scattering where photons are absorbed and re-emitted. Two photon emission is used in the model of Kirk 1985 which is extended to include directional anisotropies by Kirk, Nagel and Storey (1986). These authors calculate emergent beam patterns.

2.6 GX 1+4

The binary X-ray pulsar, GX 1+4 was first detected in 1970. (Lewin et al. 1968). The initial observations indicated a pulse period near 2 minutes. A scan of the 2' error circle, from Copernicus satellite observations (Hawkins, Mason, Sanford 1973) revealed a strong infra-red source (Glass and Feast 1973).

Subsequent measurements of the optical spectrum (Davidsen , Malina, Bowyer 1976) showed very strong Hα emission, weaker Balmer and HeI lines, as well as weak high excitation lines such as [FeVII]. Also seen were TiO. bands , identified as those of a M6III giant star. Overall the optical spectrum resembles that of a symbiotic star.

The M6 giant is the most probable, but not certain, optical counterpart in a moderately crowded field. The identification of a pulsating, X-ray source with a

red giant is unique. A finder chart can be found in Davidsen , Malina and Bowyer (1976).

Using the Hα/Hβ line strength ratio and the infra-red colours, the M giant identification implies a reddening, $A_v = 5.1$, and a distance of 10 kpc. The high intrinsic Balmer line ratios and the presence of high excitation lines suggest the star is surrounded by an optically thick cloud with a temperature of $1\text{-}2 \times 10^6$K, radius $\sim 6 \times 10^{13}$ cm and an electron number density of $\sim 10^9 cm^{-2}$ (Davidsen , Malina and Bowyer 1976). The implied density is consistent with the measured X-ray column density of $N_e \sim 4\text{-}10 \times 10^{22} cm^{-2}$ (White et al. 1976). Such a cloud is also required to explain the lack of any optical modulation at the X-ray pulse period (Kreminski and Priedhorsky 1978). Scattering causes the escape time of the optical photons to be long compared to the period. Any initial optical pulsations are estimated to be suppressed by a factor of ~1000.

Radio observations by Duldig (1981) set an upper limit of 5mJy at 2cm. An upper limit of 15mJy was set by Wright (quoted by Duldig 1981). More recent radio mapping have found two weak radio sources near GX 1+4 (Manchanda 1990, IAUC 4871). Neither is co-incident with the optical candidate or the X-ray position of GX 1+4 . There is no 2-10 keV X-ray flux from either position (Skinner et al. 1990, IAUC 4879).

A lower limit of 20 days has been set on the orbital period by the lack of any orbital modulation at X-ray wavelengths (Doty et al. 1981). At longer periods only systems with smaller (<2 $M_\odot$) mass functions have orbits larger than the radius of an M6III star. Based upon, apparently regular changes in the pulse period derivative Cutler, Dennis and Dolan (1986) suggested that the orbital period was 304 days. They postulated that the orbit is eccentric and so upon each periastron passage the mass accretion rate is increased and hence the $\dot{P}/P$ varies. Support for a 304 day period comes from an apparent modulation in X-ray flux during the 1980's. (Greenhill et al. 1989). Another possible cause of a ~300 day change in $\dot{M}$ is a Mira type pulsation of the giant companion.

There is some uncertainty whether the true pulse period of GX 1+4 is ~2 or ~4 minutes. Several authors find that the most prominent period is at 2 minutes (e.g. Coe et al. 1981, Rickets et al. 1982, Dotani et al. 1989). At higher energies there is evidence that the true period is 4 minutes. The most convincing evidence that the true period is near 4 minutes comes from Koo and Haymes (1980) who found no 2

min. peak in their χ^2 periodogram. When the data was folded on a 256.2 sec period only a single peak was found. This contrasts with the double peaked profiles found by Strickman, Johnson, Kurfess (1980) and Kendziorra et al. (1982). The latter authors found that there were significant differences between alternate pulses. Elsner et al. (1985) noted that the intrinsic pulse shape and intensity variations could produce an apparent odd/even pulse difference. Variations between pulses are much greater than expected from counting statistics. This possibility is rejected by Kendziorra et al. because they found greater differences between odd and even pulses than between odd/odd or even/even pulses.In order to inter-compare data taken at different epochs the pulse period is taken as being near 2 minutes.

Until the 1980's GX 1+4 was undergoing continuous spin up (Cutler, Dennis and Dolan 1986, Elsner et al. (1985) contain lists of prior period determinations). The rate of period change was $\dot{P}/P \sim 0.02\ yr^{-1}$; the fastest known of any X-ray pulsar. The luminosity and spin up rate of GX 1+4 is consistent with the compact object being a neutron star rather than a white dwarf.

Between 1980 and 1986 there were very few observations of GX 1+4 . A pulse period could not be determined by Beurle et al. (1983) because of the on/off source rocking motion used. From 1982 X-ray observations at E>180 keV (mean energy 340 keV) Jayanthi et al. (1987) reported a period of 120.6±0.2 sec. Doubt is cast upon this measurement because of the low flux levels and the consequent difficulty in choosing the correct period. Within the analysis two other, apparently less significant periods were found (i.e. 108.8 sec, 112.8 sec.). Two years later, in February 1984, Damle et al. (1989) found a period of 95.2 sec. It is uncertain whether a sufficiently large period range was searched. This period has been subsequently modified to 108 sec (Leahy as quoted by Sako 1990). Since 1986, several measurements of the pulse period have been made including those of the University of Tasmania's ADFA X-ray groups (see Chapter 8). GINGA measurements in March 1987, March 1988 and August 1989 yielded periods of 110.223±0.003 sec.111.59±0.02 113.626±0.002 respectively (Sako et al. 1990 and references therein). When compared to the 1980's trend these observations require a change in period behaviour from spin up to spin down. This change was confirmed by MIR/HEXE observations in October 1987 and September 1988 which showed periods of 111.04±0.05 sec.and 112.359±0.0005 sec. (Mony et al. 1989). The most recent measurement using the MIR-HEXE experiment (Sunyaev et al. 1990) gives a period of 114.60±0.05 sec.

There are three possible scenarios for the pulse period history during the 1980-86 period. If the preferred 120 second period of Jayanthi et al. is correct then GX 1+4 would have undergone a rapid spin down of $dP/dt = 1.7 \times 10^{-7}$ s/s following the Ariel VI measurement in 1980. A similar magnitude spin down has been observed from 4U0900-40 (Hayakawa 1981). Following this spin down, a time of spin up ($dP/dt = 6 \times 10^{-8}$ s/s) comparable to that of the 1970's is required to match the 1987 GINGA observations. Alternatively if the 112.8 sec period of Jayanthi et al. is accepted a similar by less drastic history of spin down followed by spin up is required. The revised period of Damle et al would not fit well into either history. Such a spin up-down history was suggested by Greenhill et al. (1989). The third scenario is one where a gradual change from spin up to spin down occurred. In this case the shortest period of Jayanthi would be accepted while the period suggested by Manchanda et al. would have to be rejected. This final scheme is favoured by Sakao (1990).

Coincident with this change in period derivative there was a marked decrease in the X-ray brightness of GX 1+4 . During the 1970's the X-ray luminosity was near 10^{37} erg s^{-1}. However, EXOSAT observations in 1982 and 1983 failed to detect GX 1+4 . Severe upper limits were set (Hall and Develaar 1983, Mukai 1987). In 1986-1987 the flux was higher, but not at the same levels as reported during the continuous spin down regime of the 70's.

There are no consistent changes in the optical spectrum with X-ray state, on Nov 4 1983, during the low state, no Hα emission was visible. (Whiteoak et al. 1983) However, the Hα line strength was near that of the 1970's during all other observations which included the low state and subsequent brighter, spin down period (Davidsen, Malina, Bowyer 1977). The high excitation lines were invisible in mid 1988 (Gotthelf et al. 1988) but were probably present in 1986 when Cowley, Hutchings and Crampton took their spectrum showing [OIII] emission.

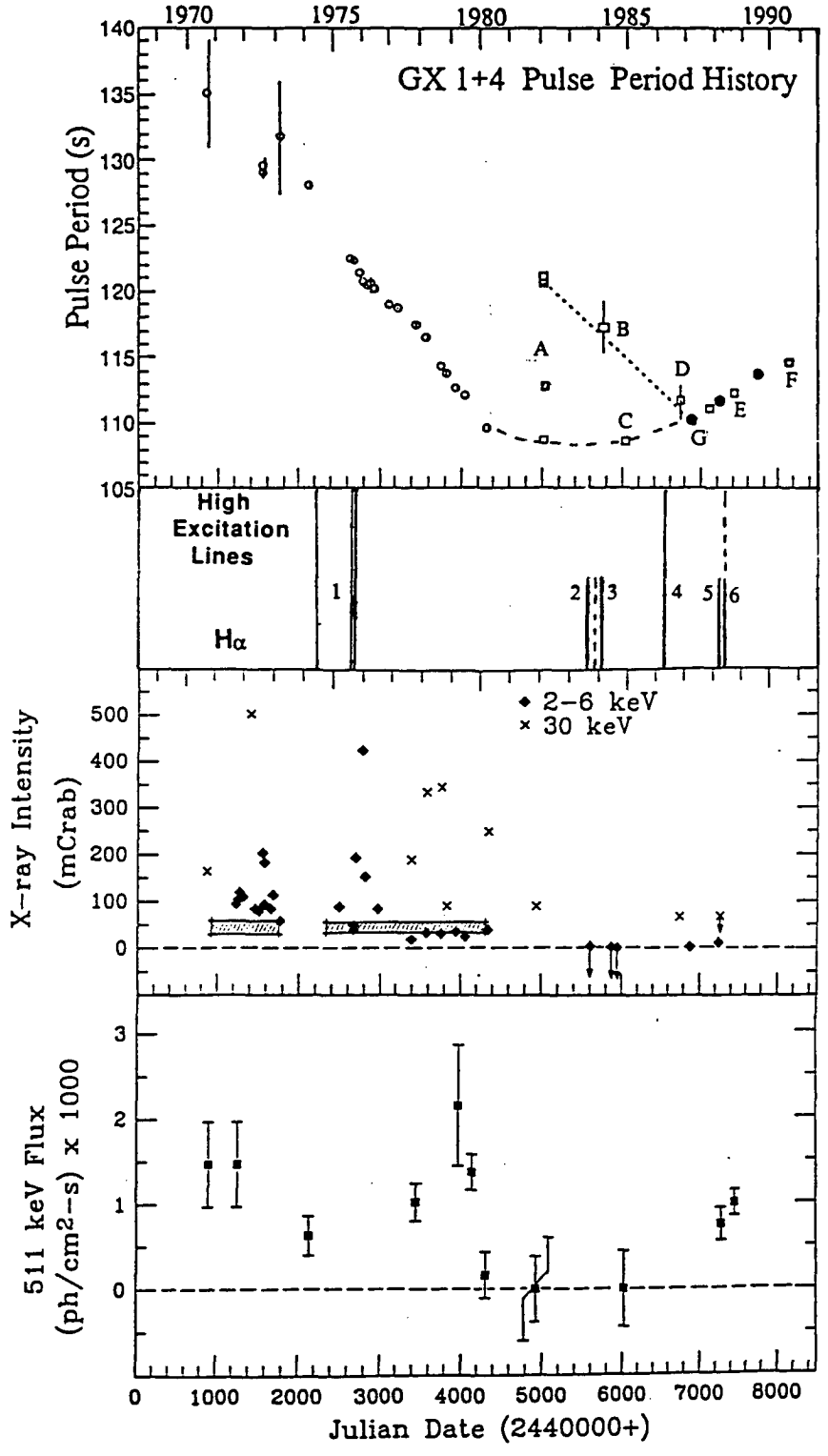
GX 1+4 Pulse Period History
Pulse Period (s)
1970
1975
1980
1985
1990
A
B
C
D
E
F
G
High Excitation Lines
Hα
1
2
3
4
5
6
2–6 keV
30 keV
X-ray Intensity (mCrab)
511 keV Flux (ph/cm²-s) x 1000
Julian Date (2440000+)

The changes in X-ray flux have a curious parallel with the intensity variations of the galactic centre annihilation line source (McClintock and Leventhal 1990). The crudely determined position of the 511 keV line source is entirely consistent with the position of GX 1+4 . A comparison of the brightness of GX 1+4 and the 511 keV source is made in Figure 2.3. Such correlated behaviour suggests that the 511 keV line source is GX 1+4. Also shown is the pulse period history and an indication of the characteristics of the optical spectrum. The changes in pulse period and X-ray brightness indicate a major change in the accretion process of GX 1+4 .

Like most other pulsating X-ray binaries GX 1+4 has a more sinusoidal pulse shape at higher energies. Above 20 keV the pulse profile consists of a single broad peak when folded on an ~2 min period. No distinct modulation was found in the 70-250 keV range. An 3σ upper limit of 3.6×10^{-3} photon $sec^{-1}cm^{-2}keV^{-1}$ was set in this energy range (Coe et al. 1981). The fractional pulsed flux (fpf) is typically 0.1-0.5 above 20 keV. There is some evidence for an increase in amplitude with energy (White, Swank and Holt 1983, hereafter WSH83).

At lower energies the pulse profile is more complicated in structure. Multiple peaks and often a sharp dip is seen superimposed on a very wide pulse. There is also evidence for a 180° phase change in the pulse profile at about 10 keV (WSH83). Similar phase reversals are also found in other high luminosity X-ray pulsars such as 4U0900-40 (WSH83).

The hard X-ray spectrum of GX 1+4 can generally be modelled with a power law with a photon spectral index near $\alpha = 0.4$. Alternately a thermal bremsstrahlung spectrum with temperature kT = 30-40 keV can be used. (e.g. Kendziorra et al. 1983). An exception is the very steep $\alpha = 4.1$ power law determined from 0S0-8 data (Dennis et al. 1980). Using the same data Market et al. (1979) however found that α varied from 1.5 to 2.2. At lower energies a spectral index of $\alpha = 1.2 - 1.6$ is found (Parsignault and Grindlay 1978, Becker et al. 1976).

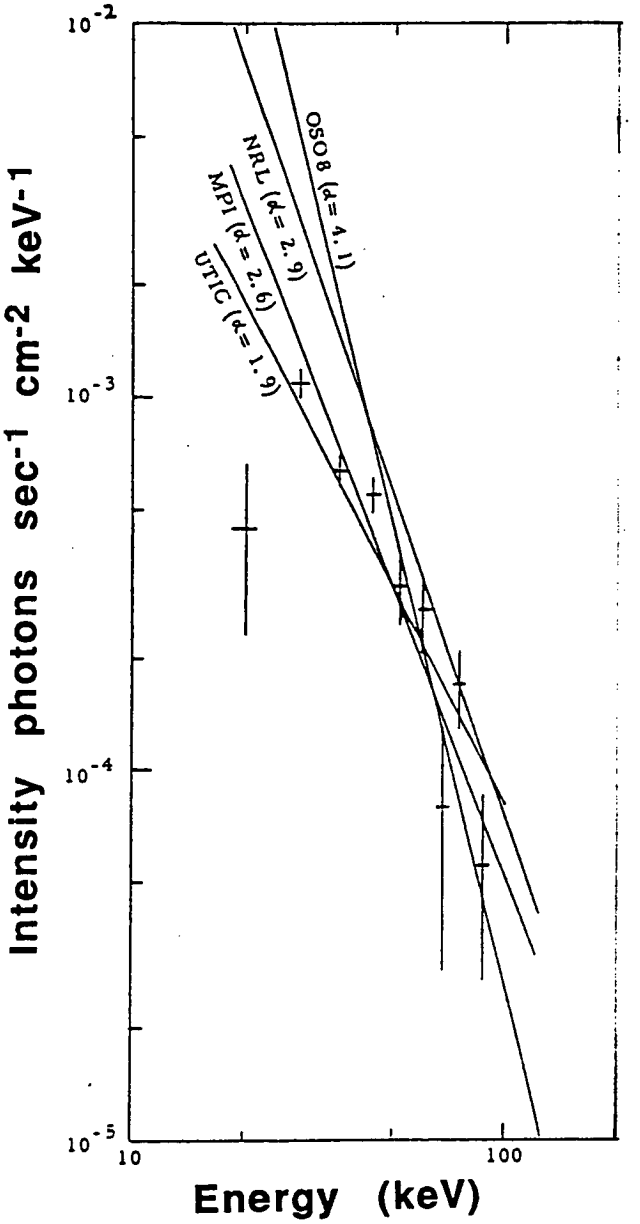

Fig 2.4 Diagram showing the pivoting behaviour of GX1+4 from Beurle et al. (1983).

Bearing in mind that GX 1+4 is variable on all time scales, the above difference in spectral index between high and low energies suggests that the spectrum is more complex than a power law. Using HEAO-2 data WSH 83 found a power law, with $\alpha \sim 1$, that is cut-off at higher energies. The cutoff factor used is exp $((E_c - E)/E_f)$ where for GX 1+4 the cutoff energy (E_c) is 10 keV and the folding energy (E_f) is ~45 keV. It was noted that the cutoff was so gradual as to be barely discernable. A cutoff power law spectrum was also employed by Ricketts et al. (1982). In this case the cut-off energy was found to be 30 keV and $\alpha \sim 1$.

Even though simple power law or thermal bremsstrahlung spectral models do not adequately represent the spectrum, they provide a useful means of inter-comparing observations. A positive intensity/spectral index correlation is found for GX 1+4 . Similarly there is an anticorrelation between intensity and estimated temperature when a thermal spectrum is applied (Watts 1983). The spectrum pivots about a fixed energy as illustrated in Figure 2.4 taken from Beurle et al. 1983. This pivoting behaviour is similar to that seen in sources such as Cyg X-1 , A0620-00, Cen X-3, Her X-1 , Cir X-1 and Cyg X-3 (Thomas et al. 1977). Amongst the bright LMXB this pivoting is called Sco X-1 like behaviour.

As with Sco X-1 and its ilk, the pivoting spectral changes can be explained by Comptonization of the source spectrum, by a surrounding hot cloud. In this model it is not temperature or spectral index that varies but the optical depth of the cloud. Watts (1983) concluded that changes in the radius of the scattering cloud could explain the range of photon index/temperatures as measured during the pre 1980 observations. A factor of 3 change in radius of a cloud of temperature 30 keV, is enough to explain the observed range of spectral index (4.1 to 2.1). Recently Damle et al. (1987) and Mony et al. (1989) have applied the Comptonization model to measurements of GX 1+4 during the recent low luminosity state.. They found a temperature of ~30 keV and ~15 keV respectively. The corresponding optical depths were 6 and ~8 for the spherical cloud case.

At low energies (<20 keV) both the spectral index and folding energy are observed to vary with pulse period. The spectrum is hardest (α lowest and E_f highest) when GX 1+4 was faintest (Ricketts et al. 1982, WSH 83, Kendziorra et al. 1982, and Dotani et al. 1981.) There is also evidence for a phase dependence in the column density (Dotani et al. 1981).

In the long term (years) the column density is variable ranging from 0.4×10^{22} cm^{-2} (Ricketts et al. 1982) up to possibly $\approx 23 \times 10^{22}$ cm^{-2} (Becker et al. 1976). This maximum value is strongly dependent upon the continuum model used by the authors. Generally the column density is about $N_H \sim 5 \times 10^{22}$ cm^{-2}.

A broad fluorescence iron line has been detected. The central energy is 6.3±0.2 keV with an equivalent width of ~450 ev to 2.2 keV (Ricketts et al. 1982, WHS 83). The line strength is modulated with pulse phase being most intense when GX 1+4 is brightest.

Chapter 3

Analysis Methods

Though this be madness, yet there is method in it.

William Shakespeare

The explorations of space end on a note of uncertainty
.... We measure shadows
.... we search among ghostly errors of measurements....

Edwin Hubble, 1935

3.1 Introduction

In this chapter the analysis methods used within this thesis will be introduced. It is split into two sections; the first deals with X-ray energy spectral reduction, the second is a review of temporal analysis techniques.

To determine an input source spectrum a model of the detector response is required. The interaction of X-rays with a xenon filled detector is discussed leading the formulation of a mathematical model. The χ^2 minimization method of source spectrum parameter estimation is explained. Finally more direct spectral reduction methods are introduced.

The second section consists of a review of various temporal analysis techniques with particular emphasis upon the methods used within this thesis. A more general introduction is that given by Fullerton (1985). The discussion of the Fourier transform and its statistics owes much to the review of van der Klis (1988).

The analysis of periodic signals is discussed first. The Fourier transform and its relevant properties are introduced with an emphasis upon the statistics of the power spectrum and the means of handling unevenly sampled data. This is followed by a brief look at phase folding, arrival time techniques and time domain methods.

3.2 Spectral Analysis

3.2.1 The Interaction Process

The interaction of an incident X-ray photon with the detector gas can occur in one of three ways; pair production, Compton scattering and the photoelectric effect. At energies below 100 keV the dominant mechanism is the photoelectric effect. Within the University of Tasmania's detector the gas Xenon is used because its high atomic number (Z = 54) which results in a high absorption coefficient for >20 keV photons. The principle absorption edges are at 34.56 keV for the K edge and an average of 5.1 keV for the 3 levels of the L shell edge. The M shell absorption is ignored since it has a much smaller transition probability than either the K or L shell absorption at the energies of interest (10 - 120 keV).

There are two possible forms of the photoelectric effect. In the first case an electron is ejected and another higher level electron takes its place emitting a

fluorescence photon. The yield of fluorescence photons for the K and L shells are 0.89 and 0.103 respectively. Thus most fluorescent photons come from K shell transitions. These transitions (L_{III} - K, L_{II} - K, M_I - K, N_{II} -K) have a weighted mean energy of 30 keV.

In the Aüger effect the initial absorbing electron is ejected, as in the photoelectric effect, however the fluorescent photon, instead of being emitted from the atom, ejects another higher level electron. The resulting, second electron, has an energy equal to the difference in energy between the energy level of the original photo-electron and energy level from which the Aüger electron came. In the case of xenon most (0.897) Aüger electrons result from L shell photo-absorptions. The range of electrons in xenon, at one atmosphere pressure, is very short being, 0.03cm at 10 keV and 2-3 cm at 100 keV. Therefore, the initial X-ray and photoelectron will most likely interact within the same cell or an adjacent cell and so be registered as a single event.

The fluorescent photon can escape the detector . The probability that a photon will escape is mainly dependent upon detector geometry and gas pressure. The slight dependence upon photon energy will be ignored. At a pressure of 1 atmosphere of xenon the typical radiation length of a K edge photon (30 keV) is 18 cm which is comparable to the depth of the 1983 UT detector (21 cm UT83). The escape fraction is reduced in the UT86 detector because at its 2.5 ATM working pressure the raditation length is about 8 cm as compared to the active depth of 19.5cm. Thus a mono-energetic X-ray source with E_c>35 keV will produce two peaks; one at E_c>E_{edge} and another at E_c- E_{edge}. Since the majority of fluorescent photons are produced by K edge transitions then E_{edge} is 30 keV. The escape ratio is defined as the ratio of the number of counts in the escape peak to the total number within both peaks.

The fluorescent photons (E_f) that do not escape the detector will be absorbed practically simultaneously with the initial photon (E_p), in another cell. These dual events have an easily recognized signature; two simultaneous events, one with an energy near the shell edge energy (30keV for xenon). Escape gating records the energy of each individual event and rejects all events that do not have this signature. Charged particles, Compton and neutron interactions have only a small probability of producing such a combination. Thus escape gating allows the background to be markedly reduced.

The reduction in background does not mean there is a commensurate improvement in the sensitivity of the detector. Escape gating not only rejects background events but also all single interactions from the source. Also it can only be used at energies greater than the shell edge energy. With xenon filled detectors many sources are detectable only below the K_{edge} energy of 35 keV. The sensitivity of a detector, in the background limited case (the norm in X-ray astronomy), to a point source is

$$S_{min} \propto T_{obs}\, \Delta E \frac{B(E)^{-1/2}}{\eta(E)} \qquad 3.1$$

where T_{obs} is the observation time, ΔE is the energy range over which counts are binned, B(E) is the background count rate over ΔE and $\eta(E)$ is the detector efficiency. Escape gating will reduce the detector efficiency with respect to the normal, ungated, mode by some factor κ. An improvement in sensitivity will be achieved only if the background is reduced by a factor of at least κ^2. A value of $\kappa \approx 1$ is found for the UT86 detector.

Escape gating has a second advantage. Since the energy of the fluorescent photon is known, the total energy of the incident X-ray ($E_x=E_p+E_f$) can be reconstructed with the detector energy resolution at E_P instead of at E_x. This results in an improvement in energy resolution particularly just above the K_{edge} (35keV in xenon) energy.

Because of the finite energy resolution of the detector the fluorescent photon will not necessarily have an energy of 30keV (xenon mean K_α,K_β energy). Thus when both interactions have an energy near E_{edge} (i.e. $E_X=2E_{edge}$ = 60keV for xenon) there is a significant probability that the wrong interaction will be chosen as the fluorescent event. This produces a marked drop in sensitivity at twice the edge energy. With respect to the UT86 detector, this effect is discused in detail by Greenhill et al. 1990.

For every 1 keV deposited within the gas $\lesssim$37 electron-ion pairs are produced. The electron-ion pairs are accelerated by the electric potential set up within each cell of the detector. When the electrons reach the high field region near the anode they ionize further atoms causing an avalanche. A gain of ~10^3 is used in the UT xenon detectors. With some gas mixtures gains of 10^5 to 10^6 can be achieved. Because of their higher mobility the electrons are collected within 1 μsec while the ions drift toward the cathode on a 10 - 100 μsec timescale. The anode pulse is not measured.

The initial electron-ion pair production and subsequent avalanche are statistical in nature. The final pulse has a spread in sizes which is approximately Poissonian, giving the detector a finite energy resolution. The energy resolution is defined as the percentage Full Width Half Maximum (FWHM) of a mono-energetic peak to the energy of the peak ie.

$$R(E) = \frac{FWHM\ (keV)}{E_{peak}\ (keV)} * 100\% \qquad 3.2$$

The resolution varies approximately as $E^{-1/2}$. Therefore doubling the incident energy doubles the size of the electron pulse and improves the resolution by a factor of approximately $\sqrt{2}$. In escape gated mode the improvement in energy resolution with respect to normal mode is $\sqrt{E_P/E_X}$.

3.2.2 Mathematical Model of a Detector

The overall response of a balloon borne proportional detector can be considered as the combined effects of atmospheric transmission (T_A), window transmission (T_W) and the filling gas absorption ($1-T_G$), escape and energy resolution. Suppose $N(E,\gamma_1,....,\gamma_j)$ is the incident photon differential source spectrum above the atmosphere described by parameters $\gamma_1,....,\gamma_j$ The observed pulse height spectrum is given by (Stein and Lewin 1967).

$$P(E')dE' = \int_0^\infty N(E,\gamma_1,....,\gamma_j)\ T_A\ T_w(1-T_G)$$

$$*\left[F_k\ R(E-E_kE') + (1-F_k)\ R(E,E')\right]\ dEdE'$$

$$= \int_0^\infty N(E,\gamma_1,....,\gamma_j)\ Q(E,E')\ dEdE' \qquad 3.3$$

Here F_k is the K shell fluorescence escape probability per detected photon with energies above the K edge energy E_k. The energy resolution is gaussian in nature. The resolution function used is given by

$$R(E,E') = \frac{1}{\sigma\sqrt{2\pi}} exp\left[-\frac{(E-E')^2}{2\sigma^2}\right] \qquad 3.4$$

where 2σ is equivalent to the FWHM energy resolution.

Thus the final count rate in the i_{th} bin is :

$$P_i = \int_{E_i'}^{E_{i+1}'} P(E')\, dE' \qquad i = 1,m \qquad 3.5$$

where m is the number of detector channels.

3.2.3 χ^2 Minimization

The method generally used to model the source spectrum from the observed pulse height spectrum is the method of χ^2 minimization. An input differential photon spectrum with j parameters $\gamma_1,....,\gamma_j$ is assumed. This spectrum is folded through the detector response of Equation 3.3 and then integrated into pulse height channels with the same energy boundaries as the data. The observed channel counts are then compared with the model counts and the χ^2 statistic per degree of freedom, ν, is computed.

$$\chi^2_\nu = \frac{1}{m\text{-}j} \sum_{i=1}^{m} \frac{(C_i - P_i)^2}{\sigma_i^2} \qquad 3.6$$

As before, m is the number of channels and j is the number of model parameters, ν is the number of degrees of freedom (ν=m-j) and σ_i is the error in the i_{th} channel. The measured and model count rates are C_i and P_i respectively. The errors are based upon Poisson statistics and are given by

$$\sigma_i = \sqrt{\frac{C_s}{t_s} + \frac{C_b}{t_b}} \qquad \text{counts/sec}$$

or

$$\sigma_i = \sqrt{\frac{K_s}{t_s^2} + \frac{K_b}{t_b^2}} \qquad \text{counts} \qquad 3.7$$

K_s,K_b = total source pointing and background counts

C_s,C_b = source pointing and background count rates (counts/sec)

t_s , t_b= observation time on source and background

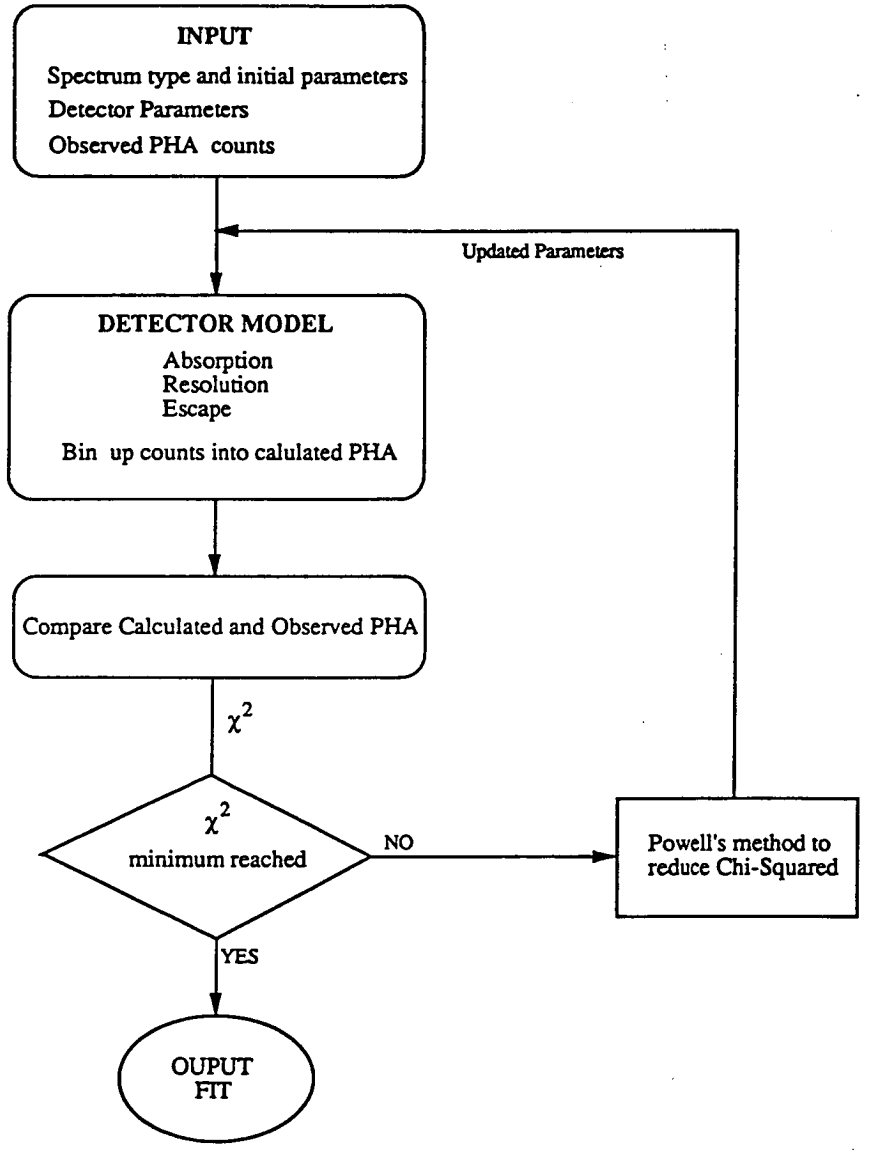

Fig 3.1 Flow chart showing the sequence of calculations used in the χ^2 modeling of the source PHA spectra. To find the confidence region the counter model is repeatedly applied on a grid of parameters for a given spectral mode

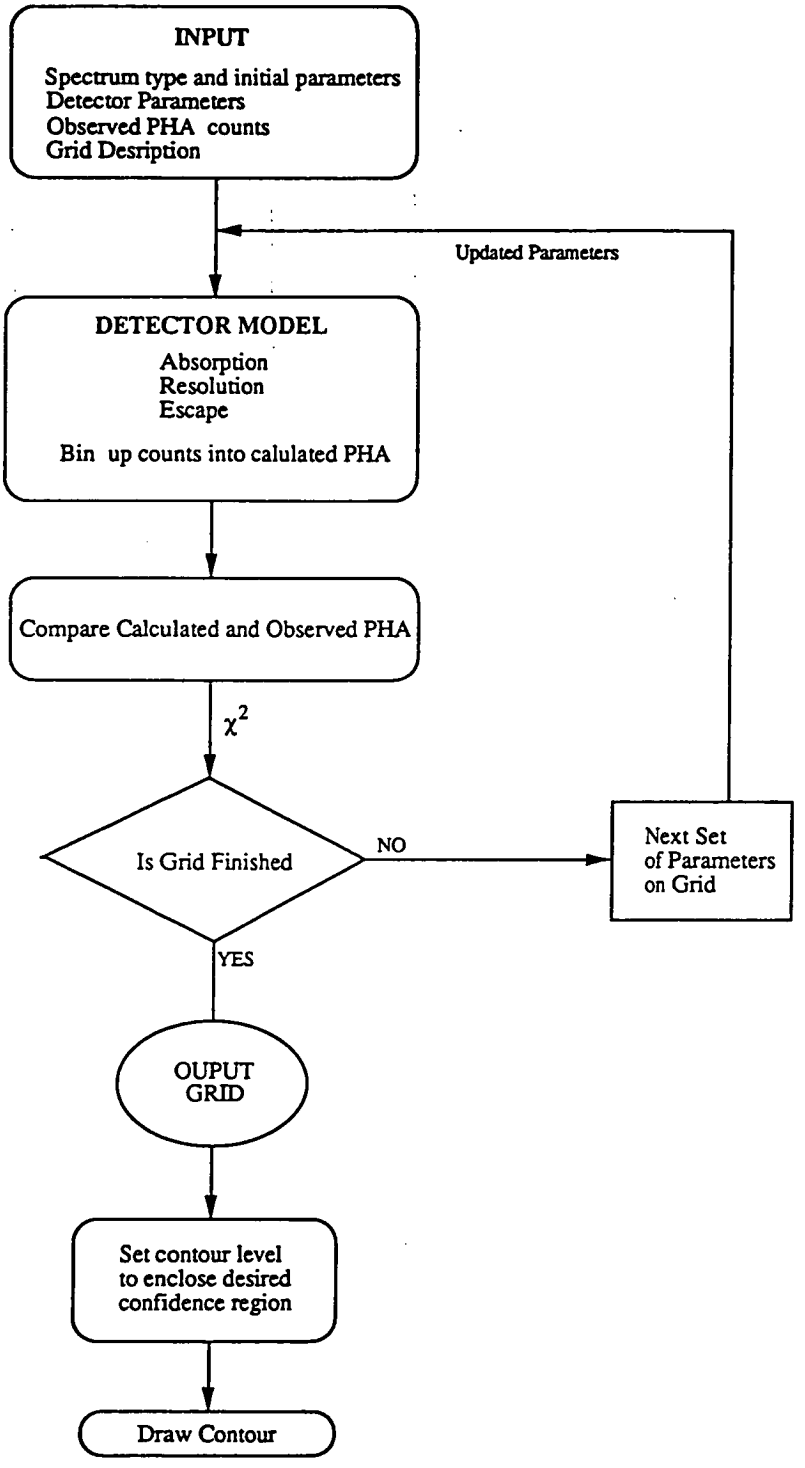
INPUT
Spectrum type and initial parameters
Detector Parameters
Observed PHA counts
Grid Desription
Updated Parameters
DETECTOR MODEL
Absorption
Resolution
Escape
Bin up counts into calulated PHA
Compare Calculated and Observed PHA
χ^2
Is Grid Finished
NO
Next Set of Parameters on Grid
YES
OUPUT GRID
Set contour level to enclose desired confidence region
Draw Contour

After calculating the χ^2 value the input spectrum parameters are adjusted to reduce the χ^2 value. The process is continued till a minimum chi-squared value is found. The adjustment of the parameters and χ^2 minimization is based upon the non-linear least squares routine described by Powell and Macdonald (1972). The program was written by D.J. Watts and R. Thomas and modified by D.P. Sharma and the author. A schematic block diagram of the χ^2 minimization spectral reduction technique is shown in Figure 3.1.

The resulting parameters are the best fit values for a chosen spectral type. An unacceptable choice of spectrum is indicated by an improbable value of the minimum reduced chi squared. Even a reasonable (90% confidence) final χ^2_ν does not imply that the chosen spectrum is a true representation of the source spectrum. The implication is that the assumed energy spectrum produces a reasonable representation of the observed pulse height energy spectrum given that the correct detector model has been used.

Non-linear least squares methods can fail to find the global minimum. However this is uncommon when simple models with reasonable initial parameter estimates are used.

3.2.3.1 Confidence Intervals

Once a minimum χ^2 fit has been determined then the confidence intervals (e.g. 68% ≡ 1σ or 95%) need to be calculated for the best fit parameters. This requires computing the chi-squared upon a grid within the parameter space. For two parameters the 68% and 90% confidence levels form contours upon the χ^2 surface. The 1 σ and 90% levels (2 parameters) are given by

$$S_L(68\%) = \chi^2_{min} + 2.3$$

$$S_L(90\%) = \chi^2_{min} + 4.6 \qquad 3.8$$

The offset values are given by Lampton, Margon and Bowyer (1976) and are the χ^2 for 2 degrees of freedom (dof) for the corresponding significance level e.g. $\chi^2_2(0.32)$ and $\chi^2_2(0.01)$.

In the case of a multi-parameter (p parameters) fit the confidence level S_L is a p-1 dimensional surface. It is often desirable to obtain constraints upon a subset q, of the p parameters. This is done by projecting the original p dimensional volume onto the desired subspace. For each point on a grid of sub-space parameters the remaining p-q parameters are used to minimize the chi-squared value. As a generalization of Equation 3.8 , the (1-α) confidence region incorporates all χ^2 values less than

$$S_L(\alpha) = \chi^2_{min} + \chi^2_q(\alpha) \qquad 3.9$$

The offset level is the α significance level of the chi-squared distribution with p degrees of freedom. Note that the χ^2_{min} is the minimum chi-squared for the entire parameter set. Two spectral fits can be said to be different at the 1-α confidence level if there is no overlap of their respective confidence regions.

3.2.4 Direct Spectral Reduction

To overcome the ambiguous nature of the χ^2 minimization technique direct spectral reduction can be achieved with two methods; apodization (Dolan 1972) and via eigen-solutions (Blisset and Cruise 1979) of the resolution function.

Equation 3.3 can be rewritten as an m dimensional matrix

$$\mathbf{R^{-1}C = R*F_k*(I-T_B)*T_W*T_A*N} \qquad 3.10$$

where **C** is the observed data, in column matrix form, R is the resolution matrix, $\mathbf{F_k}$ is the escape matrix, I the Unit matrix and $\mathbf{T_G, T_W, T_A}$, are the column matrices describing the transmission by the counter gas, window and residual atmosphere. Finally **N** is the input source spectrum. All except **R** can be easily inverted. However, because of its $E^{-1/2}$ dependence, **R** is nearly singular. Therefore direct inversion of **C** is unstable. To invert **R**, Dolan uses the method of apodization. The i_{th} element of $\mathbf{R^{-1}C}$ is given by

$$(\mathbf{R^{-1}C})_i = C_i - S_i(\tfrac{1}{2}(C_{i+\mathcal{L}} + C_{i+\mathcal{L}}) - C_i) \qquad 3.11$$

where $\mathcal{L}$ (the apodization length) is dependent upon the resolution such that $S_i=(\sigma/\mathcal{L})^2$

The apodization and χ^2 minimization methods were compared by Watts and Thomas (1979). They found that count rate errors propagate and are enlarged by a factor ≈3 in the final spectrum when using the apodization technique. The eigen value method suffers from a similar problem. Thus direct spectral reduction is limited to high signal to noise ratio observations. The apodization method can be used to find the input spectrum form which can then be refined using the χ^2 minimization method.

3.3 Temporal Analysis

There are two objectives in the analysis of a time series; firstly to detect and then quantify any signal present. The signal may be either deterministic, e.g. a regular sinusoid, or a stoachastic process. Generally different techniques are used for each case. Fourier or phase folding methods are used for deterministic signals while time domain methods, e.g. autocorrelation, are used for random processes. In either case, to identify a signal and then to put error estimates upon its parameters, requires a good knowledge of the statistics of the analysis technique.

3.3.1 The Fourier Transform

Any signal X(t) can be decomposed into the superposition of infinite series of sinusoids; for example

$$X(t) = \frac{1}{N}\sum_j a_j \cos(\omega_j t - \phi_j)$$

$$= \frac{1}{N}\sum_j A_j \cos(\omega_j t) + B_j \sin(\omega_j * t) \qquad 3.12$$

where

$$A_j = \sum_k X_k \cos(\omega_j t_k)$$

$$A_j = \sum_k X_k \sin(\omega_j t_k)$$

The coefficients A_j, B_j and the time series X_k can be written as the discrete transform pair.

$$a_j = \sum_{k=0}^{N-1} X_k \, e^{2\pi \, i \, j \, k/N}$$

$$= \sum X_k \, e^{-i\omega t_k}$$

$$= \sum X_k \cos(\omega t_k) + X_k \sin(\omega t_k)$$

$$X_k = \frac{1}{N} \sum_{j=-N/2}^{N/2-1} a_j \, e^{-2\pi \, i \, j \, k/N} \qquad 3.13$$

Here the discrete time series X_k of N numbers (k=0, N-1) of total duration T is sampled at intervals $t_k = kT/N$ is transformed into the frequency series a_j sampled at frequencies $\omega_j = 2\pi\nu_j = 2\pi j/T$. This means that $2\pi jk/N = \omega_j t_k$. The input series is completely described if the frequency domain is sampled from 0 Hz to the Nyquist frequency $\nu_\gamma = \nu_{1/2} = 1/2 \; N/T_k$ at frequency intervals of $d\nu$. At zero frequency $a_j = \Sigma \, X_k = N_{ph}$ the total number of photons.

Generally the input time series is totally real and so the output frequency series is symmetrical i.e. $|a_j| = |a_{-j}|$ and $a_{-N/2} = a_{N/2}$. Thus the a_j's need only be calculated over the positive frequency range j=1,N/2 Often only the amplitudes of the frequency series are required. In this case, using the normalization of Leahy et al. (1983), the resulting powers can be written as

$$P_j = \frac{2}{N_{ph}} |a_j|^2 \qquad 3.14$$

Using Parseval's theorem the total variance of the data is

$$Var(X_k) = \frac{N_{ph}}{N} \sum_{j=1}^{n/2-1} P_j + \frac{1}{2} P_{N/2} \qquad 3.15$$

which can be expressed as a fractional root mean squared variation

$$r = \sqrt{\frac{\frac{1}{N}\mathrm{Var}(X_k)}{\bar{X}}}$$

$$= \left[\frac{\sum_{j=1}^{n/2-1} P_j + \frac{1}{2} P_{N/2}}{N_{ph}} \right]^{1/2} \qquad 3.16$$

When the above normalization is used a sinusoidal signal $X_k=A\sin(2\pi\nu_j T_k)$ will cause a spike at ν_j in the power spectrum of

$$P_{j,sine} = \frac{1}{2} \frac{N^2 A^2}{N_{ph}} \qquad 3.17$$

The theoretical, delta function response of the Fourier Transform (FT) to a sinusoidal signal is modified by two effects; the finite length of the observation and sampling that is discrete and equally spaced in time. An observation is only a small section, or window, of an infinite series. The final transform is the convolution of the data's actual Fourier Transform with the window's transform. The transform of a square window is a sinc function. Thus a sinusoidal signal will produce a widened peak (width 1/T) with side-lobes instead of a delta function. By modifying the window, i.e. by weighting the data, the amount of power in the side-lobes can be suppressed (Press et al. 1986). Windowing can distort steep low frequency spectra (e.g. Very Low Frequency Noise) making them less steep. This is most serious for power spectra with power law slopes greater than two (Deeter 1983).

The effect of evenly spaced discrete sampling is known as aliasing. The sampling function is a series of delta functions at the times when each sample is taken. The transform of the sampling function is an infinite series of delta functions at frequencies $\nu = 0,\pm N/T,\pm 2N/T\cdots$ i.e. at multiples of the Nyquist frequency. When the initial data contains a signal with a frequency higher than the Nyquist frequency power peak is reflected about the Nyquist frequency. For example if a series, sampled at 100 Hz (ν_γ=50Hz) and has a sinusoidal signal at 60 Hz (20 Hz above the Nyquist frequency) a peak will appear in the power spectrum of 40 Hz. Aliasing can be viewed as being able to fit an evenly sampled sinusoid equally well

with a higher harmonic sine function as with sine function with the fundamental frequency. The effects of windowing and aliasing are illustrated in Figure 3.2 and Figure 3.3.

In practice aliasing is not such a problem. Data is generally not instantaneously sampled but binned over a sample time dt. The data's Fourier Transform is convolved with the binning window. Any peak in the data's transform is multiplied by the factor,

$$B(\nu) = \frac{\sin(\pi\nu T/N)}{\pi\nu T/N} \qquad 3.18$$

This sinc function has a value of 1 at $\nu=0$ and $2/\pi$ at the Nyquist frequency, and 0 at the sampling frequency. In the above example the 40 Hz peak will be suppressed by a factor of $\mathrm{sinc}(0.6\pi)\approx 0.5$ (power amplitude reduced by 0.254). An alternative way of looking at this effect is that higher frequency signals are smoothed by the binning. Unfortunately this function also reduces the sensitivity of the Fourier transform as the signal's frequency approaches the sampling frequency. The binning factor is squared when the power spectrum is considered. The effect of binning upon the amplitude of an alias peak is illustrated in Figure 3.3.

Aliasing is also markedly suppressed by even small amounts of unevenness in the sampling. The two window functions sampling and binning can be combined to produce a window function that contains all the information about the timing of the observation. Since the final transform is the convolution of the actual Fourier transform with the window's transform, the true transform could, in principle, be recovered by a deconvolution. The noise in the transform usually precludes this option. However, by comparing the window's transform with the observed data transform, spurious peaks can be identified.

If the frequency of an input sinusoidal signal falls between two Fourier sampling frequencies the power will be split between the nearest bins. The power spike is reduced by a factor of between 1 (on a Fourier frequency) to 0.454 (halfway between two adjacent Fourier frequencies); the average being 0.707. This factor is given approximately by a $\mathrm{sinc}^2(x)$ function where x is the fractional distance between adjacent Fourier frequencies.

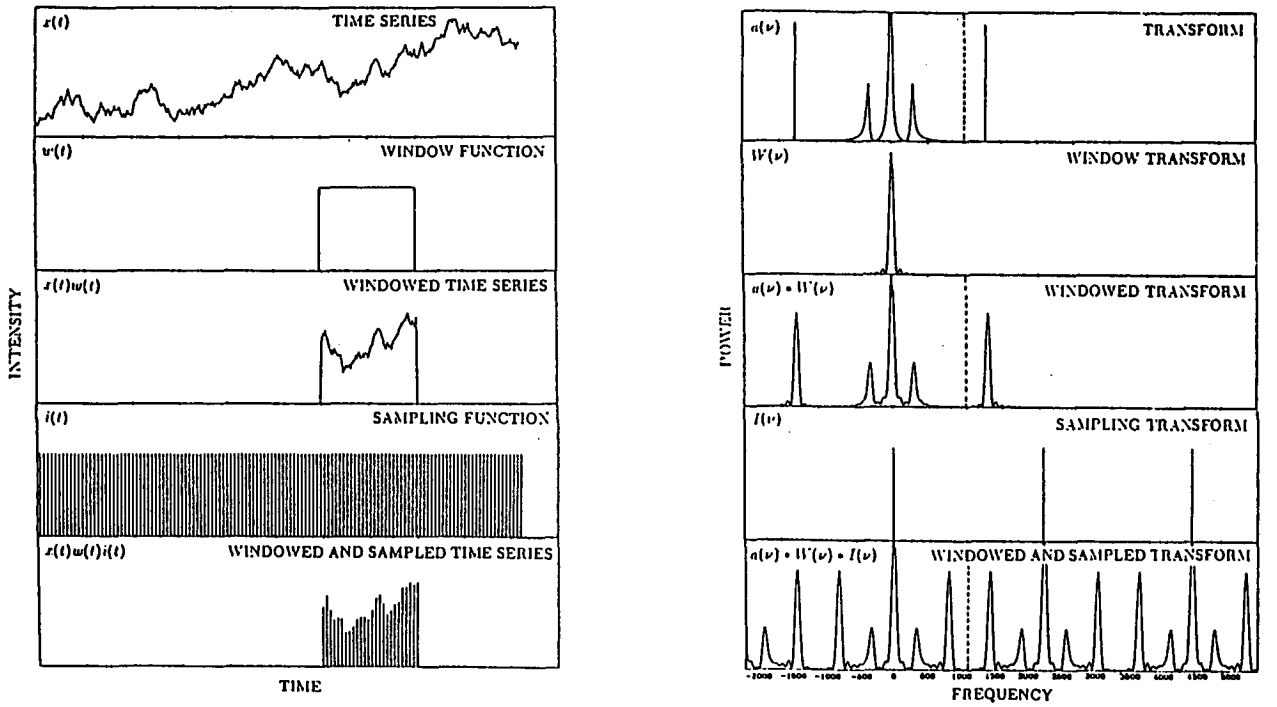

Fig 3.2 This diagram illustrates the double convolution of the time series in both the time (left) and frequency (right) domains. The infinite time series is observed for a limited amount of time (window or several windows). The truncated time series is then binned at the sampling period to form the final discrete limited series. In the frequency domain the transform of the time series is convolved with window transform and the then the sampling transform. The final power spectrum contains power outside the Nyquist frequency (vertical dashed line). These peaks are reflected about the Nyquist frequency to frequencies below the Nyquist frequency forming alias peaks. What is not shown is the reduction in amplitude of the alias peaks caused by the time domain binning which smooths the time series. This diagram is taken from van der Klis (1987).

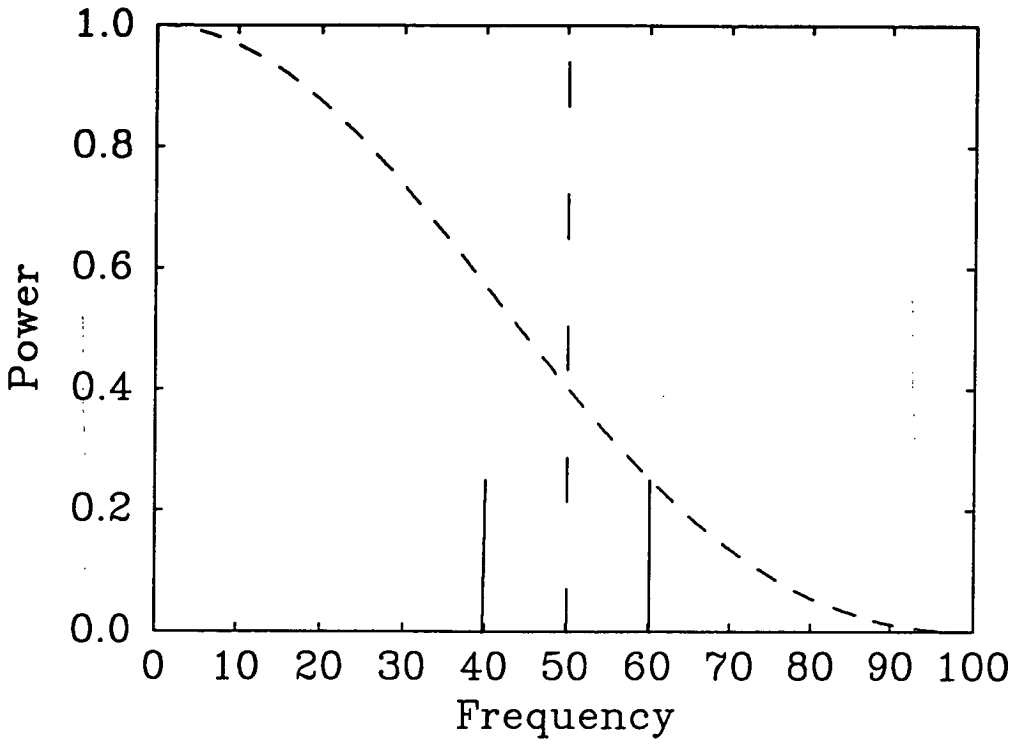

Fig 3.3 An example of the effect of aliasing. A signal sampled at 100 Hz contains a 60 Hz signal that is aliased to a frequency of 40 Hz. The amplitude is governed by the sinc^2 function of Equation 3.18.

3.3.2 Power Spectrum Statistics

The reason for choosing the apparently awkward normalizations of Equations 3.14 and 3.17 is that, in the absence of a signal, the output powers are χ^2 distributed with a mean of two. This holds true for many types of noise distributions.

For a single transform the output powers are chi-squared distributed with 2 degrees of freedom (dof), and a variance of 4. This distribution is very noisy. Increasing the length of the observation, T, with the same relative time intervals, δt, does not improve the noise, but only increases the number of powers. However as pointed out by Scargle (1982) this does not mean that taking longer data runs is useless. As the observation length increases the ratio of the signal power to the noise power increases, in proportion to the number of samples (N). There are two other equivalent ways of reducing the noise powers in an observation of fixed length. The power spectrum can be binned (W old bins per new bin) in frequency or M consecutive shorter transforms can be made and then averaged. In the latter case the N_{ph} is the number of photons in a single transform. Both methods reduce the frequency resolution. The two methods can be combined. The resulting power spectrum is still χ^2 distributed but with 2MW dof. The final power spectrum has a mean of 2, when scaled by 1/MW and a variance of 4/MW. For large MW this χ^2 distribution approaches the normal distribution with a mean of 2 and standard deviation $\sqrt{2/MW}$.

3.3.2.1 Dead Time Effects

If the input data do not have a white noise (Poisson) distribution the resulting power spectrum need not follow the above χ^2 distribution. If correlations exist between data points there will be correlations between the powers.

The most common cause of a non-poisson data distribution is dead time. There are two simple forms of dead time. The first is, when, after the detection of a photon there is a constant length time interval in which no further photons can be detected. The incident λ, and observed, μ, count rates are related by

$$\mu = \frac{1}{1 + \tau_{dead}\,\lambda} \qquad 3.19$$

This produces a correlation between adjacent time bins i.e. at the Nyquist frequency. The resulting power spectrum slowly rises toward the Nyquist frequency. This type of dead time always exists in count rate data from proportional counters. The UT83 detector had $\tau_{dead} = 10\mu sec$ and UT86 detector had $\tau_{dead} = 100\mu sec$. A similar effect is caused by data frame overflows during the Alice Springs (AS86) flight (see Section 7.3.2).

The second common form of dead time is when no more than a fixed number of photons can be detected within a sample time. This changes the distribution of the counts from Poisson to binomial. This does not introduce any correlations between the data points and so only the mean level of the powers is affected. In the case where only a single photon can be detected within a sample time the average power becomes

$$<P_{j,noise}> = 2e^{\tau_{sample}\lambda} = 2(1-\mu\tau_{sample}) \qquad 3.20$$

In the case where only a subset of the events are used (e.g. selected by energy) the above equation becomes

$$<P_{j,noise}> = 2(1-\mu_s\tau_{sample})$$

$$= \frac{1-\lambda_s e^{\tau_{sample}}}{1-\mu_s\tau_{sample}} \qquad 3.21$$

where μ_s and λ_s are the observed and selected incident count rates.

Usually the dead time process is more complicated than either of the above processes. In the case of the UT86 detector both types occur simultaneously, along with frame overflows. The photometers at Mt. Canopus are affected by both the non-poisson nature of the dark current, constant dead time and ringing set off by cosmic rays. An example of a complete analysis of dead time effects is given by Tennant (1987). To avoid the need for a detailed knowledge of the dead time behaviour the distribution of powers can be rescaled by a factor of the average power, $\bar{P}$. Either the χ^2 distribution or for large MW the normal distribution can be used. This methodology completely overlooks any intrinsic white noise which will appear as a rise in the mean level of the power spectrum.

3.3.2.2 Signal Detection

We will assume that the output powers consist of two separate components

$$P_j = P_{j\ noise} + P_{j\ signal} \qquad 3.22$$

This assumption is justified if the signal count rate is small compared with the background rate.

The probability that a given power $P_{j,noise}$ in an averaged power spectrum with ν=2MW dof, will exceed a threshold power $P_{Threshold}$ is given by

$$Prob(P_{jmax} > P_{threshold}) = Q\,(MW\ P_{Threshold}/2MW) \qquad 3.23$$

In this case the probability Q is the integral χ^2 distribution (Walpole and Myers 1978) is

$$Q_{\chi^2_\nu}(X) = \frac{1}{2^{\nu/2}\Gamma(\nu/2)} \int_X^\infty e^{-X/2}\, X^{\nu/2-1}\, dX \qquad 0 \text{ to } 1$$

$$= 0 \qquad \text{elsewhere} \qquad 3.24$$

The gamma function is $\Gamma(\nu/2)$ and ν is the number of dof. This gives the probability that the reduced chi-squared value will be greater than the value X. The methods used to calculate the above integral are given by Press et al. (1986). Note that the χ^2 distribution with 2 dof reduces to the exponential distribution (Walpole and Myers 1978). Alternatively, in the normal approximation can be used when the number of degrees of freedom is large.

$$Prob(\ P_{jnoise} > P_{threshold}\ ) = Q_{gauss}(t)$$

$$= Q_{gauss}\left(\frac{P_{threshold} - \bar{P}}{2/\sqrt{MW}} \right) \qquad 3.25$$

where $\bar{P}$ is the average noise power level. The probability of exceeding the threshold level ($x=t+\bar{P}$) is given by the integral normal distribution

$$Q_{gauss}(x) = \frac{1}{2\pi}\int_{x}^{\infty} e^{-t^2/2}\,dt \qquad 3.26$$

The method used to calculate this integral is given by Bevington (1969). We can define a threshold power, $P_{Threshold}$, that has a small probability, ε (1-ε confidence level), of being exceeded by chance. Thus if a power P_j does exceed $P_{Threshold}$ then there is a large, 1-ε probability that P_j contains a signal. In setting the 1-ε confidence level of $P_{Threshold}$ we must consider the number of independent trails (N_{trial}) or number of frequencies searched. The value of ε' required is given approximately ($\varepsilon'<<1$) by

$$\varepsilon' = \frac{\varepsilon}{N_{trial}} = Q_{\chi^2_\nu}(\,MWP_{Threshold}/2MW\,) \qquad 3.27$$

3.3.2.3 Upper Limits

If no signal exceeds $P_{Threshold}$ an upper limit P_{ul} can be set. The procedure is to first set a level P_{exceed} which has a small δ (e.g. δ = 0.05) probability of being exceeded. Then we find the maximum power P_{max} in the frequency range of interest. The difference gives the 1-δ confidence level upper limit

$$P_{ul} = P_{max} - P_{exceed} \qquad 3.28$$

The logic behind this procedure is as follows : if there was a signal with power P_{signal} it would have exceeded $P_{ul} = P_{max} - P_{exceed}$ with (1-δ) confidence but since we know that there is no signal then we can state that $P_{j\ signal} < P_{ul}$ with (1-δ) confidence.

Without knowing P_{max} (i.e. before making an observation) the sensitivity of a search can be found as

$$P_{sensitive} = P_{Threshold} - P_{exceed} \qquad 3.29$$

In a sense $P_{sensitive}$ is an upper limit to P_{ul} i.e. if a signal is above $P_{sensitive}$ then it will be called a detection.The schematic power spectrum showing the various thresholds is shown in Figure 3.4.

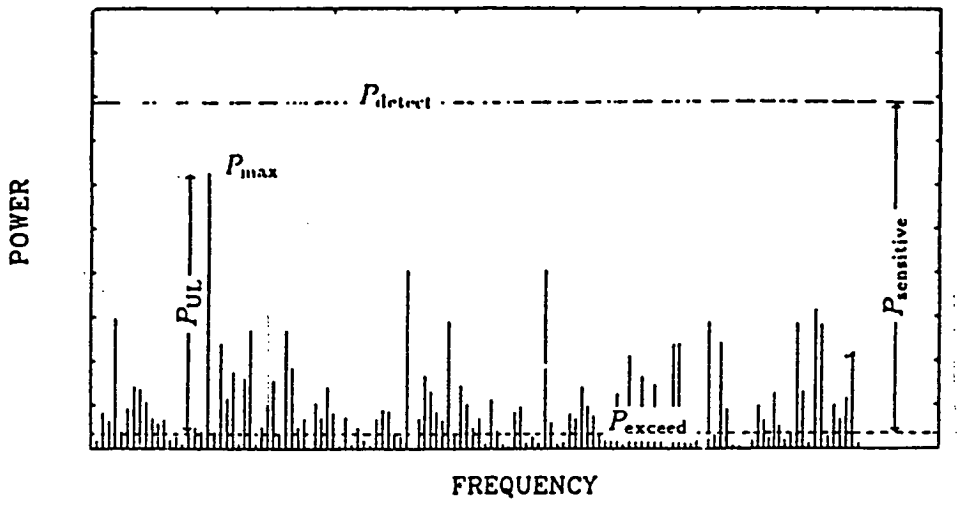

Fig 3.4 The meaning of the upper limit P_{ul} and sensitivity power level $P_{sensitive}$ in terms of the maximum measured power P_{max} and the generally exceeded power level P_{exceed} is illustrated. This diagram is from figure 4.1 of van der Klis (1987).

3.3.2.4 A Signal is Detected

If a power does exceed P_{detect} the power cannot be directly converted to an amplitude using Equation 3.17 because, recalling Equation 3.22, the signal power contains some noise power. We can put a (1-α) confidence limit upon any noise in the signal by considering

$$\alpha = Q(MW\, P_{noise\ limit}/2MW) \qquad 3.30$$

Then we can say with (1-α) confidence that any signal has power

$$P_{j\ signal} \geq P_j - P_{noise\ limit} \qquad 3.31$$

This power is then converted to an rms percentage by

$$r = \sqrt{\frac{W * \sum P_{j\ signal}}{N_{ph}}} = \sqrt{\frac{\int P_{signal}(\nu)\, d\nu}{I}} \qquad 3.32$$

Here I is the mean count rate. This must be corrected for the smoothing affect of the data binning (Equation 3.18) and the affects of dead time. The latter correction was found to be less than 3% of the signal for all observations within this thesis.

3.3.2.5 QPO Upper Limits

In order to set quantitative upper limits on any QPO component the power spectra must be searched for statistically significant peaks. There are three possible approaches which all ultimately rely upon the χ^2 distributed nature of the powers. The first method is to test the power spectra for a deviation from the expected χ^2 distribution. Three tests were used: the sign test, the runs test and the Kolmogorov-Smirnov (K-S) test.

THE SIGN TEST

The sign test, tests the null hypothesis that the difference in the means of the data and test distributions is zero (μ_1-μ_2=0). It counts the number of positive (r_+) and

negative (r_-) deviations with respect to the expected mean. In the case of power spectra with the Leahy normalization the expected mean is two. The test statistic R follows the binomial distribution with p = 0.5. The two tailed test on the null hypothesis H_o is found by comparing the value $r^* = \min(r_+, r_-)$ with the critical probability nearest to the wanted significance level

$$\alpha = \text{Prob}(r<r^*/H_o \text{ true}) \qquad 3.33$$

when the total number of points is greater than (~20) the critical region can be formed by using the normal approximation to the binomial distribution with

$$\mu = np$$

$$\sigma = \sqrt{npq}$$

In the presence of a broad peak there should be an excess of positive deviations. Because of dead time the expected mean need not be 2 but can be estimated from the mean high frequency ($\gtrsim$50Hz) powers.

THE RUNS TEST

The runs test also tests the null hypothesis $\mu_1-\mu_2=0$ but it looks for an excess or lack of a runs in the positive or negative deviates. A run is a sequence of consecutive positive or negative deviates. Both a sequence such as + - + - + - or - - - + + + is very unlikely. For small numbers of points the critical region is calculated from the number of possible combinations. A table of these are given by Walpole and Myers (1978). When the number of points is greater than ~20 the distribution of runs approaches the normal distribution with

$$\mu_{uv} = \frac{2n_1n_2}{(n_1+n_2)} \qquad 3.34$$

$$\sigma_\mu^2 = \frac{2n_1n_2(2n_1n_2-n_1-n_2)}{((n_1+n_2)^2\,(n_1+n_2+1))} \qquad 3.35$$

where n_1 and n_2 are the number of positive and negative deviates. If a large enough peak exists there will be a run of positive deviates. This will also occur if the low frequency mean is different from that of the high frequency powers.

Both the sign and runs tests are based upon the assumption that the data distribution is normal. The distribution of powers rapidly meets this condition when the number of degrees of freedom exceeds twenty as is the case with most of the power spectra considered. The sign and runs tests are also very sensitive to the correct choice of the mean.

THE KOLMOGOROV - SMIRNOV TEST

The Kolmogorov-Smirnov (K-S) test measures the difference between two cumulative distributions. It finds the maximum value of the absolute difference between the data's cumulative distribution and the test cumulative distribution In the case of the power spectra with Leahy normalization the expected distribution is χ^2_{2MW} with a mean of two (M is the number of spectra co-added and W is the number of frequency samples binned together)

$$D = \text{Max} (Sn(x)-Pn(x)) \qquad 3.36$$

The distribution of D can be calculated (to a useful approximation) in the case for the null hypothesis (the two distributions, Sn and Pn are the same), thus giving the significance level,

$$\text{Prob}(D>\text{observed}) = Q_{KS}(\lambda) = 2 \sum_{j=1}^{N} (-1)^{j-1} \exp(-2j^2\lambda^2) \qquad 3.37$$

In the above equation $\lambda = \sqrt{N}D$ where N is the number of data points. The calculation becomes asymptotically accurate for larger N. The routine applying the K-S test is based upon that given by Press et al. (1986). The K-S test will detect the skewing of the power's distribution away from the expected χ^2_ν distribution is the presence of a peak.

PEAK TESTS

Another method which is similar in concept to the runs test is that of Mereghetti and Gridlay (1987). This searches for n_p successive adjacent powers above a threshold power.

$$P_{threshold} = Q_\nu^{-1}[(\alpha/n_p)^{1/2}] \qquad 3.38$$

Here α is the confidence level (e.g. 0.05) and n_p is the number of trials (i.e. the number central frequencies searched).

The final search strategy is to bin up the power spectra and search for a peak greater than a threshold power given by

$$P_{threshold} = Q_v^{-1}[\, \alpha/n_{trial} \,] \qquad 3.39$$

where N_{trial} is the number of frequency bins. In order to search most sensitively for a peak the frequency binning width must equal the width of any possible feature. However, the binning may split the peak between two bins rendering it undetectable. So, not only does the bin width need to be varied, but for every width tested, a set of frequency shifts (e.g. 1/4,1/2,3/4 of a bin) must be used. The overall effect of this search strategy is to make the setting of an overall sensitivity limit difficult because the individual trials (each combination of bin width and shift) are not independent. The only way to set an upper limit is to perform a large number of simulations. Because of this inter-dependence this method was used only as a guide to any possible peaks.

If a peak is found the excess power, above the noise limit power, is summed and this is converted to an rms percentage signal using Equation 3.32. However if no statistically significant peak is found the confidence level must be converted to a rms percentage upper limit. This is done by generating simulated QPO power spectra.

3.3.3 Calculation of the Fourier Transform

3.3.3.1 The FFT Algorithm

The Fourier transform can be calculated directly from Equation 3.13. This is an N^2 process and requires the calculation of trigonometric functions. The fast Fourier transform (FFT) is an NlogN process and does not require the use of trigonometric functions. This gives a vast improvement in speed for even moderate numbers of data points. However, the FFT is limited to evenly sampled data and most algorithms also require blocks of 2^n data points, where n is a positive integer. Another limitation upon the calculation of the FFT is sometimes the sheer volume of numbers that need to be stored. For example, using special memory handling routines the μVax3500 can just handle a 2^{23} point FFT. This is only 28 minutes of

data sampled at 5kHz. A method for overcoming this storage limit is expounded by Hocking (1989). Some of the intricacies of the FFT are discussed by Press et al. (1986).

3.3.3.2 Unevenly Sampled Data

When the data are not sampled at completely regular intervals the FFT algorithm can not be used. If there are only short gaps within the data stream these can be filled with interpolated points. However, this introduces extra noise into the final power spectrum. To analyze unevenly sampled data two basic approaches are available; phase folding or the evaluation of Equation 3.13.

An algorithm for doing the discrete Fourier transform (DFT) is given by Deeming (1975). By using a recursion relation (Kurtz 1985) this routine can be speeded up by a factor of 3 to 6. Because of the accumulation of round off errors this method is limited to about 2000 points. As with the evenly sampled case the powers are χ^2 distributed when using the Leahy normalization. In the presence of a signal the powers are no longer simply distributed. The sine wave case is discussed by Gorth (1975). To overcome this problem Scargle (1982) modifies the square of Equation 3.13 to

$$P(x) = \frac{1}{2}\left\{ \frac{\left[\sum_j X_j \cos\omega(t_j-\tau)\right]^2}{\sum_j \cos^2\omega(t_j-\tau)} + \frac{\left[\sum_j X_j \sin\omega(t_j-\tau)\right]^2}{\sum_j \sin^2\omega(t_j-\tau)} \right\}$$

$$\mathrm{Tan}\,(2\omega t) = \frac{\sum_j \sin(2\omega\tau_j)}{\sum_j \cos(2\omega\tau_j)} \qquad 3.40$$

This apparently radical change in the form of Equation 3.13 produces only small changes in the power spectrum even in the presence of a signal (Horne and Balinus 1986). Also this form of the DFT is exactly equivalent to the least squares methods (e.g. Lomb 1976). A major disadvantage of this method is that it is computationally very slow.

Recently two speed improvements have been introduced. Recursion relations can be used (Press and Teukolsky 1988, who include FORTRAN code) or the FFT can be used to calculate the cosine and sine sum terms (Press and Rybicki 1989). This latter method changes the Scargle modification from being a 100 N^2 method to a ~100 NlogN process. The bulk of the analysis in this thesis was done before these modifications were known to the author.

With even spacing there is a natural set of frequencies i.e. $\Delta\nu=1/T$ from 0 Hz to the Nyquist frequency. In the case of unevenly spaced data the Nyquist frequency can not easily be defined. Also there is no obvious set of natural frequencies. Within the data stream there is information up to frequency of $\omega_{max} = \pi/\Delta T_{min}$ where ΔT_{min} is the smallest separation between samples. Some sort of average sampling rate may be more appropriate to set the Nyquist frequency. The finest frequency sampling that can be used is 1/T . Generally a coarser sampling in frequency will be more practicable. The natural set of frequencies is formally given by the nulls of the spectral window (Scargle 1982).

The window function is given by

$$W(\nu) = \sum e^{i2\pi\nu t_k} = \sum e^{i\omega t_k}$$

$$= \sum_{k=1}^{n} (\cos\omega t_k)^2 + (\sin\omega t_k)^2 \qquad 3.41$$

which is the Fourier transform of the arrival times. In the case of even spacing this is a sinc^2 function with $\omega(0)=1$ (normalization of Deeming 1975) and nulls at $\Delta\nu=1/T$. A similar sort of structure is seen in the window function of an evenly spaced data set but there are no alias peaks at the Nyquist frequency. It also shows, as a peak with a height near unity, any regular sampling period within the data.

This form of the window function assumes instantaneous sampling and cannot be generalized to cover variable length integration times (Pomman 1981). Also with the Scargle form of the DFT the window is not explicitly defined for unevenly

spaced data. In both cases a pseudo-window can be generated by substituting the data, preserving the sampling timing, with a high frequency sine wave.

3.3.4 Phase Folding

Many astronomical sources have markedly non-sinusoidal pulse profiles e.g. the Crab pulser. In these cases Fourier type techniques spread the power amongst multiple peaks thus reducing the ability to detect the periodic signal. To overcome this limitation, phase folding methods may be used. Also phase folding is unaffected by uneven sampling.

Conceptually Three methods are very simple. For each trial period the phase for each data point is calculated and the value added to the corresponding phase bin. Then some test is applied to the phased light curve to determine whether a significant variation, beyond that for random data, exists. The simplest test used is the Pearson's χ^2 test for constancy (e.g. Leahy, Elsner, Weisskopf 1983), with high values of χ^2 indicating the presence of a period. The resulting periodogram values are also χ^2 distributed (dof = number of phase bins) and so any peak can tested for significance.

Another statistic used is the Q method of Warner and Robinson (1972).

$$Q = \frac{1}{N_b} \frac{\sum_{i=1}^{N_b} n_i \varphi_i^2}{N} \qquad 3.42$$

Here N_b is the number of phase bins and n_i is the number of points in the i_{th} phase and φ_i is the average count rate within the i_{th} phase bin. In some cases the data sampling, the chosen period and phase binning cause an uneven distribution of data points amongst the phase bins (some $n_i = 0$), or all the data points fall near the boundaries of the phase bins. Overall, such pathological cases cause the value of the test statistic to be dependent upon the number of bins used. Careful choice of the number of phase bins, e.g. N_b prime, usually avoids this problem.

An alternative solution is to use overlapping phase bins e.g. the methods of Stelligwerf and Jurkevich (see Swingler 1989 for a comparison with other Fourier methods). These methods use the ratio of data's variance to the variance of the phase folded data as the test statistic.

In the phase folding methods the period interval between statistically independent trial periods is $\Delta P = P/T_{obs}$ (P is the period being searched and T_{obs} is the time span of the data). In order to be sure of detecting a peak the period sampling interval should be 5 times finer than the sampling interval. The phase folding methods are much slower than the DFT because of the fine period sampling required to locate the peak in the power spectrum. In general period searches using the DFT, with suitable normalization, are preferable to phase folding because the resulting distribution of powers is well defined. However, given a period estimate, phase folding can yield an accurate period by fitting the resulting periodogram peak (Leahy 1989).

As an example of the response of the Fourier and phase folding methods consider a square wave. The Fourier methods will produce a series of peaks in the periodogram at the odd harmonics while the Q method will produce a single peak at the fundamental frequency.

The statistical nature of the periodogram produced by many phase folding techniques is difficult to define because of the interdependence of overlapping phase bins. To set upper limits simulations must be used.

The best estimate of the period is not necessarily at the peak value of the statistic. A least squares fit to the periodogram peak with the errors in the fitted period being determined using Monte Carlo simulations (Fernie 1989, Leahy 1989).

3.3.5 Period Searches with Arrival Time Data

Arrival time data, where each photon is tagged with a time, can be searched for periods in one of two ways. Phase binning can be used with the number of events in each phase bin subjected to a statistical test, based upon the Poisson distribution or a circular statistics can be used. Circular statistics test the concentration of the arrival times in phase. Several are discussed by Protheroe (1987a). The most commonly used is the Z_k statistic (i.e. Protheroe, 1987b)

$$Z_k = \frac{2}{N} \sum_{j=1}^{k} \left\{ \sum_{k=1}^{n} (\cos\omega t_k)^2 + (\sin\omega t_k)^2 \right\} \qquad 3.43$$

This is equivalent to summing the K_{th} harmonic of a signal. The Z_k is χ^2_{2k} distributed in the absence of a signal. When a signal is present the response of Z_k is dependent upon the type of the signal. The power, the ability to correctly reject the null hypothesis (no signal), is dependent upon the shape of the underlying signal. The Rayliegh test (k=1) is most sensitive to broad sinusoidal signals while at higher values of K the Z_k test is more sensitive to narrow, pulsed, signals. Note that when k=1 Equation 3.43 is equivalent to the amplitude of the window function (cf Equation 3.41).

Other circular statistics suffer from this same problem of being selective. In order to produce a more general test De Jager (1989) introduces the "H" statistics. Compared to other statistics is not quite as sensitive as the Rayliegh test for sinusoids and for peak widths <6% the Z_{10} test and Protheroe's (1987a) Υ_n statistic are more sensitive.

3.3.6 Aperiodic Variability.

Often no underlying periodic signal exists. This does not mean that there is no information to be gained from the time variations. Even completely random variations with no preferred time scale (white noise) may constrain models. The aperiodic variability of many sources, particularly Cygnus X-1, is modelled in terms of shot noise (Terrell et al. 1972). A series of decaying oscillating shots can give rise to red noise and quasi-periodic oscillations (Lamb 1986). Methods of recovering, in the time domain, the underlying structure are given by Scargle (1981).

The first step is to determine if there is excess variability above that expected from photon statistics. This is most commonly done using the Pearson's χ^2 statistic which can also be used to estimate the percentage excess variation (Forman et al.1976, Li et al.1978). The basic χ^2 procedure has been greatly expanded in scope by Collura et al. (1987) (see Amburster et al. 1987, for an application) to yield the characteristic time scale with errors, for unevenly spaced data.

The most widely used method to find the signal's characteristic time scale is the auto correlation function (ACF). In its basic form , with modifications for counting statistics, time resolution and finite observing time (Wiesscopf et al. 1975), the auto-correlation function is limited to continuous evenly sampled data. A discrete

correlation function (DCF) can be formed by the sum of product pairs (Edelson and Krolik 1988). These forms result in some distortion and loss of information. Scargle (1989) uses the inversion of the discrete Fourier transform (Equation 3.13) to calculate the ACF for unevenly spaced data, with full information recovery.

Related to the ACF are the structure functions (Simonetti, Cordes, Beechan 1985) and the variation function (Maejima et al. 1984). The variation function is the square root of the data variance due to intrinsic variability, on the time scale of the time bin t_b, normalized by the average flux.

$$\eta = \frac{\left[V(t_b) - X(t_b) \right]^{1/2}}{X(t_b) - Y(t_b)} \qquad 3.44$$

where $X(t_b)$ is the mean counts per time bin t_b including background $Y(t_b)$ is the background per bin and $V(t_b)$ is the total variance. The Poisson noise is subtracted in the numerator.

The variation function (VF) is equivalent to integrating the source power spectrum at time scales $t_b \geq \tau$. It approaches zero in the absence of any intrinsic noise and in general increases with decreasing t_b in the presence of source variability. In particular $\eta \propto t_b^{1/2}$ for white noise. The size of the power law slope increases when red noise is present. The variations function response to a periodic signal is a sharp drop at the time scale of the periodicity.

3.4 Application of these methods

The FFT and VF were used to analyze the optical noise behavior of Sco X-1. Because of the effects of telemetry overflows and gaps in the UT86 data stream, the methods applicable to unevenly spaced data must be used to search for QPO and coherent signals from Sco X-1 (Chapter 6). The pulse period of GX 1+4 was determined using the χ^2 phase folding method. The Q method was used throughout this thesis, e.g. to determine the period of magnetometer oscillation during the 1983 flight.

Energy spectral reduction of Sco X-1 and GX 1+4 was carried out using the minimum χ^2 method.

Chapter 4

Balloon Borne Observatories :

Brazil (1983) and Alice Springs (1986)

What goes up must come down.

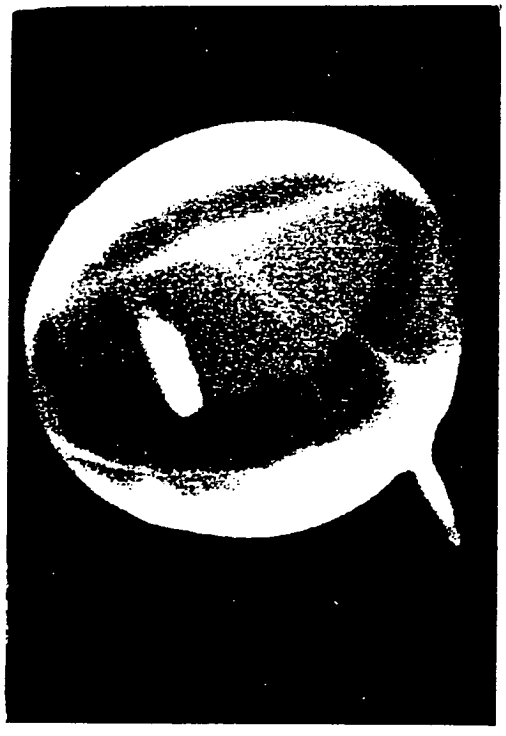

4.1 Introduction

The X-ray observations presented within this thesis were obtained using two different detectors flown upon similar platforms. The initial University of Tasmania detector (UT1) (Greenhill et al., 1977b) was successfully flown during 1976 and 1978 (Duldig 1981, Duldig et al. 1977, Greenhill et.al. 1977c) using an equatorial mounting. During these flights the field of view was 7° x 20° FWHM. In order to study sources close to the galactic centre the field of view was reduced to 2° FWHM. This requires better pointing accuracy and stability. To achieve 0·2° accuracy the equatorial mount was replaced with a micro-processor controlled altitude-azimuth (alt-az) mount. This platform/detector was flown in collaboration with Imperial College on March 20 1983 from Cashoeria Paulista, Brazil (hereafter referred to as the UTIC83 flight). Launch services were provided by Instituto de Pesquisas Espaciais. This flight occurred before the author joined the X-ray astronomy group.

The UTIC83 flight ended in a combined balloon and parachute failure that resulted in the destruction of the payload. This allowed the complete redesign of the UT detector. A new alt-az platform was constructed. In collaboration with the University College (ADFA) University of NSW, Canberra, Astronomisches Institüt Tübingen (AIT), and Instituto di Astrofisica Spaziale at Frascati (IAS), the new UT detector (UT2) was flown on the 26th November 1986 from Alice Springs Australia (the AS86 flight).

The general layout of the 1983 and 1986 platforms can be seen in Figures 4.1,4.2 and 4.3,4.4. A schematic diagram showing the relationships between the various 1983 on-board and ground station sub-systems in Figure 4.5. A similar diagram shows the on-board sub-sytems of the 1986 payload (Figure 4.6).

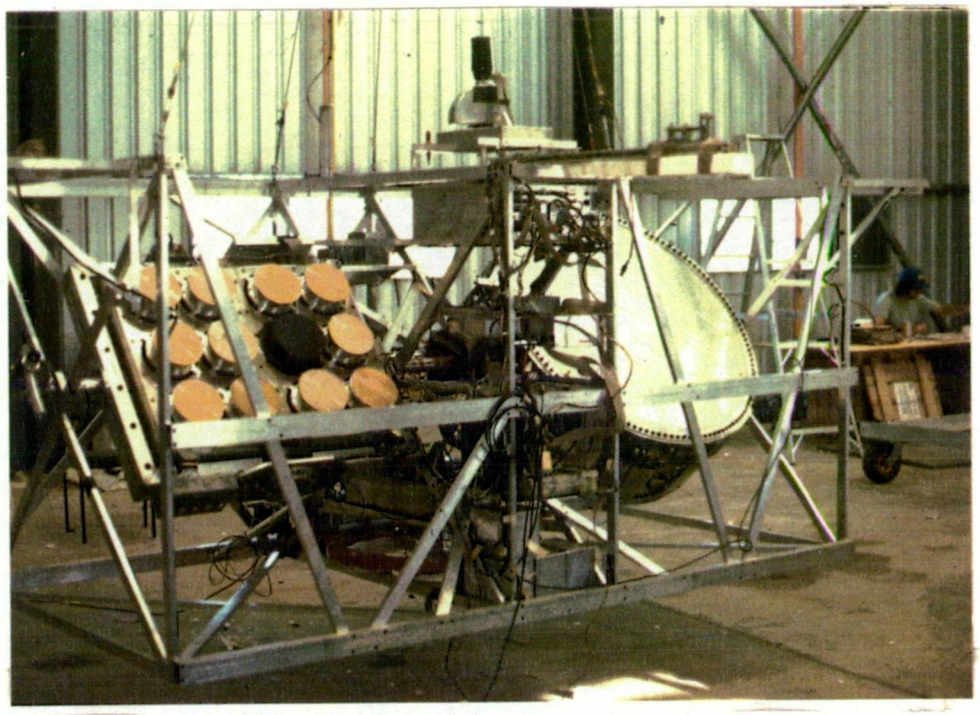

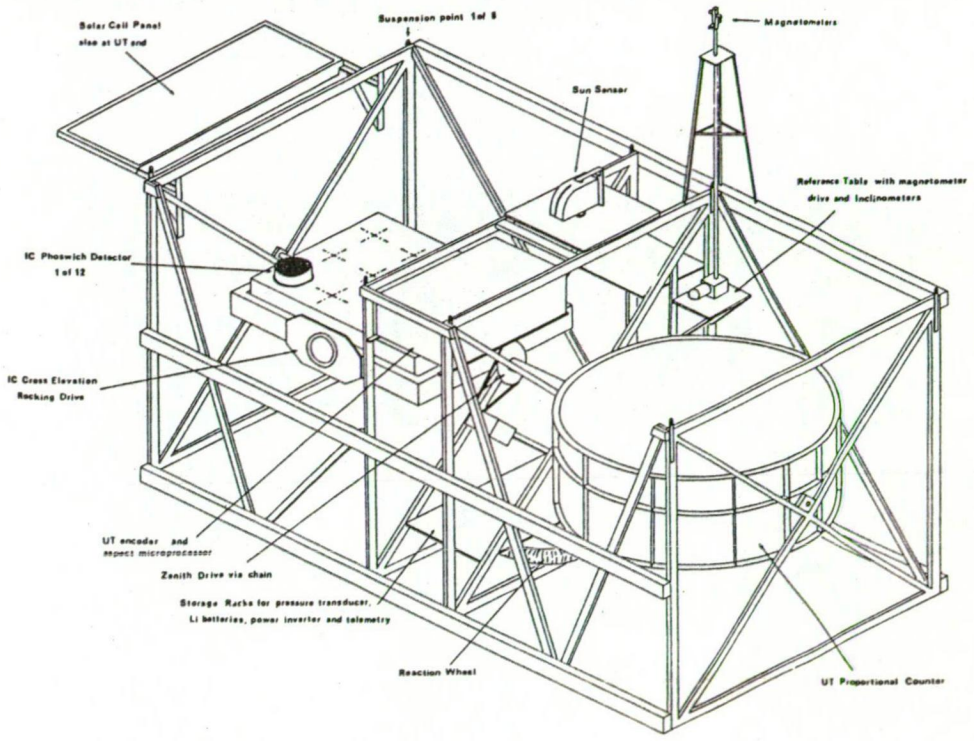

Fig 4.1 and 4.2 A photograph and diagram showing the major elements of the UTIC83 platform (Watts 1983).

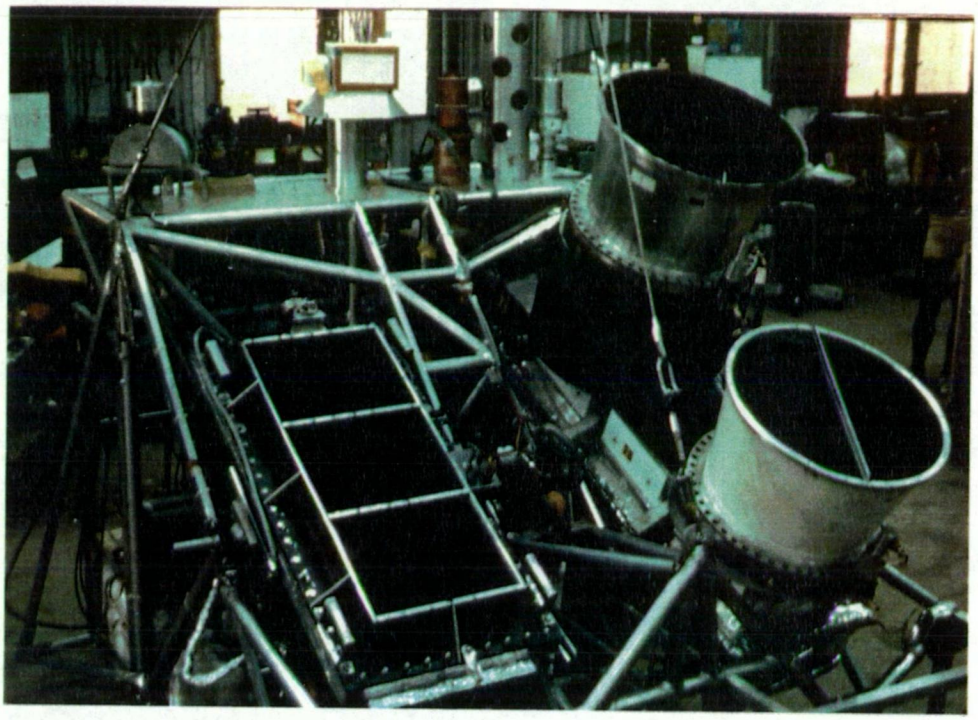

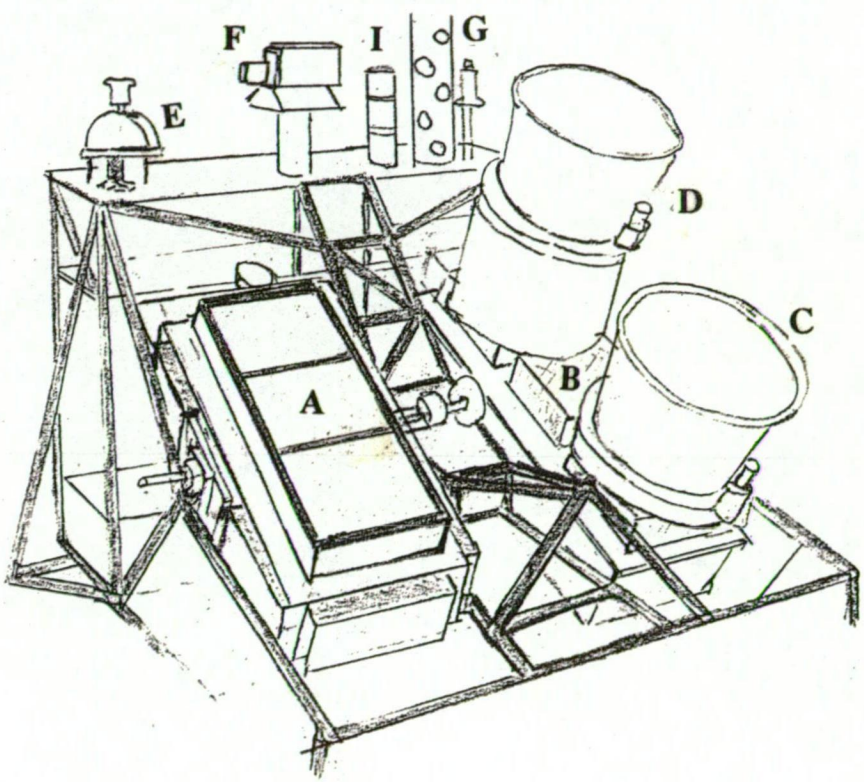

Fig 4.3 and 4.4 A photograph and diagram of the AS86 payload. **A**: University of Tasmania detector, **B**: ISAS detector, **C**: AIT RMC, **D**: Optical/X-ray RMC, **E**: sun sensor, **F**: sun tracker, **G**: AIT 3-axis magnetometer, **I** radio beacon.

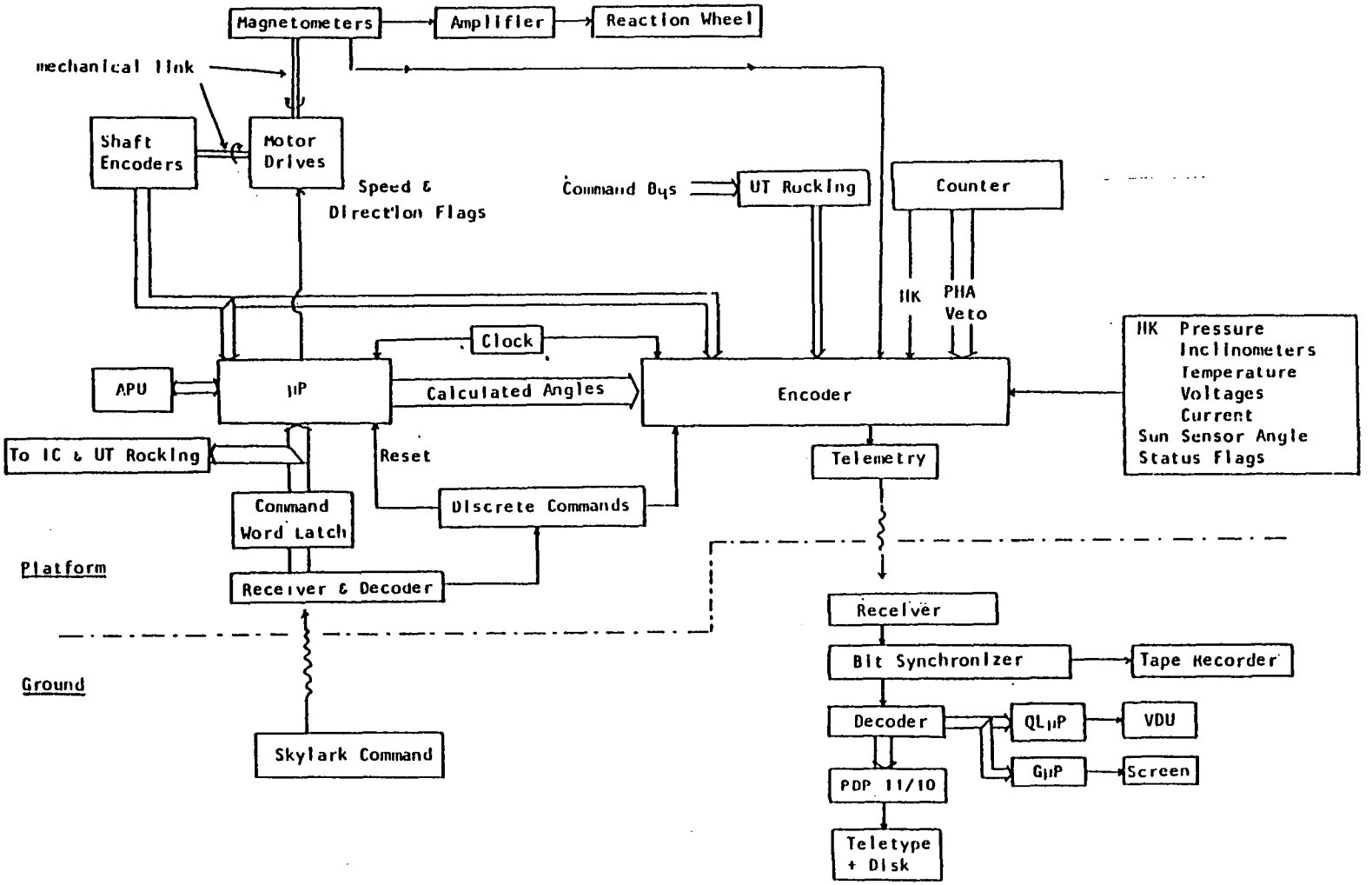

Fig 4.5 A block diagram of the balloon and ground station segments used in 1983.

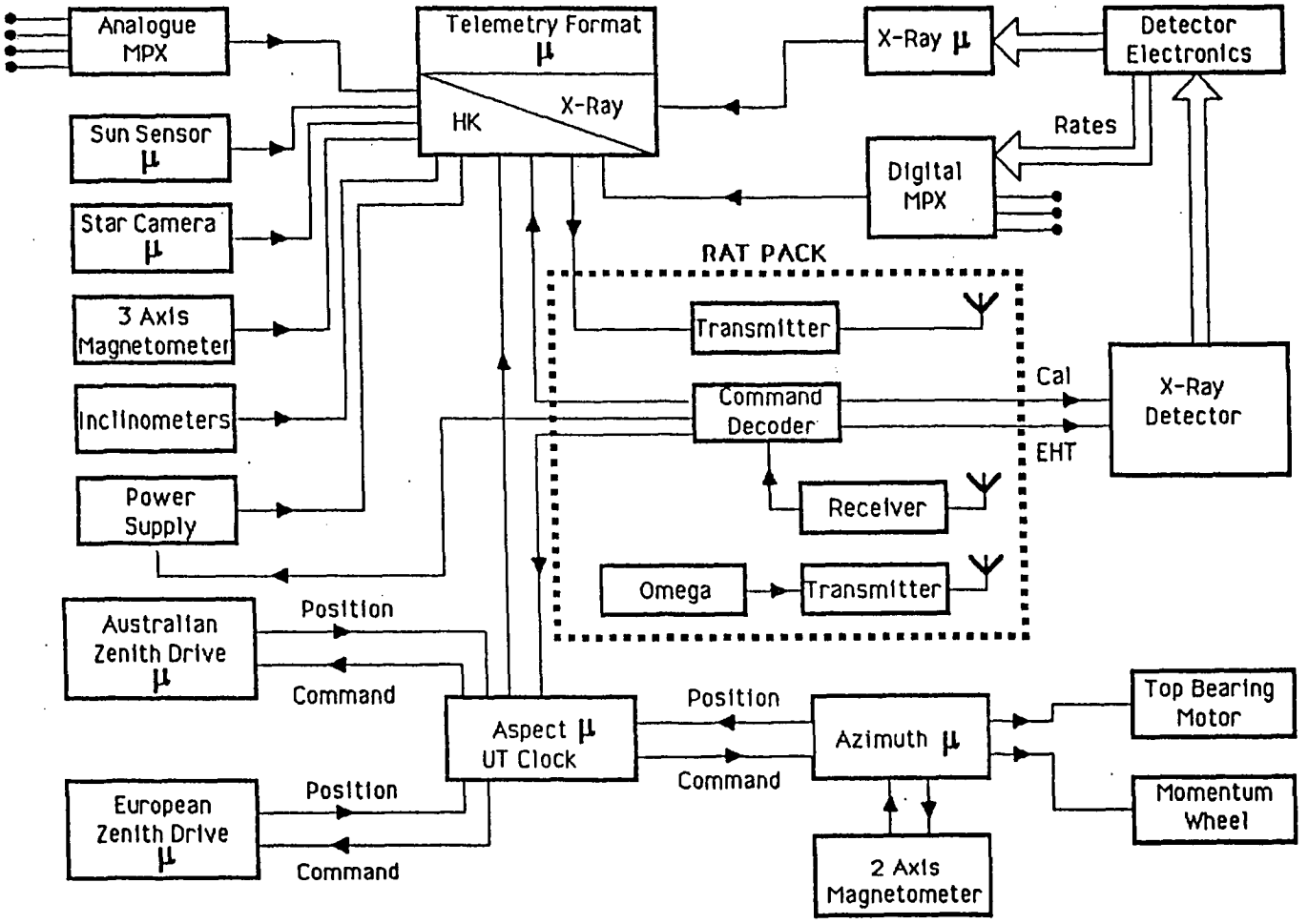

Fig 4.6 Block diagram of the AS86 platform electronics.

4.2 The Detectors

4.2.1 UT1 Detector

The UT1 detector was a multiwire, multianode proportional counter with an effective area of 5200 cm^2 , active depth of 21 cm, filled with a mixture of 95% xenon and 5% methane at a pressure of one atmosphere. The detector itself consisted of six stacked octagonal trays. Successive trays were stacked cross wise to maintain the detector's rigidity. The top five trays made up the active volume. Each tray had 21 anodes (EHT 2300 volts) with a cathode wire between each anode and a plane of cathodes between each layer of anodes. Above the top tray, just below the Al window, there is an earthed array of wires spaced 1 cm apart. This formed the ground plane of the top tray.

The anodes of each tray are wired together in groups of three, called a cell. Each cell has its own pre-amplifier. The pre-amplifier outputs from each tray are fed through the detector wall via one of five output ports, to the signal processing circuitry. Each output port forms a sector of the detector. A layer of guard detectors around the sides of the active volume and the bottom tray form a five sided active veto system.

The outputs from each cell are first passed to the veto logic, then amplified, differentiated (10 μsec time constant) and added to the similarly treated outputs of up to three other cells. These event pulses are then passed to one of eleven peak detectors. The combined signal charges up a capacitor with a long time constant and triggers a lower level discriminator (LLD). A pulse height analyzer (PHA) reads the maximum voltage of the capacitor using an 8 bit analogue to digital converter. This is done while the LLD is logically high. The LLD remains logically high for 10 μsec allowing enough time for the event pulse to decay. When the LLD goes low the capacitor is discharged with a time constant of 2.2 μsec. Both the lower level discriminator and the total energy range can be adjusted. Because of telemetry restrictions the PHA output was limited to 19 channels out of the possible 256.

In order to get the best overall gain and energy resolution from the detector the gains of each cell's amplifier are matched. During laboratory tests, an energy resolution of 25% FWHM at 60 keV was achieved. The counts in each PHA

channel are accumulated for two seconds. Also the counts in channels six to fourteen are summed into 4 msec count rates and inserted into the telemetry stream.

The veto logic rejects events if three or more cells are triggered within 10 μsec. Also rejected are any pulses that occur within the time span from 2μsec before till 4μsec after any event with the guard cells. These events are largely due to charged particles. All vetoed events are counted and the rate output to a veto channel in the telemetry format.

Further background reduction is achieved using a graded shield consisting of, from the outside inwards; Pb (1.14 gram cm^{-2}), Sn (1.8 gram cm^{-2}) and Cu (0.022 gram cm^{-2}). The inner layers absorb the fluorescence photons generated by the preceding layer. Sealing the top of the detector is a 0.5mm thick aluminium window. The collimator also reduces the extraneous count rate. The tin collimator's field of view (FOV) was measured during ground tests as 2.16° FWHM.The FOV may be larger than this value. During previous flights the collimator had been damaged by differential pressures across the window/collimator combination. The alignment and testing of the collimator was preformed by Dr. D Watts (Watts 1983).

The detector is mounted in a one metre diameter pressure vessel which is divided into two hermetically sealed sections: the detector volume and a surrounding volume containing the collimator is filled with methane. Above and below the detector the methane is contained by ten layers of mylar sheeting (0.134 g cm^{-2}). The purpose of the methane bubble is to relieve stress upon the aluminium window as the external atmospheric pressure drops from one atmosphere to ≈3mb. Even so, because of the flexible nature of mylar, pressure differences of 50mb can be produced across the Al window. To maintain a pressure balance, as measured by a transducer mounted in the collimator section, methane is vented or added to the methane bubble. A schematic diagram of the detector is given in Figure 4.7.

The efficiency of the detector is governed by both the transmission of the window and the absorption of the detector gas. The combined (mylar, methane, Al window) transmission of the window, along with the total detector efficiency is given in Figure 4.10.

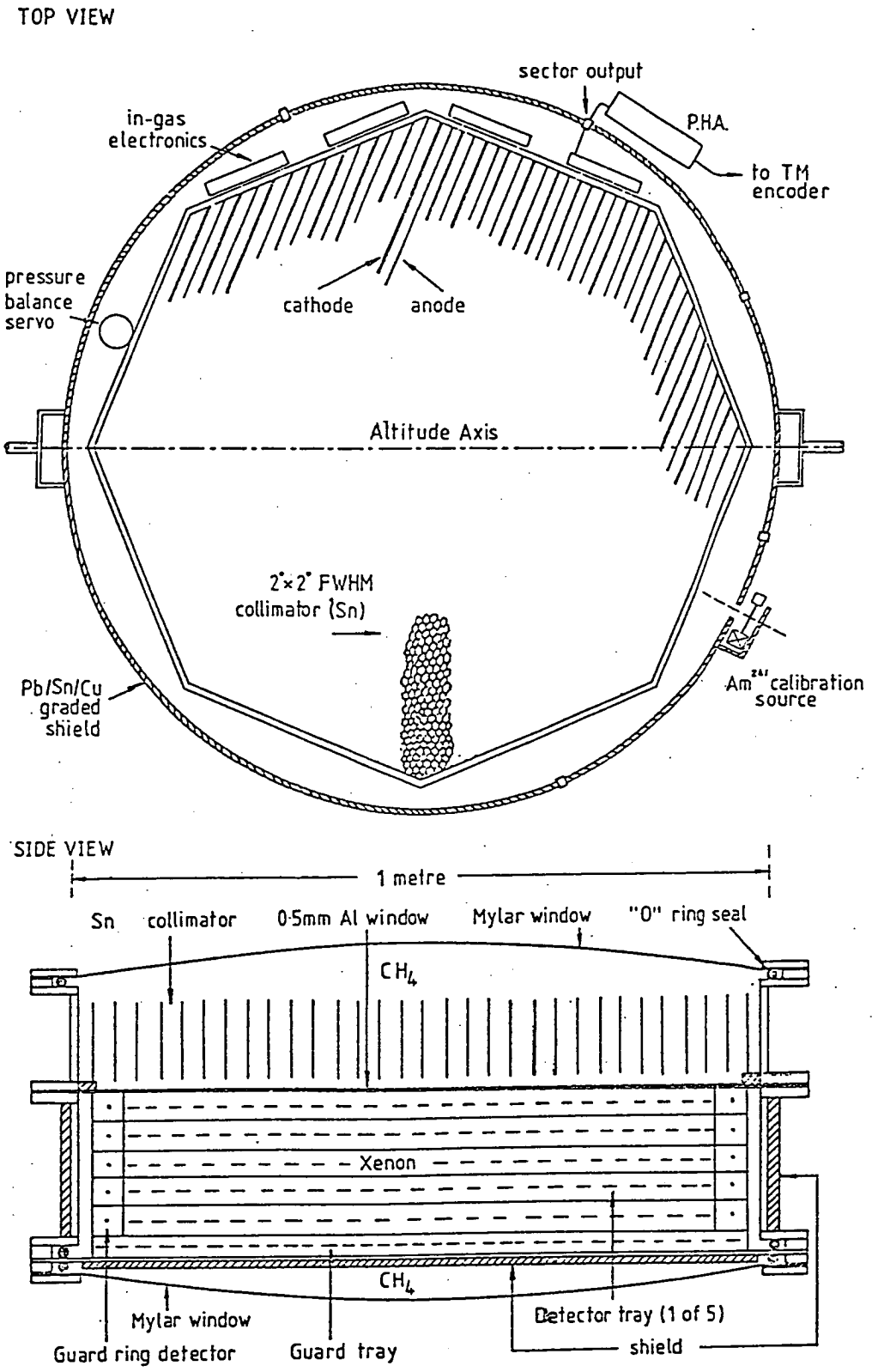

Fig 4.7 Top and side views of the UT1 (1983) detector.

4.2.2 Imperial College Detector

For the UTIC83 flight Imperial College provided a detector consisting of 12 identical NaI/CsI phoswich scintillators sensitive to the energy range 20 - 200 keV. The total effective area was 1680 cm^2. The resolution was 22% at 122 keV. Above each scintillator was a tantalum honeycomb collimator that gave a 2° x 2° FWHM field of view. A plastic scintillator shield was used to reject any charged particle events entering the collimator or passive shield. To obtain background observations the detector was rocked in azimuth.

4.2.3 The UT2 Detector

The new University of Tasmania's detector was built as a rectangular multiwire multianode proportional counter with an sensitive area of ~2000 cm^2 and active depth of 19.2cm. It was filled with a mixture of 95% xenon and 5% methane at a pressure of 2.5 atmospheres. The detector is described in detail by Sharma et al (1987) and the schematic diagrams of Figures 4.8, and 4.9 show its structure.

The wire array of the detector was contained within a 1001 x 458 x 230 mm stainless steel (3mm thick) pressure vessel strengthened externally by ribs. The interior was polished to reduce outgassing. The window is two carbon fibre, 5 mm thick, sheets that sandwich an aluminium honeycomb. To separate the carbon fibre from the detector gas a thin (200 micron) aluminium sheet was glued to the underside of the window. The window / pressure vessel interface was sealed using an "0" ring and secured by numerous bolts. The collimator was made by drilling circular holes (4mm) in lead alloy block 38mm thick. The wall thickness between holes was 125 microns. The drilling was done by a numerically controlled drill in the Engineering Department of the University of Tasmania and at University College (ADFA). Two blocks were stacked to give a 3° FWHM field of view.

The detector wire array sits within the pressure vessel and consists of 7 layers of 12 cells (32 x 32 mm). Each cell is a single anode (EHT 3100 V) surrounded by an earth plane of cathodes. Each layer of anodes the cathodes are spaced 8 mm apart. To minimize any outgassing only the EHT decoupling capacitors and resistors for each anode are within the pressure vessel. The detector was evacuated and heated to ≈50°C for 5 days to further reduce any outgassing.

A six sided veto system was built for the UT2 proportional counter. The side and bottom cells are used as guard cells. Upon the detector ends, nickel cathode strips above and below each anode are used as end guards (Figure 4.9). Any X-ray interacting near the ends of the detector will cause a pulse upon both the cathode strips and the anode. Higher energy photons will produce a voltage on the cathode strips further away from the wall. The sum and ratio of the cathode strip and anode voltages is used as the veto signal (Smith and Truner 1981). This procedure reduces the energy dependence of the cathode strips response.

A top guard (Smith and Turner 1982) is incorporated into the UT2 detector. However, because of top guard gain variations caused by pressure induced distortions in the window the top guard veto was not used. A layer of closely (1.25mm) spaced wires is set just below the entrance window and held at a small negative (~-20V) voltage. Compton electrons produced within the collimator/window will be slowed by the voltage applied to the front guard. This allows rise time discrimination to be used. Provision was made for the recording the rise time of each top layer event. Any event is rejected if it occurs within 10 μsec of a veto pulse. All events that trigger two or more cells are rejected. The pulse processing has a dead time of 5 μsec.

If an event is made up of two interactions (e.g. an X-ray photon and its fluorescent photon) the energies of both are recorded. It is possible to extend this to triple events where the initial photon has an energy >70 keV and so can produce two fluorescent photons. In rare cases the initial or fluorescent photon triggers two adjacent cells. Triple events were vetoed. Post flight analysis can use the energies of double events to preform escape gating.

Passive shielding is achieved using a 1 mm thickness of lead and the 3 mm stainless steel body of the pressure vessel and the aluminium of the wire frame.

The design of the detector was mainly by Dr J. Greenhill, Dr G. Salmon and Dr A Giles., construction of the wire array was by Dr D.P Sharma (Sharma et.al. 1987). The pressure vessel was built by Mr Barry Wilson and Mr Max Mason. Each anode and end guard cathode has a separate pre-amplifier. The pulse shaping and veto logic electronics is performed by the Detector Analogue and Digital (DAD) signal processing electronics designed and built by D. Warren and Dr. J. Greenhill. The DAD electronics also time tags each event to the nearest millisecond using an internal crystal oscillator. Top layer events are flagged. After

all processing is complete the serial events are reformatted, buffered and passed to the Telemetry microprocessor. Further details of the detector electronics is given in the MIRRABOOKA proposal volume MXG-PAY-0003.

Using an Olivetti M21, an interface card and an extensive suit of software written by Dr. A. B. Giles the EHT of each cell or group of cells can be switched on or off. The Olivetti was also used to gather and display PHA spectra. Background subtraction and Gaussian profile fitting could also be performed enabling the resolution of any section of the detector to be quickly found. This greatly assists in testing and cell gain matching. During pre-flight tests an overall resolution of 20% at 60 keV was attained.

4.2.4 The 1986 European Detector

For the 1986 flight the Instituto di Astrofisica Spaziale (IAS) provided a multiwire multianode proportional counter. It has an active depth of 15 cm, effective area of 2700 cm^2 and is filled with xenon-isobutane mixture at 5 atmospheres pressure. The 50 cells (30 x 30 mm) are arranged in 5 layers of 10 cells. A resolution of $\approx$15% at 60 keV is achieved for the whole detector. The window is formed from two 200 μm thick aluminium honeycomb sheets. The detector is strengthened by two aluminium clamps.

Background rejection is accomplished using the side and bottom cells as a 3 sided anti-coincidence veto system. Also the background is reduced by the combination of 1 mm lead and the 2 mm thick stainless steel body. The detector is described in more detail by Ubertini et. at. (1981).

Instead of a passive collimator, two synchronized rotation modulation collimators (RMC) were provided by Astronomisches Institüt Tübingen (AIT). These yield modest resolution (<20") imaging over a 4° FWHM field of view. (Thienhardt et al. 1984). The sun can be used to check the platform pointing in which case a photo-diode replaces the proportional counter as the detector. An on board micro-processor produces a correlation map from which azimuth and zenith offset can be determined.

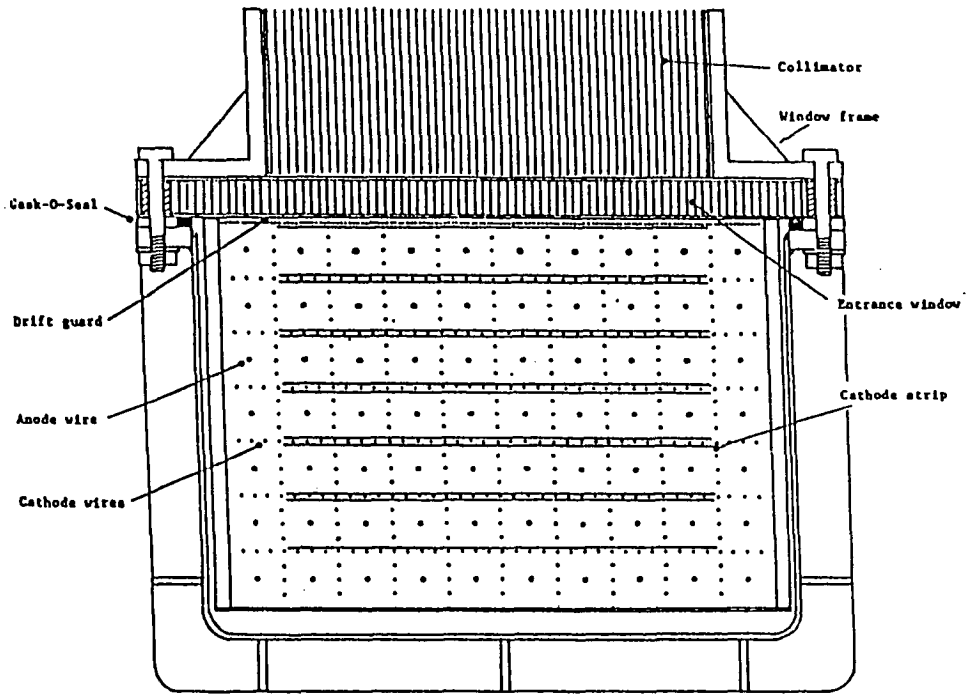

Fig 4.8 End view of the UT2 detector showing the 7X20 array of cells. The outer layer of cells are the veto cells.

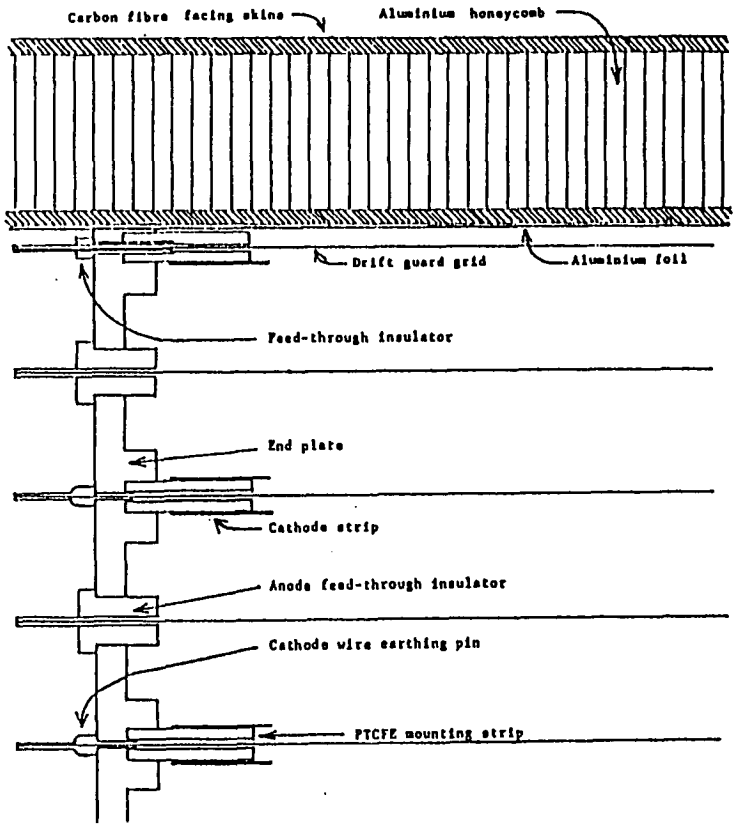

Fig 4.9 End view of the UT2 (1986) detector giving details of the entrance window, top tray drift guard and the cathode strips that make up the end veto system.

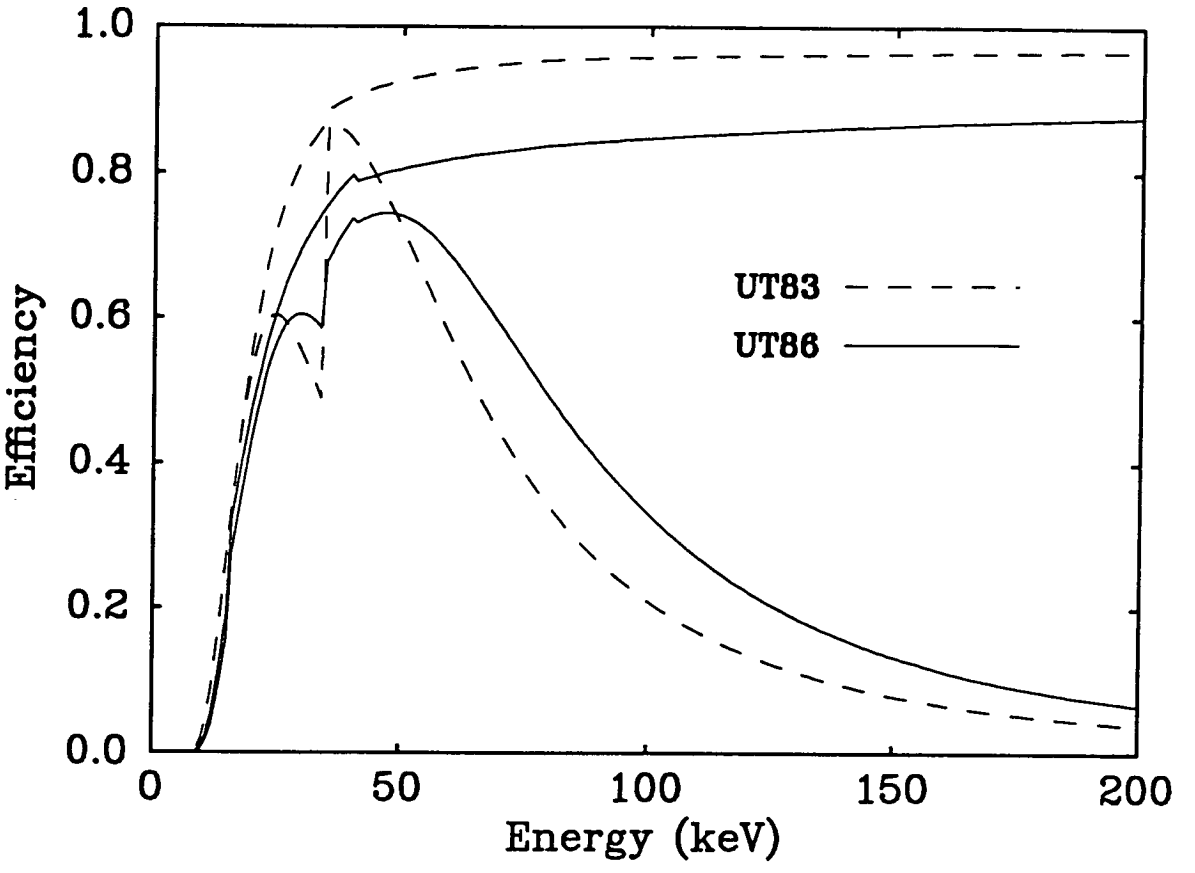

Fig 4.10 The window transmission (upper curve) and overall detector efficiency curves of the UT1 (1983) and UT2 (1986) detectors. The UT2 (1986) window was more absorbant than anticipated because of heavy metal contamination of the glue used to bind the carbon fibres. Atmospheric absorption is not taken into account.

4.3 The Azimuth Servo System

The servo system consists of five components: the aspect micro-processor, two axis magnetometer and shaft encoder, the reaction wheel, and a suspension bearing motor. The local geomagnetic field is used as the azimuth reference.

All the navigation sensors are calibrated in a process akin to boxing a ship's compass. The payload is suspended under a non-magnetic frame away from any magnetic materials. At approximately 10° intervals, in azimuth, the platform is leveled and the true azimuth determined (Sprent 1986). The difference between the true and magnetically measured azimuth form the sensor's calibration curve. The calibration also provides a test of the entire payload, telemetry and ground station system.

The magnetic field as sensed by the 2-axis magnetometer needs to be corrected for changes in the variation of the earth's magnetic field with latitude and longitude. Also the local geo-magnetic field is distorted by the platform. A magnetic variation map, offset and magnetometer calibration are stored in the ground station computer. These two offsets are combined and sent to the payload by tele-command.

The aspect microprocessor (μp) calculates the azimuth and zenith of a source given the balloon's latitude, longitude, the sources right ascension and declination, azimuth offset, and the Universal Time (UT) from an onboard clock. There are three modes of operation; manual, tracking and rocking. In manual mode the aspect μp directs the detector to a specified azimuth and zenith angle. In pointed mode the source is smoothly tracked. The rocking mode is similar to the pointed mode except the detector is periodically moved off source in zenith by up to ±10°. The movement in zenith angle can be made in one of three patterns; scanning back and forth through the source position (triangular), moving off and onto source (square) and moving alternately between a point above, on and below the source (staircase). The rocking mode allows regular sampling of the background, enabling more accurate background subtraction particularly in the presence of zenith angle variations in the background counting rate.

Two magnetometers mounted at right angles to each other upon, a non-magnetic tower are used to sense the local magnetic field. One magnetometer is aligned with the magnetic east/west direction and so is nulled. The other (north/south)

magnetometer is used to remove the 180° ambiguity in the direction of the east/west magnetometer. Upon command from the aspect microprocessor, the 2-axis magnetometers are moved to a new azimuth, causing the east/west magnetometer to become non-zero. This is the signal G' in Figure 4.11. This voltage is amplified, with velocity feedback and used as an error signal (G). The error signal is fed to a voltage to frequency converter that triggers a monostable pulse generator. The pulses drive, via a FET power amplifier the DC torque motor of the reaction wheel. Thus the power supplied to the reaction wheel is proportional to the error signal. Through conservation of angular momentum the entire platform rotates in the opposite direction to the reaction wheel. The error signal also drives the top bearing motor drive ensuring that no momentum is transferred from the balloon to the platform. A schematic representation of the servo system is given in Figure 4.11 along with a sketch of error signal curve. The response curve (insert of Figure 4.11) is split into three regions, a dead zone within ≈0.1° of the null, a steep response region within 1° of the null and gentler response region beyond 1°. The gain and velocity feedback components are adjusted to give critical damping to the motion of the platform.

The azimuth shaft encoder for the driving magnetometers is mounted at the base of the magnetometer tower. In order to stop twisting the shaft and wiring there are two sets of limits. One, in the software of the azimuth microprocessor defines a prime 400° region, the other approximately 600° wide region, is set by limit switches. Upon hitting a limit switch the magnetometers are moved back into the prime circle.

During the 1983 flight the zenith and azimuth were only read to the nearest ≈0.2°. This was improved to ≈0.1° for the 1986 flight.

The pointing algorithm, and details of the aspect microprocessor used for the 1983 flight are given by Watts (1983). During the 1986 flight the algorithm was slightly modified, as discussed in Chapter 5 (Equation 5.7). The typical cycle time of the aspect program is ≈0.1 sec, making updates practically instantaneous.

The servo system of the UTIC83 platform achieved a stability of ≤0.25° in azimuth. Imaging using the RMC required better stability (0.1°). This stability was achieved after several refinements in the basic control system.

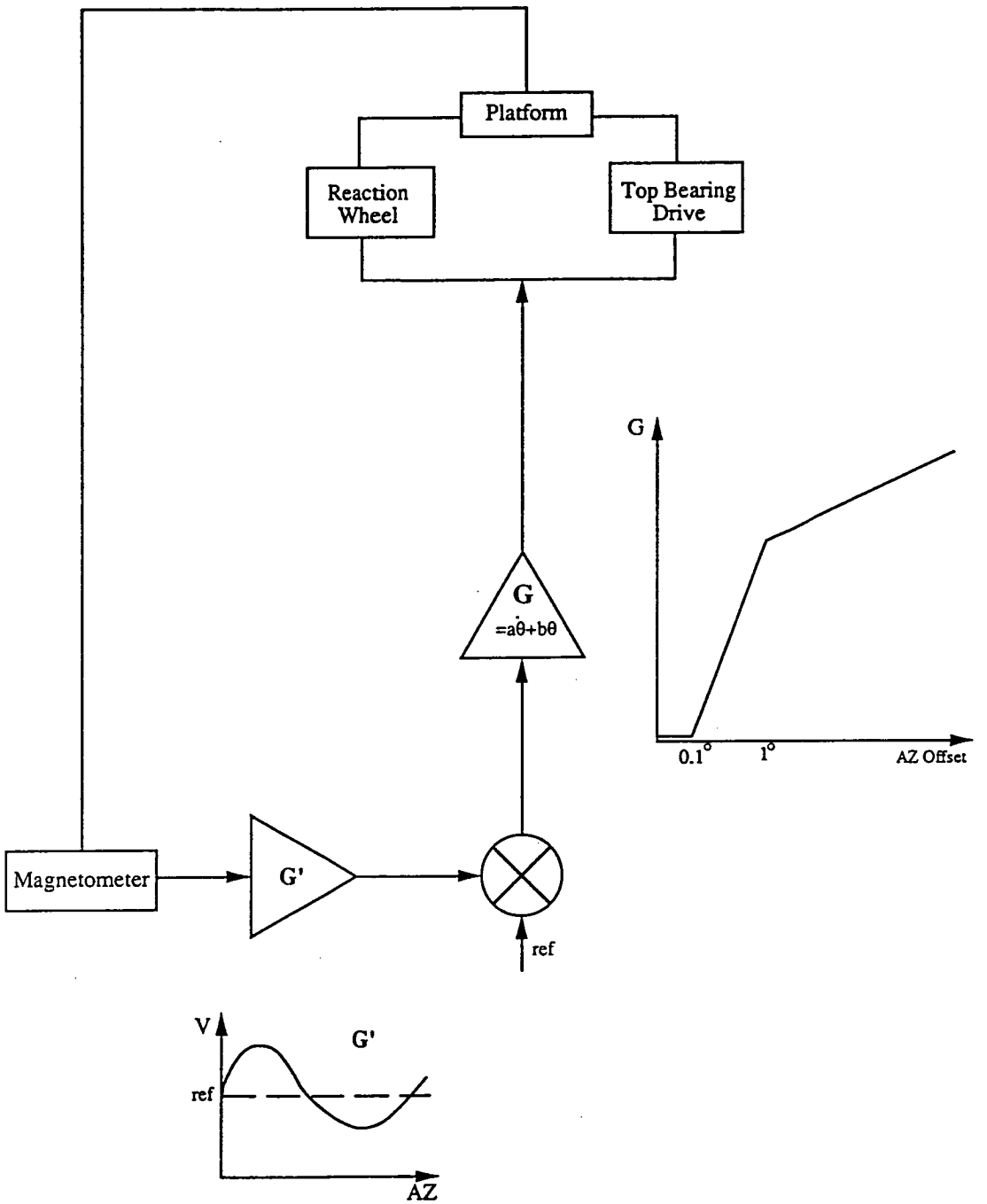

Fig 4.11 A block diagram of the servo system. The link between the magnetometer and platform is via the earth's magnetic field. The magnetometer response, G', is approximately sinusoidal. Also shown is a schematic representation of the feedback signal (G).

4.4 Navigation Sensors.

Upon the UTIC83 platform there was also a 3-axis magnetometer supplied by Imperial College, and a sun sensor designed by M.W. Emery of the University of Tasmania. In Chapter 5 both these instruments are used to determine the final pointing solution.

During the 1986 flight there was an expanded number of navigation sensors; two 3-axis magnetometers (one supplied by AIT the other by ADFA), an ADFA sun sensor an AIT two axis sun tracker and a pair of inclinometers. The sun tracker determines both the altitude and azimuth of the sun relative to the platform.

All ADFA magnetometers were of the single component flux gate type, with a range of ≈600 milli-orsteads. The output voltage of each unit is given by

$$V = 2(V_0 + 0.004\,H\cos\phi) \qquad 4.1$$

where V_0 is the reference voltage (2·4 volts nominally), H the ambient field in milli-orsteads and ϕ the angle between the the magnetic field vector and the magnetometers positive axis. The telemetry contains information upon the output and reference voltages of each individual magnetometer.

The sun sensor was slightly different between the 1983 and 1986 flights. In the UTIC83 flight it was a quadrant shaped box with a pair of closely spaced slits while in 1986 the sun sensor was a semi-circular box with two oppositely situated vertical slits. Refer to Figures 4.1, 4.2 and 4.3, 4.4. In both cases the operation was similar. As the sun sensor rotates, about a vertical axis, the sun's light briefly passes through the slit striking a photo-transistor. The gaussian voltage profile is differentiated and a pulse generated. The difference in azimuth between the sun pulse and an index pulse is measured by a shaft encoder. A 2048 bit (0·175° resolution) encoder was used for the UTIC83 flight. The azimuth angle accuracy was increased to 0·088° by using a 4096 bit encoder during the 1986 flight.

The platform azimuth (PAZ) is then determined using

$$PAZ = SAZ - (\Psi - \varepsilon) \qquad 4.2$$

where SAZ is the sun's azimuth, Ψ the azimuth difference between the sun and the index pulse and ε is the azimuth offset between the index pulse and the optical axis of the detector. The sun sensor becomes less accurate when the sun is higher in the sky and becomes totally inoperative when the sun is shadowed by the balloon ($ZEN_{sun} < 15°$). In Chapter 5 there is a discussion of the effects of tilts upon the azimuth as measured by the sun sensor and the 3-axis magnetometer.

4.5 Telemetry Formats

Different approaches were used in the UTIC83 and AS86 flight campaigns toward telemetry encoding and decoding, resulting in completely different formats. The UTIC83 encoding and decoding was by hardware while. During the 1986 flight, all data was formatted by an onboard microprocessor. The design and construction of which is due to C Ashworth.. Decoding was also done in software.

In 1983 a subframe containing 90 bits, split into two types of 16 bit words, was sent every two seconds. The first, 'A' word contains a subframe identifier (0-31) in the first 5 bits and the PHA/Housekeeping data in the remaining 11 bits. The 'A' word was followed by 4, 16 bit 'B' words that contained the fast (4 msec) count rate information. The allocation of information to each subframe of the A word is given in Figure 4.12. The overall bit rate was 1440 bits/sec. For more detail see Watts (1983) and Duldig (1981).

The telemetry format used in 1986 consisted of frames containing 190 8 bit words. Each frame has two main sections, the housekeeping (10 bytes) and the X-ray data (128 bytes). Frames are sent approximately 10 times a second. The layout is given in the top of Figure 4.13.

In the housekeeping data the first byte identifies the frame, the next 8 bytes give the housekeeping information and the last byte gives the number of bytes of X-ray data lost due to the frame overflowing. The allocation of the housekeeping bytes is given in Table 4.1.

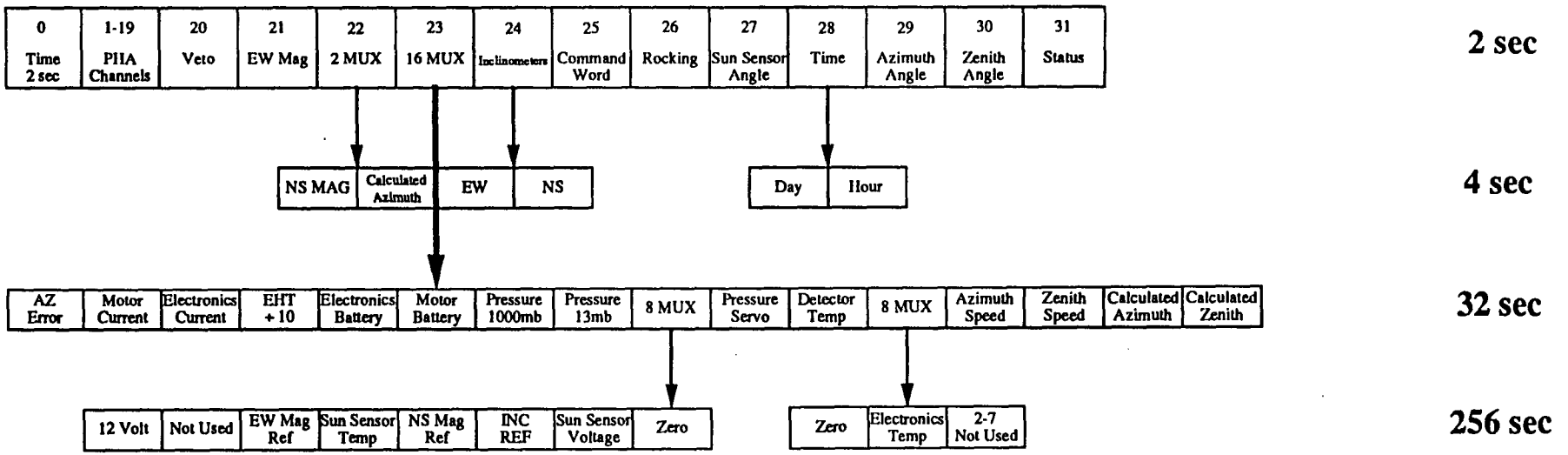

Fig 4.12 The allocation of information to the 'A' word in the UT83 telemetry format. Also given is the sampling interval for each variable.

Table 4.1

1	Measured and calculated Zenith for both detectors.
2	Measured and Calculated Azimuth. Aspect Clock (days, hours, min, sec).
3	Two Axis Magnetometer Voltage EW NS. Command Register. Command Verify , 8 bit flags-----
4	Three Axis Magnetometer Voltages (UD, EW, NS), Sun Sensor
5	Veto rates.
6	Anode Events, Dead Time, Error Type, Error Count, Float Pressure.
7	RA, DEC, LAT, LONG.
8	Azimuth and Zenith Offset, Inclinometer Voltages.
9	Three Axis Magnetometer Reference Voltages (UD,EW,NS).
10	Two Axis Magnetometer Reference Voltages Azimuth Servo System Error Voltage, 4 spare bytes.
11	Rock Mode, spare, Clock (Year, Month), EHT Voltage, spare.
12	Temperatures : Detector electronics, Detector, EHT Power, Magnetometer Tower, Tasmanian Electronics, 2 spare.
13	Battery Pack Voltages and Currents, Voltage On +5v and +12v supplies.
14	Manual Mode Azimuth and Zenith Angles, 2 spare bytes.
15	Aspect Camera Information (not used in 1986).

The X-ray data comes in groups of 3 or 5 bytes corresponding to single and double events. The layout of these (single and double event) bytes is given in Figure 4.13. The 3 bits reserved for the pulse rise time were not used. The TIMEL counter is in units of 1 msec and rolls over every 64 msec. Upon a TIMEL rollover three bytes are sent, containing TIMEHL (0-15, 64 msec units) and TIMEHH (0-57, 1024 msec units). The TIMEHH counter is reset every minute. The overflow flag and overflow count were not implemented because of problems with the timing updates. The effects of these timing problems and frequent frame overflows are discussed in Chapter 6.

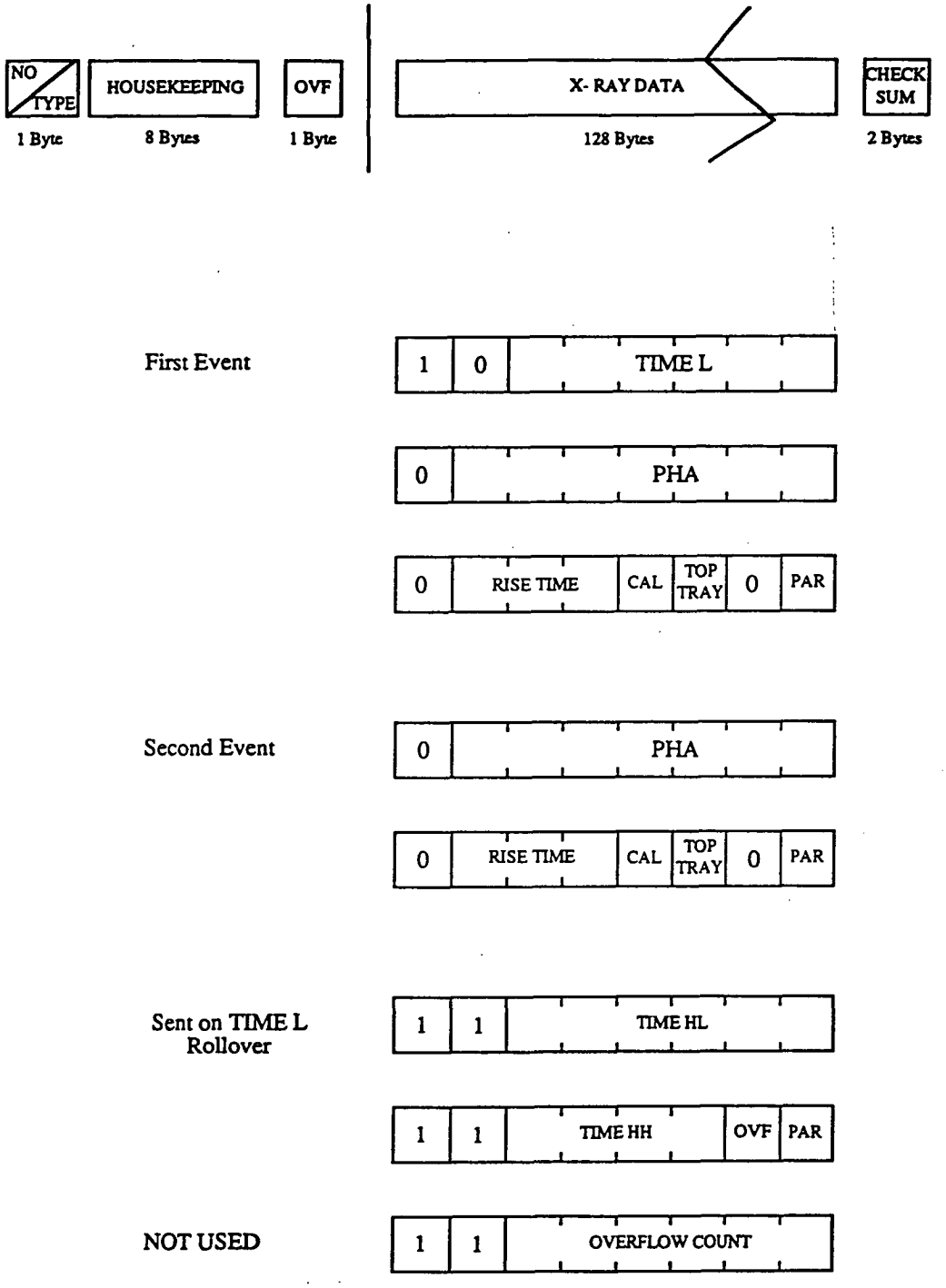

Fig 4.13 The allocation of bytes within the SDLC frame used in the 1986 flight. The layout of the X-ray bytes i.e. also given, See Table 4.1 for the allocation of the housekeeping information.

4.6 Telemetry and Tracking

During the 1983 flight, balloon launch, tracking, radio communications and balloon services were performed by the Instituto de Pesquisas Espaciais. Tracking with both Omega and RD65 1.6 GHz antennae were used. The Omega on board receiver sends its output to the ground station, where it is decoded to yield the balloon's latitude and longitude.

Data was transmitted at different frequencies for the UT and IC detectors. Data was transmitted in 8 and 4 bit pulse coded modulation at 93 KHz and 52.5 KHz. The tele-command channel was at 30 KHz. The cut-down, ballast drop, battery pack switching and other discrete commands were sent via the tele-command channel. Also on board were a homing beacon, radar reflectors and navigation lights.

During the AS86 campaign our collaborators at University College (ADFA) provided balloon launch, tracking and communication facilities. They also supplied all on board ranging and telemetry (the RAT package of Figure 4.6) equipment. Telemetry was PCM bi-phase with a carrier frequency of ~250MHz. The data rate from the UT2 detector and balloon housekeeping was 12 Kbit/sec.

4.7 Power Supply

Power was supplied for both payloads by 28 volt Li batteries, placed to balance the weight of the detectors. Power inverters provided regulated 5v, 12v, ±15v and 24v supplies. The batteries were split into two switchable packs during the 1983 flight and three packs during the 1986 flight. During 1983 only one set of batteries was used at a time. In order to prevent and feedback between the motors and electronics via the batteries, the motors and electronics were run from separate battery packs during the 1986 flight. The 1983 and earlier flights used solar panels rated at 2·5 amps at 30 volts to supplement the batteries.

4.8 Ground Stations

The structure and capabilities of the ground station data display and payload control have been increased between successive balloon campaigns.

For the 1983 flight in Brazil there were two ground stations set up. One was at the launch site, Cachoeria Paulista and the other down-range at Bauru. The general layout of the ground station components is given in Figure 4.5. The incoming PCM signal is synchronized and the subsequent TTL data and signals are passed to a tape recorder (TEAK A-33005XE using commercial tape) and real time analysis computers. For post flight analysis the tape recorder can be used in place of the receiver.

For real time analysis the TTL signal is passed through a decoder and then to a PDP 11/10 computer and two micro-processors. The PDP 11/10 outputs a hard copy of the incoming data either to a teletype, hard disk or floppy disk. The software was written in machine code by Dr. M. Duldig (Duldig 1981). The quick look micro-processor (QLμP) monitors the housekeeping data, displays it on a VDU and passes the aspect information onto a graphics micro-processor (GμP). The GμP calculates the celestial co-ordinates of the detector's optical axis. Included in these calculations is the effect of tilting on the 2-axis driving magnetometer output and on the look direction (Warren 1980, Watts 1981). A map of the sky is then displayed. Further improvement to this system such as the display of star positions and a star field camera were overtaken by the substantial expansion of the ground station by Dr. A.B. Giles and Dr A. Sprent for the 1986 campaign.

During the AS86 flight the data from the the FM demodulator was directly recorded using RACAL instrumentation supplied by ADFA. To analyse the data in real time four mini computers (Osborne1) were used. These shared a common data bus from the bit synchronizer/decoder combination (Figure 4.14).

The housekeeping computer decodes and displays the 90 housekeeping parameters. Every minute it dumps the screen display to a printer as a permanent record of the flight.

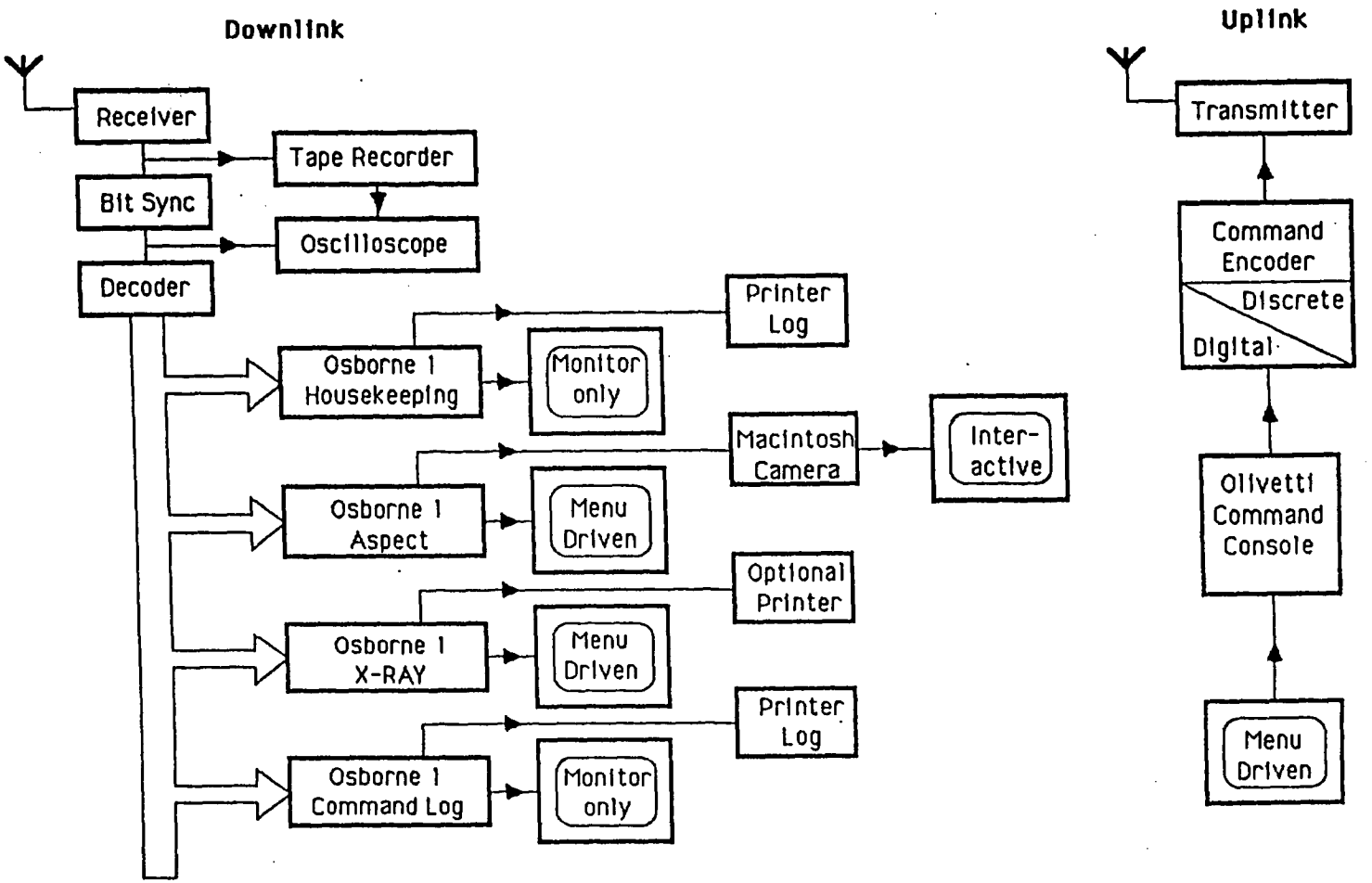

Fig 4.14 The ground station used in 1986.

Aspect calculations, using the appropriate housekeeping data and stored calibrations, are performed by a second Osborne mini-computer. The calculated look directions as measured by the servo system, 3-axis magnetometers and sun sensor are up-dated every few seconds. This allows the direct comparison of the performance of the navigation sensors. This capability proved extremely valuable during the 1986 flight. The aspect computer passes on the decoded star field camera output and payload pointing information to a Macintosh personal computer. The Macintosh contains a copy of the bright star catalogue and a catalogue of hard X-ray sources. It was capable of displaying both camera stars and those form the catalogue allowing instant recognition of any pointing errors. The display routines were written by Dr. A. Sprent and were also used for observation planning.

The X-ray analysis computer provides real time pulse height analysis (PHA), with graphic display of the X-ray data. Several, menu driven modes were allowed: escape gating, background subtraction and PHA of top tray events only. These displays and a statistical analysis could be dumped to a printer.

The final computer was used to log onto printer all commands sent to and confirmed by the payload's telemetry micro-processor. An Olivetti M24 PC was used to encode commands sent to the payload.

4.9 Flight Performance

4.9.1 UTIC83

The balloon was launched from Cachoeria Paulista, Brazil at 6:40 (UT) on 26th March 1983. It remained at a float attitude, corresponding to a vertical atmospheric absorption of 4.1 g/cm^2 between 11:20 and 17:00 UT. The flight ended with a balloon failure at float altitude. Apparently the balloon burst and became entangled with the parachute. The payload was completely destroyed upon impact. Four sources were observed, Sco X-1, SS433, MR2251-178 and SMC X-1.

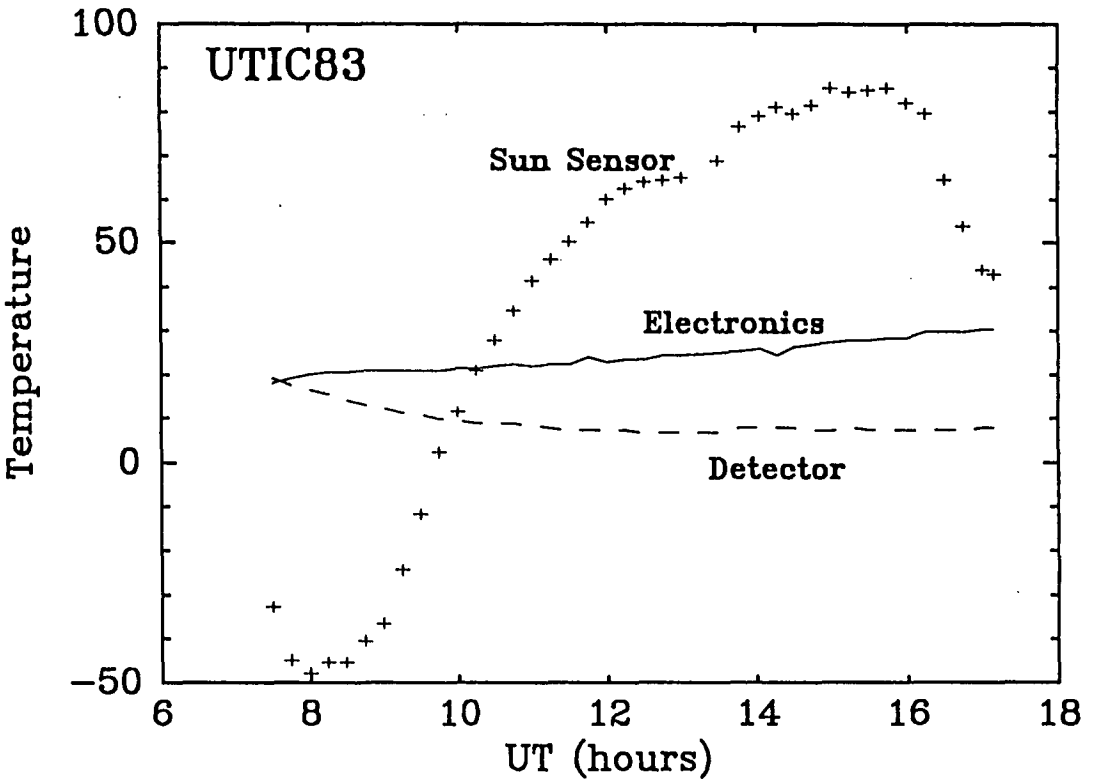

Fig 4.15 The temperature variations during the UTIC83 Brazil flight.

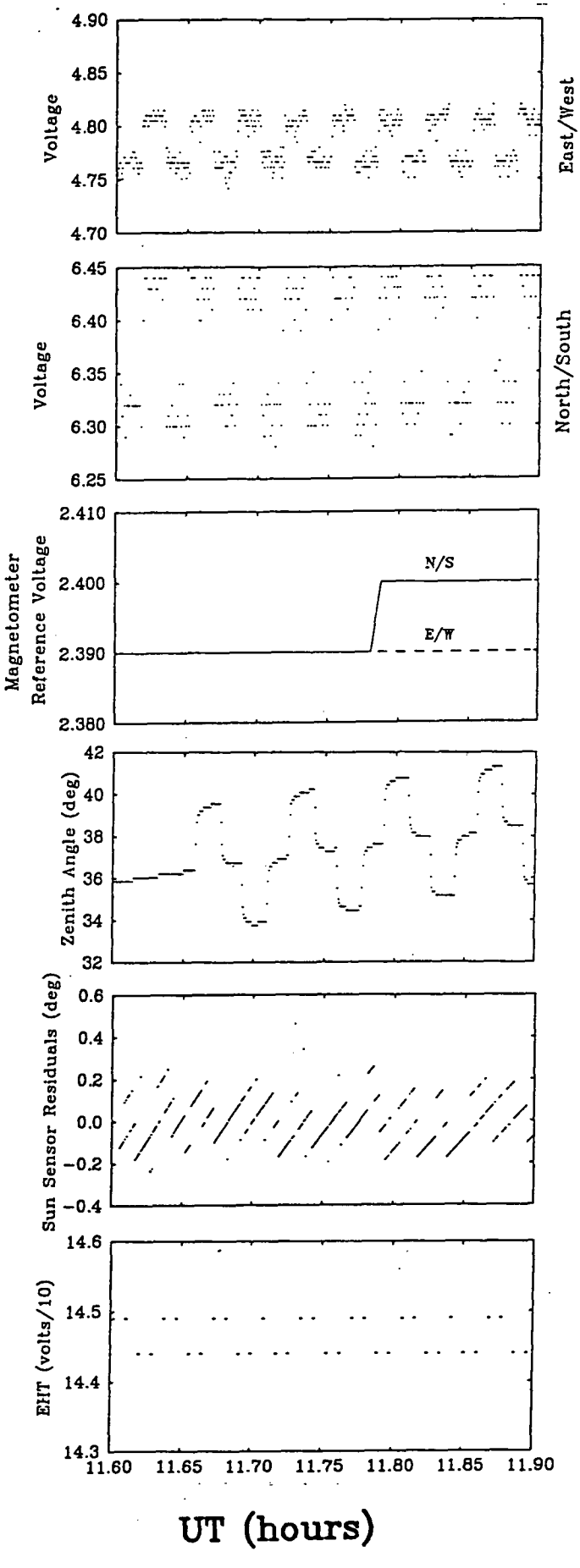

Fig 4.16 The voltage oscillation of the East/West and magnetometers. The magnetometer reference voltages are only sampled every 256 sec and are constant within the measurement accuracy. There is no constant phasing with the rocking. A staircase rock was used as can been seen in the fourth panel. The sun sensor varies by $<\pm 0.2^{\circ}$ about the trend caused by the combined platform and solar motions. However the EHT voltage shows a regular up/down pattern with a period near 2 min.

The on-board temperature remained relatively constant despite the low outside temperature and strong solar heating as evidenced by the sun sensor temperature ranging from -30°C to +80°C (Figure 4.15). The servo system worked well at most times during the flight being stable (±0.15°). Between 15:42 and 16:00 the platform performed two swings in azimuth. The actual cause remains unclear. However, this enabled a good determination of the azimuth dependence of the background counting rate.

At one point both the East/West (E/W) and North/South (N/S) magnetometers appeared to show large oscillations in viewing direction (Figure 4.16). Such oscillations, known as dither, are possible within any servo system. The magnetometer oscillations started at 9:59:22 ±22 sec, then slowly grew in amplitude to 0.04 V and 0.14V for the E/W and N/S magnetometers respectively. The voltage change in the nulled E/W magnetometer corresponds to an azimuth change of ≈1.5°. Using the Q method (Section 3.3.5) the period was found to be 119.529±0.023 sec (Figure 4.17). The shape, when folded at this period was a square wave with a 50% duty cycle and a transition time at less than six seconds. By comparing transition times at the beginning, middle and end of the oscillation data set, the period was found to be constant. The N/S and E/W magnetometer voltages remained strictly in phase throughout the 3 hours the oscillations lasted. The dither even remained during the swing between Sco X-1 and SS433. The upper levels of the E/W magnetometer's square wave variation is 4.8V which is the voltage expected when the magnetometer is nulled.

The inclinometer (roll) voltage was also found to oscillate with the same period but was antiphased with the magnetometers. The variation was also a square wave with a peak to peak amplitude equivalent to a 0.1° change.

An obvious source of a 2 min period is the rocking motion of the detectors. The UT detector was started rocking, with a 4 minute period at 9:44 UT and a 2 minute rock was started at 10:37 UT. A staircase rock was used in both cases. The Imperial College detector scanned in azimuth with a period of 3 minutes. However, the detector motions is unlikely to be the direct cause of the oscillation. The oscillations did not start until 15 minutes after the rocking was started and did not continue during the MR2251-178 observation even tough a similar 4 min staircase rock was used. The rocking and magnetometer variations did not remain

in phase, since the rocking was stopped and restarted several times (see Figure 4.16).

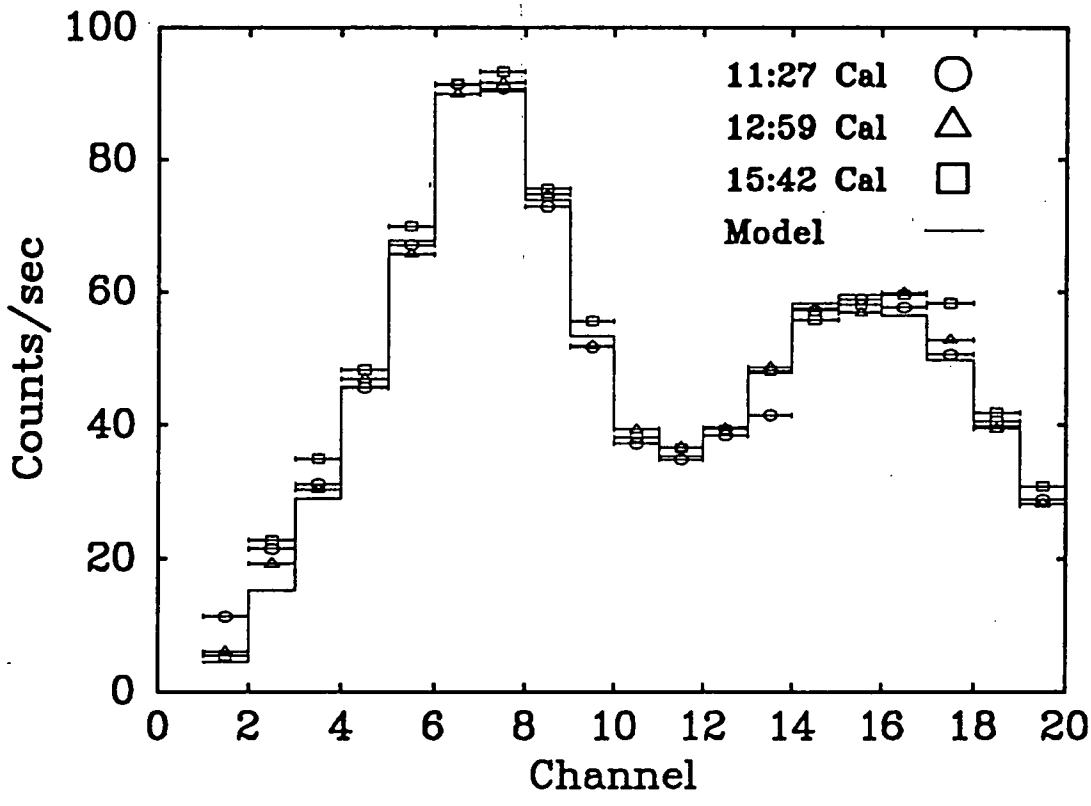

The UT83 calibration spectrum. During the Brazil flight three spectra of an Am^{241} source were made. There was no significant drift in the detector gain. Using the χ^2 minimization method the calibration spectrum was modeled in order to determine the escape fraction (52%) and resolution (42% at 60keV).

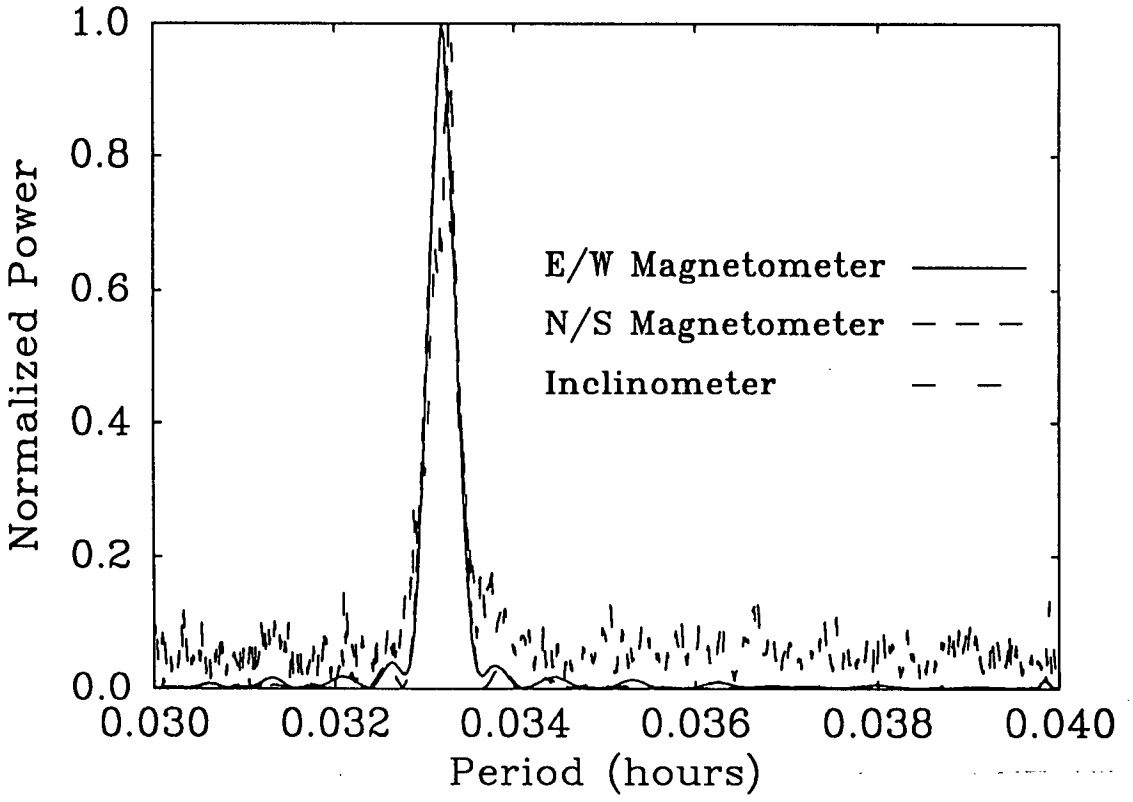

Fig 4.17 Q period searches revealing the ≈ 2 min period for the North/South , East/West magnetometers and the inclinometer.

To search for any physical azimuth oscillation the sun-sensor output was carefully examined. After removing long term trends, no obvious periodic signal was visible. Any periodic signal must be less than the 0.4° range of the sun-sensor fit residuals (Figure 16 panel 5). Similarly, the Imperial College 3-axis magnetometers showed no obvious periodicity. Smoothing the residuals suggested a period near 2 min. A Q method search of the difference between the actual sun sensor azimuth and that calculated (using the tilt corrected magnetometer output, sun's position, balloon position and telemetered offsets) showed a weak signal at near 120 sec. Thus any azimuthal oscillation must be smaller (≤0.4°p-p) than the 1.5° amplitude indicated by the E/W magnetometer.

It is possible that the motion in azimuth was only the horizontal component of a larger motion. An elliptical motion about an axis was considered. The inclinometer would not respond to a purely pendulum motion since it is based upon a pendulum. Computer simulations using the known response of the magnetometers were performed. Initially elliptical motions about the E/W and N/S magnetometer axes was considered. These axes were roughly aligned with the pitch (= look direction) and roll physical axes of the platform, since both Sco X-1 and SS433 were setting nearly due west (Az=270°) at the time of observation. A square wave response could be produced when the magnetometers described an ellipse tilted 45° to the vertical and had a ratio of semi-major to semi-minor axes of 2 (B/A =2). Shifting the centre of the ellipse in azimuth or zenith caused a drop in the mean level of the magnetometer response, but not the amplitude. Increasing the ratio B/A, decreased the transition time but also decreased the amplitude of the voltage variation. The shape of the variation was changed asymmetrically if the angle of the ellipse was changed away from 45°. There was some uncertainty in the dip angle and field strength as seen by the magnetometers. Decreasing the dip angle (50°-40°) decreased the amplitude of the magnetometer response. No combination of reasonable local field strength, dip angle, ellipse orientation and ellipse eccentricity could simultaneously produced a square wave type response with a small transition time and the correct voltage amplitude without requiring an azimuth oscillation bigger than the ±0.2°amplitude limit set by the sun sensor.

In doing a sun sensor simulation it was found that, because of the limited azimuth angle resolution (0.1756°), the on-board micro-computer's calculation of object azimuth was only changed value every 117 to 125 seconds during the Sco X-1 observation i.e. when the oscillations started. Similarly every second change

occurred every 72 to 111 second for SS433. So the initial forcing mechanism was probably the calculation of the source azimuth. Each update in azimuth is accompanied by an error signal and a driving of the reaction wheel. Such forcing would maintain phase throughout both Sco X-1 and SS433 observations. During the MR2251-178 observations the updates in azimuth were much more rapid because the source was near the zenith and so moving rapidly in azimuth.

The motion of a servo system similar to that employed in the UTIC83 flight is described by Nishimura (1984). The motion of the platform is governed by the torques exerted by the twisting tension in the suspension cables,the reaction wheel and the the top bearing drive. The equation of motion of such a system with velocity feedback (G in Figure 4.11) is given by

$$\ddddot{\theta} + Ja\dddot{\theta} + (Jb+\omega_0^2)\ddot{\theta} + \omega_0(Ba+c)\dot{\theta} + \omega_0 Bb\theta = 0 \qquad 4.3$$

If the payload is allowed to swing freely with the motion governed solely by the torque of the suspension cable then the gondola will oscillate with an angular frequency of ω_0 , the free angular frequency.The angle of the reaction wheel, ϕ , is governed by the error signal (G in Figure 4.11) which consists of gain and velocity feedback components i.e.

$$G = J\dot{\phi} = a\dot{\theta} + b\theta \qquad 4.4$$

where J is the ratio of the moments of inertia of the reaction wheel and platform, θ is the error angle of the detector. The constants a and b are the velocity feedback and loop gains of the error signal and are determined by the wheel drive electronics. The constants A, B and C are derived from J, a, b and ω_0. In deriving Equation 4.3 the disturbance signal is assumed to be linear. This is a good approximation to the actual sinusoid near the null. The above equation is a 4th order linear homogeneous differential equation, which is readily solvable by the methods outlined by Hurewicz (1975, pp 66-69) and Kreyzig (1979, pp 104-107 4th ed). The general solution of Equation 4.3 is a pair of exponentially damped sinusoids. The two damping time constants and two resonant periods can be found by solving the 4th order polynomial characteristic equation. Bairstow's method is used (Kuo 1972 pp 116-124) to solve the characteristic equation.

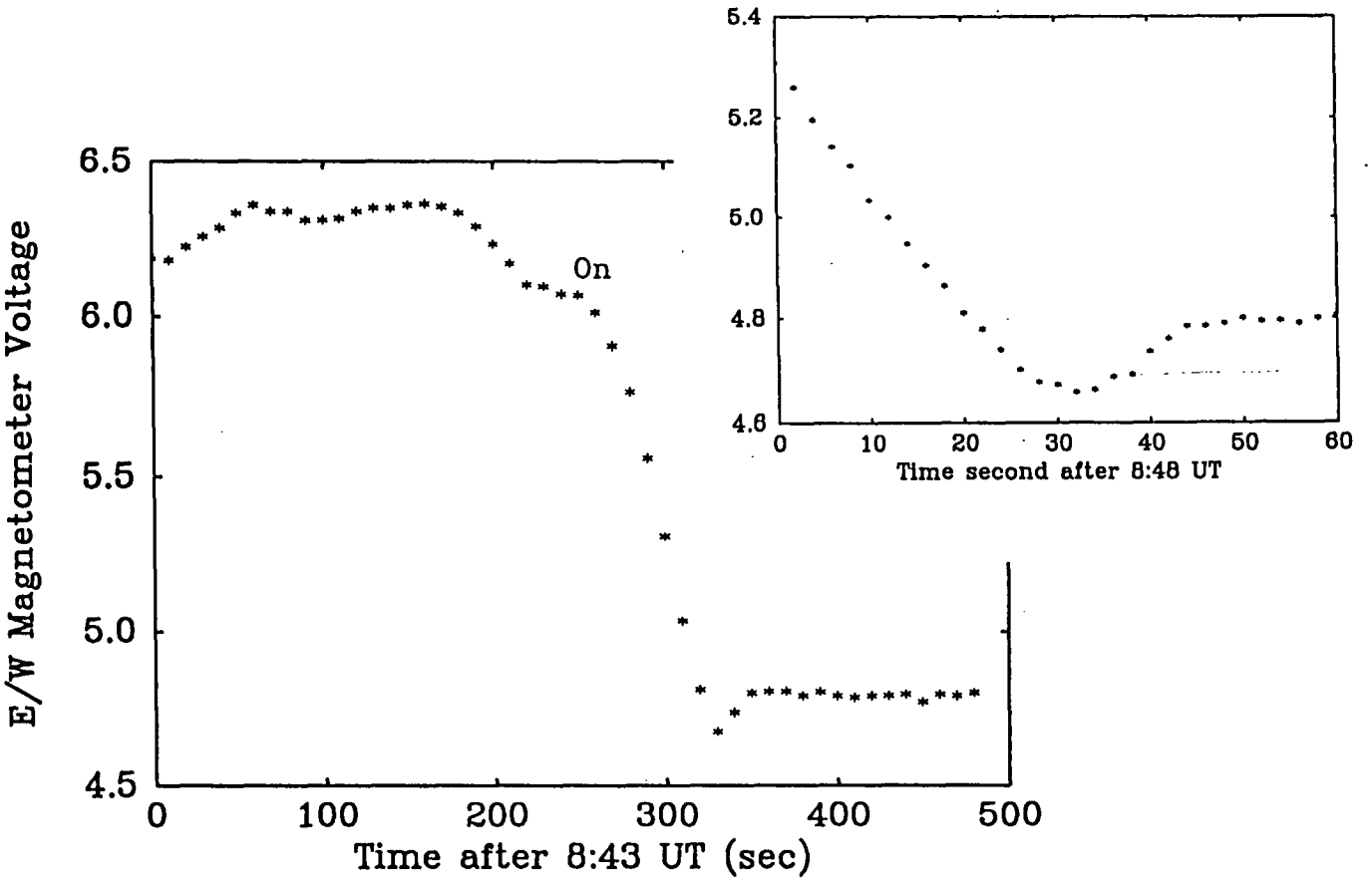

Fig 4.18 The servo system switch on. The subsequent variation in East/West magnetometer voltage shows that the UTIC83 platform was criticaly damped.

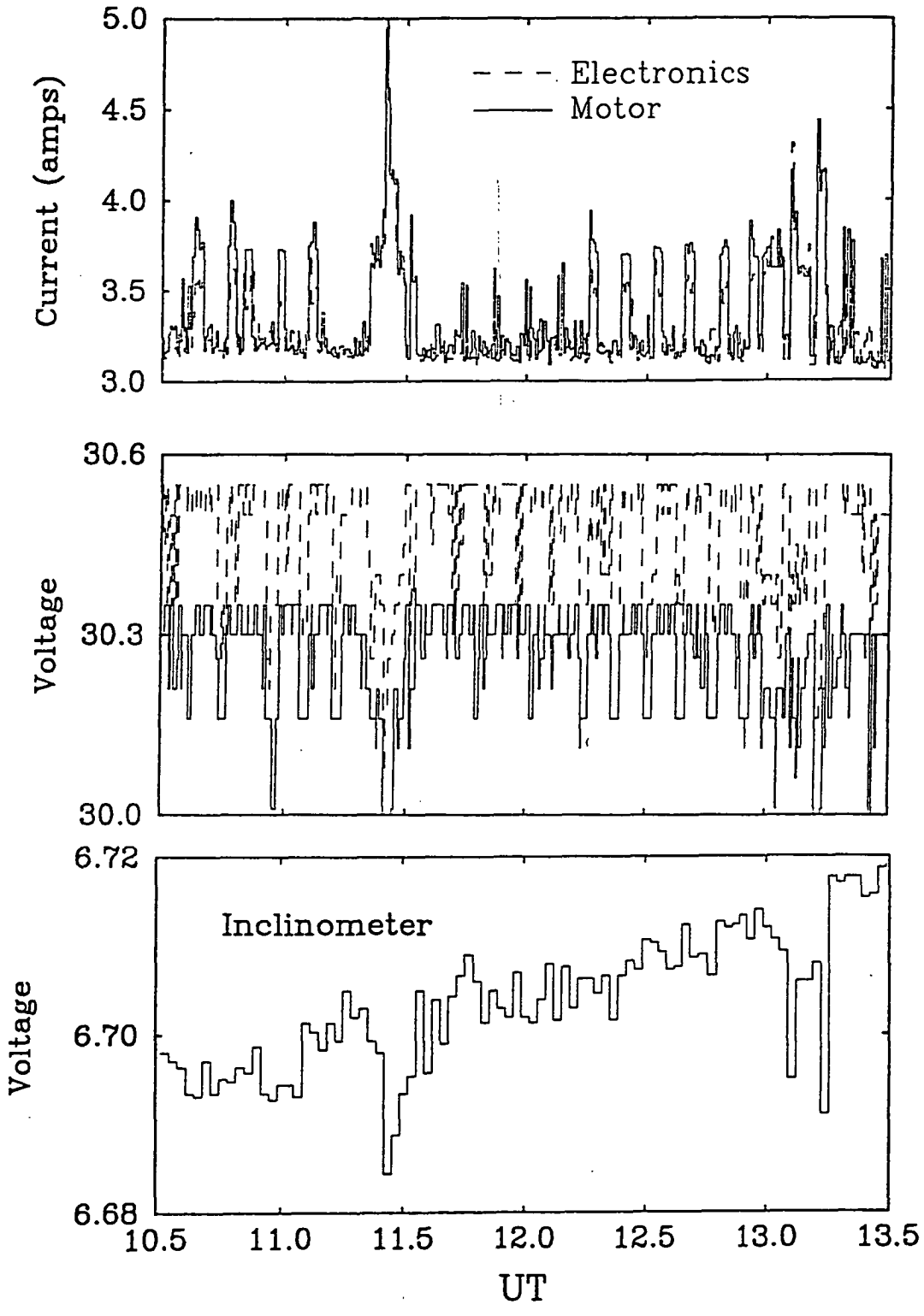

Fig 4.19 The effect of the motors drawing current on the battery voltages and the inclinometer voltage. Swings between sources occurred at ≈11.4 and 13.2 hours UT.

The parameters used were $I_{wheel} = 1.3$ kg m^2, $I_{platform} = 300$ kgm^2, $\tau = 0.5$ kg m^2 (torque at the suspension ropes), and $\omega_0 = 19.5$ minutes. Calculation of the payload angular moment involves approximations to the distribution of the on-board mass e.g. the detectors were considered point masses. The free precession period is taken from the rotation period of the gondola just before the servo system was switched on. This is a very uncertain measure of the free angular period. Also there are some simplifications involved in deriving Equation 4.3. Bearing in mind the uncertainties the estimated damping time constants are 3 and 200 sec for resonant periods of 350 and 19 sec. During the 1981 Dec 2nd, flight dither with an amplitude of 0.2°p-p and period of 6 minutes was observed (Watts 1983). Thus the above estimate is probably an underestimate of the long period. The relative timescales of the damping and period should remain the same.

It is thus expected that any long period oscillation will be dumped within a fraction of one cycle, and so cannot be maintained even with constant reinforcement. The short period oscillations is damped slowly and so could be maintained if reinforced. The platform was critically or overdamped as suggested by the theory. This is shown in Figure 4.18 which is the azimuth history of the platform just after the servo system was activated. The indicated damping time constant is about 15 seconds which is in reasonable accord with the above estimate.

There appears to be no means to produce and maintain a physical oscillation with a large effect upon the magnetometers without producing an azimuth variation larger than that measured by the sun-sensor and IC 3-axis magnetometer. The amplitude of any azimuth variation must be smaller than 0.4°p-p. Any long period oscillation cannot be maintained because of strong damping within the servo system. Therefore some other mechanism must be responsible for the variation in the magnetometer and inclinometer outputs.

It was found that when the motors drew current both the motor battery and electronics battery voltages dropped. The electronics battery voltage drops in turn caused a small and generally undetectable drop in the reference voltages used throughout the payload. Changes in the reference voltages will cause corresponding changes in the various house-keeping parameters. This is readily seen during the swings between sources (e.g. the inclinometer reference voltage Figure 4.19). A small change in magnetometer reference voltage could easily cause

the reference voltage to move from one A/D level (0.01V) to the next. Any changes in reference voltage are amplified by the factor of 2 gain used in the difference amplifier.

Both effects would magnify any small changes in reference voltage. Comparing the E/W magnetometer reference voltage, telemetered every 32 seconds, with the E/W magnetometer voltage both were in the same state (high or low voltage) in 18 out of 23 cycles. The cycles were selected from periods of stable tracking. Using the sign test we can reject the null hypothesis that the two voltages are uncorrelated at the 99.9% confidence level. If the drawing of battery current was affecting the magnetometer reference voltages then similar effects should be seen in other housekeeping parameters. The detector temperature was seen to switch between two levels separated by one precision bit. If the data is represented as a sequence of high (H) and low (L) states, a pattern of 2H2L (i.e. 4 x 32 = 128 second) is visible. This simple pattern is interrupted every 4th cycle when one H state is missed. The approximate period is 4/32 x 128% shorter than 128 sec i.e. 120 seconds. This pattern of one bit switching is most easily seen in the EHT voltage (indicated on Figure 4.16 bottom panel) since there are no other variations in EHT during the flight.

In summary, the magnetometer oscillations were apparently initially caused by the platform oscillation set up by the approximately 2 min updates in source position. This azimuth oscillation was probably partially reinforced by the two/four minute staircase rock motion. The azimuth/zenith oscillation caused a regular drain upon the batteries, producing a drop in reference voltages. This drop, being quantized and amplified, produced the large variations in magnetometer output. Reference voltages for the inclinometer and temperature sensors were also affected producing oscillations in their outputs. The oscillations ceased when the MR2251-17 observation was commenced because the azimuth updates were at much shorter intervals (10-20sec) and so there was no reinforcement by the 4 minute rock cycle.

The detector performed more poorly than expected. The resolution was 42% at 60keV. This was probably caused by outgassing, or contamination during the long storage between the November 1982 flight attempt and the flight in March 1983. Secondly the low energy (<30 keV) background was very high. Except for the first channel the background energy spectrum could be successfully fitted with a power law with index $\alpha = -1.418 \pm 0.003$. The first channel appears to be smaller in energy width than the rest. A comparison between float energy spectra for the

UTIC80, 81, 83 flights and the AS86 flight is given in Figure 4.20. The high background at low energies is probably due to inefficiencies in the veto system. This high background greatly reduced the detector's ability to discern sources.

4.9.2 Alice Springs 86 Flight

The balloon was launched at 21:20 UT on the 19th November 1986 from Alice Springs airport. The payload hit the ground on takeoff, possibly disorientating the navigation sensors. Also the platform was sent into a rapid spinning motion. A float altitude, corresponding to a vertical atmospheric depth of 3.1 grams/cm^2, was achieved between 0 and 8 hours UT on the 26 Nov 1986. Cut-down was performed just before sunset. After cut-down the parachute apparently opened late, decelerating the payload rapidly (~10g). The steel ladder cables supporting the payload snapped. After crashing, the destruction was completed by a fire amongst the unused lithium batteries. The payload was found and later the UT detector was recovered. It has now been fully rebuilt.

The on-board temperatures remained approximately constant at between 10 - 20°C throughout the flight. The outside temperature, as measured on the magnetometer tower, ranged from -30°C to +20°C. The latter temperature is due to direct solar heating of the sensor. All on-board reference voltages remained stable. The tilt of the platform was always less than 0.45°. A summary of some house-keeping parameters are plotted in Figure 4.21.

During the 1986 flight there were a number of problems that greatly reduced the amount and quality of data received. The aspect determination became uncertain because the driving magnetometers were badly offset (~173°). This offset was induced either during the rough launch or during ascent when the payload was rapidly spinning. The ability, using the aspect ground station computer, to compare the computed azimuths of the sun sensor, 3-axis and driving magnetometers enabled a fair estimate of the actual azimuth. There was also significant uncertainty in the sun sensor index error, being 29.3 ± 0.4°. The two 3-axis magnetometers were the most reliable aspect sensors. The UT 3-axis magnetometer output was extensively used in the postflight analysis. Due to a combination of miss-matching between individual magnetometers and the proximity to the top bearing drive, the calibration curve of the UT 3-axis magnetometer had a large amplitude. In future the magnetometer tower will be somewhat shorter.

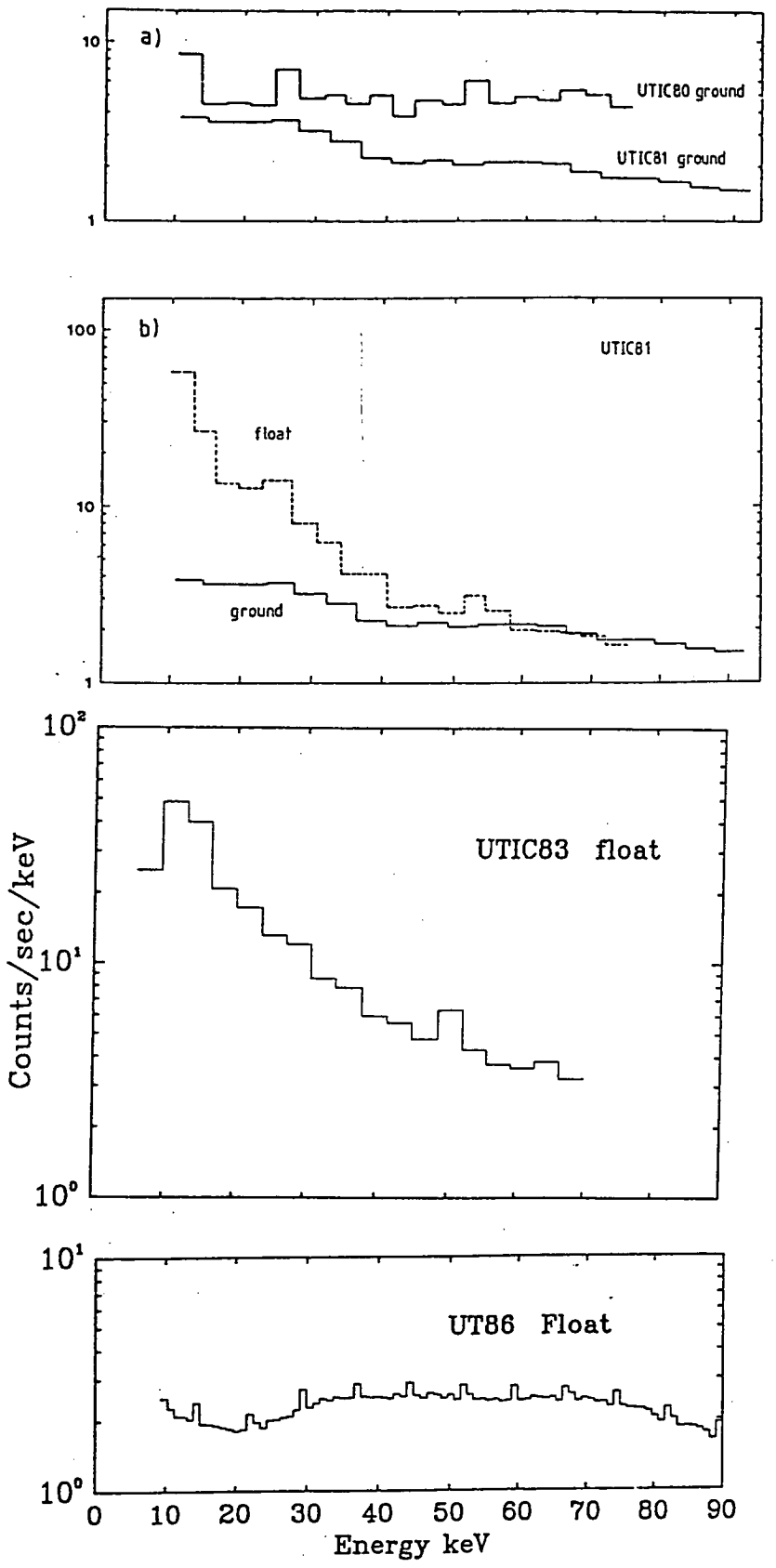

Fig 4.20 A comparison of the UT80,81,83,86 background counting rates.

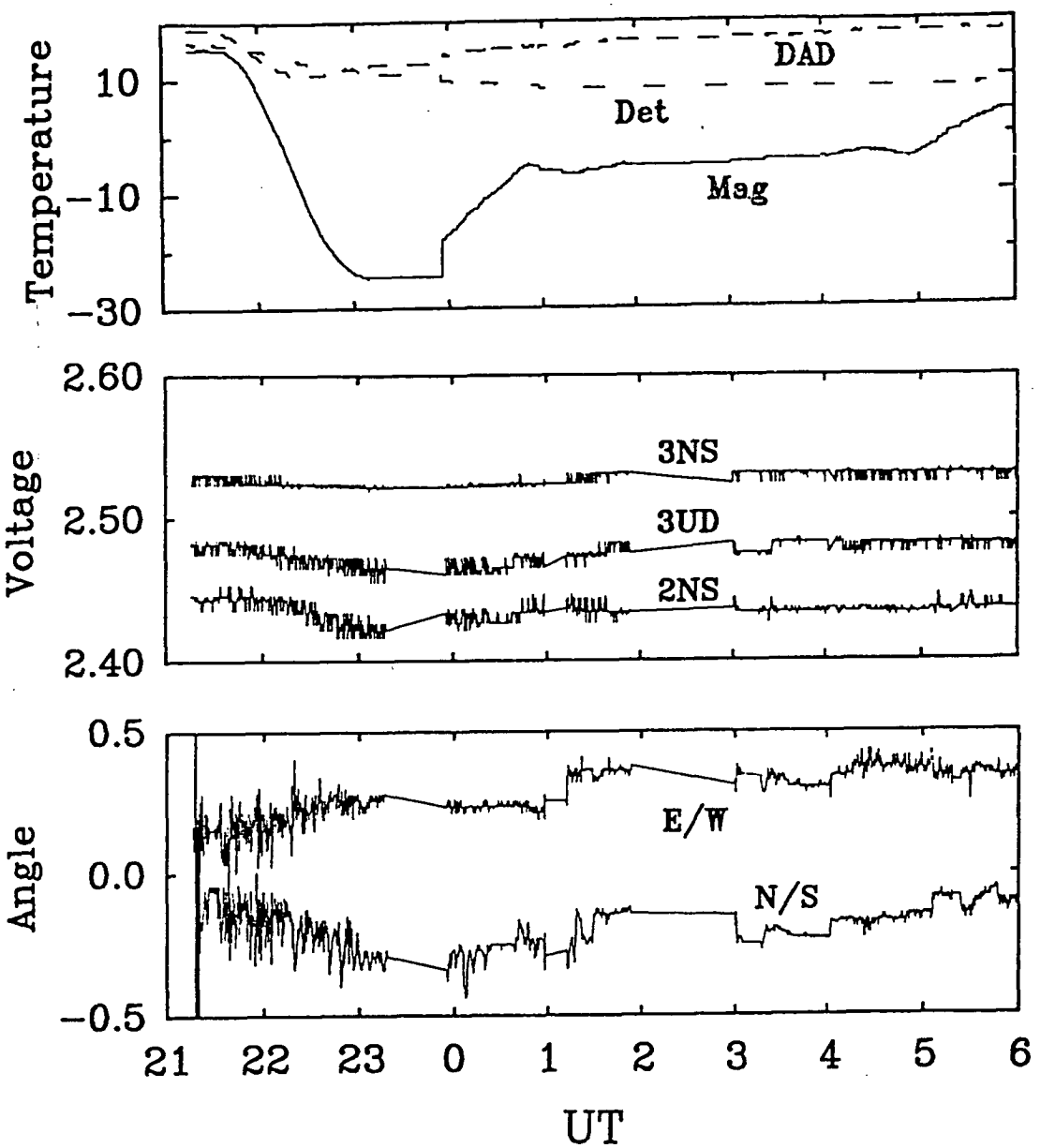

Fig 4.21 The top panel shows various temperatures on the AS86 platform. Some magnetometer tower temperature information is missing. The reference voltages for the 3 axis north/south (3NS) and vertical (3UD) magnetometers in addition to the 2 axis north/south (2NS) magnetometer is shown in the middle panel. The pitch (N/S) and roll (E/W) inclinometer angles are shown in the bottom panel

Another major problem encountered in controlling the platform were spontaneously occurring unpredictable resets of the on-board aspect micro-processor. Upon reset; all parameters, except clock time, were set to zero, thus causing the platform to slew rapidly off-source. It is thought that radio interference caused charging of the capacitors upon the reset lines. This is being overcome by larger capacitors and more shielding upon the reset lines. Some data was lost when the telemetry micro-processor was reset. At these times the EHT was switched off. At one point in the flight, data was lost when the on-board clock apparently stopped. The clock itself probably did not stop but the latch containing the time was not updated.

The total background count rate was about 250 cts/sec. These counts included several types of spurious events. A number of events which had a PHA channel number of 127. There was an upper level discriminator (ULD) set at channel 126, but this only vetoed single events allowing double events with a first event energy in channel 127 to be recorded. The overall effect was to add ~3% to the count rate as bad events with a channel number equal to 127.

Some double events had a total energy less than 30 keV, even taking into account the resolution of the detector. Considering the ratio of L to K shell fluorescence efficiencies in xenon, about half of these anomalous double events could be attributed to L shell fluorescence. Only a few of the rest could be attributed as co-incident single events which would amount to ≈2.6 events over the entire energy range at a count rate of 250 cts/sec. The remaining anomalous events are probably caused by charged particles.

The A/D converter used on the detector PHA showed an eight bit period in the widths of the energy channels, causing every 8th channel to have a high count rate A similar effect is suspected along with poor low level discrimination for the strange shape of the low channel count rates (Figure 4.22). The procedure used to reduce this effect is explained in Section 6.4.2.

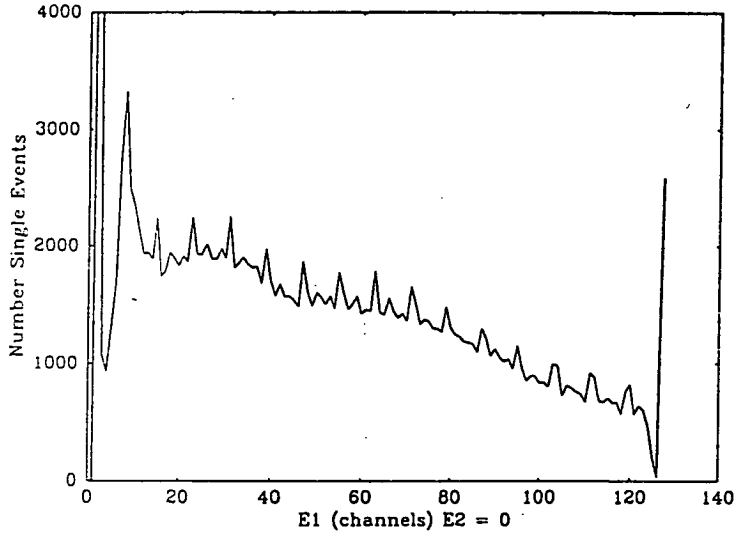

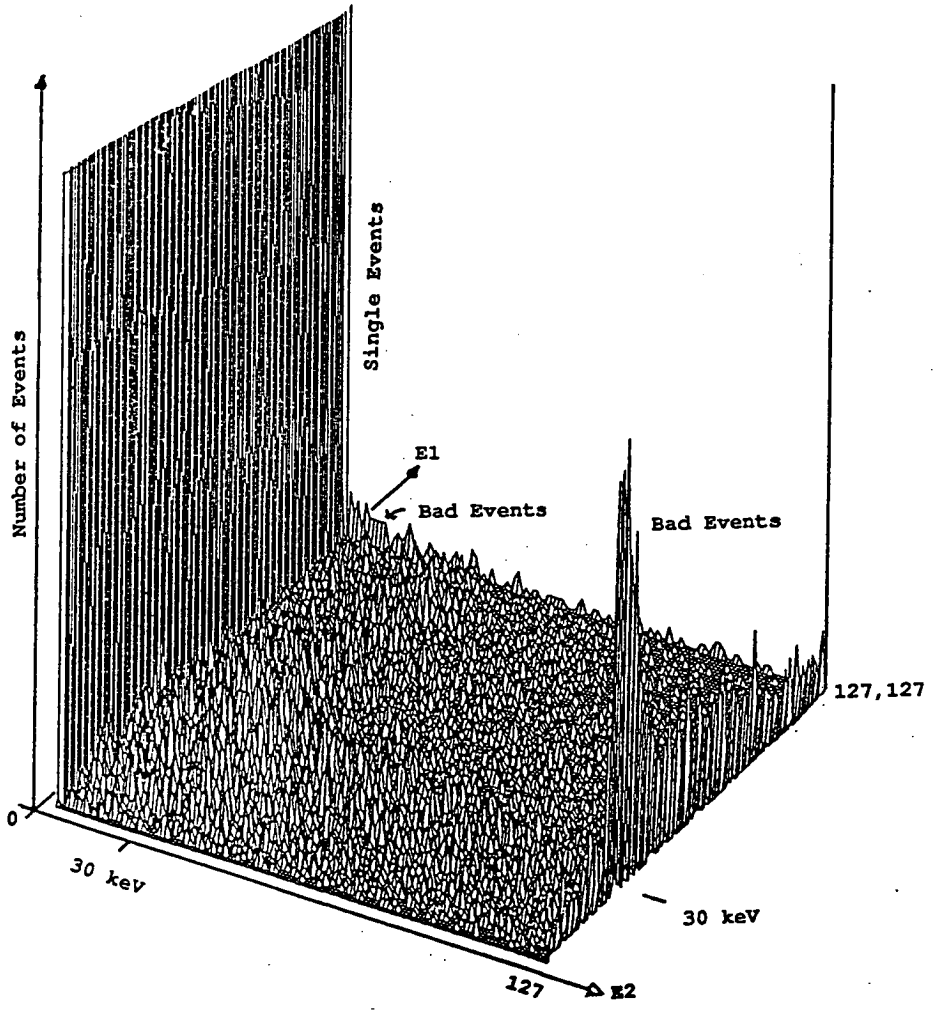

Fig 4.22 A 2D hidden line plot showing the distribution of events with respect to channel number. Note the escape peak near 30 keV. There is a wall of single events which are displayed separately. All events are affected by the A/D converter's 8 bit cyclic bin width variation. Bad events are those which have either or both photons in channel 127.

About 25% of all frames overflowed. The overflow data was lost with only the number of lost bytes recorded. These frequent overflows of the X-ray data frame gave rise to a number of effects in the data. In the frame by frame data a count rate dependent sensitivity became apparent. At higher count rates more counts are lost. The data is lost evenly with respect to energy. The overflow effect was first noted when a soft source like Sco X-1 was compared to the background. For a soft source the high energy counts are at the same level as the background. However, because of the higher overall count rate the number of high energy counts is suppressed to the point where the on source high energy counts of Sco X-1 were below the background. The resulting background subtracted spectrum preferentially shows negative count rates at high energies. A count rate overflow calibration was formed and applied to all the frame by frame data.

At the 1 millisecond level an overflow creates a time gap between the last event recorded and the first event recorded in the next frame. The FFT algorithm cannot be used to search for periodicities. The waiting time distribution is no longer exponential and so the assumption of a Poisson count rate distribution, underlying the setting of a period detection threshold is not valid. By selecting data unaffected by overflows and by using a Discrete Fourier Transform these affects are overcome in the temporal analysis of the 1986 Sco X-1 data.

Also the overflows caused many time updates to be either missed or corrupted. These timing problems were compounded by errors in the behaviour of the TIMEL, TIMEHL and TIMEHH counters of the X-ray clock. These errors included incorrect rollovers, incrementing forward and backward jumps and early or late 1 minute resets. The delimitation of frames was made difficult by data rolling over from one frame to the next even when the frame was not full. The inevitable scrambling of some frames by radio interference compounded the difficulty of creating an accurate 1 millisecond clock. Many of the timing problems were fixed by a program written by Dr. A.B Giles. Remaining timing problems were corrected interactively by the author. The guiding principle was to make the smallest change required to bring the X-ray clock in line with a frame counter since the regular cycling of the frame types was robust.

As the count rate increases a greater proportion of frames become filled to the 127 byte capacity of the X-ray data frame. Overflows and timing problems cause many frames to be rejected because of the resulting invalid structure. Thus as the

count rate increases there is an increasing bias toward frames with a greater proportion of single events. Such an increase in the proportion of single events per frame is seen at count rates above 30 events per frame.

The detector itself worked well except for two flare like increases in the counting rate. These are discussed in more detail in relation to the Sco X-1 observations in Chapter 6. The resolution during the flight was 24% FWHM at 60 keV even though the individual wire resolution was about 9% with a less than 1% variation along its length. The overall resolution can be improved with better gain matching. There was insufficient time in pre-flight preparations to match the individual gains more uniformly. It is planned that the cell address of each event will be included in the telemetry for the next payload. This will allow an energy calibration to be performed upon each wire. Any gain changes or illumination effects can then be removed in post flight analysis. The escape fraction was measured using an Am^{241} source at 35%. Mote Carlo simulations by Dr. A.B. Giles suggest a figure near 25% (Greenhill et al 1990b).

The Am^{241} calibration source produced the highest count rates observed during the flight. At these count rates the bias toward frames with a high proportion of singles is acute. The 60 keV peak consists of a mixture of double and single events while the escape peak is almost exclusively composed of single events. Thus the escape peak will be favoured increasing the measured escape fraction. Calculations show that this effect can account for the difference between the measured and simulation values of the escape fraction.

4.9.3 Evaluation of Escape Gating

The PHA channels were slightly smaller than the nominal 1keV (i.e. 0.9375 keV) with 30 keV being at channel 32. During the 1986 flight the PHA channel of each event was recorded allowing post-flight application of escape gating. An event is considered as a fluorescent double if one photon of a pair falls within a window 30 keV $\pm$ W wide. If both photons fall within the window the one closest in energy to 30 keV is taken as the escape photon. The width is set at 2.5 σ, where σ is the energy resolution at 30 keV. The window was set at $\pm$ 11 keV (10 channels) about 30 keV (channel 32).

The background rate of singles , doubles (energies added) and fluorescent doubles is illustrated in Figure 4.23. The most noticeable feature is the deep drop in the

count rate near 60keV. An at twice the escape energy anomaly was first reported by Spooner et al (1986). They predicted an increase at 60 keV. The width of this dip is the same as the window used to select the 30keV escape photon. This window narrows with improved detector resolution. The anomaly $2E_{escape}$ is intrinsic to the escape gating method when applied to a detector with finite energy resolution. Inevitably some photons will be incorrectly reassigned as escape photons. Counts will be redistributed in energy, reducing rates near $2E_{escape}$ and increasing the rate just outside the anomaly. Statistical calculations and Monte Carlo simulations By J.G Greenhill and G.L Salmon (reported in Greenhill et al. 1990b) reproduced the anomaly.

The observations of the hard spectrum X-ray pulsar GX 1+4 (Chapter 8) provide a sensitivity test of escape gating. The significance of detection in the normal and escape gated modes is listed below in Table 4.2

Table 4.2

Energy (keV)	σ_N	σ_G	K
35-50	11.5	6.1	0.53
50-75	7.2	5.0	0.70
75-114	2.6	2.6	1.00
	4.7	6.8	1.43

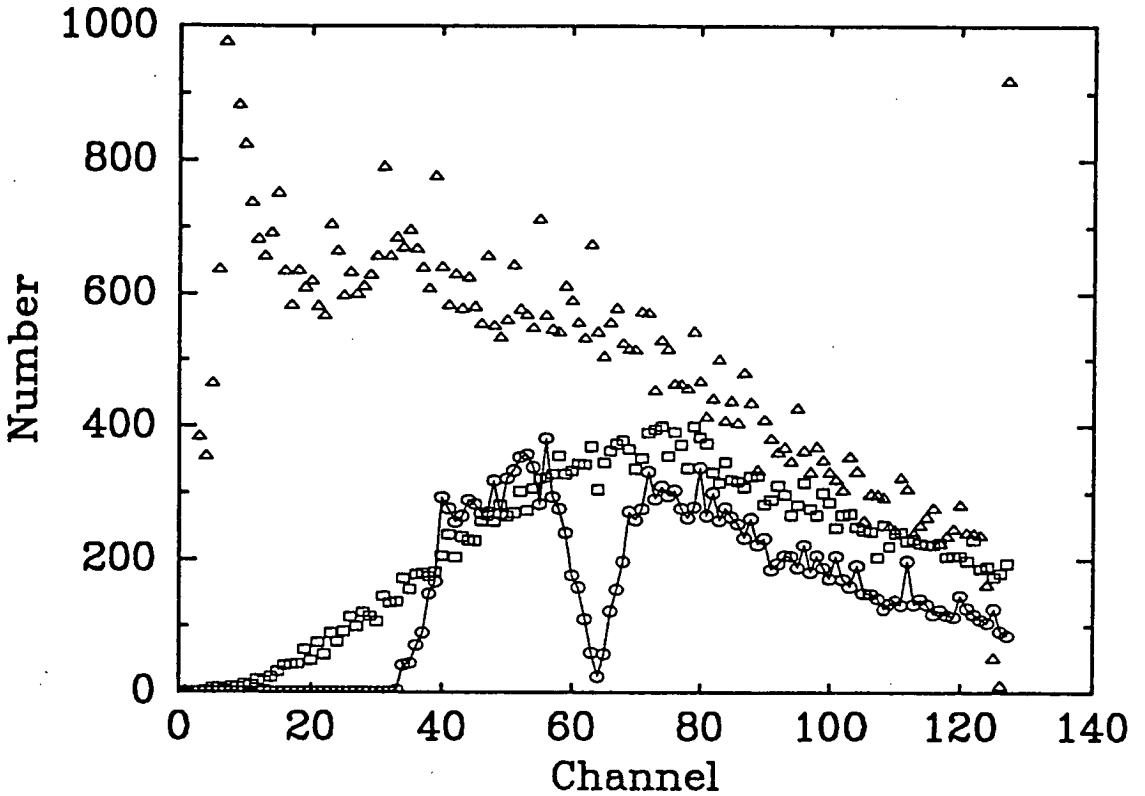

Fig 4.23 A PHA spectrum of the single (Δ), double (□) and escape gated (O) events. The escape gated mode produces an anomaly at twice the escape peak energy.

At lower energies (30-40 keV) the gated mode efficiency is low. Also there is little difference between the background rate of fluorescent and normal mode doubles. At higher energies the fluorescent double rate drops more rapidly than the doubles rate (Figure 4.23). Simulations by Dr. A.B. Giles , show a increase in gated mode efficiency with energy. Above about 40 keV the ratio of the normal and gated mode background counting rates is approximately constant.(i.e. ≈4.1). Using this ratio and the relative fluorescence gated efficiency as calculated by Mote Carlo detector simulations the expected value of fractional gain in sensitivity or figure of merit, K is 0.7 (Greenhill et al. 1990b). The value of K is measured by the ratio of the of the detection significance of GX 1+4 in the gated and normal modes. As can be seen from Table 4.2 the measured and predicted sensitivity are comparable in the 50-70keV. The final row of Table 4.2 gives the detection efficiencies obtained from the pulse profile of GX 1+4. At these energies, particularly between 85 and 105keV, the pulse profile consists of a narrow (≈0.4 phase) spike. The detection efficiency is the number of sigma this spike is above the background. The increase in the detection efficiencies and figure of merit is due to the exclusion of the near background counts from GX 1+4 when it is off (i.e. the phases away from the spike).

Considering the relatively poor resolution of the detector significant improvement can be expected from fluorescent gating. Thus a figure of merit greater than one seems achievable.

A smooth spectrum can be formed by combining the gated and normal mode spectra. The normal mode spectrum is used to fill the gap near 60 keV in the gated mode spectrum. Such a spectrum for GX 1+4 is shown in Figure 4.24. This spectrum constitutes the first astronomical observation using escape gating.

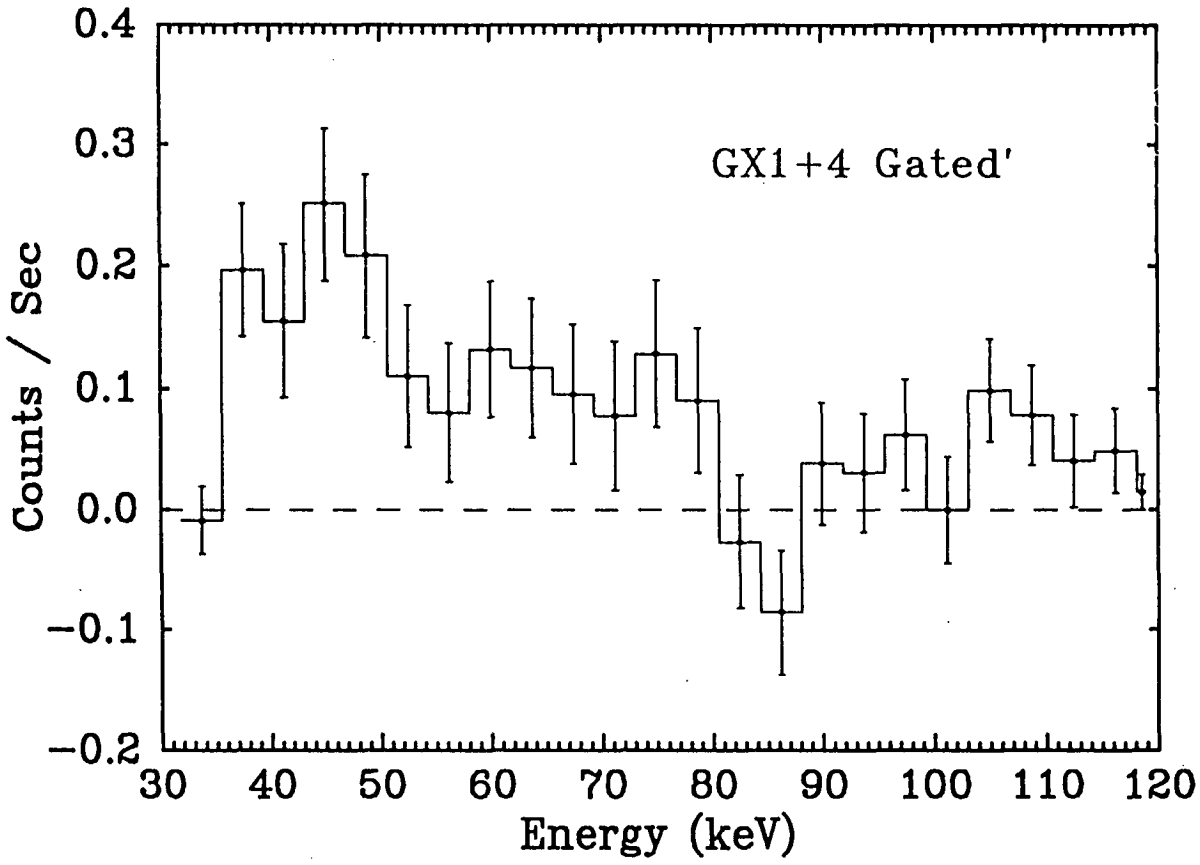

Fig 4.24 A gated mode spectrum of the X-ray pulsar GX 1+4. Escape gated events, outside the anomaly, are combined with normal double events within the anomaly window.

Chapter 5

UTIC83 Flight Observations

To work independently of results ; this is perfect work.

Augustus Digman

5.1 Introduction

The University of Tasmania, Imperial College collaborative payload was launched from Cachoeira Paulista, Brazil, on the 26 March 1983. A float altitude of 4.2 gcm^{-2} was maintained for 7 hours. During this time four targets were observed Sco X-1, SS433, MR2251-178 and SMC X-1. The observing procedure (except for SMC X-1) used was to rock on and off source in zenith angle following the sequence, source, a background above the source at a lower zenith angle (low rock), source, a background below the source at a higher zenith angle (high rock). This procedure allows accurate background subtraction to be accomplished even in the presence of strong zenith angle variations. Later in this chapter the observed variations in background count rate as well as the observations of the target sources are discused. Firstly the means for determining an accurate aspect solution including the effects of platform tilts are considered in detail.

5.2 Tilt Corrections

Before the energy spectrum or time variability of a source can be investigated an accurate attitude solution must be found. This is basically a transformation from the detector horizontal co-ordinates (azimuth and zenith) to celestial co-ordinates (the right ascension and declination). This transformation becomes more involved once platform tilting is considered. Firstly the simple case of an untilted platform will be described, using the following definitions:

λ = Longitude of balloon (positive westward from Greenwich)

ϕ = Latitude

α = Right Ascension (RA)

δ = Declination (DEC)

EE = Equation of Equinoxes

H = Hour angle

AZ = Azimuth

Z = Zenith ALT = Altitude = 90 -Z

LT = Local Solar Time

UT = Universal Time

LAST = Local Apparent Sidereal Time

GMST = Greenwich Mean Sidereal Time

$GMST_1$ = GMST at 0^h UT on the day of launch

The latitude and longitude of the balloon was determined by the launch organization INPE using both Omega and RD65 1680 MHz ranging. The adopted ground path consists of series of straight line segments that pass through position determinations.

On board the UTIC83 there were three aspect sensing systems; the two axis driving magnetometers, the Imperial College (IC) 3-axis magnetometers and the Tasmanian sun sensor. The sun-sensor is the prime aspect sensor used in the subsequent analysis.

The sun sensor measures (SAZ); the angle between an index mark (nominally aligned with the detector) and the sun's azimuth. Thus the detectors true azimuth (AZ_{det}) is given by

$$AZ_{det} = AZ_{sun} - (SAZ + FAC) \qquad 5.1$$

where FAC is the mis-alignment between the sun-sensor index direction and the viewing direction of the detector. In the case of the UTIC83 flight FAC was measured as 1.7°.

To obtain the sun's azimuth in Equation 5.1 several steps are required. Firstly the local apparent sidereal time is found

$$GMST = 1.0027390093UT + GMST_1 \qquad 5.2$$

$$LAST = GMST + EE - \lambda \qquad 5.3$$

then using sun's apparent position (as interpolated from the ephemeris) the sun's hour angle is calculated.

$$H_{sun} = LAST - \alpha_{sun} \qquad 5.4$$

Finally the transformation from celestial to horizontal co-ordinates is applied

$$\sin(\,ALT\,) = \sin\delta\,\sin\phi + \cos\delta\,\cos\phi\,\cos H$$

$$\cos(AZ') = \frac{\sin\delta - \sin\phi\,\sin(ALT)}{\cos\phi\,\cos(ALT)} \qquad 5.5$$

The inherent quadrant ambiguity is resolved by using sin(H). If sin(H) is positive then AZ = AZ' otherwise AZ = 2π -AZ'

The reverse transformation from horizontal to equatorial co-ordinates is now needed to find the detectors pointing direction upon the sky.

$$\sin\delta = \sin(ALT)\,\sin\phi + \cos(ALT)\,\sin\delta\,\cos Z$$

$$\cos H' = \frac{\sin(ALT) - \sin\phi\,\sin\delta}{\cos\phi\,\cos\delta}$$

$$\text{if} \quad \sin(ALT)\ \text{positive} \qquad H = H'$$

$$H = 2\pi - H' \qquad 5.6$$

Notice that the forms of the two co-ordinate transformations are identical with the roles of ALT, δ interchanged with those of AZ, H respectively. This property simplifies computation by the use of only one sub-routine (Duffet-Smith 1979).

With these equations round off errors can be a problem when a source is near the meridian. Numerical singularities also occur when the object or observer is located at a celestial or geographic pole respectively. Both cases are very unlikely. These traps should be borne in mind when designing an on-board aspect controller. These problems can be alleviated by using an alternative form of the equatorial to horizontal co-ordinate transformation.

$$\cos Z = \sin\delta\,\sin\phi + \cos\delta\,\cos\phi\cos H$$

$$\tan(CAZ) = \frac{\dfrac{\sin(CLAT)}{\tan(PD)} - \cos(CLAT)\cos H}{\sin H}$$

where

$$\text{CLAT} = \text{Co-latitude} = \phi + \pi/2$$

$$\text{PD} = \text{Polar Distance} = \delta + \pi/2$$

$$\text{CAZ} = \text{AZ} + \pi/2 \qquad 5.7$$

When the platform is tilted the sun-sensor and magnetometer measure the azimuth within a reference frame fixed to and hence moved with the solid body of the platform. We are thus dealing with a co-ordinate transformation and not a solid body rotation within a fixed axes system.

Within a tilted azimuth/zenith reference frame the sun-sensor actually measures the angle between the suns tilted azimuth and the platforms tilted azimuth (really the index mark but the offset FAC is small and hence any errors are very small). This angle in the tilted frame is not generally the same as that in the untilted frame. In order to find the detector's true pointing direction two steps are required. Firstly the detector's tilted azimuth needs to be calculated using the sun's tilted azimuth. This is done by applying the forward co-ordinate transformation to the sun's untilted horizontal co-ordinates using Equation 5.1 which is rewritten to indicate that we are dealing with tilted co-ordinates. Here, and in subsequent equations, "dashes" indicate that the co-ordinates are in a tilted co-ordinate frame.

$$AZ'_{det} = AZ'_{sun} - (SAZ+FAC) \qquad 5.8$$

Secondly the tilted co-ordinates of the detector, the tilted zenith angle as measured with the shaft encoders and the above azimuth, must be transformed into an untilted reference frame.

The required transformation can be accomplished by a single rotation about an axis or a combination of two or more rotations about perpendicular axes. The most straight-forward pair of rotations is a rotation θ about the Z' axis followed by a rotation or tilt of ε about the Y' axis as in Figure 5.1. Like the azimuth/zenith (X points north and Y points east) and RA/DEC systems a left handed co-ordinate system, with X" pointing in the platform azimuth direction and Y" pointing toward the IC detector, is adopted. Rotations follow the left hand screw rule i.e. +ve is clockwise when looking down the axis of rotation. The number of "dashes" indicate the number of rotations applied.

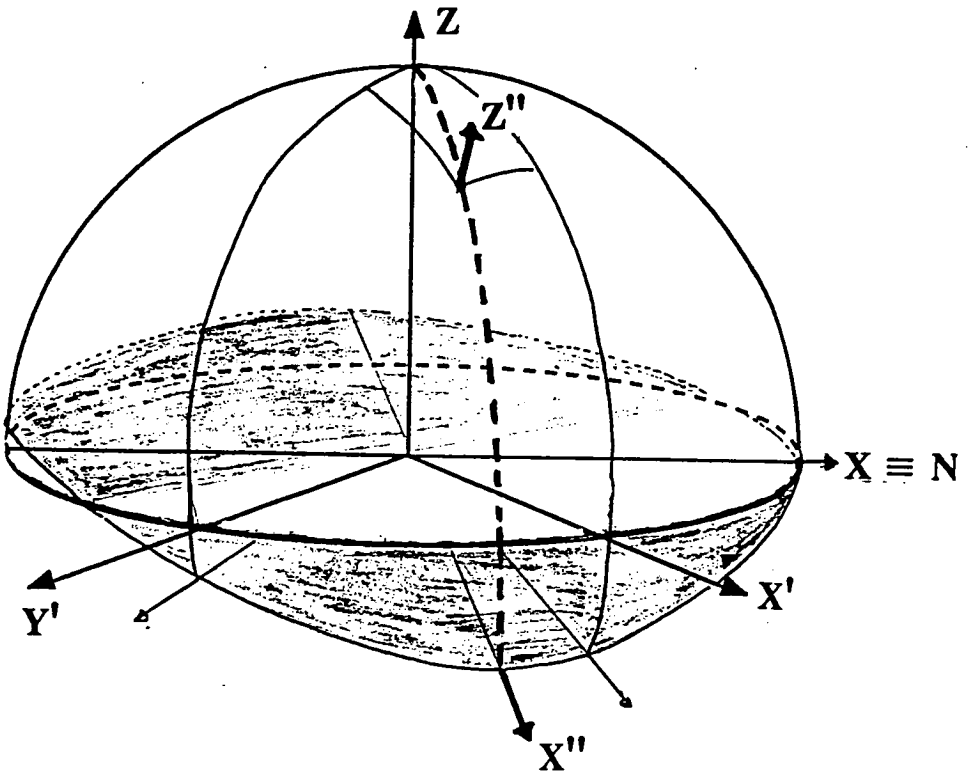

Fig 5.1 Diagram showing the sequence of rotations required to transform North/East co-ordinates to the tilted system of the detector. Firstly there is rotation about the Z=Z' axis which aligns the X axis with the untilted azimuth of the detector. The next transformation can be thought of as either applying the pitch and roll rotations or applying a single rotation by ε about the Y' axis.

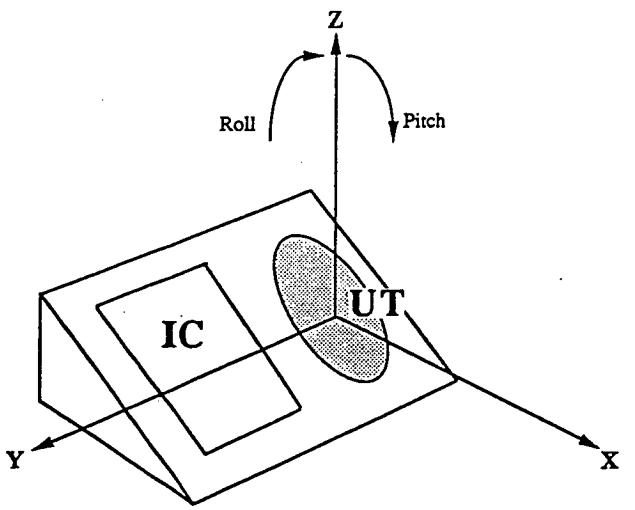

Fig 5.2 The left handed conventions for the directions of the X and Y axes and the positive sense of the pitch and roll rotations.

Since in general three dimensional rotations are non-commutative it is advisable to use a single rotation. The above pair of rotations can be easily thought of as a single rotation about an axis perpendicular to the tilt direction and also in the horizontal plane. This pair can also easily be reversed to yield the original co-ordinates by applying a $-\varepsilon$ rotation about the Y" axis followed by a $-\theta$ rotation about the Z=Z' axis. Note this transformation and its inverse do not require a rotation about any tilted axis.

In the left handed azimuth/zenith co-ordinate system the position vector is given by

$$P = \begin{bmatrix} X \\ Y \\ Z \end{bmatrix} = \begin{bmatrix} \sin Z \cos AZ \\ \sin Z \sin AZ \\ \cos Z \end{bmatrix} \qquad 5.9$$

The three transformation matrices corresponding to rotations about the principle axes are

$$R_X = \begin{bmatrix} 1 & 0 & 0 \\ 0 & \cos\alpha & -\sin\alpha \\ 0 & \sin\alpha & \cos\alpha \end{bmatrix}$$

$$R_Y = \begin{bmatrix} \cos\varepsilon & 0 & \sin\varepsilon \\ 0 & 1 & 0 \\ -\sin\varepsilon & 0 & \cos\varepsilon \end{bmatrix}$$

$$R_Z = \begin{bmatrix} \cos\theta & -\sin\theta & 0 \\ \sin\theta & \cos\theta & 0 \\ 0 & 0 & 1 \end{bmatrix} \qquad 5.10$$

Taking the two rotations separately; firstly the Z axis rotation yields (after contraction)

$$P' = R_Z P = \begin{bmatrix} \sin Z \cos(AZ-\theta) \\ \sin Z \sin(AZ-\theta) \\ \cos Z \end{bmatrix} \qquad 5.11$$

followed by a Y axis rotation

$$P'' = R_Y P' = R_Y R_Z P = R_T P$$

$$P'' = \begin{bmatrix} \cos\varepsilon \sin Z \cos(AZ-\theta) - \sin\varepsilon \cos Z \\ \sin Z \sin(AZ-\theta) \\ \sin\varepsilon \sin Z \cos(AZ-\theta) + \cos\varepsilon \cos Z \end{bmatrix} \qquad 5.12$$

$$R_T = \begin{bmatrix} \cos\theta \cos\varepsilon & \sin\theta \cos\varepsilon & -\sin\varepsilon \\ -\sin\theta & \cos\theta & 0 \\ \cos\theta \sin\varepsilon & \sin\theta & \sin\varepsilon \cos\theta \end{bmatrix} \qquad 5.13$$

The inverse transformation

$$R_T^{-1} = R_T^T = \begin{bmatrix} \cos\theta \cos\varepsilon & -\sin\theta & \cos\theta \sin\varepsilon \\ \sin\theta \cos\varepsilon & \cos\theta & \sin\theta \sin\varepsilon \\ -\sin\varepsilon & 0 & \cos\varepsilon \end{bmatrix} \qquad 5.14$$

which results from a $-\varepsilon$ rotation about the Y" axis followed by a $-\theta$ rotation about the Z'=Z" axis i.e.

$$P = R_T^{-1} P = R_Z \cdot R_Y \cdot P''$$

$$= R_Z^{-1} R_Y^{-1} P'' \qquad 5.15$$

The total tilt is composed of two components; pitch and roll. Applying the left hand screw rule a positive pitch is a downward (toward lower altitude) tilt along the look azimuth direction while a positive roll is an upward tilt in the direction clockwise perpendicular to the look azimuth (toward the Imperial College detector). These conventions are illustrated by Figure 5.2. By considering the two spherical triangles of Figure 5.3, using Napier's analog, the relationship between the pitch (P), roll (R), total tilt (E) and the angle between the tilt direction and the look (pitch) direction (ω) is found to be

$$\tan Y = \tan R \cos P$$

$$\cos\varepsilon = \cos Y \cos P$$

$$\tan\omega = \tan Y / \sin P \qquad 5.16$$

Taking the arctangent of the equation yields the right handed sense of ω which by a couple of quadrant checks can be changed into the left handed sense.

The Z axis rotation angle θ is the sum of the detector's azimuth and ω i.e.

$$\theta = AZ + \omega \qquad 5.17$$

Since the detector azimuth is unknown an iterative scheme must be used. A good starting approximation is given by Equation 5.1. The forward transformation is then successively applied to the sun's azimuth and zenith until there is only a small change (ΔAZ_{sun}, ΔZ_{sun}) in the required azimuth and zenith corrections. The layout of the method can be seen in the flow chart in Figure 5.4.

The final forward transformation yields a tilted azimuth and zenith such that:

$$AZ' = AZ - .\theta + \Delta AZ$$
$$Z' = Z + \Delta Z \qquad 5.18$$

where ΔAZ and ΔZ are the final corrections. As mentioned earlier the total transformation can be thought of as a single rotation about the Y' axis. Therefore the purpose of the initial Z axis rotation is to define the Y' axis. Considering this it is reasonable to partially reverse the transformation by adding θ so that

$$AZ^* = AZ + \Delta AZ$$
$$Z^* = Z + \Delta Z \qquad 5.19$$

Geometrically this means that the X',X^* and Y',Y^* axes are aligned. This partial back transformation makes the comparison between the tilted and original co-ordinates easier.

The azimuth and zenith corrections, as a function of θ and Z, resulting from the forward transformation (ε=1°,AZ_{det}=60°) are shown in Figures 5.5. The corrections reach a maximum when the tilt direction is perpendicular to the look azimuth (i.e.$\theta\pm$90°). Also note that the azimuth corrections became very large at low zenith angles especially when (Z<ε°). Near the zenith this is only a small motion against the sky. The azimuth correction is equal to the tilt at a zenith of 25°. The zenith corrections are always less than or equal to the tilt.

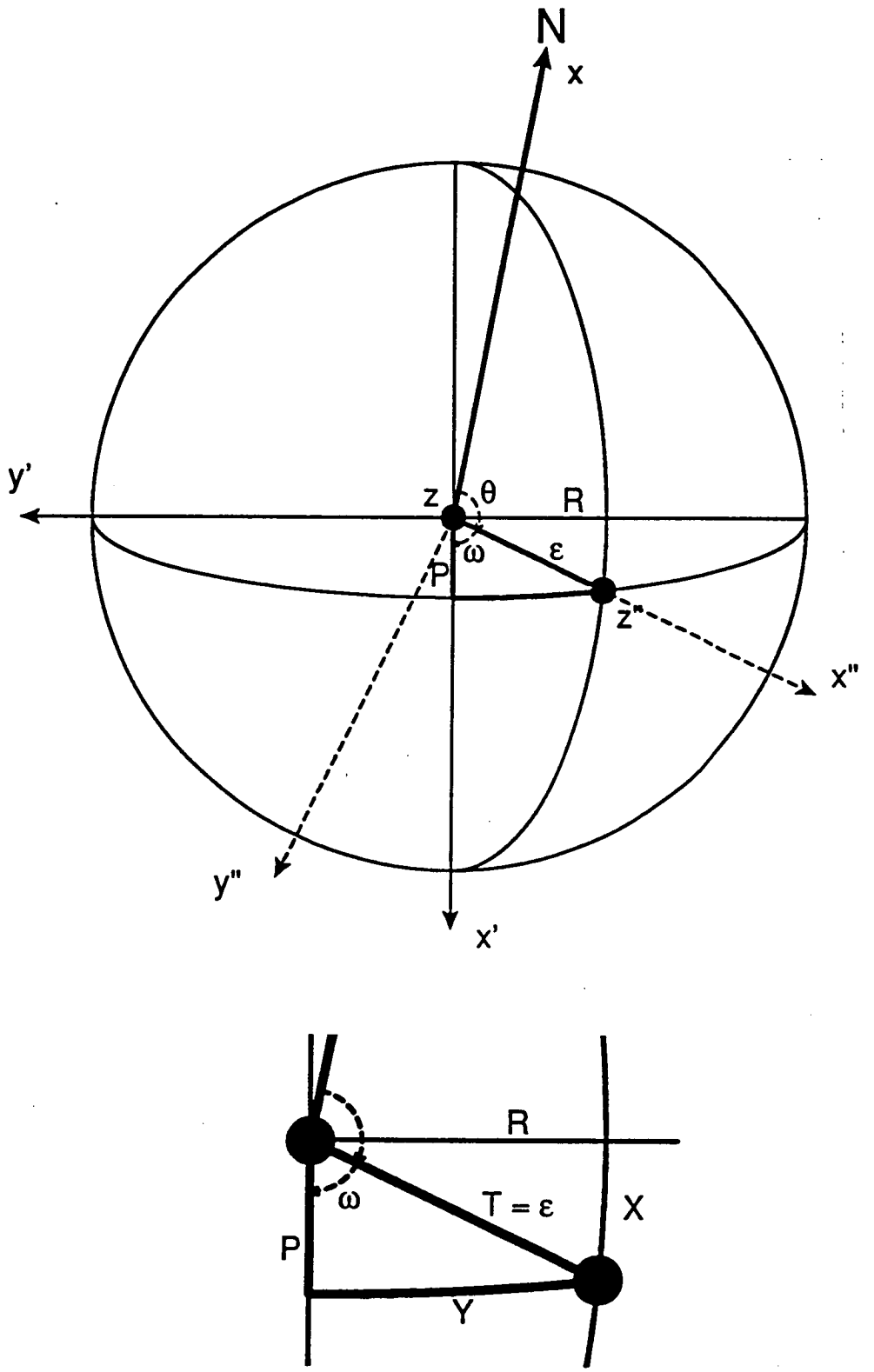

Fig 5.3 This figure is an overhead view of Figure 5.1. Included in the main diagram are the details of the spherical triangle used to calculate the size and direction of the total tilt. See equation 5.16.

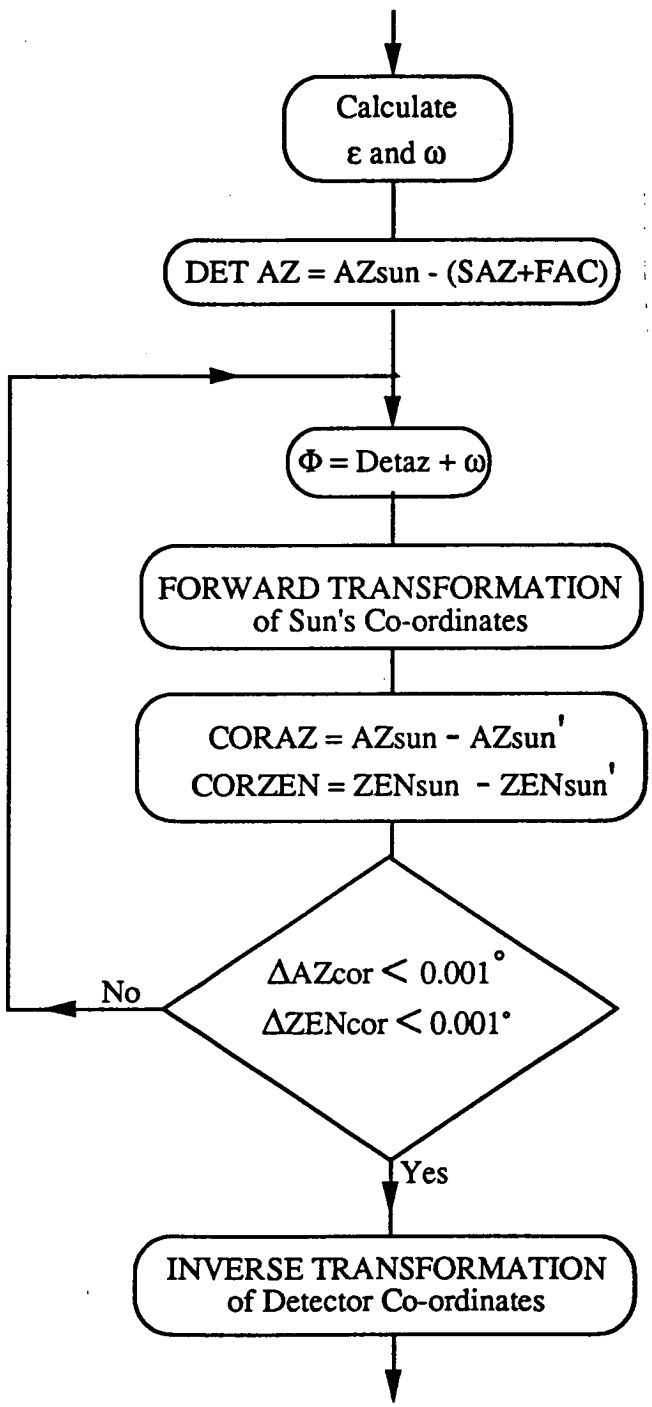

Fig 5.4 Flow chart showing the steps used to calculate the azimuth and zenith corrections caused by the tilt of the sun sensor.

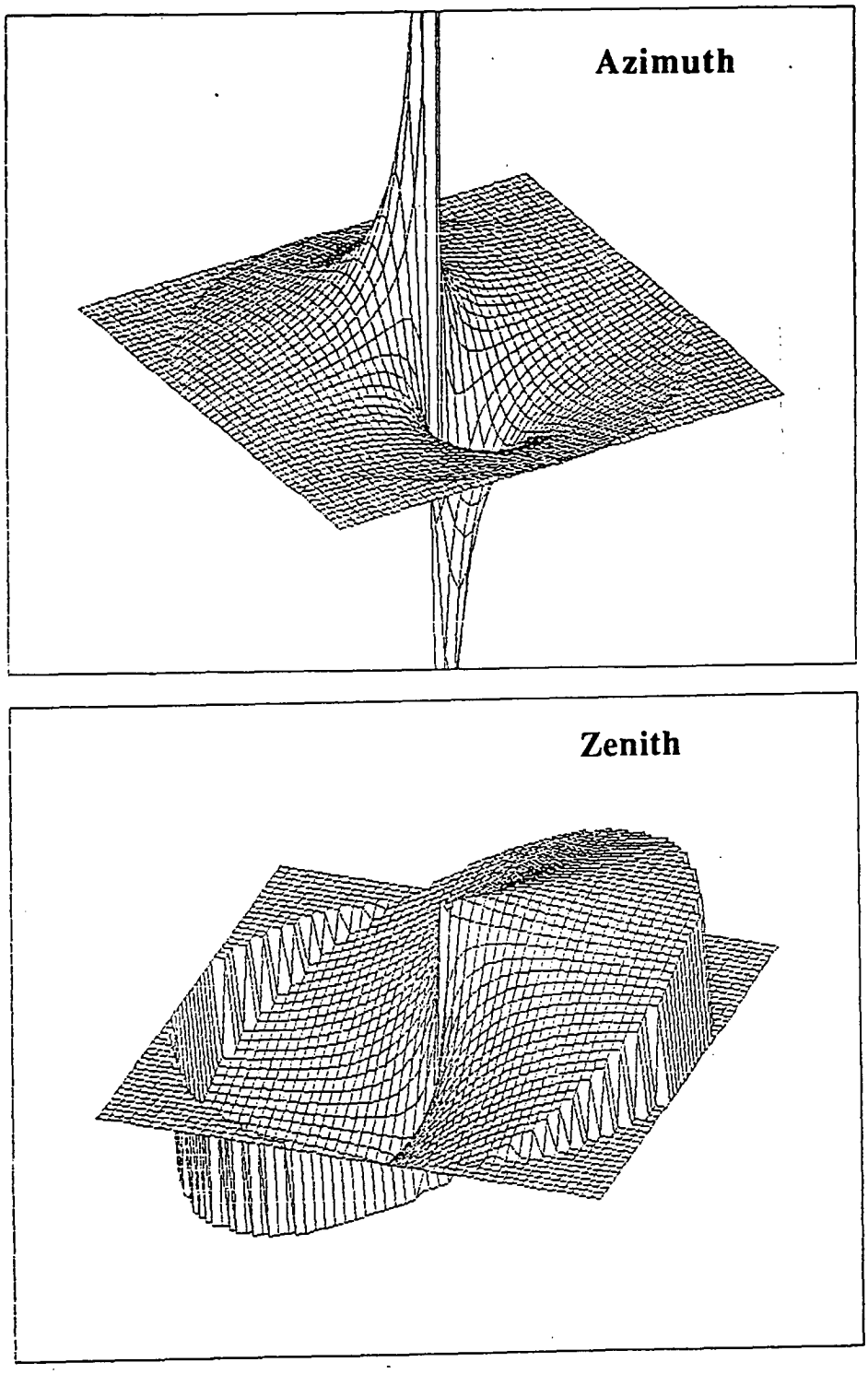

Fig 5.5 Two dimensional plots showing the azimuth and zenith error angle caused by a sun sensor tilt calculated for a grid of azimuths and zenith angles. In both cases there is a discontinuity along the line ±90° of the tilt direction. The effects of a tilt are greatest at the zenith.

It was found that all three equations of the forward transformation were required in order to resolve quadrant ambiguities. This is particularly true in two regions; $Z<\varepsilon°$ and $|AZ-\theta|$ within ε of $\pm 90°$.

There are three possible ways to perform the inverse transformation from tilted to untilted co-ordinates. Firstly, either of the $R_P R_R$ or $R_R R_P$ (rotations about the pitch and roll axes) transformations could be used. This pair of combined rotations are non-commutative. The difference in final position is small given that the pitch and roll are small. In other words, by applying the small angle approximation ($\cos\theta=1, \sin\theta=0$) the above pair of transformations become commutative. The method adopted was the third possibility; the use of the direct inverse of the forward transformation (Equation 5.14).

5.3 UTIC83 Flight Aspect Solution

In analyzing the aspect information of the UTIC83 flight a discrepancy between the azimuth calculated using the IC 3-axis magnetometer and the UT sun sensor because apparent (Figure 5.6). The difference ranged from 0.1° to 0.8°. Generally the difference is about 0.5°. A major increase occurs around the time of local noon (13 hours UT) indicating that the error is caused by a tilting of the sun sensor. A platform tilt will also affect the output of the 3-axis magnetometer. The formalism of the previous section can be used to correct the measured azimuths of both sensors. The induced azimuth error will be different for each sensor because of the difference in tilt direction with respect to the different reference directions, i.e. the sun and magnetic north.

Unfortunately, only one (roll) of the two inclinometers was correctly functioning. This made it necessary to explore a wide range of possible pitch inclinations in order to match the sun sensor azimuths with those of the 3-axis magnetometer. Pitch angles up to a degree were indicated by initial trials.

The procedure for correcting the sun sensor's azimuth is outlined in the previous section in relation to equations 4.16 to 4.18. The iteration was stopped when the change is required azimuth and zenith correction was <0.01° Generally it was found that less than three iterations were required in order to find the true azimuth.

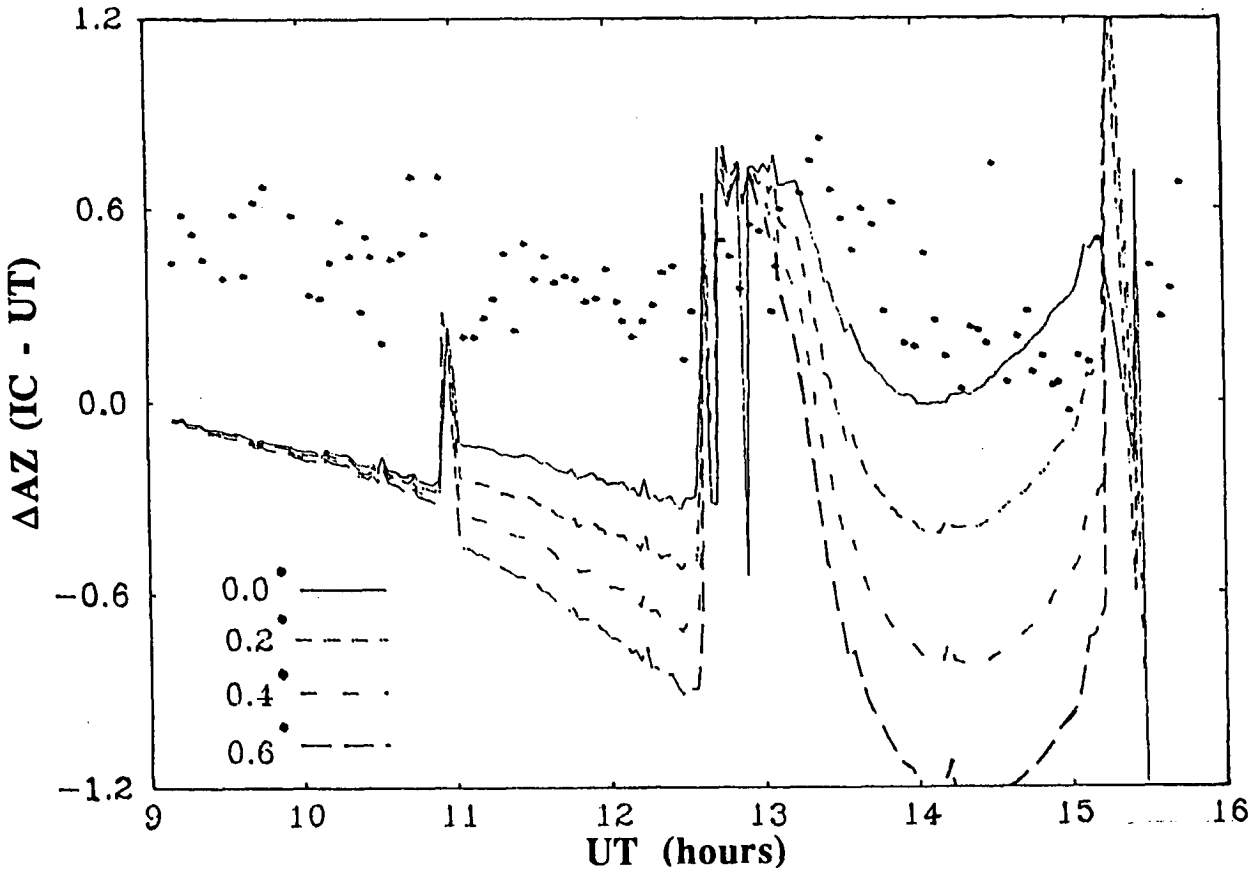

Fig 5.6 The points are the difference between the azimuths as measured by the Imperial College 3-axis magnetometer and the University of Tasmania sun-sensor. The various curves show the induced azimuth error when the sun-sensor is tilted by the measured roll angle and the indicated pitch angle.

The effect of tilts were found to be much smaller in the case of the 3-axis-magnetometer and so a non-iterative method was used. The magnetometers are less sensitive to tilts because the dip angle is ≈60° (low in the sky) as compared to the sun which passes close to the zenith. The total tilt and its direction were calculated with respect to magnetic north assuming a pitch angle and using the measured roll and azimuth. The forward transformation was used to find the tilted orientation of the magnetometer axes. The components of the magnetic field along the tilted axes were found and a new azimuth calculated using Arctan(AZ) = Y/X where X is the look azimuth and Y is toward the IC detector. The difference between the initial azimuth and the new azimuth was used as a additive correction to the the initial azimuth. Initially no account was taken of any possible physical misalignment between the axes of the IC 3-magnetometer and the platform.

The magnetometers are responding to the on-board magnetic field which is a distortion of the local (specific latitude, longitude and height) geomagnetic field. The platform will cause a difference between the actual and sensed direction of magnetic north, and dip angle. The offset in magnetic azimuth is calibrated, along with all other navigation sensors, in a procedure akin to 'boxing' a ship's compass. The correction has already been applied in calculating the initial magnetic azimuth. Tilting will cause a minute change in the calibration. This second order effect is ignored. However, the difference between the on-board and local dip angle has not been calibrated. Since no on-ground calibration of dip angle-azimuth variation is available one was constructed from the flight data. The measured dip angle (DA) is calculated using

$$\cos(DA) = \frac{Z}{\sqrt{X^2 + Y^2}} \qquad 5.20$$

where X, Y, Z are the outputs of the three axes (look Az, look Az-90°, vertical). The local geomagnetic field is poorly determined, especially at balloon altitudes, in the region of the UTIC83 flight path. A multi-pole model of the earth's field was used to calculate the magnetic deviation and dip angle along the flight path. These calculations were performed by Dr. J. Humble in this department. A plot of the difference between the measured dip angle and the local geomagnetic dip angle versus azimuth is shown in Figure 5.7. An approximate sinusoid is fitted. This calibration curve was used to estimate the platform dip angle in the calculation of the 3-axis magnetometer's response to a tilt.

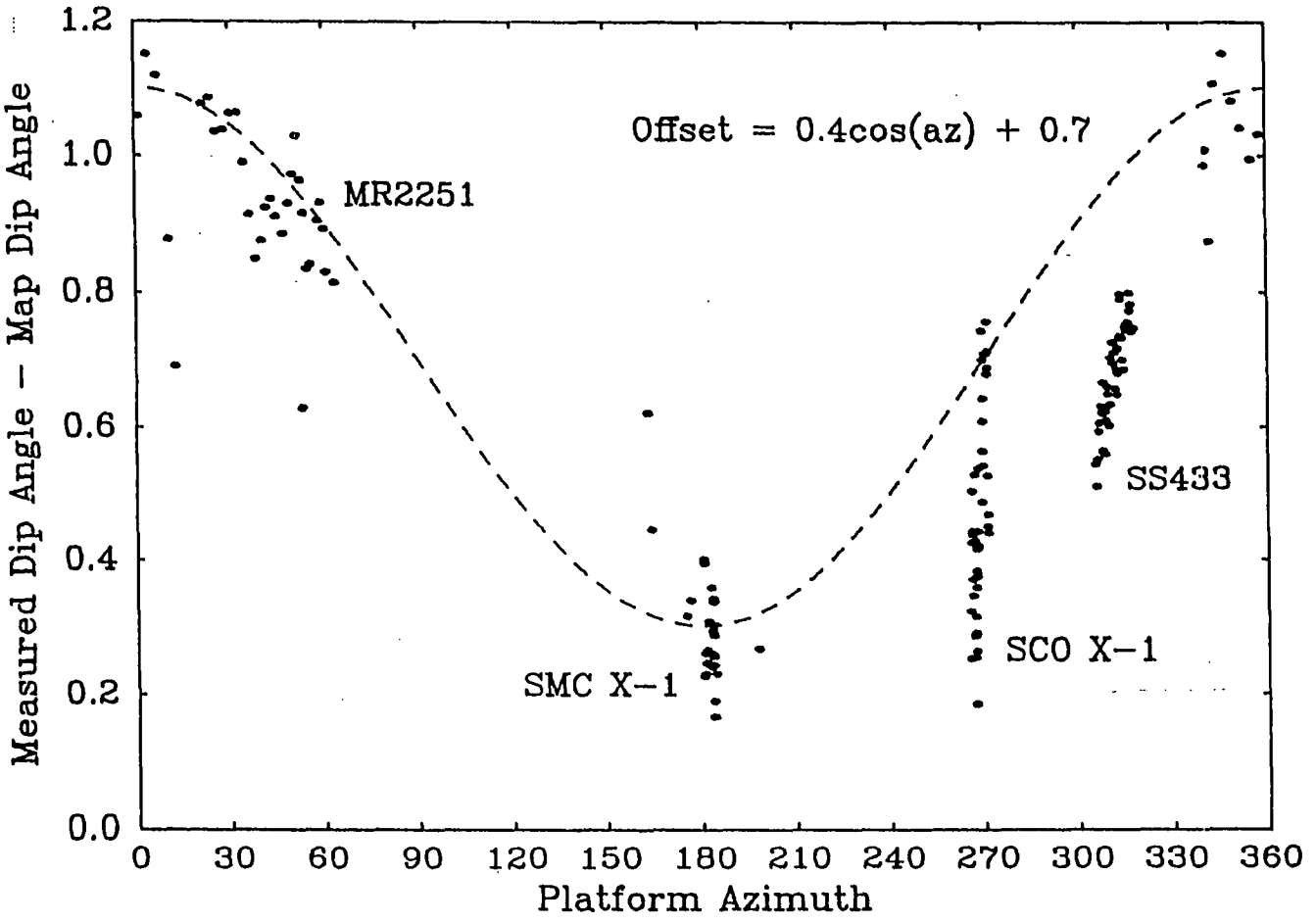

Fig 5.7 Calibration of dip angle using data from the flight. The cosine curve is used as the correction curve.

Assuming various pitch angles, the above procedures were used to correct both the sun sensor and 3-axis magnetometer azimuths. It was anticipated that when the two sets of azimuths agreed then the correct pitch history had been established. However, there is an ambiguity in the possible pitch especially if leveling and alignment errors are considered. Firstly, for each correction, there are two possible pitches, (i.e. in opposite directions) that will yield the same azimuth offset. This ambiguity is compounded because the roll inclinometer could have a levelling error of ±0.2° It was found that a larger levelling error required smaller pitches to bring the two azimuths into agreement. There is also an unknown, but small (<0.5°) offset between the magnetometer and sun sensor. This offset would be caused by the physical misalignment of the magnetometers with the principle axes of the platform.

There are some guides to the possible size and direction of the pitch angle. There are limits upon the possible levelling and misalignment errors. The pitch angle is expected to be similar in size to the roll angle. The most likely cause of a platform tilt is a shift in the centre of mass as ballast is released. This should affect the pitch and roll in a similar fashion. Another constraint is that, like the roll angle, the pitch angle should vary smoothly. The roll angle could be fitted well with a quadratic. The most useful constraint comes from the two azimuth swings. At these times the total tilt could be estimated. As the tilted magnetometer is moved around in azimuth the measured dip angle will vary with an amplitude equal to the total tilt. From the phasing of the variation the direction of the tilt can be estimated.During the azimuth swings just before the sun sensor became in-operative the total tilt was found to be 0.35° toward the IC detector. This estimate, along with the smoothness and size constraints eliminates one of the two orientations of the pitch.

Given these considerations a reasonable but not unique aspect history can be found. Figure 5.8 shows that close agreement can be found between the two sets of azimuth offsets. This solution requires a -0.2° levelling error in the roll inclinometer and a +0.27° azimuth offset between the 3-axis magnetometer and the sun sensor. The adopted pitch and roll histories are given in Figure 5.9. In the latter part of the flight the sun sensor was shadowed by the balloon and so no accurate pitch could be found. The 0.35° tilt toward the IC detector implies a pitch angle of -1°. A small section of sun sensor data after the SMC observation (near 17 hours UT) and just before the end of the flight indicated a near zero pitch. In Figure 5.9 both possible pitch histories are indicated.

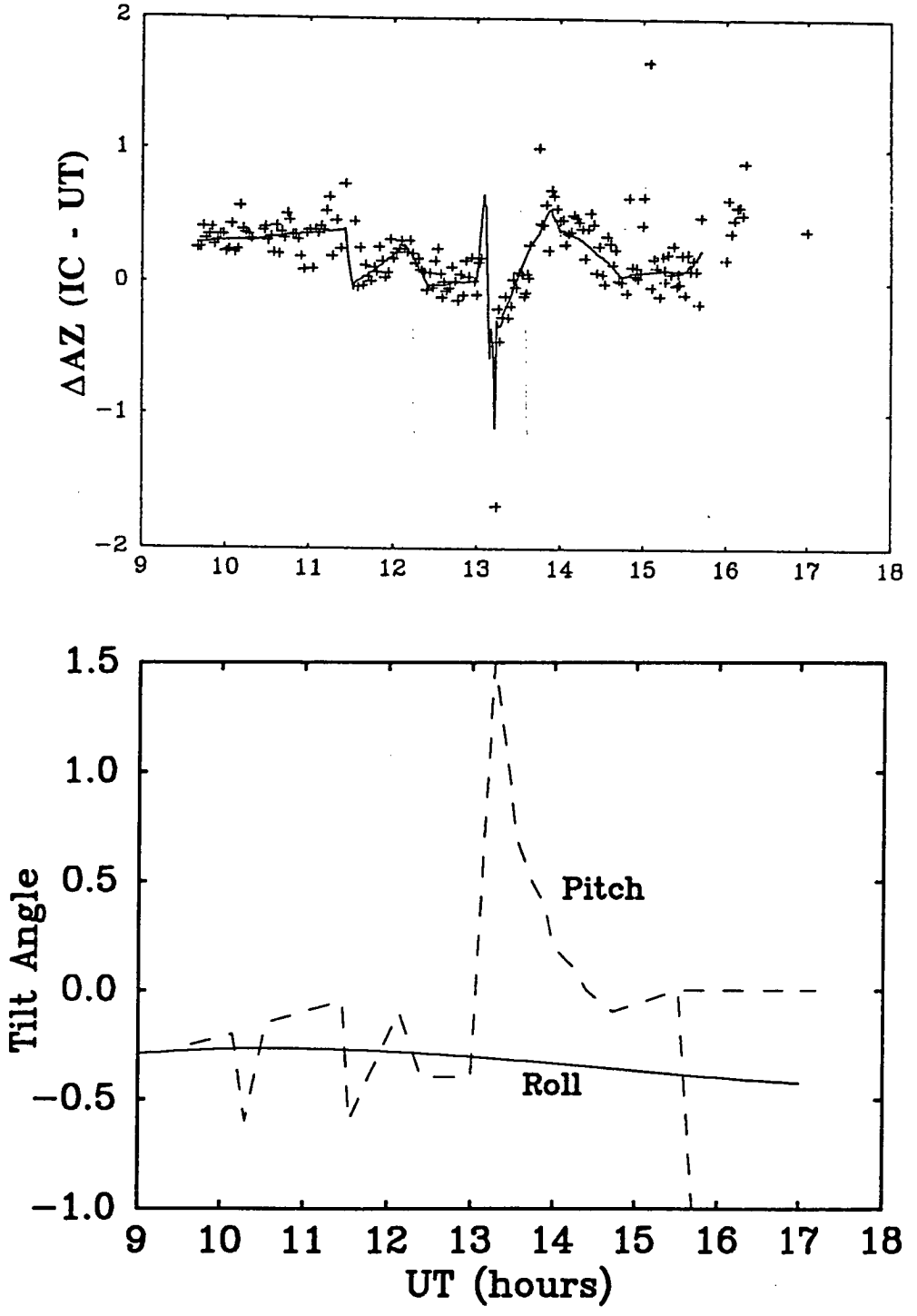

Fig 5.8 A close match between the magnetometer (+) and sun sensor azimuth offsets can be found. This particular match used the dip angle calibration of Figure 5.7 and assumes a -0.2° levelling error in the roll inclinometer and 0.27° offset between the IC 3-axis magnetometer and sun-sensor.

Fig 5.9 The adopted pitch and roll histories. During the SMC observations there was little sun-sensor data and so the derived pitch is uncertain; possibly ranging between -1° and 0°. Both possibilities are indicated.

5.4 Background Variations

Prior to the observations of the SMC the payload made two rapid swings in azimuth. The more extensive swing occurred with the detector pointing at a zenith angle of 51°. The other swing was at a zenith angle of 71°. A further scan in azimuth (zenith angle = 36°) was made when the detector was moved from SS433 to MR2251-175. The counting rates where binned into 10 sec. averages . The longest azimuth swing provided little data in the azimuth range 0°-150°. The counting rates at other zenith angles were linearly rescaled to those of the 51° swing. This was done using a mutiplicative factor based on the ratio of the average count rates over the 0°-150° azimuth range. The resulting counts were then binned in azimuth. There was clear evidence of an azimuthal variation with the count rate being highest at 270° (west) and a minimum at AZ=90° (east). The fractional modulation increased from 3.7%p-p at 8.5-19.5keV to 17%p-p at 45-55keV. Over the 55-72keV range the peak to peak modulation drops to 8.5%.

A similar east/west anisotropy is observed in the primary cosmic ray flux (Cooke 1971) The amplitude of this anisotropy increases toward the equator. There is also a north/south anisotropy. Below 1MeV the spectrum of atmospheric photons is determined by their energy loss via Compton scattering. A north/south but not an east/west anisotropy has been observed at γ ray (Ryan et al. 1979) and at X-ray wavelengths (Fishman 1981). The difference in anisotropy orientation is probably not due to difference in latitude between present observations and those of Fishman. Palestine Texes is only about 10° further north than the flight path is south. Charged particles do have an east/west anisotropy and so could explain the observations if the background count rate was primarily due to charged particles rather than γ rays.

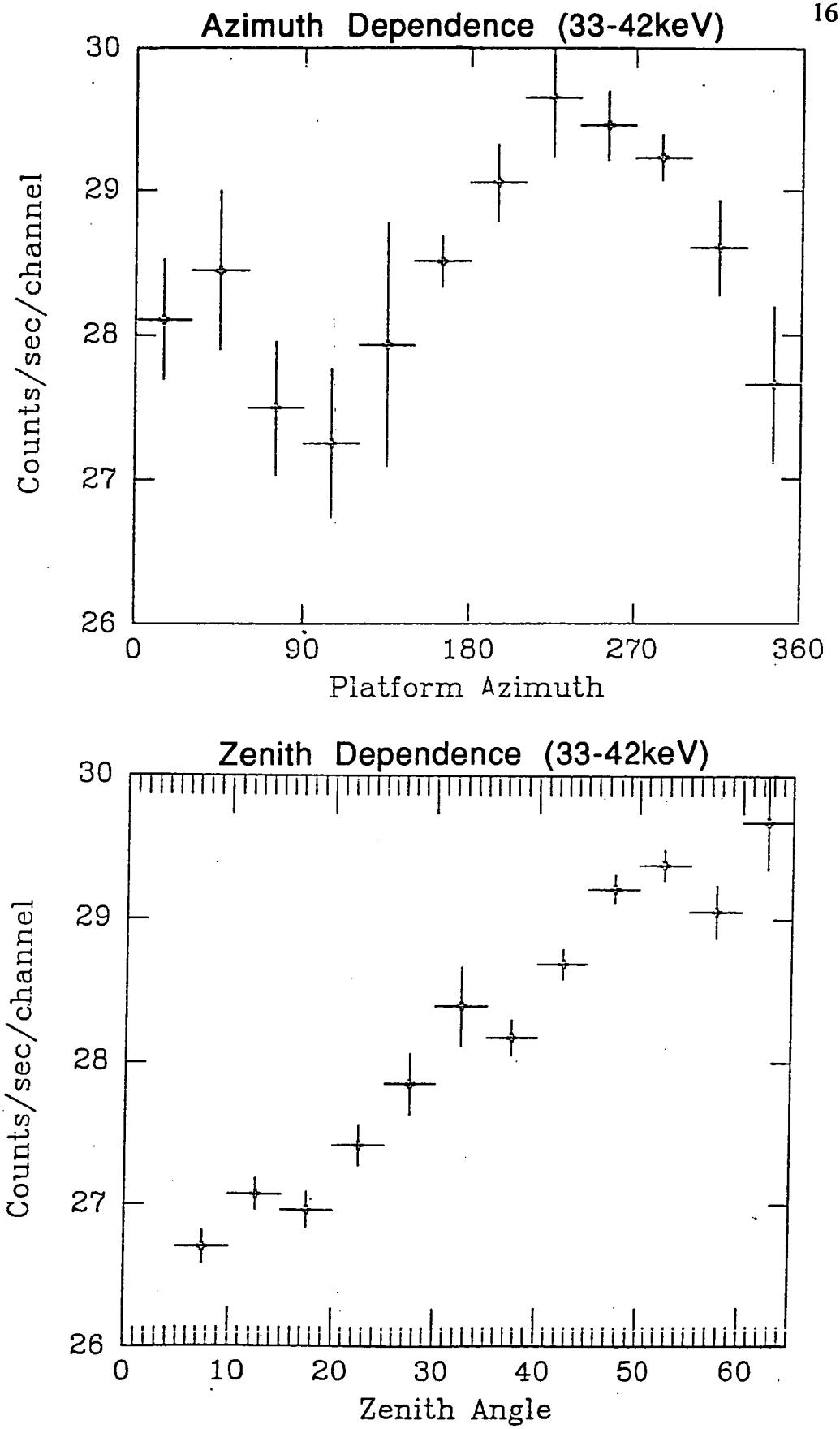

Fig 5.10 The azimuth and zenith dependence of the background. The azimuth changes are for a zenith angle of 51°. Between 0-150° azimuth includes data from swings at zenith angles of 37° and 71°. This data is scaled to the 51° count rates. Both azimuth and zenith data sets have been binned.

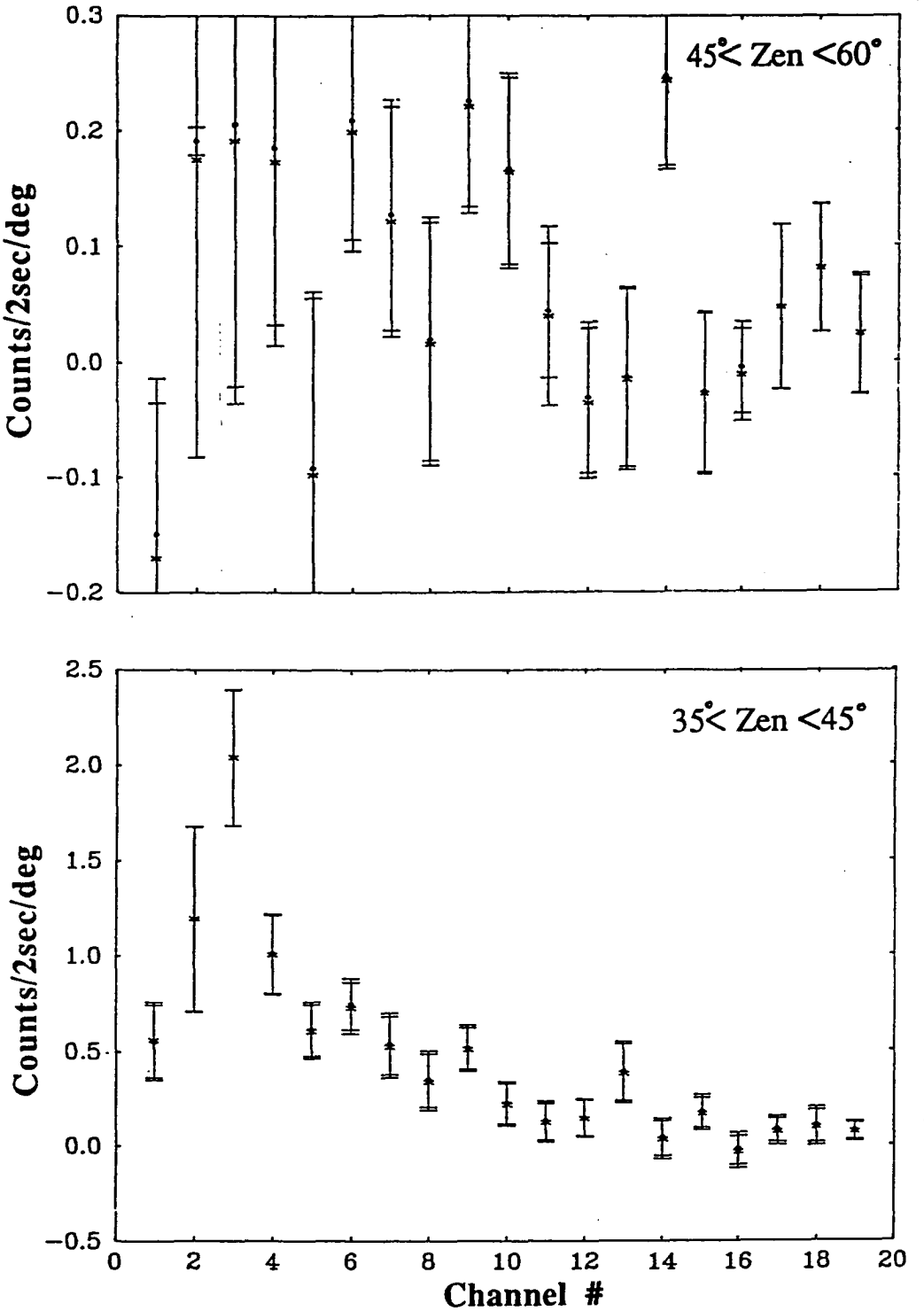

Fig 5.11 The slopes as from least squares fits of the count rate zenith angle trend for each individual channel. Data from each rock is fitted separately. The errors are the standard errors of the fit. The upper panel is from the Sco X-1 observation while the lower panel is from the SS433 data set. Data in channel 1 is unreliable.

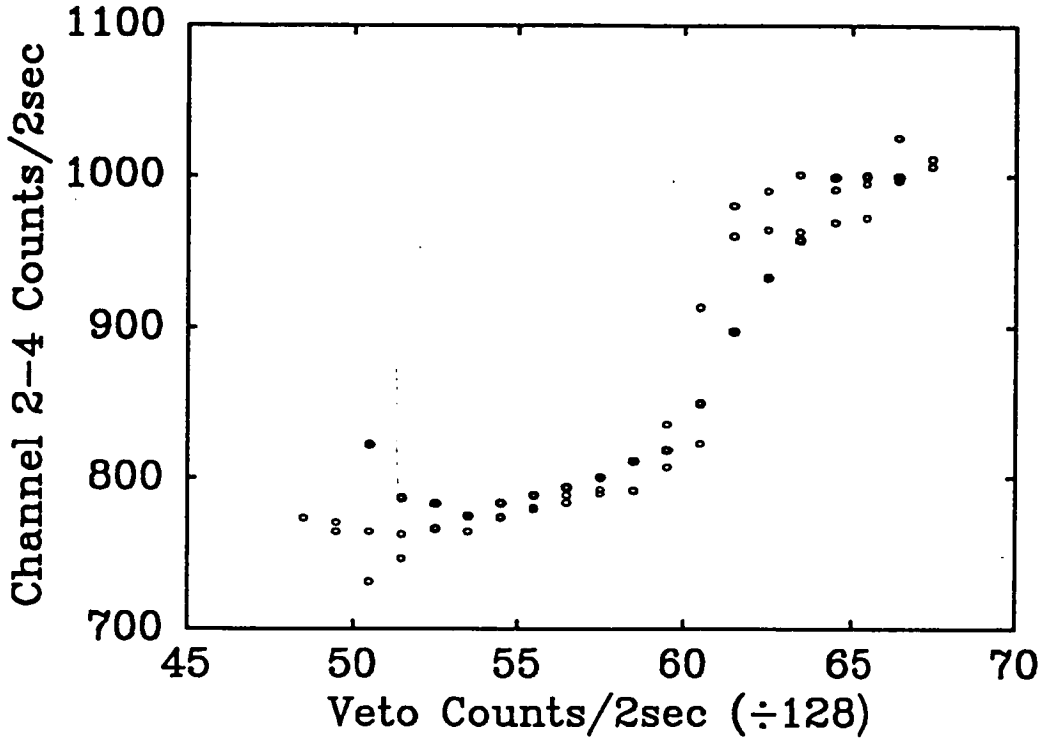

Fig 5.12 Individual two second integrations from the Sco X-1, SS433 and MR2251-178 observations are binned to show the correlation of low energy count rate and veto rate. At higher energies the trend is less pronounced.

The variation of the X-ray and γ-ray background flux with zenith is much more widely observed. This variation is a major source of difficulty in determining the correct source flux. During the UTIC83 flight the background counting rate increased steadily between 10° and ~45°. The fractional change in count rate steadily increases with energy being 0.05%/deg at 6keV to 0.28%/deg at 70keV. The absolute change in count rate is about 0.1 cts/2sec/deg in the lowest energy channels and 0.03cts/sec/deg above channel 10 (40keV). The trend flattened out above 45°. An example of the background azimuth and zenith dependence is shown in Figure 5.10. The change in slope with energy is shown in Figure 5.11 for the SS433 and Sco X-1 backgrounds.

The UT background during the UTIC83 flight was unusual in that it could be well represented by a power law (α=1.4) over the entire 6 to 70 keV band. In the UTIC81 flight there was a similar background spectrum. It is believed that the high count rate at low energies is the result of inefficiencies in the veto system. A positive correlation is found between the count rate and the veto rate (Figure 5.12). The correlation is less evident at higher energies. This relationship could also be the result of inefficiencies in the veto system or due to a physical correlation between the X-ray and charged particle fluxes.

A leaky guard system would respond to any angular dependence in the charged particle background which should be well correlated to the X/γ-ray background. The detector will present different surface areas to the background distribution. In zenith the the high energy background is expected to peak at a an angle of about 110° (Costa et al. and references therein 1984). At high zenith angles the detector presents a large surface area to this maximum in the background. A tilted detector will also present a larger or smaller surface area to the maximum of the charged particle east/west anisotropy.

No matter what the exact cause of the azimuth and zenith dependence of the background counting rate these variations must be corrected for in the data analysis procedure.

5.5 Data Analysis Procedure

The adopted aspect solution was applied throughout the flight. In periods when the sun sensor was shadowed by the balloon, the 2-axis driving magnetometer azimuth was used. The output of the 2-axis magnetometer were corrected for tilting using the methods described by Warren (1980). Only the observations for the SMC relied upon the magnetometer. In this case the aspect solution is much more uncertain.

Each 2 second integration was characterized as being either a source, confused source, background, or contaminated background observation. An integration was considered a source observation if the look direction was within 1.1° (1/2 field of view, FOV) of the source position. The list of potential sources was based upon the HEAO A4 catalogue.

A background integration was considered as such if the look direction was greater than 2.2° (=FOV) away from any listed source. Any look directions between 1.1° and 2.2° were considered as a contaminated background and not used. Any integration in which two or more objects were within the field of view (FOV) were classed as confused observations. The brightest source within the FOV was noted. Data taken while the detector was moving from one rock position to another was rejected because of suspicions of electrical interference from the motor drives.

The average count rates of the two rock backgrounds can be taken as the source background. When this is done all sources show a low energy excess above that expected from escape photons. At energies below 20keV (channels <6) practically all source photons are absorbed by the atmosphere and so any counts at these energies must be due to escape and the transfer of counts from higher energies due to the finite energy resolution of the detector (42% FWHM at 60 keV). The escape fraction for the UT83 detector is ~50% and so the number of counts below 20keV should be roughly equal to the count rate 30keV higher in energy (i.e. 35-50keV). The observed excess is caused by a slight error in the background subtraction method caused by the source pointing not being exactly half way between the high and low background pointings. This results from variable tilting, the need to reject some source and background data as being inappropriate, and because of the movement in zenith during pointings. The problem is overcome by linear interpolation in zenith of the background data. The PHA spectra for Sco X-1 and

SS433 show no low energy excess. This procedure is not applicable to the MR2251 data because the low rock data is apparently contaminated by a unknown source called TAS X. In this case the counts must be corrected for both the background dependence with azimuth and zenith. A similar analysis can be undertaken for the Sco X-1 and SS433 observations but was not used because of the higher statistical uncertainty in the final PHA spectra.

The count rates are corrected to a standard azimuth (280°). For each channel the count rate azimuth variation, as determined from the swings, was binned in azimuth and a smooth curve drawn through the data. This curve is used to produce a table of additive correction factors. The size of these corrections must decrease with zenith angle since there cannot be any azimuthal change at the zenith. A linear drop in the amplitude was adopted. A sin(zen) dependence would be physically more plausible. However, the difference is small and so the simplest (linear) variation in amplitude was used. There is not sufficient data to elucidate the form of amplitude change with zenith.

The variation in background counting rate with zenith angle is more complex having several different regimes. i.e. <10° (TAS-X), 10°-45° (MR2251, Sco X-1, SS433) and >45° (Sco X-1, SS433) A linear fit (count rate v zenith angle) of the background data was performed for each PHA channel, over each zenith range. Also in order to avoid possible long term time variations separate fits were made of the backgrounds from the Sco X-1 SS433 and MR2251 observations. There is only a small overlap in the zenith angle ranges covered by the observations of the Sco X-1 and SS433 and no overlap with the MR2251 data. The slopes from the fits were plotted against energy (channel numbers) and a smooth curve drawn through the data. Generally the rate of count rate change is greater at lower energies and practically zero at energies above 45 keV. The SMC observation had no rocking and so there is little background information. The variation in background was found from two short sections of background data before and after the SMC data. Fortunately the SMC was making its upper meridian transit and so there was little change in zenith angle. The smoothed slopes were used to correct each integration to a standard zenith angle (50° for Sco X-1, 20° for MR2251, and for 50° SMC X-1).

After correction, consecutive two second integrations, of the same type (source, background etc.) were summed together. Finally these individual pointings were averaged together to form a source, high and low background, confused source and contaminated PHA spectra. The average of the high and low rock backgrounds, are subtracted from the source spectrum.

5.6 RESULTS

5.6.1 Sco X-1

Sco X-1 was observed for a total on source time of 1400 seconds between 9.6 and 11.3 UT, at zenith angles between 36° and 57°. The average line of sight atmospheric depth was 6.4 g cm^{-2}. Also, the average source/viewing direction distance was 0.65° which corresponds to a 72% collimator transmission efficiency. The final background subtracted PHA spectrum is shown in Figure 5.13. As can be seen there was only a marginal detection. Since Sco X-1 is one of the brightest X-ray sources in the sky this low level detection demands an explanation.

The sensitivity of the detector was greatly reduced by a combination of several factors. Firstly, there is the 28% reduction in collimator transmission because of the poor absolute pointing. At low energies, where Sco X-1 is brightest, the sensitivity was reduced by observing through a substantial atmospheric depth and greatly reduced by the high background at low energies. The final contributing factor is that Sco X-1 was fainter than usual during our observations. The intensity at 30 keV was 6.7×10^{-4} photons $sec^{-1}cm^{-2}keV^{-1}$ (Beurle et al., 1983). This result is from the simultaneous observations using the Imperial College detector.

To test quantitatively if the above circumstances were sufficient to render Sco X-1 barely detectable the IC spectrum was folded through the UT detector's response to produce a PHA spectrum. This method amounts to a single pass through the χ^2 minimization spectral reduction procedure. The energy resolution was 43.5% at 60 keV and the escape fraction was 52% respectively. The simulation indicated that a 1.9σ detection over the entire 7-71 keV range should be possible. This is in agreement with the observed 1.01σ detection over the same energy range. Over the 22-42 keV range the actual detection is 2.2σ while the simulation produces a 1.8σ detection.

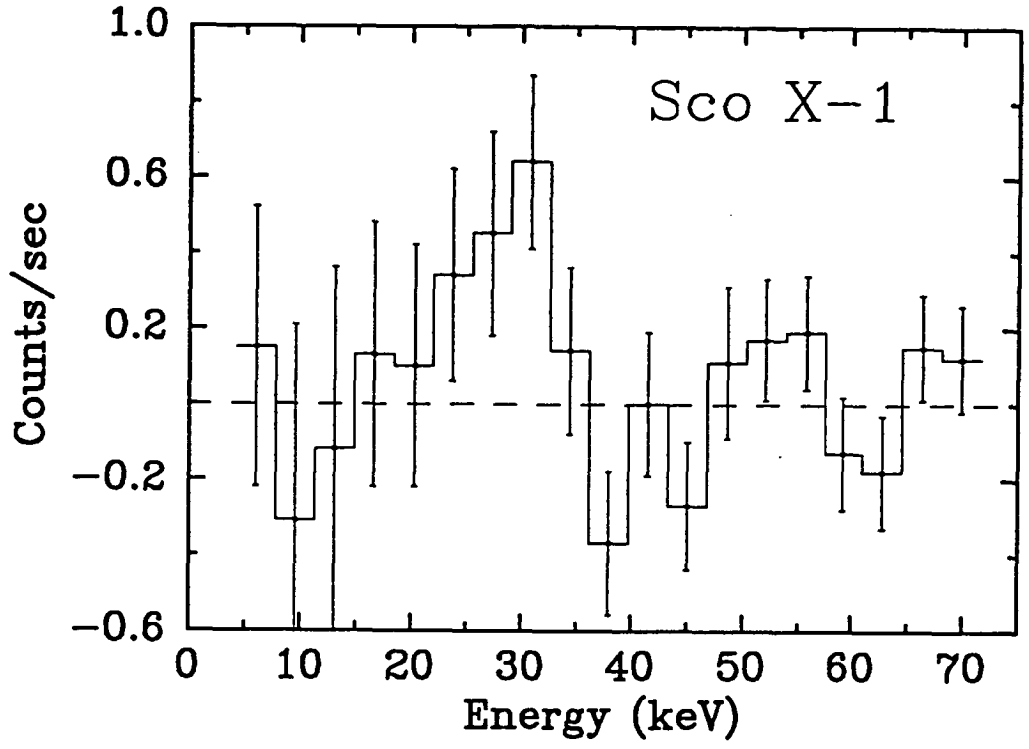

Fig 5.13 The PHA spectrum of Sco X-1. The background used is the linear interpolation of the high and low rock pointing. Channel 1 is unreliable. It is probably narrower in energy width and more susceptible to noise than the other channels.

5.6.2 SS433

SS433 is a very well known binary system consisting of a normal low mass star and a compact companion. A recent mass determination (>4.3Mʘ) (Leibowitz as quoted by Tanaka 1989) suggests that the compact object is a black hole rather than a neutron star. Like most LMXB the optical light output is dominated by an accretion disk. The system is highly variable with flaring at both X-ray and radio wavelengths. At optical and infrared wavelengths variability on time scales ranging from hours to days has been reported. The most remarkable feature of SS433 are the oppositely directed relativistic jets. These jets manifest themselves as rapidly moving optical emission lines and are seen directly in high resolution radio maps. The material in the jets is being accelerated to a speed of 0.26c. The most likely acceleration mechanism is Lyman α line locking. Superimposed on the orbital period of 13 days is the 164 day precessional period of the jets. A review of the properties of SS433 can be found in Margon (1984).

The radio spectrum is non-thermal. At energies below 20 keV the X-ray spectrum consists of a thermal spectrum with low energy absorption Above 20 keV the spectrum becomes non-thermal with a hard power law tail. In the environment of a black hole inverse Compton scattering of stellar photons could produce X-rays with power law spectrum up to 100keV. A model of the interaction of the beams with the surrounding medium also predicts a power law spectrum. The expected power law index is α = -2 (Begelman et al. 1980).

The total on source observation time was 1590 seconds between 11.53 and 12.96 UT. The average zenith angle was 42° which corresponds to a line of sight atmospheric depth of 5.7 g cm^{-2}. The average source offset distance was 0.6°(40% collimator transmission). Between 21 and 43keV there is a positive flux at the ~2σ level. The upper limits and tentative fluxes from the UT and IC detectors are compared to the Ariel 6 and HEAO 1 results in Figure 5.14. The variability of SS433 is indicated by the 3 curves. These correspond to the power law spectrum observed when SS433 is at low, intermediate and high brightness. The UT observations are consistent with the IC limits at the 2σ level. Both sets of limits are consistent with an α=-2 power law spectrum, specially when SS433 is faint. The implied power law index is greater than the α=-1.4 to -1.7 seen from Gyg X-1. Thus it seems that the hard X-ray production mechanism may not be the same for the two black hole candidates.

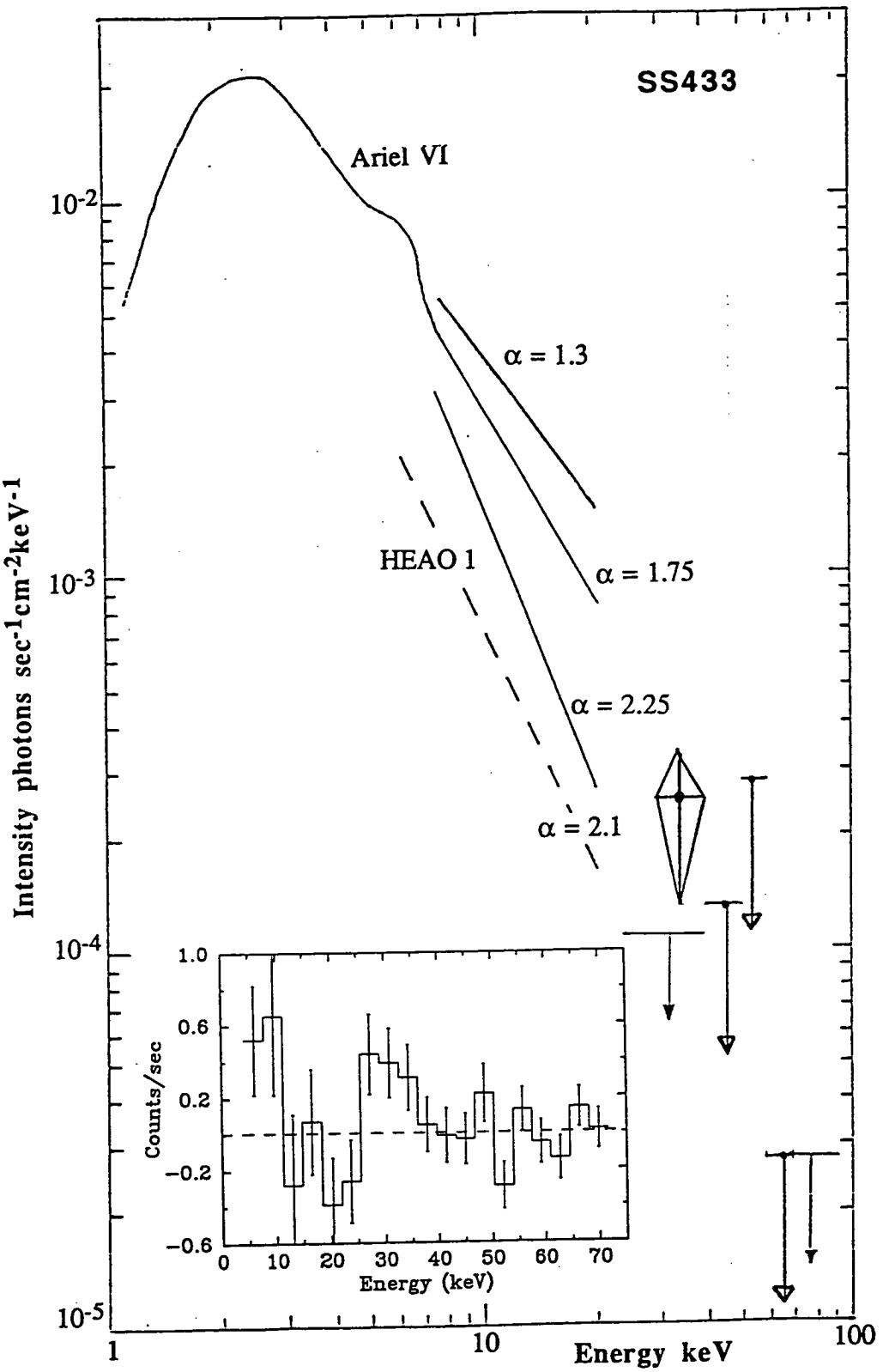

Fig 5.14 The PHA and corresponding flux spectra of SS433. The backgrounds used were uncorrected interpolations between the high and low rock pointings. The tentative flux point between 18 and 40 keV has 1σ error bars. The 2σ upper limits (open arrows: UT, closed arrows: IC) are shown. This figure is based upon figure 5 of Beurle et al (1983).

5.6.3 SMC Observations

The region near the very luminous 0.7 sec X-ray pulsar was observed for 1150 sec between 15.96 and 16.65 hours UT. The average zenith angle was 49°. The corresponding line of sight atmospheric depth is 6.4 g cm^{-2}. Two short background observations of 172 sec and 100 sec duration, bracket the SMC observations. No rocking was made during the observation. At the time the SMC was making its upper meridian transit and so was moving little in zenith angle.

Although the target was SMC X-1 the effects of the platform tilts caused either or both of SMC X-2 and SMC X-3 to be in the FOV during most of the observation. During most of the UT observation, SMC X-2 was apparently much closer to the centre of the field of view. However, the aspect solution is very uncertain. Since no sun-sensor data was available the azimuth was estimated from the UT 2-axis driving magnetometers. Obviously no check could be made upon the pitch at the time. From the sun-sensor data prior to the SMC observation and from the swings the pitch is extrapolated as being about -1°. If the pitch was zero degrees the detector would have been pointing at SMC X-1. A source is tentatively detected however its background subtracted PHA spectrum is not self consistent showing large differences in count rate in adjacent channels. Also there is a large excess of counts at low energies. Both aspects of the spectrum suggest an error in the determination of the background. There is no prospect that improved analysis would change the situation because of the limited duration and large source distance of the backgrounds available.

Using the most likely pointing solution the average viewing direction from SMC X-1 was ~2°. Less than 300 sec of data were obtained with SMC X-1 solely in the field of view and so no meaningful upper limits can be set. Beurle et al. (1983) from a simultaneous observation set upper limits of 6.6×10^{-5} photons cm^{-2} sec^{-1} keV^{-1} (16-48keV) and 1.4×10^{-5} photons cm^{-2} sec^{-1} keV^{-1} (48-104keV). These limits are consistent with SMC X-1 being near the minimum of its ≈60 day cycle. The results indicate the presence of a source, probably SMC X-2. Because of the short duration and large azimuth distance from the SMC the background is unreliable. No background subtracted spectrum consistent with an celestial source could be determined.

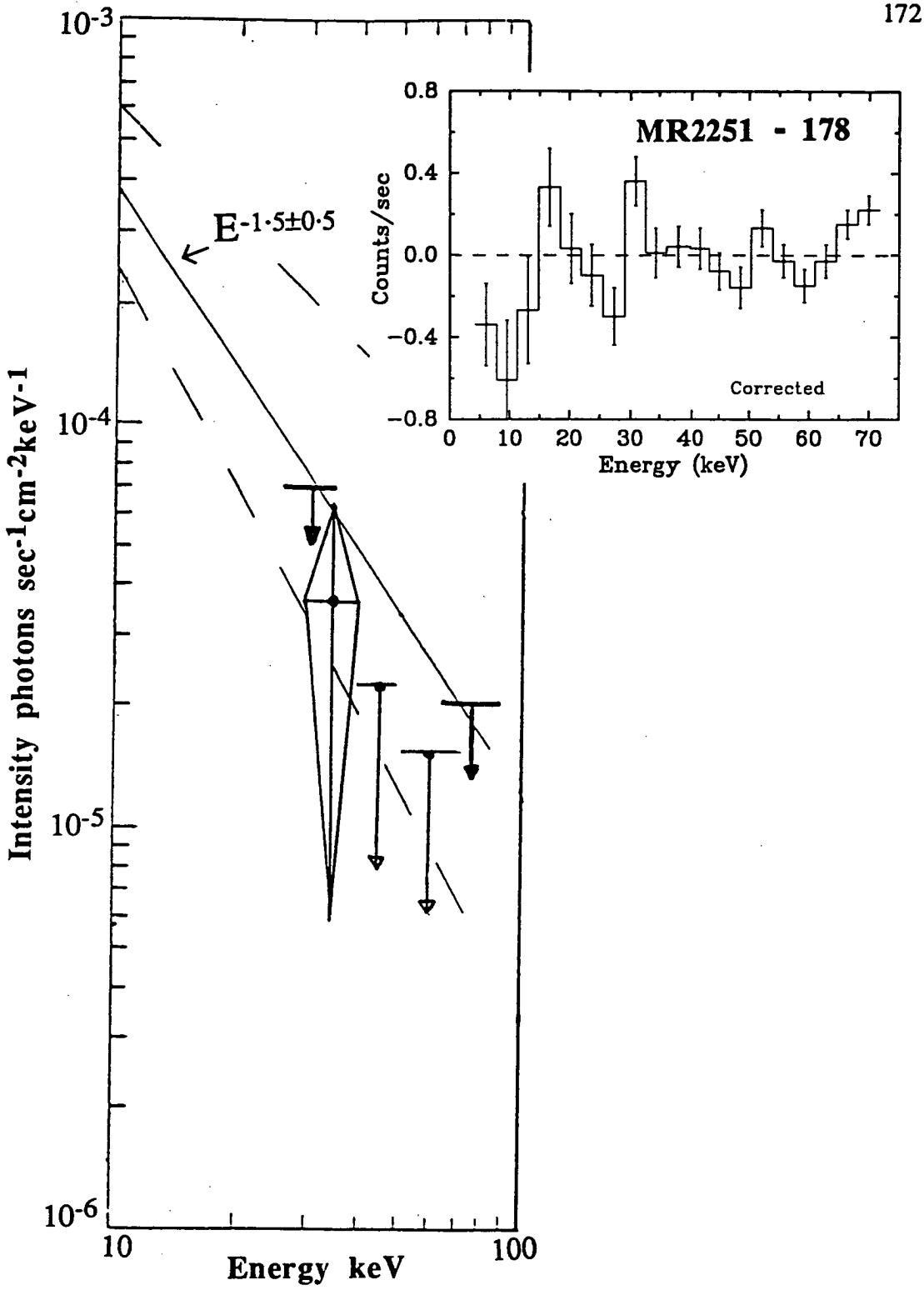

Fig 5.15 The PHA and corresponding flux spectra of the MR2251-178 pointings. The count rates have been corrected for the variations in azimuth and zenith angle. The zenith angle trend between 10° and 30° is used for the correction. The errors are based upon Poisson statistics only. No account is taken of the uncertainties introduced by the correction procedure. One sigma errors are shown on the tentative flux point between 18 and 40 keV. The upper limits (open arrows: UT, closed arrows: IC) are at the 2σ level. This figure is based upon a figure in a preprint of Beurle et al (1983).

5.6.4 MR2251-178

The QSO MR2251-178 was initially discovered as a low energy X-ray source (Ricker et al. 1978). It is similar to other low redshift QSO's except for the extreme width (23,000 km s^{-1}) of its Hα line. At optical wavelengths MR2251 is variable by up to 2 magnitudes. At medium X-ray energies it is variable in both intensity and spectral shape. The 3-10 keV power law index ranges from 1.52 to 1.72 (Halpren 1984).

A total of 3228 seconds worth of on source data was gathered from the direction of MR2251. The observations were made over the 6°-24° zenith angle range between 13.3 and 15.5 hours UT. The average line of sight optical depth was 4.3 g cm^{-2}. Fortunately the platform tilt partly offset the effects of the poor absolute pointing. However, the low zenith angle background data was contaminated by a bright unknown source. Aside from halving the amount of background data available this source made it vital to extrapolate the lower altitude background data to the zenith angle of MR2251-178.

There was no significant flux detected over the entire 7.8-72 keV range (see the inset of Figure 5.15). The upper limits are compared to those from the IC detector and EINSTEIN satellite data. These upper limits are not stringent enough to usefully constrain the slope of the spectrum. This is especially true considering MR2251-178 is variable (Figure 5.15).

5.6.5 TAS-X

The low zenith rock of the MR2251-178 observation contained a bright unknown source. It has been dubbed TAS-X. The inset of Figure 5.16 shows a plot of the excess count rate in the low zenith rock. The triangular variation in the low rock count rate is typical of a source transiting the field of view (see also the top panel of Figure 5.18). A map showing the positions of the high rock pointings and the range of possible positions of TAS-X is shown as Figure 5.16. The estimated position is at $\alpha = 22^h\ 52^m$ ($\pm 1^m$) and δ = -20° 45' (±20') .In this region there are no known X-ray sources. The IC detector did not scan this area because it was rocking in azimuth.

Initially the zenith angle trend between 30° and 10° was extrapolated to the TAS-X zenith angle. The resulting background subtracted PHA count rate spectrum is

shown in Figure 5.17. It is very soft with an excess of counts below 20 keV. There are about three times as many counts as expected from ≈40 keV escape photons. Some but not enough of these low energy counts are due to resolution smearing. The count rates below 20 keV are inconsistent with any plausible detector model. Ignoring the lowest energy channels the PHA spectrum can be modeled with a power law with spectral index α=-2.8±0.7 and I_{30}=4.4x10^{-4} photons cm^{-2} $sec^{-1}keV^{-1}$. Such a spectrum is softer than many X-ray sources but similar to that of LMXB and X-ray transients.

Another possible celestial soft X-ray source is a long duration solar flare. On the 26th of March there were a number of small X-ray flares. At the same time as the TAS X observations there was a X-ray (0.5 - 8 Å) flare observed by the INP and GOES satellites (*Solar Geophysical Data: comprehensive reports* #469 Part II). The timing, duration and overall light curve is similar to that of TAS X. The sun at RA = 17.5^m and DEC=1.9° was well outside the field of view. It is difficult to imagine how a flare could have affected only the vertical background while there is no evidence of any affect by other flares in our X-ray data.

The excessive low energy count rate suggests that TAS-X is not a celestial source. An electron precipitation event may explain TAS-X. Electron precipitation events have been best studied in the context of auroral sub-storms. However they do occur at all latitudes. Electrons are accelerated by downward pointing "V" shaped electric potentials (Hudson 1979). The electrons interact with the upper atmosphere at heights near 90 km producing X-rays via the bremsstrahlung process. In passing through the atmosphere the X-rays suffer both photoelectric absorption and Compton scattering. They can penetrate to balloon altitudes (up to 10 g cm^{-2}). Monte Carlo simulations of the interactions , by Pilkington (1971), show that the X-ray spectrum softens with both vertical and horizontal distance from the initial precipitation event. By the time the X-rays reach balloon altitudes they have spread to cover up to ~25° diameter region of the sky. Collimated detectors view a softer source when the source is larger than the field of view. Combining both effects spectra with e-folding energies as low as 15keV can be produced. Generally the observed spectra have e-folding energies between 15-60keV and occur on all timescale from milliseconds to many minutes (Pilkington 1972 review). Examples of various mid latitude X-ray events can be found in Cline et al. (1977), Haynes et al. (1968), Manchanda (1972).

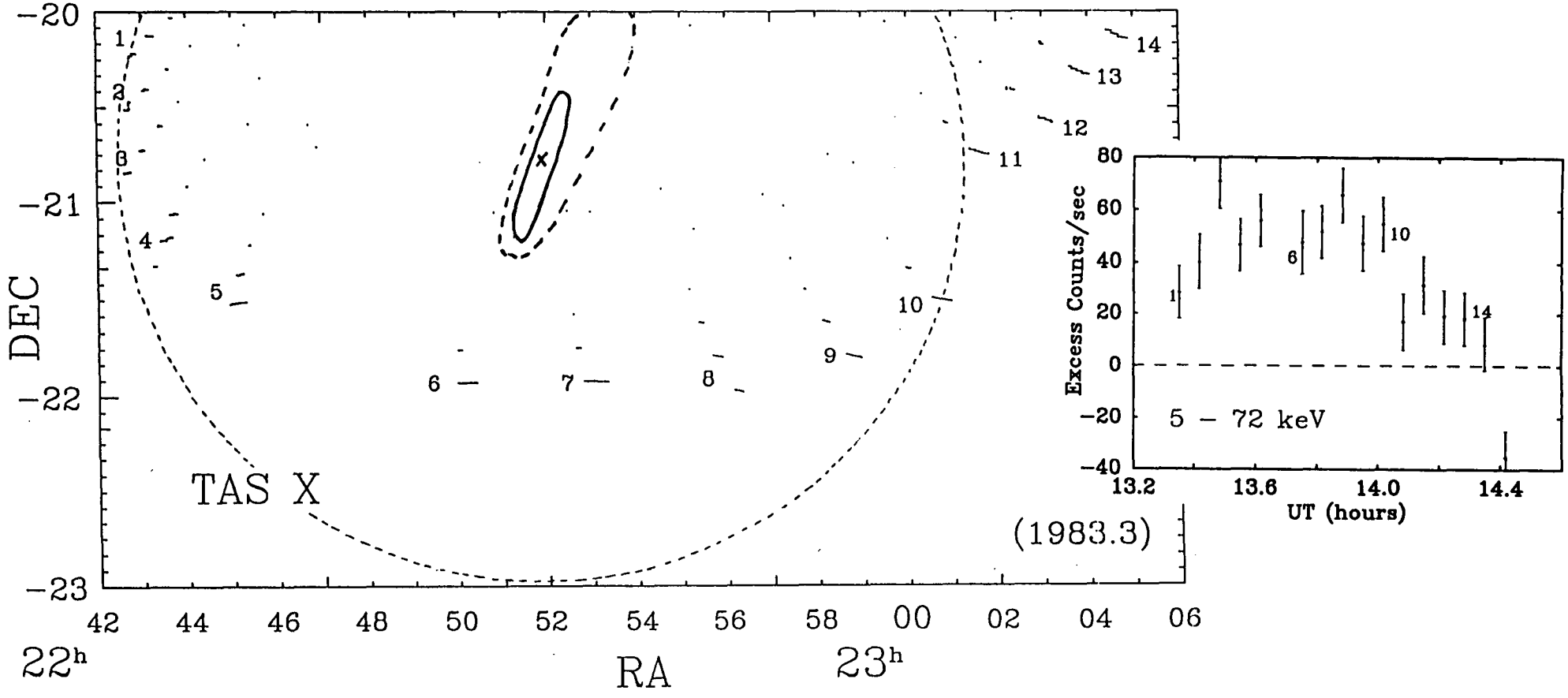

Fig 5.16 A map of the low zenith rock of the MR2251-178 observation showing the most probable position of any TAS-X. The inner region will include both rock 1 and 10 within the field of view. The insert shows the excess count rate versus time in which no corrections were applied to the counting rates.

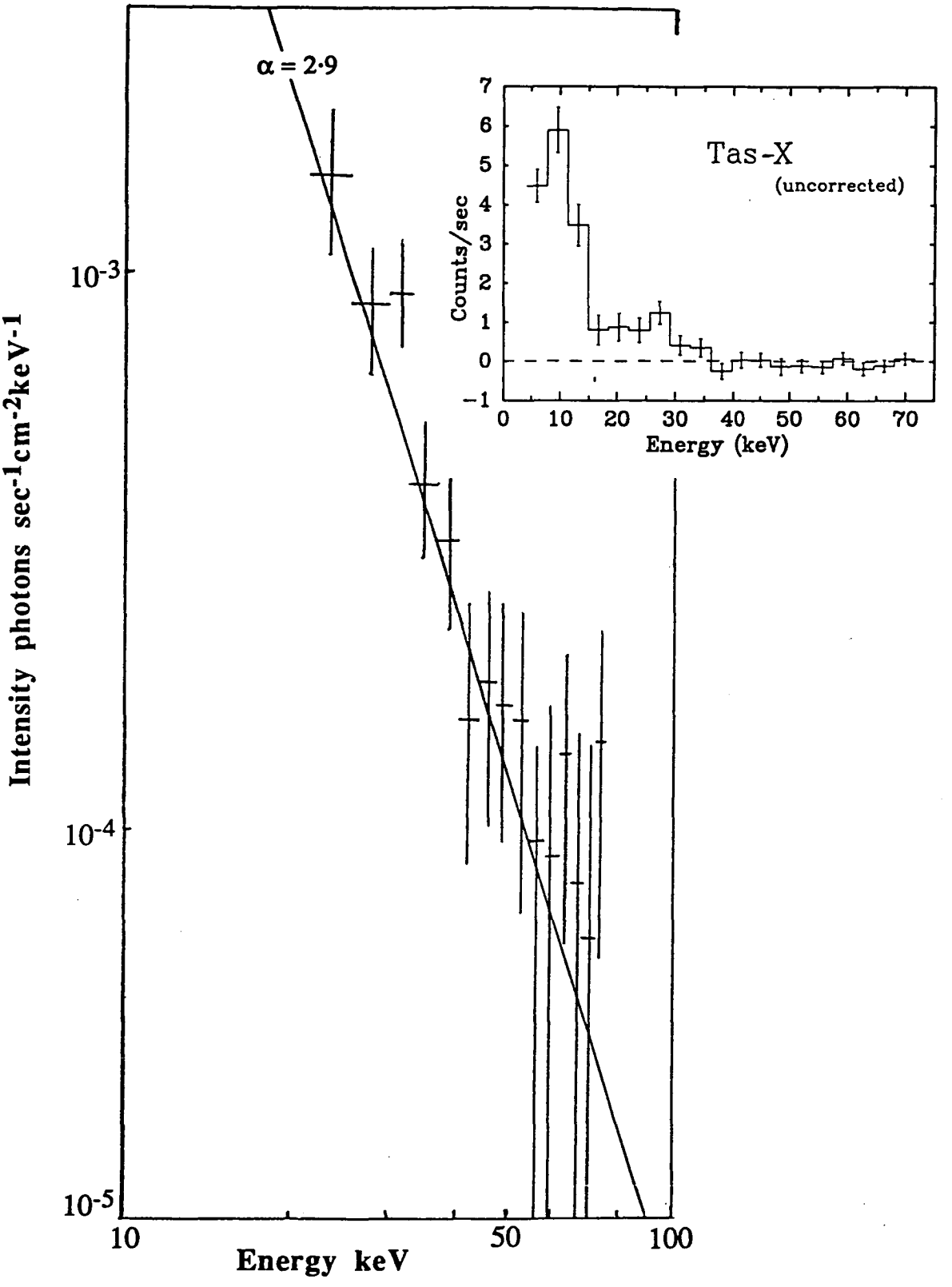

Fig 5.17 The power law model of the uncorrected PHA spectrum for TAS-X. All data below 20 keV was ignored in the model.

Although electron precipitation events can have similar spectra and durations as TAS-X they usually have a wide angular extent. This is at variance with the triangular response in zenith angle and the lack of a similar effect in the IC detector. Also they are very variable with time.

Alternatively TAS-X can be viewed as a variation in the background counting rate. Since the low energy background rate is so high the low energy excess of TAS-X can be explained by a small fractional error in the determination of the background. This is especially true considering that the background at the zenith of TAS-X (<5°) is an extrapolation from data at zenith angles between 10° and 30°. At the lowest energies the sign of the zenith angle (10°-30° range) dependence becomes negative i.e.. the low energy count rate increases with decreasing zenith angle. If the slope became even more negative at lower zenith angle (<10°) then the spectrum of TAS-X would become more reasonable.

To extend the background information to smaller zenith angles the MR2251 pointings were considered as backgrounds. There is a smooth transition between the TAS-X counts and those of MR2251 and the high rock (see Figure 5.18). When slopes of the linear 6°-10° count rate - zenith trend (see Figure 5.19) are used, most of the TAS-X excess flux is removed. There is still an excess in the lowest channels. See the PHA spectrum of Figure 5.20.

This remaining excess may be explained by noise within the detectors. The discriminators were set just above the noise threshold. So any gain changes in the amplifiers or increases in the noise level would increase the counting rate markedly. The TAS X observations could well be affected by slight gain changes brought on by the higher interference from the motors which are driving the detector fastest in azimuth at this time. Channel 1 is very unreliable. Its background count rate is lower than channel 2 which given the power law form of the background with respect to energy suggests that channel 1 is not of the same energy width as the others. The other low energy channel (2 and 3) show the strongest correlation with veto rate.

The triangular light curve of TAS X-1 is a natural consequence of the background increasing steeply toward the zenith since the detector viewing direction was transiting the meridian. TAS X-1 is brightest when the zenith angle is lowest (observation 6 of Figures 5.16 and 5.18).

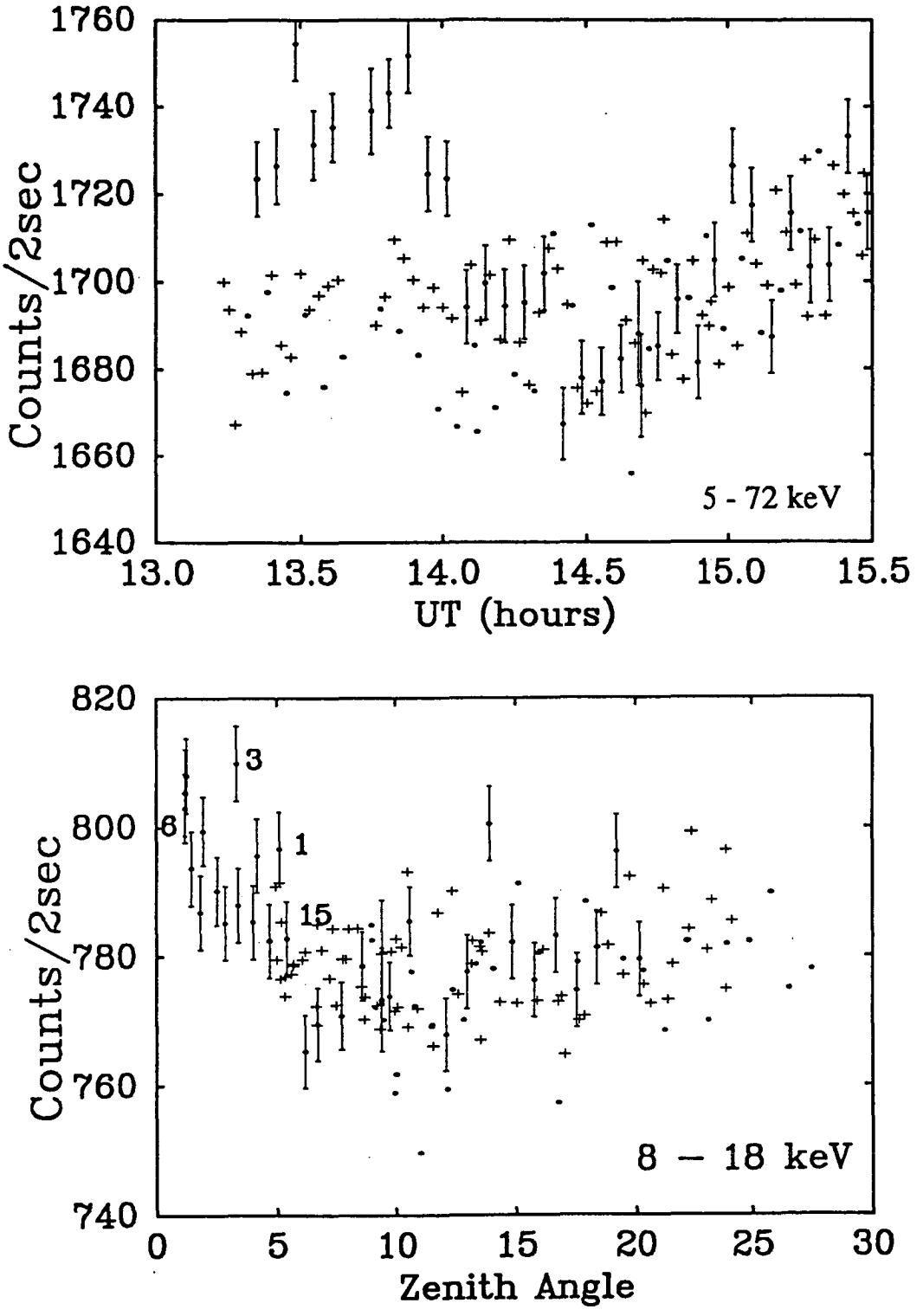

Fig 5.18 The counting rates versus time and zenith. The crosses indicate the counting rates from the MR2251-178 and high rock pointings. In the plot against zenith angle shows the MR2251 data (5°-10°) beginning to trend upward at lower zenith angles. The TAS-X data (low rock) has an approximately triangular change in zenith FWHM of ≈5° indicating a point-like source near the zenith.

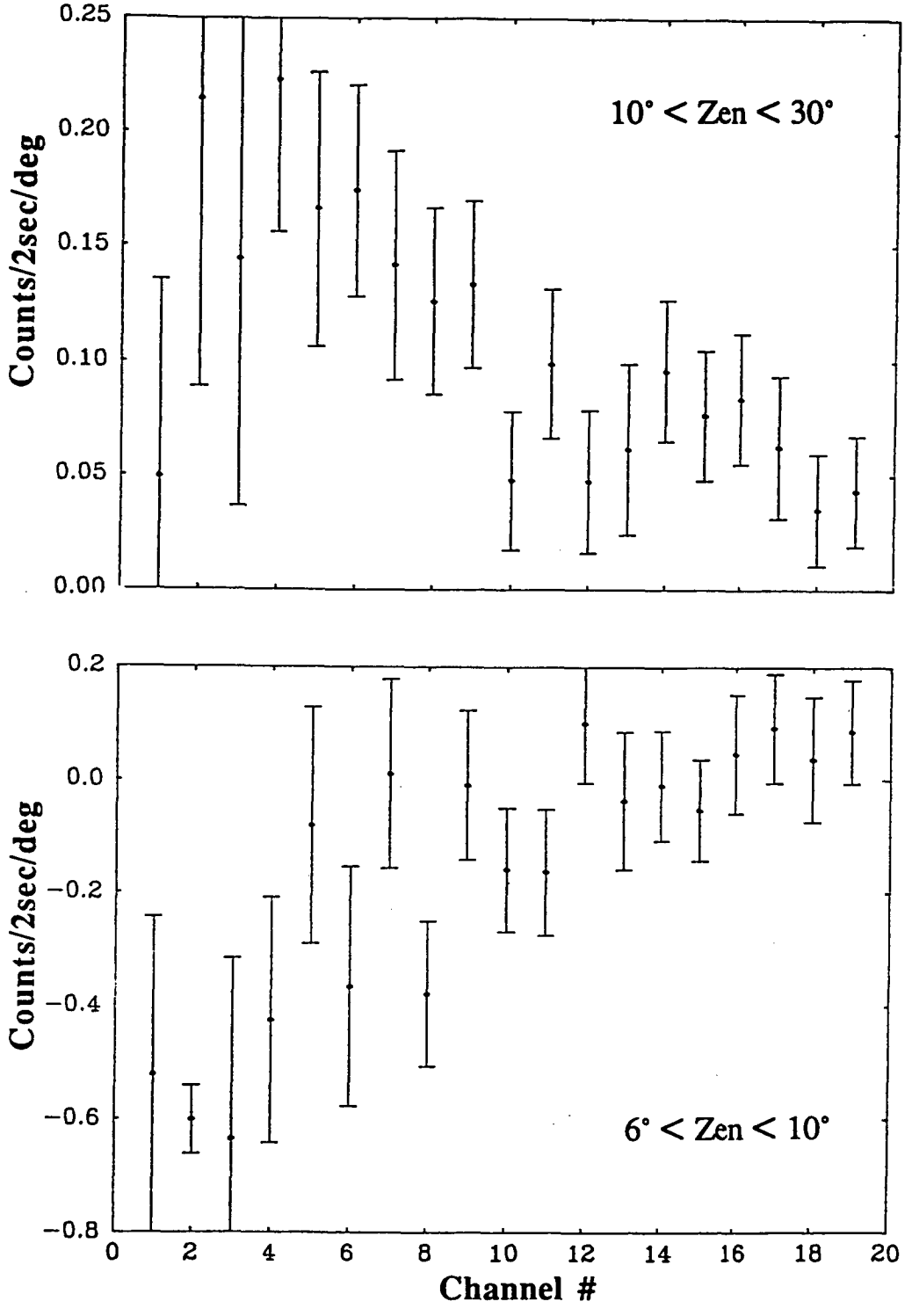

Fig 5.19 The change in zenith angle trend is illustrated by the changes in fitted slope above and below 10°. The low energy count rates change from increasing to decreasing with zenith angle.

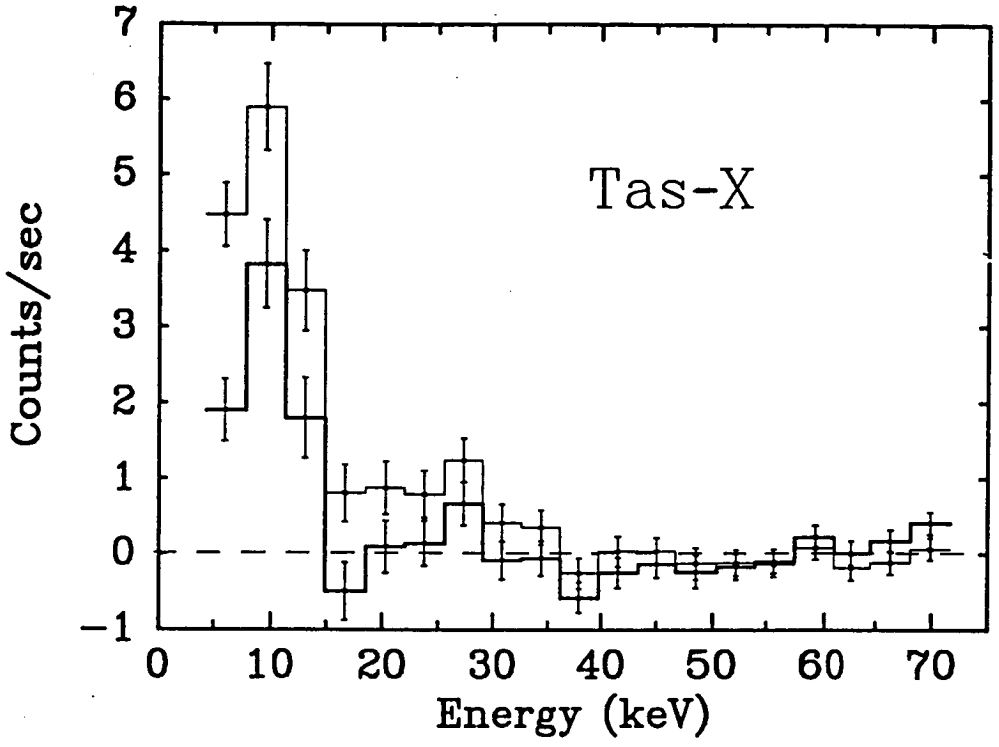

Fig 5.20 The uncorrected and corrected (using the 6°-10° slopes) PHA spectra of TAS X. When the zenith corrections are applied there is no significant excess above 15 keV. The errors are based solely upon Poisson statistics and take no account of the uncertainties introduced by the corrections.

There are two possible origins for TAS-X. It is a soft transient source near $\alpha=22^h\ 52^m$ $\delta=-20°\ 45'$ with a steep spectrum $\alpha=-2.8\pm0.7$ or a radical change in the behaviour of the background at low zenith angles would completely eliminate the need for an external source. Finally, TAS-X can possibly be explained as the X-rays from an electron precipitation event near the zenith.

5.7 Conclusion

Platform tilts were shown to have potentially a major affect upon the final pointing solution. Small tilts ($\leq 1°$) can lead to large errors in the azimuth determined using sun-sensor and to a lesser extent magnetometer navigation sensors. The co-ordinate transformations to and from the tilted reference frame were applied to the sun-sensor and 3-axis magnetometer data to arrive at an accurate aspect solution for the UTIC83 flight. The solution is not entirely unique because one inclinometer was inoperative and there were unknown levelling and offset errors.

The high background rate at low energies and its zenith angle dependence can be explained in terms of a leaky veto system. The observed east/west anisotropy in background counting rate can also be explained in the same manner.

A combination of several factors resulted in none of the targets being confidently detected. These factors were the intrinsic weakness of the sources, the generally high line of sight absorption, poor absolute pointing and the high low energy background. Sco X-1 was not well detected. Upper limits placed upon the >30 keV flux from SS433 favour power law indices ≥ 2. The MR2251-178 upper limits are not stringent enough to have any bearing upon the debate concerning the origin of the cosmic X-ray background. A source, probably SMC X-2, was detected in the Small Magellanic Cloud but with insufficient confidence to fit a spectrum. The one source confidently detected is of unknown origin. TAS-X is either a very soft (index 2.8 ± 0.7) X-ray transient near $\alpha = 22^h\ 52^m$, $\delta = -20°\ 45'$ an overhead electron precipitation event or most likely an effect of the changing background in combination with extra noise in the detector.

Chapter 6

Hard X-ray Observations of Sco X-1

If it waddles like a duck, and quacks like a duck
-then maybe it is a duck.

Sidney van den Bergh (1980)

6.1 Introduction

During the 20th November, 1986 flight two observations were made of Sco X-1; a drift scan between 3:28 and 3:45 UT and a pointed observation between 4:39 and 5:03 UT. Based upon the AIT 3-axis magnetometer data and a sun sighting made with the rotation modulation collimator an aspect solution is available during the later part of the flight. It was found, by Dr D.P.Sharma, that there was a 1.75° difference between the azimuths determined using the AIT and UT 3-axis magnetometers. This offset was approximately constant during the Sun and GX1+4 observations. Examining the drift scan count rate suggested that a 1.2° offset would match the time of maximum count rate with the expected time of transit. When this offset is applied to the drift scan the collimator corrected counts are constant. This 1.2° offset was adopted for both the drift scan and the pointed observations of Sco X-1. At present there is no satisfactory explanation for the discrepancy in azimuth. During the drift scan the peak collimator transmission was approx 75% while during the tracked observation the efficiency was 70% to 80%. The average line of sight atmospheric depth was 3.1 g/cm^2.

There are two timing regimes involved within the following data analysis. The 1 msec. data is used to search for any QPO and the frame count rates are used in the spectral analysis. The data on each time scale were analyzed over slightly different time spans which are illustrated in Figure 6.1.

6.2 Temporal Analysis

The timing problems, caused by irregularities in the X-ray data frame format, were corrected in a two step process. A FORTRAN computer program written by Dr. A.B. Giles was used to identify and correct most of the timing problems as discused in Chapter 4. However not all the timing problems were found or completely corrected. The 1 msec times were edited manually by the author. Errors included backward and forward time jumps caused by incorrect setting of the HL counter, missed clock resets, the HL counter being un-incremented after a missed frame, and the HH roll-over not being executed properly when preceded by a double event. When a frame or frames are missed the HL counter remains out of step until its next roll-over.

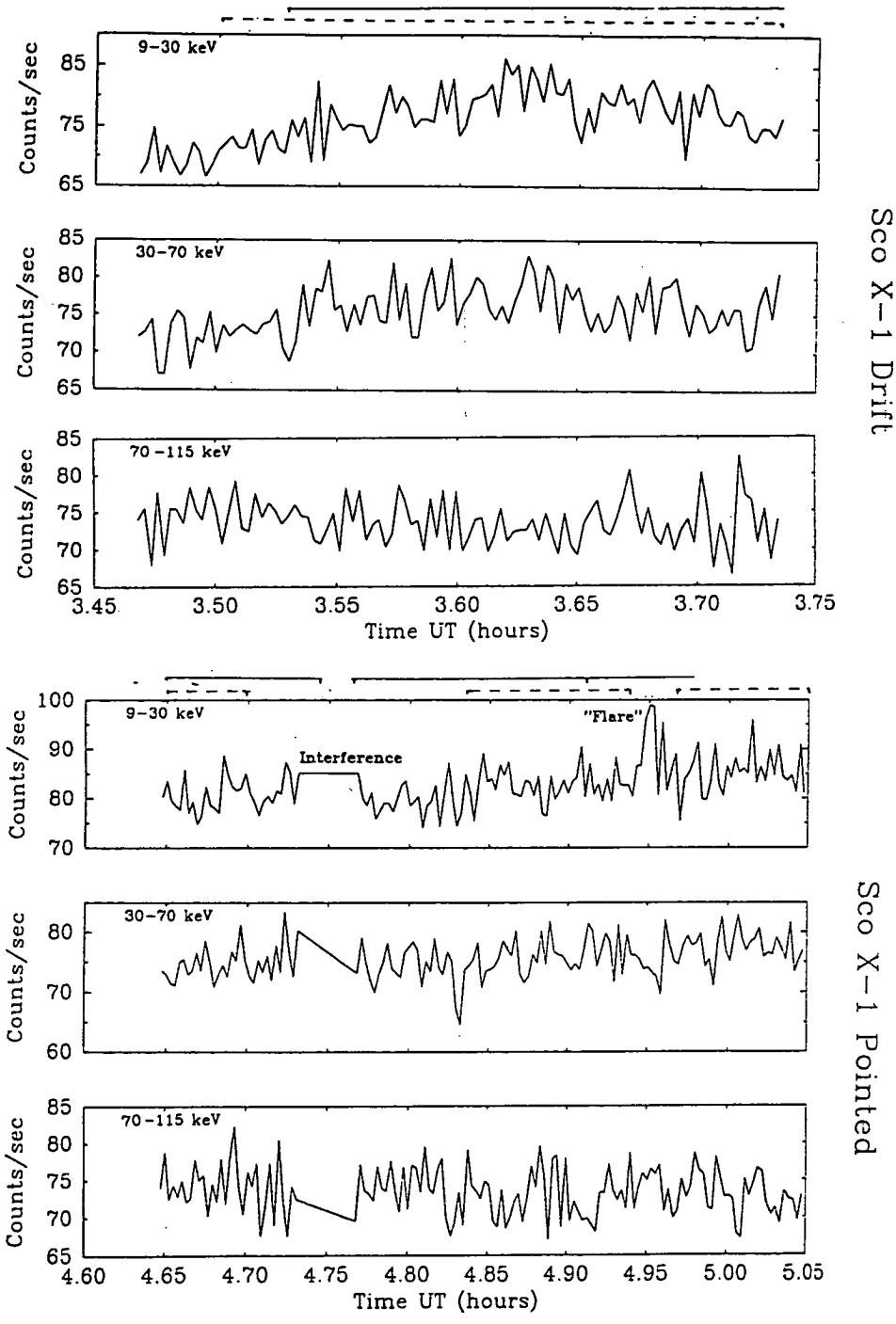

Fig 6.1 Plots of the count rate in three energy ranges during the drift and pointed observations of Sco X-1. The dashed and solid line represent the time spans of the spectral (frame rate) and timing (1 msec.) analysis respectively. The "flare is only in the lowest energy data.

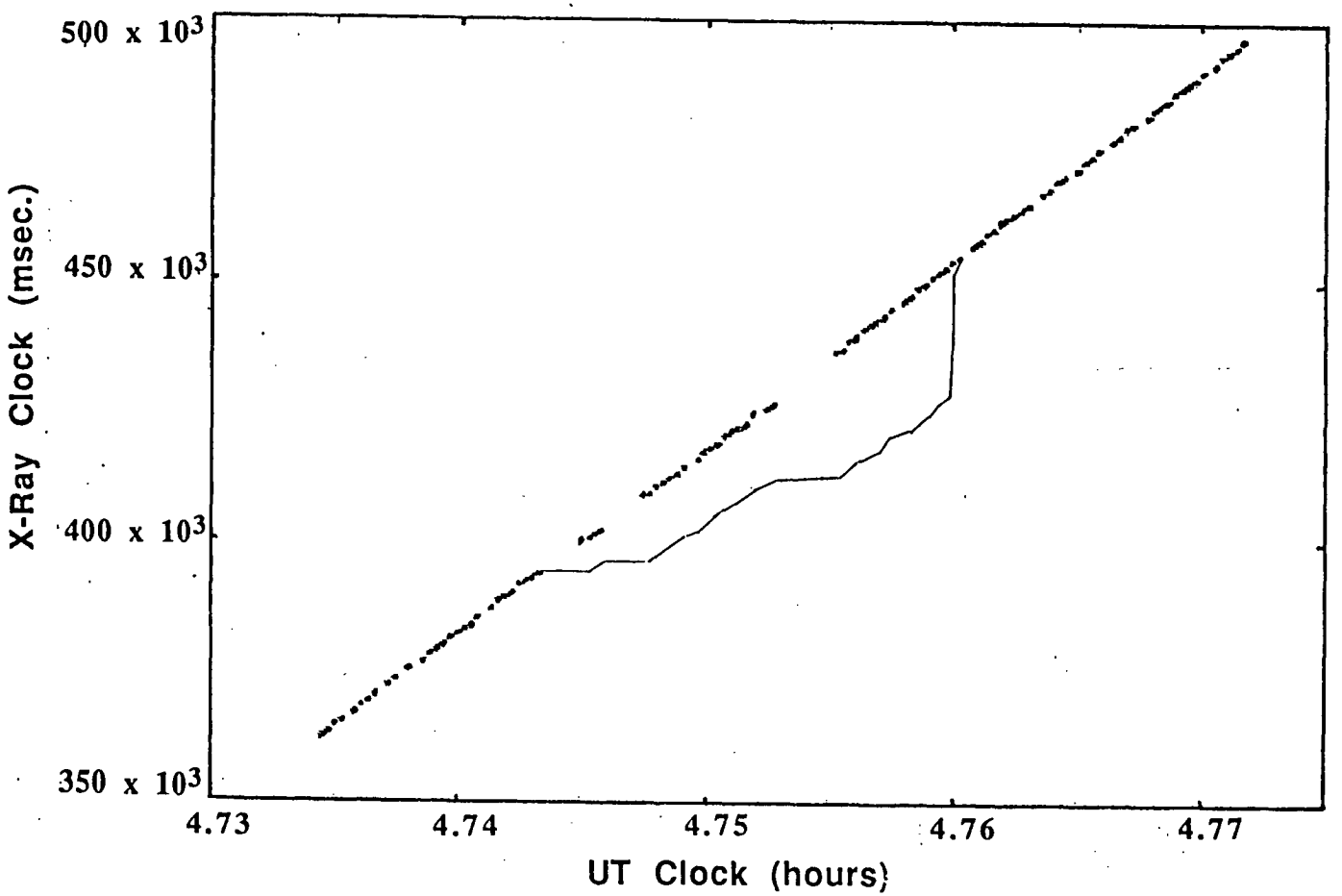

Fig 6.2 An extreme example, during a period of radio interference, of the timing errors. The fine or X-ray clock is calculated from the 1 msec arrival time data. The millisecond clock time of the first event in every new UT clock second is plotted against the UT clock time. The solid curve is the original clock data while the points are for the corrected data. In this example only the major clock errors were corrected. This section of data is not used in any subsequent analysis.

At one point, between 4:44:30 and 4:45:30 there was a series of large ~700 msec time gaps in the X-ray clock. These gaps correspond to a period where many frames were lost through radio interference. The X-ray clock times where corrected by adjusting the HH and HL counters so as to make the relation between the X-ray and UT clocks linear. The process is illustrated by Figure 6.2. This section of data was not used in either the timing or spectral analysis.

6.2.1 Overflow Effects

After correction for the timing problems the data consists of a series of arrival times with irregularly occurring gaps of variable length. These gaps are missing frames. Usually two frames are missed, resulting in a time gap of approximately 190 msec; each frame being about 96.56 milliseconds long. There are other gaps due to bad clock resets and short gaps (<64millisec) caused by the overflow of the data frame. Once during the flight the on-board UT clock and apparently all micro-processors stopped for about 15 minutes.

Overflows do not occur in every frame but do have an underlying periodicity. This frame period is expected to be slightly variable because of a combination of variable number of extra bits inserted between frames and the irregular filling of the telemetry processor stack before transmission.

Initially the fast Fourier transform (FFT) algorithm was used to analyze the data. The FFT requires evenly spaced data with 2^n points per transform. Between each large (>64msec) time gap in the data stream the arrival times were binned into evenly spaced continuous bins. This forms a block of data. A series of contiguous sets of FFT's were performed on each data block. When the data block did not consist of a whole number of FFT segments the remaining data was ignored. This procedure was repeated for each data block. All the normalized power spectra were then averaged together.

The normalization of Leahy et al. (1983) was used. In this normalization the powers are χ^2 distributed with 2MW (M = number of spectra averaged, W=number of powers averaged together) degrees of freedom and a mean of 2. This is true for many sorts of counting statistics.

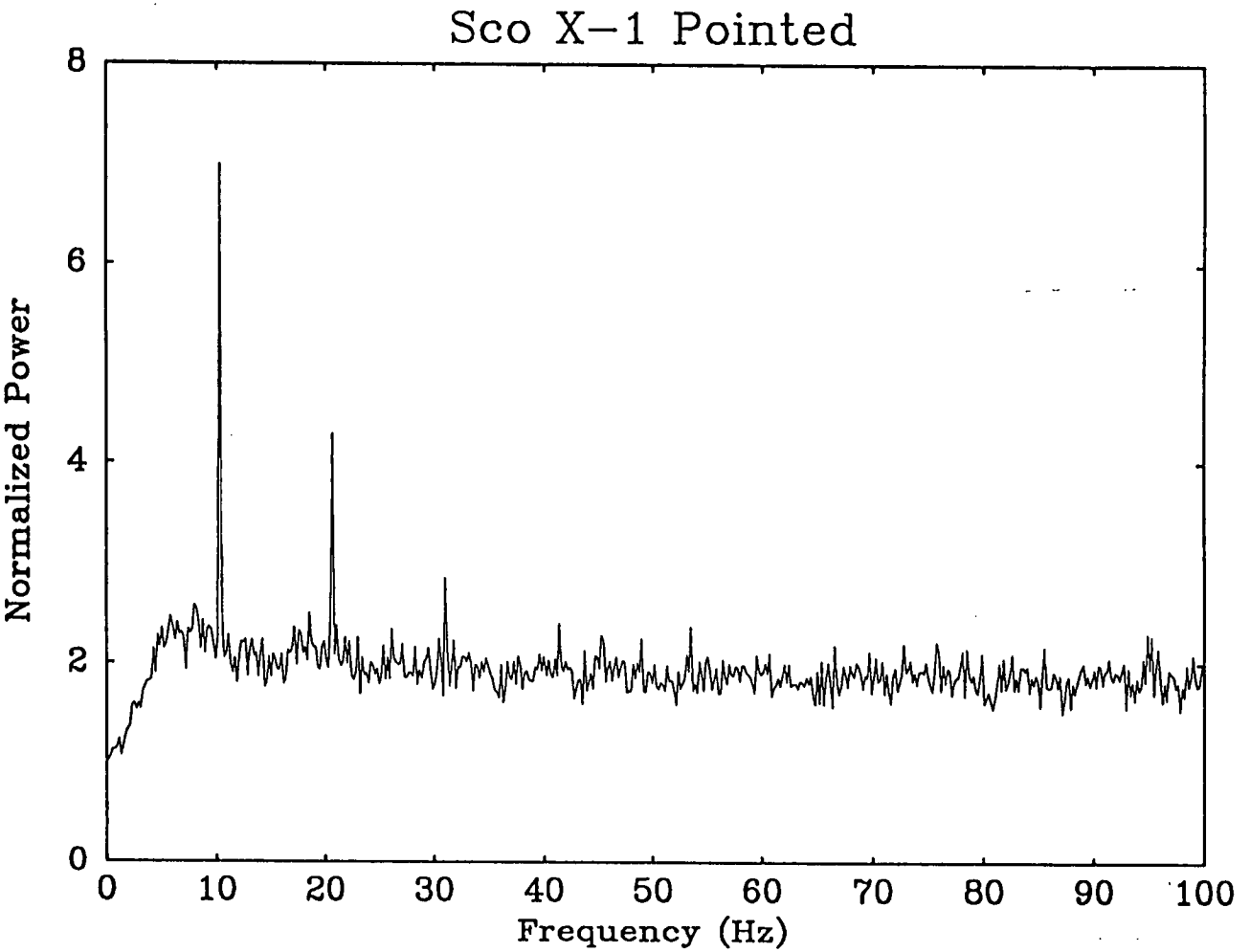

Fig 6.3 The FFT power spectrum of the Sco X-1 pointed observation. The sharp peaks are at the frame period and its harmonics. The low frequency drop off and peak near 6Hz are also visible in background power spectra.

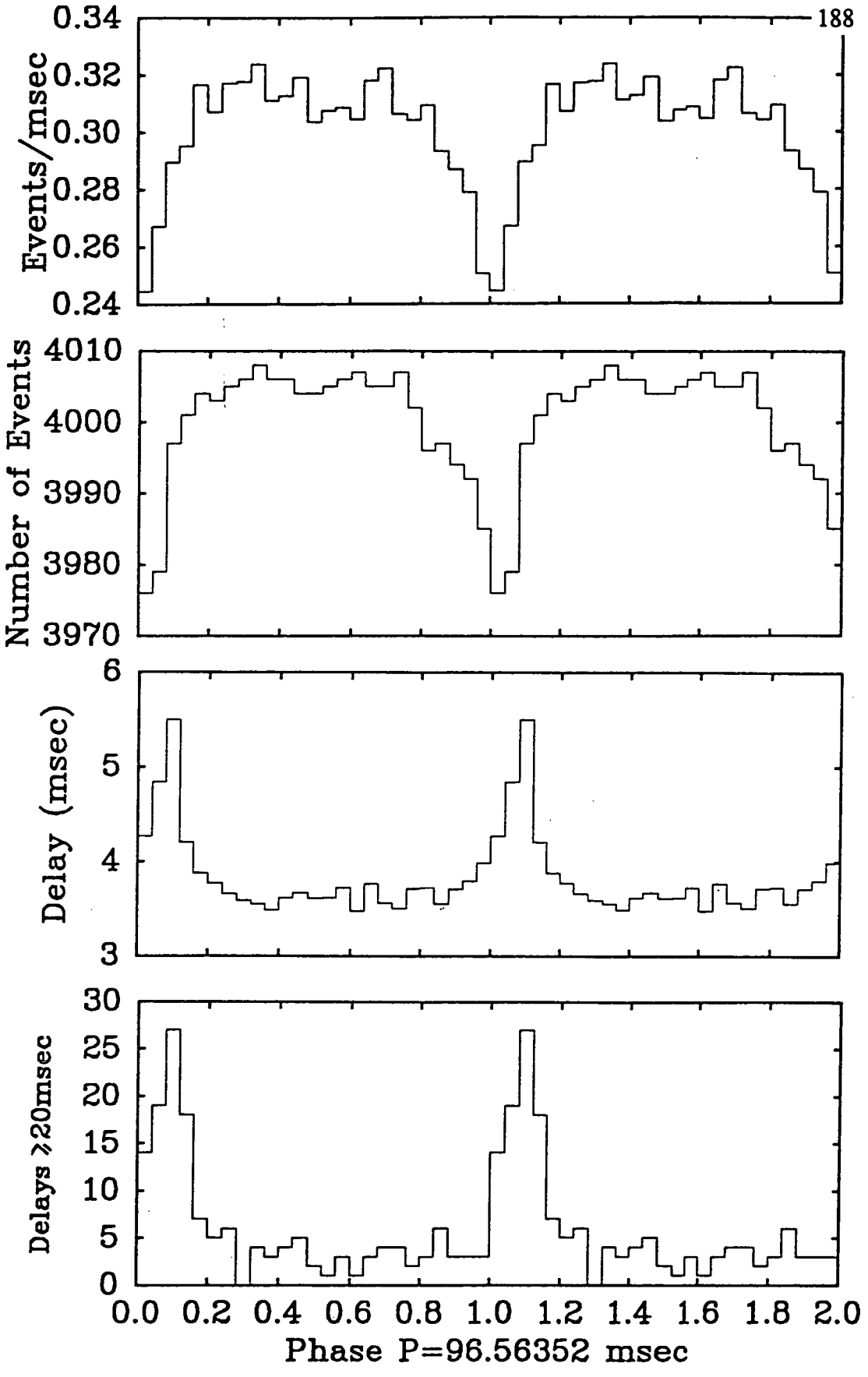

Fig 6.4 The modulation with frame period of the count rate, number of events, average delay between successive events and the number of delays greater than 20 msec. The number of long waiting times is greater than that of Poisson distributed counts.

Figure 6.3 shows the power spectrum of a Sco X-1 observation. Similar features are seen in the power spectra of the background observations. There are several notable features. The spikes are at the data frame frequency. The period is refined using the Q method. When the data is phase folded on this period a 3% modulation in the count rate is seen (Figure 6.4a). This modulation is apparent at all energies and for all types of events i.e. doubles or singles. The modulation is actually in the number of events recorded i.e. there are fewer events at the end/beginning of each frame (Figure 6.4b). The average time between events (waiting time) is also modulated. This is due to an increase in the number of long (>20msec) waiting times at the frame boundaries (Figure 6.4c). The number of these long waiting times are much higher than expected from a Poisson distribution.

This modulation at the frame period suggests the frequent overflow of the data frame. By checking the frame by frame overflow counter it was found that 25% of frames overflowed. The X-ray byte overflow counter was not reliable because of frame roll-over problems. When a frame is full the excess counts are generally not placed in the next frame but are lost. This produces a time gap until the first event of the next frame is recorded. When the data is binned this gap is filled with zero count bins, thus reducing the average count rate when the counts are phase folded with the frame period.

Not all frames overflow and the degree of overflow is variable ; explaining the slow drop off in average count rate (Figure 6.4a). A variable number of flags are sent between each frame causing an uncertainty in the beginning of each frame and changes in frame period. This is in addition to the uncertainty due to roll over of events from one frame to the next even when the frame is not completely filled. Also the random nature of the arrival of the X-rays produces a few millisecond uncertainty in the beginning time of each frame. Phase jitter causes some of the gaps to fall at phases other than zero.

Data frame overflows explain the non-Poisson distribution of the waiting times by adding longer, 20 to <64 msec , time delays between successive events at the end of the overflowed frames. A delay of 64 msec or longer would be produced by a skipped HL counter update and as such would be corrected either by the software of Dr. A. Giles or interactively by the author. Gaps longer than 96 msec are caused by missed frames.

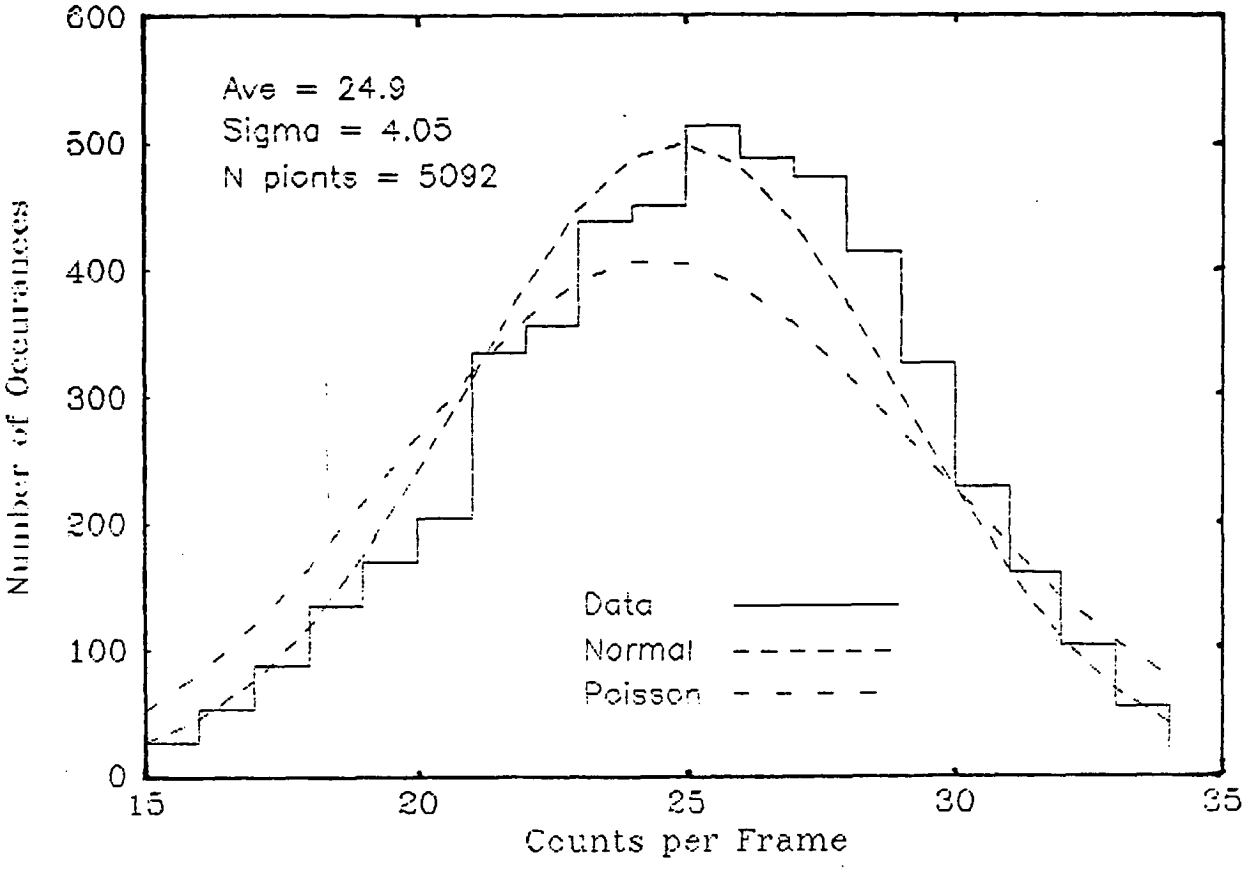

Fig 6.5 The count rate frequency histogram for the galactic centre background data. The Poisson and Normal curve have the same mean, standard deviation, and total number of points as the original data. When the data is corrected for the effects of frame overflows the count rate distribution is Normal/Poisson.

The frame count rates are not Poisson distributed. There are not enough high count rates and too many medium count rates (Figure 6.5). This distortion can be explained in terms of frame overflows. When an overflow occurs (preferentially at high count rates) the extra events are lost and so the the output count rate is lower than it should have been. This changes the average count rate and modifies any input modulation.

When overflows start to become important the input signal becomes smoothed on time scales greater than the frame period causing the low frequency drop off in observed power spectrum. As an example consider a steadily increasing input signal. The output count rate will reach a maximum count rate where all frames are full.

To check the conclusion that the distortions in the power spectrum are caused by overflow gaps, FFT's were performed upon individual frames. A single 64 point FFT could be performed on each frame. The first and last three events were ignored. The average power spectrum over the range 0-500hz showed no drop in the low frequencies i.e. in the first power value. This method is unsuitable for searching for QPO's because of the very poor frequency resolution (32 frequency bins covering 500 Hz).

6.2.2 The use of the Discrete Fourier Transform

Quasi periodic oscillations from Sco X-1 have been observed in the range 5.5 to 30 Hz. In the quiescent state the QPO have a central frequency near 6Hz. This is just the region most affected by the data frame overflows. There are two possible ways dealing with the overflow effects upon the power spectra.

The first method used was to divide the source power spectrum by the power spectrum of a background observation. The resulting ratios should follow the F-distribution since both power spectra are expected to be χ^2 distributed. A QPO in the source will produce a deviation from the expected F-distribution which can be detected with the Kolmogorov-Smirnov (K-S) test. This method was initially used and found practicable.However, it was not used extensively since it adds the noise of both the source and backgrounds together.

The second approach is to use the discrete Fourier transform directly. The Kurtz (1985) algorithm is used with the Leahy normalization. This normalization is used

instead of that of Scargle for two reasons. The Kurtz algorithm is computationally faster and yields (in the absence of a signal) powers that are χ^2 distributed from which upper limits can be obtained relatively simply. This method has the advantage of only involving the noise of the source spectrum.

As discussed in section 3.3.3.2 the concept of the Nyquist frequency and optimal frequency sampling is rather ill defined. Since most of the present data is evenly sampled, the Nyquist frequency can be safely set at ν_{max}=500 Hz (1 msec integrations) and the finest frequency sampling at $\tau=1/\delta T$. Such fine frequency resolution is generally not required in a search for QPO, further assuring the independence of individual power estimates.

Referring back to Figure 6.4 there is a gradual drop in the mean count rate toward the end of the frame. This is caused mainly by a combination of two effects. The frame period is variable. There is uncertainty in the assignment of the beginning and end events. The last event may be assigned to the beginning of the next frame and the first event may be assigned to the previous frame. This ambiguity is most prevalent when the frames are full which is when overflows are most prevalent. If an overflow occurs the time gap caused may be put near the end of the overflowed frame or the beginning of the next frame. The latter is generally the option used in the data correction software of Dr Giles. In order to assure that the data used for the DFT has exponentially distributed waiting times, and hence assure that the final powers are χ^2 distributed, the beginning and ends of the frames must be avoided. This can be done by selecting data according to the phase of the frame period. In the case of Figure 6.4 the phase range 0.3 to 0.8 is unaffected by overflows as evidenced by the constant event rate etc. within this phase interval..

6.2.3 Frame Period History

To find the phase range unaffected by overflows the frame period must be known accurately. Folding the data upon an average frame period showed slow drifts is the phase of the frame beginning (e.g. the sharp rise of Figure 6.4a) this indicates that the frame period is not constant. Initially the Q method was used to find the frame period for successive one minute sections of data. The frame period was found to vary between 96.54 and 96.62 msec (Figure 6.6). Shorter time scale changes in the frame period were suspected but because of poor statistics the Q method could not be used on data sections shorter than a minute. Also with shorter

data runs the Q period peak becomes wider making estimations of the period more uncertain. An improved frame period history allows a wider phase range to be selected for temporal analysis. An attempt was made to check the accuracy of the X-ray clock and to improve the knowledge of any period changes in the frame period. This was done by comparing the X-ray clock against both the UT clock and a frame counter.

The X-ray clock's time was found at each second roll over of the UT clock. A straight line fit to these times yielded a slope of 0.9998±0.002, indicating that the two clocks were running at the same rate. The expected one to one (slope =1) relation was then removed and the residuals examined. A regular pattern of disjoint lines was was found. This pattern is caused by having nearly 10 frames per second. The few interruption to this pattern are due to either missed UT clock updates or missed frames. None occur at places where major corrections were made to the X-ray clock.

A frame counter was constructed from the frame identifier in the housekeeping data which regularly cycles from 0 to 15. Missed frames result in a break in this sequence of the frame identifier and so can also be counted. There is an approximate straight line relation between this frame counter and the X-ray clock time at the beginning of each frame. However the fit is improved by higher order fits. When a linear trend (slope frame period and intercept offset time) is removed the residuals fall into straight line segments as in Figure 6.7a. Each segment corresponds to a different frame period while the scatter is explained by the random arrival times of individual X-ray events and the gaps caused by frame overflows. This succession of different periods causes the drifts seen in the phase folding.

Each linear segment was fitted separately for frame period and offset. The resulting frame periods and offsets are listed in Table 6.1. The start time offsets are generally small and can be explained by the mis-allocation of the first events in the frame and the random arrival of the first X-ray. However, there is one offset of 20 msec with no corresponding anomaly (bad data or complicated X-ray clock correction) in the timing. Such a large offset is unlikely (the probability of an arrival time $\geq$ 20 msec when the mean delay is 3.5 msec is 3.2×10^{-3}) and so implies that there is, despite the effort expended in cleaning the data, still some doubt whether the millisecond time scale data is totally reliable. This reduces the value of any coherent periodicity search.

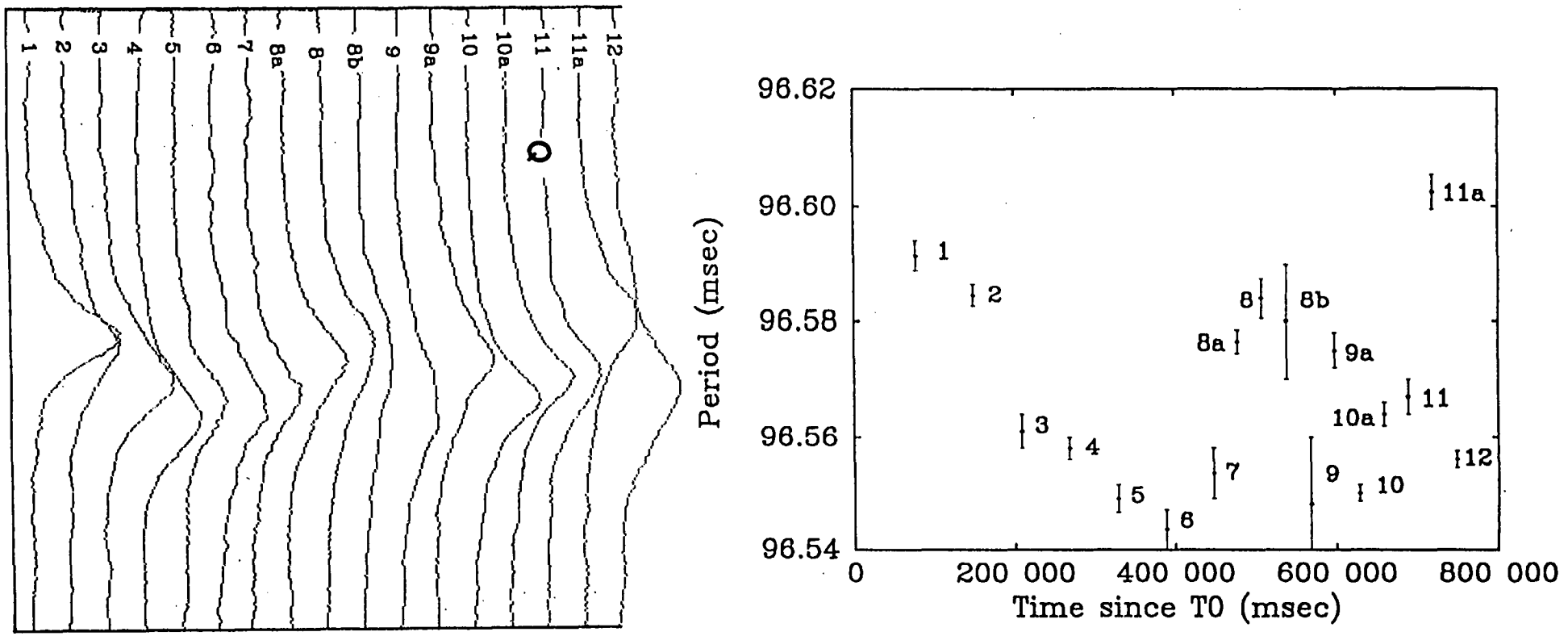

Fig 6.6 On the left is a set of stacked periodograms for successive 1 minute data sections.The Q method was used to calculate the periodograms. On the right is a plot of the period estimated from the peaks of the periodograms. The error bars are estimates of the uncertainty in estimating the position of the peaks.

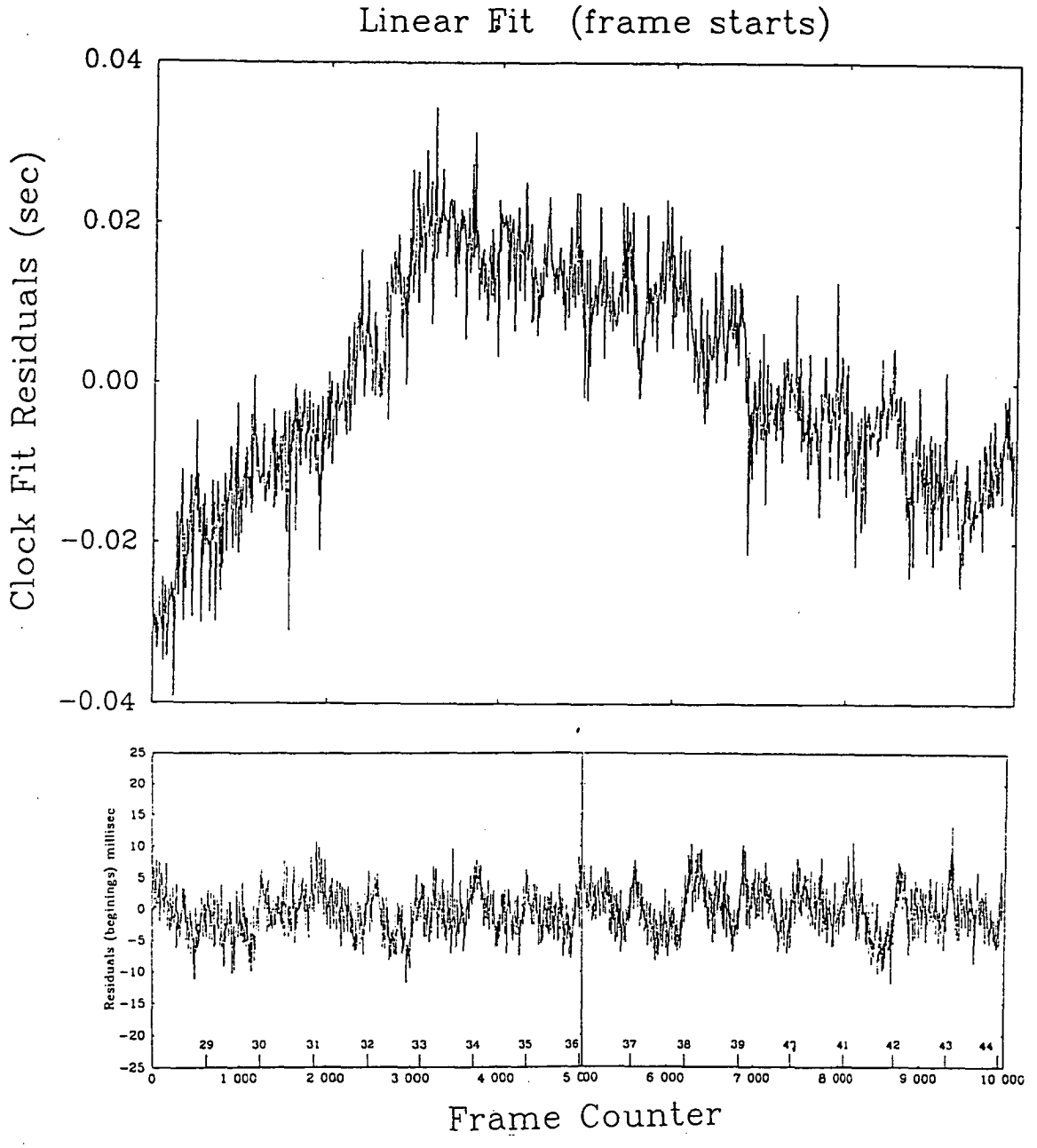

Fig 6.7 (a) The residuals of a linear, constant frame period, fit between the UT clock and the millisecond start times of each frame. **(b)** The residuals when discretely varying frame periods and frame offsets are used as the clock fitting function.

Table 6.1

T_0 (msec)	Offset (msec)	Period (msec)
Sco X-1 Drift Scan	Start time = 58745. msec	
58745.	2.8 ± 0.3	96.5497 ± 0.0004
349061.5	−5.6 ± 0.5	96.5665 ± 0.0002
715149.	−2.1 ± 0.7	96.5684 ± 0.0005
966520.	1.3 ± 0.1	96.5471 ± 0.0004
Sco X-1 Pointed	Start Time = 38085 msec	
38090.	4.7 ± 0.5	96.5882 ± 0.0004
182030.	1.1 ± 0.6	96.5560 ± 0.0020
230489.	6.9 ± 0.4	96.5378 ± 0.0007
331853.	−1.7 ± 0.4	96.5761 ± 0.0015
380136.	−4.0 ± 0.5	96.5445 ± 0.0026
438075.	4.8 ± 0.5	96.5476 ± 0.0023
471873.	3.1 ± 0.5	96.5661 ± 0.0020
510499.	−0.2 ± 0.5	96.6082 ± 0.0023
558783.	4.1 ± 0.4	96.5508 ± 0.0022
592585.	4.1 ± 0.4	96.5526 ± 0.0012
650517.	−0.9 ± 0.4	96.5679 ± 0.0009
718126.	20.0 ± 0.6	96.5593 ± 0.0016
GX 1+4 Background	Start Time = 3545 msec	
3538.	6.8 ± 0.4	96.5200 ± 0.0006
119374.	0.8 ± 0.5	96.5158 ± 0.0020
172465.	5.0 ± 0.5	96.5405 ± 0.0015
230400.	8.5 ± 0.4	96.5530 ± 0.0005

When a changing frame period is used to fold the event times the overflow modulation is more pronounced. As expected there is no general phase drift in the overflow affected phases. Also the phase jitter is reduced to about $\lesssim$0.2 phase or 20 milliseconds.

6.3 Results: Power Spectrum Analysis

The energy range over which data was selected for temporal analysis was restricted to channels 5 to 38 inclusive.(~20 to 42 keV. One channel is 30/32 (0.937) keV in width. In this range there was significant, $\geq 1\ \sigma$, excess counts in each channel. The detector has a low energy threshold near 20 keV since all counts below ~20 keV are either due to escape or resolution smearing. The analysis of the drift scan was limited to between 3:32 and 4:42 UT (SCD). During this period the collimator transmission was greater than 40%. The pointed observation was split into three sections SCP1 (3:39 to 3:44:30), SCP2a (4:45:39 to 4:55:00) and SCP2b (4:55 to 4:58 UT). Between SCP1 and SCP2a there was radio interference. The SCP2b data is at a generally higher count rate including an anomalous flare-like event. For each of these files the arrival times were binned into either 1 or 5 msec bins. The fitted frame period was used to select data unaffected by overflows and the binning was stopped and restarted at each frame change. The 1 msec bins were Fourier transformed using the DFT of Kurtz with the Leahy normalization using 2048, 4096 and 8192 data points per transform. Similarly, the 5 msec data was transformed in 1024, 2048 and 4096 point blocks.

The power spectrum of each data block was put into a frequency time image. The images for each section of data were examined visually for any transient QPO or LFN. None was seen. In none of the section's average power spectra was there any obvious QPO and only the SCP2b 8196 point transform showed any sign of VLFN in its power spectrum. The average power spectra, from each data section, were then combined by making a weighted (by number of individual spectra) average. A total spectrum for the pointed observation (SCP) and for the whole data set (SCPD) were formed. Neither showed any obvious QPO or red noise.

All the power spectra had a mean power level less than two. The average power level is $\bar{P}$=1.97. The UT2 detector can only detect at most 2 events per sample bin and so the dead time case of Equation 3.19 holds. Using Equation 3.19 with

$\mu=8.5x10^{-2}$ cts/msec the expected power level is about 1.83. Also the detector suffers from a constant dead time after the detection of an event. The dead time form of Equation 2.17 holds. The resulting form of the power spectrum (Weisskopf as referenced by van der Klis 1988) can be approximated (low frequency and small dead time) by

$$<P_{j,noise}> = 2(1-\mu*T_{dead})^2 \qquad 6.8$$

With T_{dead} = 100microsec, total count rate 250 cts/sec the expectation power level is 1.90. The observed mean power level falls between the above two estimates. Thus it seems that the interaction of the two dead time effects produces an intermediate mean power level in the presence of white noise. When the data are replaced by artificial Poisson distributed counts the mean power level is very near 2. The generated counts do not suffer from dead time. Thus the lower than two mean power level is not an artifact of the processing but is due to the dead time of detector. As a further check power spectra were formed from the GX 1+4 background observation. This showed a mean power level of 1.98 which is similar to the Sco X-1 mean power level. When testing the powers against the expected χ^2 distribution the power spectrum is rescaled so that the high frequency (>50Hz) mean power becomes two.

6.3.1 QPO Search

The power spectra were subjected to the sign and runs test over the range 0-50 Hz. Both these, test the mean. It was found that these tests were not as reliable as the Kolmogorov-Smirnov (K-S) test because the distribution of powers is basically non-normal with the mean is higher than the mode. As a consequence there are always more powers and runs below the mean than above.

The Kolmogorov-Smirnov test was applied to all the power spectra. All passed at the 95% level indicating that they follow the expected χ^2 distribution and so there was no QPO.

The method of Mereghetti et al. (1987) was then used over the frequency range 2-90 Hz. Several possible features were detected at 17.5 Hz (SCP2 4096 point), 23 Hz (SCP1 2048 point) and 50-53 Hz (SCP2 4096 point, SCD 2048 point) with 95% confidence. However, none of these features where found in both the 4096

and 2048 point transforms. The frequency binning method also detected several peaks i.e. at 86 Hz (SCPD , SCDA 4096 point), 49 Hz (SCP3 4096 point), 5.6 Hz (SCD 4096 point) and 4.4 Hz (SCP2 4096). None of these peaks were detected in the corresponding 2048 point transforms. Since no consistent peak could be found, these detections should be considered as borderline. Similar behaviour was noted in the search for optical QPO, where peaks were found in the comparison star data (see Chapter 7).

To test the sensitivity of the searches three sets of different sized Lorentzian peaks were added to the power spectra. The sets of peaks were at 6Hz 1Hz FWHM, 10 Hz 2Hz FWHM and a 15 Hz 5Hz FWHM. These are typical of the properties of QPO's during the quiescent, intermediate and flaring branches respectively. The new power spectra were searched as above. The upper limit was set by the size of the smallest peak detected. The area is converted to an rms percentage using Equation 3.32 and then into a fraction of the source flux. In all cases the central frequency was put in the worst possible position i.e. half way between two adjacent sample frequencies. When a signal falls between two frequency samples the power is spread between the two adjacent frequencies, reducing the signal power's height. By putting the test frequency between sample frequencies the most conservative upper limits are thus set.

Different block length Fourier Transforms were approximately equally sensitive to the intermediate and flaring branch peaks. The 4096 point transforms were more sensitive to the narrow 6 Hz test peaks, than either the 2048 or 8196 point transforms. This results from a better combination of frequency spacing and the number of individual spectra averaged together for each data section.

The upper limits of the different power spectra are given in Table 6.2. In summary an upper limit of between 2.2 - 2.8 %rms is set for individual data sections for any 6 Hz QPO. In the combined files the limit is 1.4%rms. Comparing these limits with previously observed 4-5% rms sizes and bearing in mind that the QPO/LFN spectrum is harder than the time constant spectrum, suggest that Sco X-1 was not in the 6Hz quiescent mode. The flaring branch limits of 0.76% to 1.6% for the individual data sections are well below the 5-10% rms values observed by EXOSAT. Therefore it is reasonable to suggest that Sco X-1 was not in its flaring state. The intermediate branch limits are between 1.8 and 2.4%rms for individual files and <1.3% in the combined files. These limits are comparable to the lowest

previously observed levels (3.5-7%rms). Intermediate branch QPO are not ruled out because of their rapid, <10min, time variations in frequency.

Table 6.2

File	Time UT (hours)	I_{mean} cts/sec	N_{spect}	Upper Limits (%rms) NB	IB	FB
SCD	3.53 - 3.7	82.37	60	2.72	2.02	1.28
SCP1	4.65 - 4.7416	85.34	37	*1.19	1.08	0.69
SCP2a	4.7608 - 4.9166	86.28	65	2.23	1.37	0.79
SCP2b	4.9166 - 4.95*	91.05	24	2.19	1.83	1.20
SCP2	SCP2a + SCP2b	87.58	89	1.03	1.07	0.76
SCP	SCP1 + SCP2	86.92	136	1.89	1.34	0.77
SCPD	SCD + SCP	85.45	196	1.40	1.15	1.15

Background level is 70.2218 cts/sec. 4096 point FFT are used. The frame period phases selected were [0.14-0.7] for SCD and SCP1 and [0.11-0.76] for SCP2a and SCP2b. * The upper limits with 2048 ptoint FFT are NB: 1.94, IB: 1.28, FB: 0.34 %rms.

An alternative possibility is to suppose that the spectrum of the QPO is strongly energy dependent. The inferred spectrum would need to be unusual. At energies below about 20keV the relative amplitude of the QPO increases with energy. There is an approximate doubling in strength between the 0.7-4.65keV and 4.65-17.5 keV bands (Priedhorsky et al. 1986, and van der Klis et al. 1987). To be compatible with our observations the spectrum of the QPO would need to drop very rapidly above 20 keV. The overall spectrum would then have a peak near 20 keV.

6.3.2 Coherent Pulsation Search

The pointed observation data sections were also searched for regular, coherent signals. The energy range ≈20 to 42 keV (5-38 channels) was searched over the

100 to 500 Hz range using the discrete Fourier transform algorithm of Kurtz (1985) and the normalization of Leahy et al. (1983). The power spectrum below about 20 Hz showed a large number of high powers. The height of the power spikes decreased with frequency. This power was not the smooth decreasing continuum expected form red noise. This noise is possibly caused by the variable frame period. All higher frequency power spectra were found to be χ^2 distributed and so are considered to be reliable. Detection thresholds were set using the methodology of Chapter 3.3 for each data section. No peaks exceeded the detection thresholds (P_{detect}). Upper limit powers were then set (P_{ul}) and converted to rms percentages of the total and source fluxes. In each 100 Hz frequency span these upper limits were corrected for the smoothing effect of the binning as per Equation 3.18. These upper limits are summarized in Table 6.3. Over the entire 100-500 Hz range only light constraints can be placed upon any coherent signal.

TABLE 6.3

	Normal Mode Search		*Gated Mode Search	
Frequency Range (Hz)	SCP1	SCP2	SCP1	SCP2
100 - 200	6.93	4.41	3.76	2.63
200 - 300	7.46	5.02	4.21	2.01
300 - 400	8.23	5.46	4.52	1.97
400 - 500	9.96	6.59	5.47	2.05
100 - 500	7.73	6.30	4.46	3.13
338 - 344	6.94	3.41 (1)	2.94 (2)	2.42 (3)

(*) All limits and detection percentages are of total count rate BGD + Source. In gated mode there was no significant detection of Sco X-1 between 20 and 40 Hz. Values are corrected for frequency binning.

(1) 99% confidence level detection at 339.394 Hz (2.946 msec).

(2) 95% confidence level detection at 343.225 Hz (2.914 msec).

(3) 99% confidence level detection at 342.526 Hz (2.919 msec).

The frequency range was restricted to 338-344 Hz as done by Hasinger and van der Klis (1987). This range encompasses any orbital Doppler shift of the 2.93 msec period initially reported by Leahy (1987b) (see Damle et al. 1989 for a more comprehensive description of the data). No periodic signal (95% confidence) was detected during the SCP1 data segment. The corresponding 95% confidence upper limit is 5.7%rms of flux from Sco X-1 . A signal (99% confidence) was detected in the SCP2 data set at a frequency of 339.394 Hz (2.946 msec). The excess power corresponds to 3.4%rms (99% confidence) of the ~20-36.5 keV flux from Sco X-1. Several tests need to be carried out to confirm this period. These include a period search of the drift scan data, phase folding different sections of data and applying different period search methods. These tests which will require a substantial amount of programing and data processing have not yet been carried out because the above results were found while the author was writing this thesis.

A search was made using only the fluorescent double events arrival times. The Z_1^2 statistic (Chapter 3.3.5) was used. Energies above 30 keV and below 115 keV are explored in this search. However since Sco X-1 has very few photons in this energy range only weak upper limits can be set i.e. about 6%rms over the range 100-500 Hz This upper limit was set using figure 5 of Protheroe 1987b.

Consideration of these upper limits and detection must be tempered by the uncertainties surrounding the X-ray clock's accuracy at millisecond time scales over periods of 10 minutes because of possible clock or data discontinuities. The above upper limits should, strictly, be seen as lower limits to the true upper limit. Since only one anomaly was found in fitting the frame period the upper limits should be a reasonable estimate of the true upper limits.

6.3.3 Red Noise

The power spectra of the 1 msec data were summed over different broad frequency ranges (i.e. 0-0.1, 0-1.0, 0-2, 0-5, 0-10, 0-20, 20-100 Hz). The excess power with respect to the high frequency (20-100 Hz) level was calculated for each spectrum for each frequency range. The excess powers are tested for significance (95% confidence) and converted to rms percentages of both the total and the source counts. In testing for significance the number of trials is one because the search is for a specific feature i.e. an excess power over a specified frequency range. The detection thresholds were set using the method of Chapter 3.3.2.2 and 3.3.2.3

using either the χ^2 or normal distribution. The normal approximation with mean of two and $\sigma = \sqrt{4/MW}$ was applied when the spectrum had $\geq$ 200 degrees of freedom (i.e. MW $\geq$ 100).

Of the 1 millisec power spectra spectra, only one (SCP2b) , showed any excess ($\approx$3%rms) over the entire 0-5Hz range. Some data sections showed an excess below 1Hz (SCP1 SCP2a,b) in only some of their power spectra. In general a limit of about 5%rms could be set upon any <1Hz red noise and <2% for <10Hz red noise.

To extend the search to lower frequencies the frame by frame data was used. The frame data covers slightly different time spans, i.e. SCD 3:32-3:42, SCP1 4:39-3:44, SCP2 4:50-4:56:30, SCP3 4:58-5:03 UT, than the 1 millisecond data. These time spans are the same as those used for the energy spectral analysis. The energy range was restricted to $\approx$20 to 42 keV (channels 18-38). The count rates of each frame were corrected for overflows (Section 6.4.1). Any missing frames were filled with their immediate predecessor. The resulting time series was transformed using the FFT algorithm.

The resulting power spectra (e.g. Figure 6.8b) were basically flat. They did not show the low frequency drop off followed by a rise to a maximum at 6-10 Hz cf Figure 6.3. This further vindicates the frame corrections. The power spectrum of the GX1+4 background observation had a mean power level, over the 2-5.5 Hz range, of 1.96. This level is not significantly different from the expected level of two. All Sco X-1 power spectra had 2-5.2Hz mean power level greater than two. Only in the case SCP3 observation was this difference significant. When testing the powers the mean power was taken as being two.

All power spectra including that of the background showed a small rise at frequencies below 1Hz. Only the drift scan, combined pointed and total power data power spectra had significant excess below 1Hz or 0.1Hz. The background spectrum showed a significant (95%confidence) excess in the 0-1Hz range amounting to 0.6%rms of the total count rate. The red noise level (<1Hz) from the drift scan corresponds to a 1.4%rms of the total counts or 1.8% of the source flux. The effects of the varying collimator transmission although mitigated by splitting the data into sub-intervals (M=9 for the drift scan) are sufficient to explain the red noise level observed during the drift scan. The 1.8% value should be considered as an upper limit to any low frequency red noise during the drift scan.

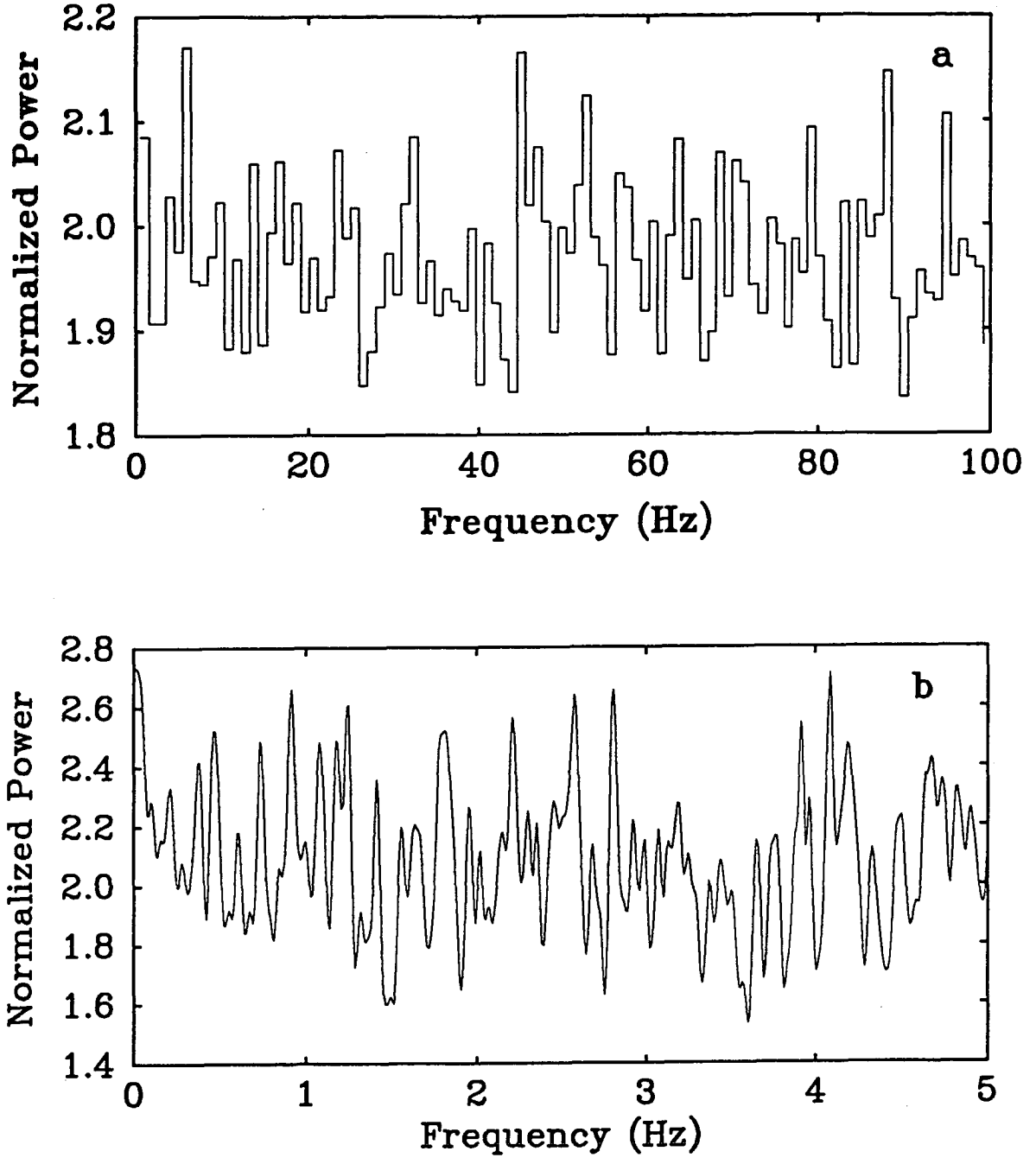

Fig 6.8 (a) Combined power spectrum of the 1 msec data binned into 1 Hz wide intervals. There is some hint of a low frequency increase in the first bin. **(b)** The combined power spectrum of the frame by frame data. The powers have been smoothed with a running 3 point mean.

The collimator transmission only changed by 10% over the entire pointed observation. Thus any introduced red noise, in the 0-1Hz range, will be about the same as that of the background observation. After removing the background level of 0.6%rms red noise Sco X-1 showed, as a fraction of source flux, 2.7%rms (0-0.1Hz) and 8.8%rms (0-1Hz) red noise during the pointed observation. During the brighter, SCP3 (4:58-5:03UT), data segment there was excess noise over the 0-5.2 Hz range amounting to about 19%rms of the source flux.

6.4 Energy Spectral Analysis

The energy spectrum analysis is based upon the frame count rate data. The pointed observation was split into three sections; 4:39 to 4:44 UT (SCP1), 4:45 to 4:56:30 UT (SCP2) and 4:58 till 5:03 UT (SCP3). Between SCP1 and SCP2 there were a large number of missed frames caused by radio interference and between SCP2 and the last section of data (SCP3) there was a flare like event.

6.4.1 Overflow corrections

The initial subtraction of the background from the Sco X-1 observations produced consistently negative counts in the high energy channels. This can be explained by the presence of frequent frame overflows. As the total count rate is increased the fraction of counts lost through overflows increases. These lost counts are lost evenly from all energy channels. At high energies, particularly for Sco X-1, there are practically no source counts and so the true count rate is equal to the background. However, because of the higher total on source count rate there are actually fewer high energy counts recorded.

The count rate/frame period phase plots of Section 6.2.1 can be used to estimate the fraction of counts lost by overflows. This is done by comparing the actual count rate per frame with that estimated from the count rate of the uncontaminated phases of the frame period. The ratio of the two rates gives a multiplication correction factor to apply to the observed count rate to yield the incident count rate. A plot of this correction factor is shown in Figure 6.9. This shows that the fraction of counts lost is between one and two percent. The correction factor seems to flatten out at high count rates. As the incident count rate increases there comes a point where most frames are full thus limiting the observed count rate.

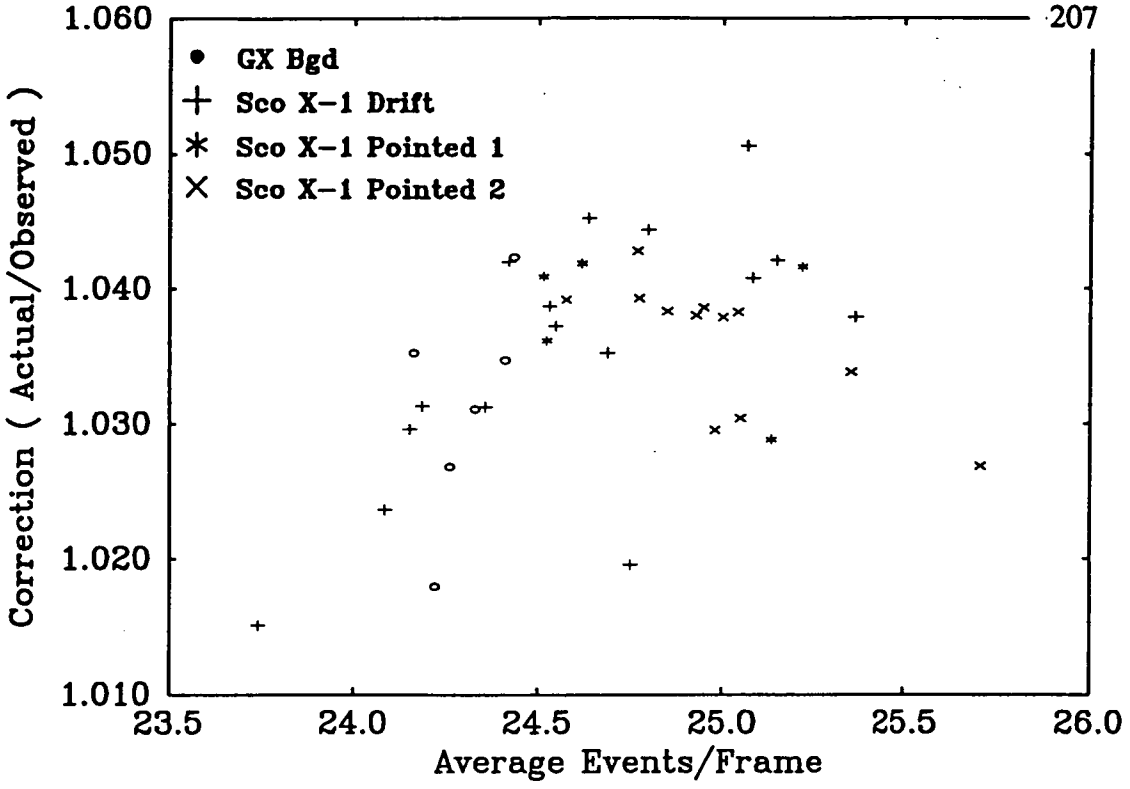

Fig 6.9 The correction to the count rate for data lost during overflows. This correction is based upon 1 minute phase plots of the count rate.

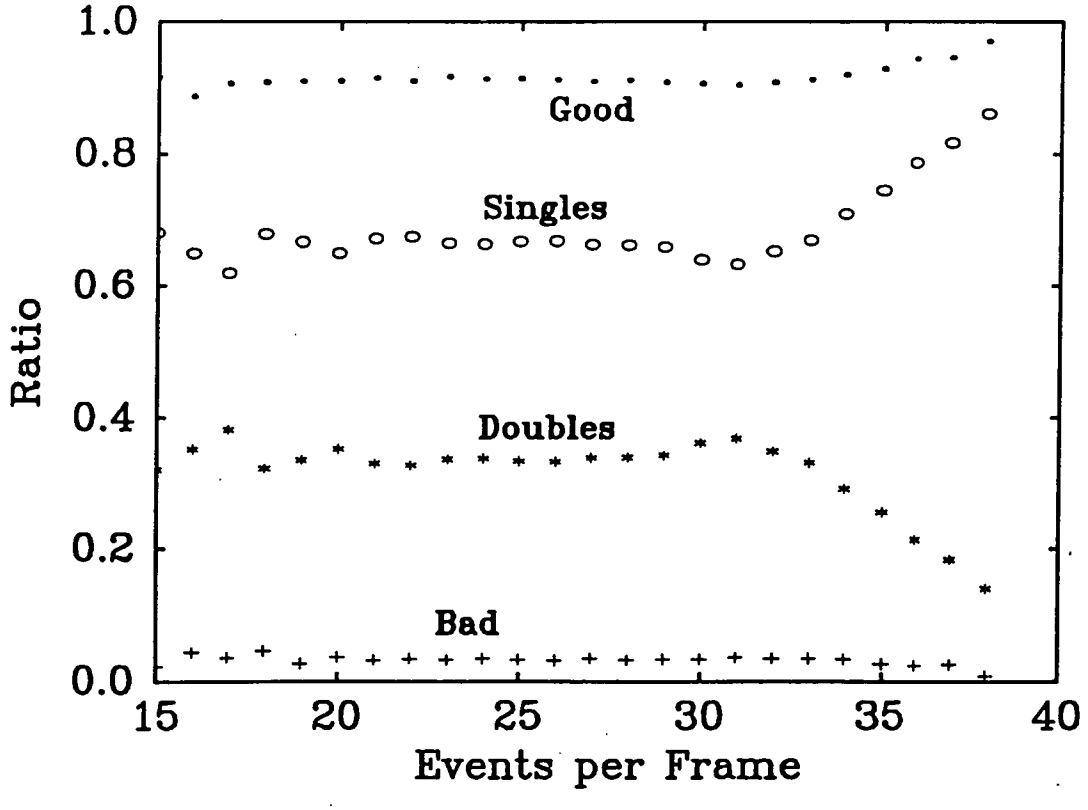

Fig 6.10 The proportion of single double and bad (channel=127) events. At high count rates the overflows create a bias toward frames with a larger proportion of single events.

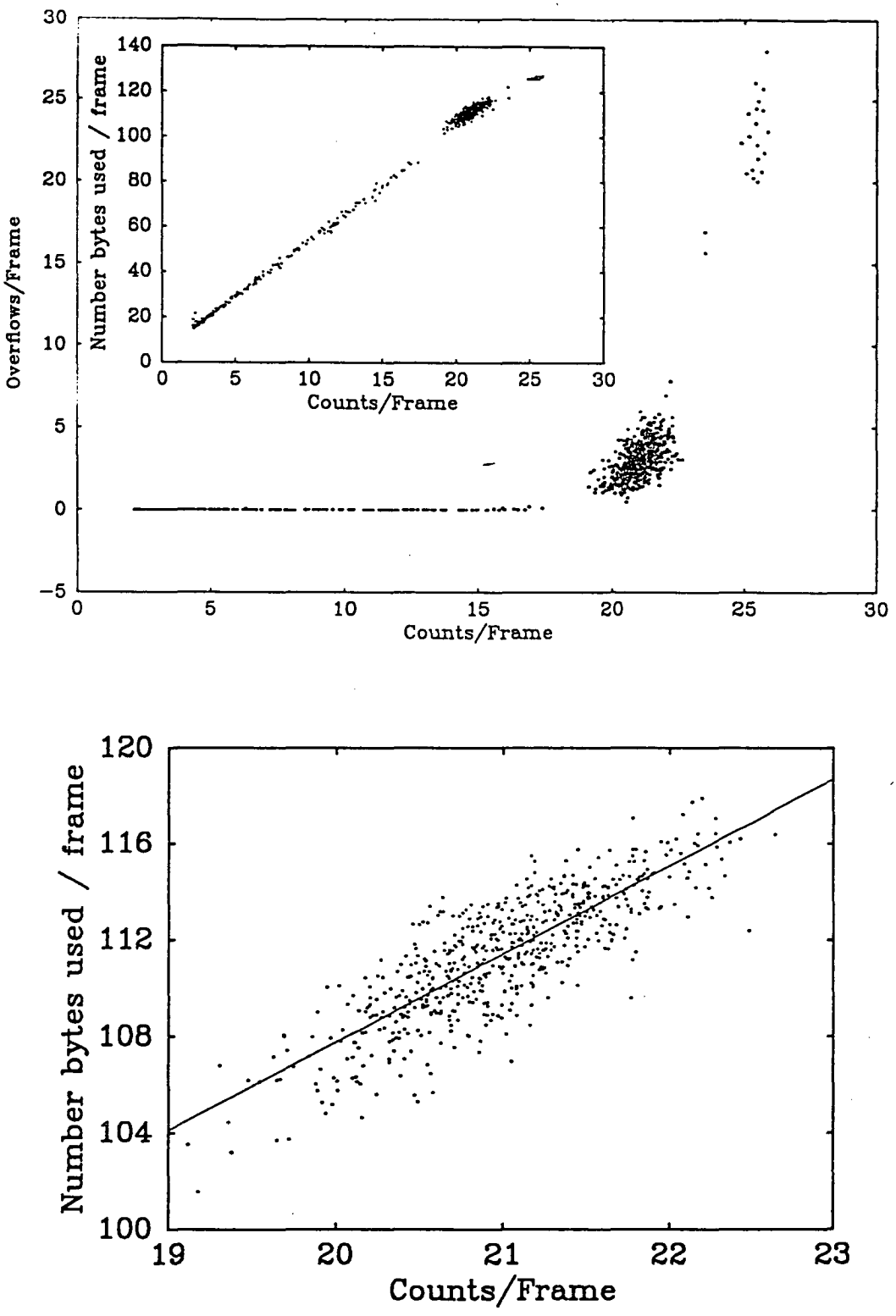

Fig 6.11 The overall relationship between the rate of overflows and the frame count rate is shown in the top panel. There is an almost linear relationship between the number of bytes used per frame and the count rate rate per frame. At the highest count rates (calibration source) most frames are full and the detector output is saturated. The lower panel shows the linear fit used to correct the data for the effects of overflows upon the count rate.

This occurs at count rate of ~34 counts per frame. This estimate is based upon a careful examination of a sample of frames which showed that the proportion of single events (3 bytes) is 0.65, and double (5 bytes) is 0.34 and that there are an average of 5 bytes lost through clock updates in each frame. As the count rate approaches this limit, and then exceeds it, only frames with a higher proportion of single events will not overflow. This effect is shown in Figure 6.10. The absolute maximum count rate is 41 counts/frame i.e. all single events.

Within each data frame there is an overflow counter. This counts the number of X-ray micro-processor FIFO bytes lost during the frame. It was found that ~25% of frames overflowed. When a frame overflows not only are the overflow events lost but also the last event of the overflowing frame and the first event of the next frame. Thus there is an average of 3.72 (0.63 x 3 + 0.34 x 5) extra bytes lost during every overflow. From a sample of 100 frames it was found that an average 3.11 bytes were lost per overflow which accords reasonably with the above estimate.

These overflow bytes cannot be directly converted to extra counts because they include clock updates and not all events are valid counts. A count is an event with a channel number between 10 and 121, or a fluorescent double with one event in channels 20-40. This definition rejects all saturated events (i.e.one or both events in PHA Channel 127), and all double events with a combined energy less than 30 keV.

The highly non-linear relation between the observed count rate and the number of overflows is shown in Figure 6.11a . The main region of interest lies between 19 and 23 counts per frame. Figure 6.11b shows an expanded plot of this region. A least squares fit yields

$$b = 104.1 + 3.65\,(x - 19)$$

or

$$b = 102.60 + 5.31\,(x - 19) - 0.42\,(x - 19)^2 \qquad 6.8$$

where b is the number of bytes used in a frame and x is the number of counts (valid events) in a frame. The slope is the average bytes per event. This is close to the expected value of ~3.72. The difference between the slope and calculated value is due to the presence of clock updates. The ratio of B/x gives the number of bytes/count. Now if E is the number of overflow bytes and t is the number of extra bytes

$$t = E + 3.75$$

$\therefore$ the number of extra counts $= t/(b/x) \qquad = (t/b)x$

$\therefore$ the true count rate is $\qquad T = x + (t/b)x \qquad = (1+t/b)x \qquad 6.9$

Alternately a multiplicative factor T/x can be used to correct the observed count rate. In the region of interest the difference between the quadratic and linear corrections is negligible. Note that the calibration source count rate is in a completely different count rate regime in which most frames have overflowed.

6.4.2 A/D Converter Correction

The A/D converter used to digitize the counter's pulse height voltages had 8 bit cyclic variation in the widths of the digital channels. This resulted in a cyclic change in the observed count rate with PHA channel as illustrated in Figure 6.12a which is a combination of all source and background data. In doing a background subtraction this effect is not totally removed. A "flat field" calibration curve was used to remove this effect.

Firstly the total count rates of Figure 6.12a were binned into eight channel wide intervals centred upon the major 7/8 excursions. These eight channel averages were then fitted with a cubic spline. The original data was divided into the cubic spline fit to yield a multiplicative correction for each untreated channel. This correction was adjusted to ensure that counts were conserved over each eight channel cycle. The "flat field" calibration is shown in Figure 6.12b.

6.4.3 Background Variations

During the 1986 flight there were five background observations. These were a pointed observation 4° away from GX 1+4, a pointed observation at the sun, two azimuth scans at O° and 51° zenith angles and a brief period just before the drift scan of Sco X-1 . A list of sources based upon the HEAO A4 catalogue was used to check the background data for the presence of any hard X-ray sources. Any data with a source within 6° of the look direction was removed. Also data affected by changes in the EHT voltage or calibration sources was removed. The observed count rates were plotted against zenith angle for different energy bands. As an example, Figure 6.13 shows the total count rate versus zenith angle.

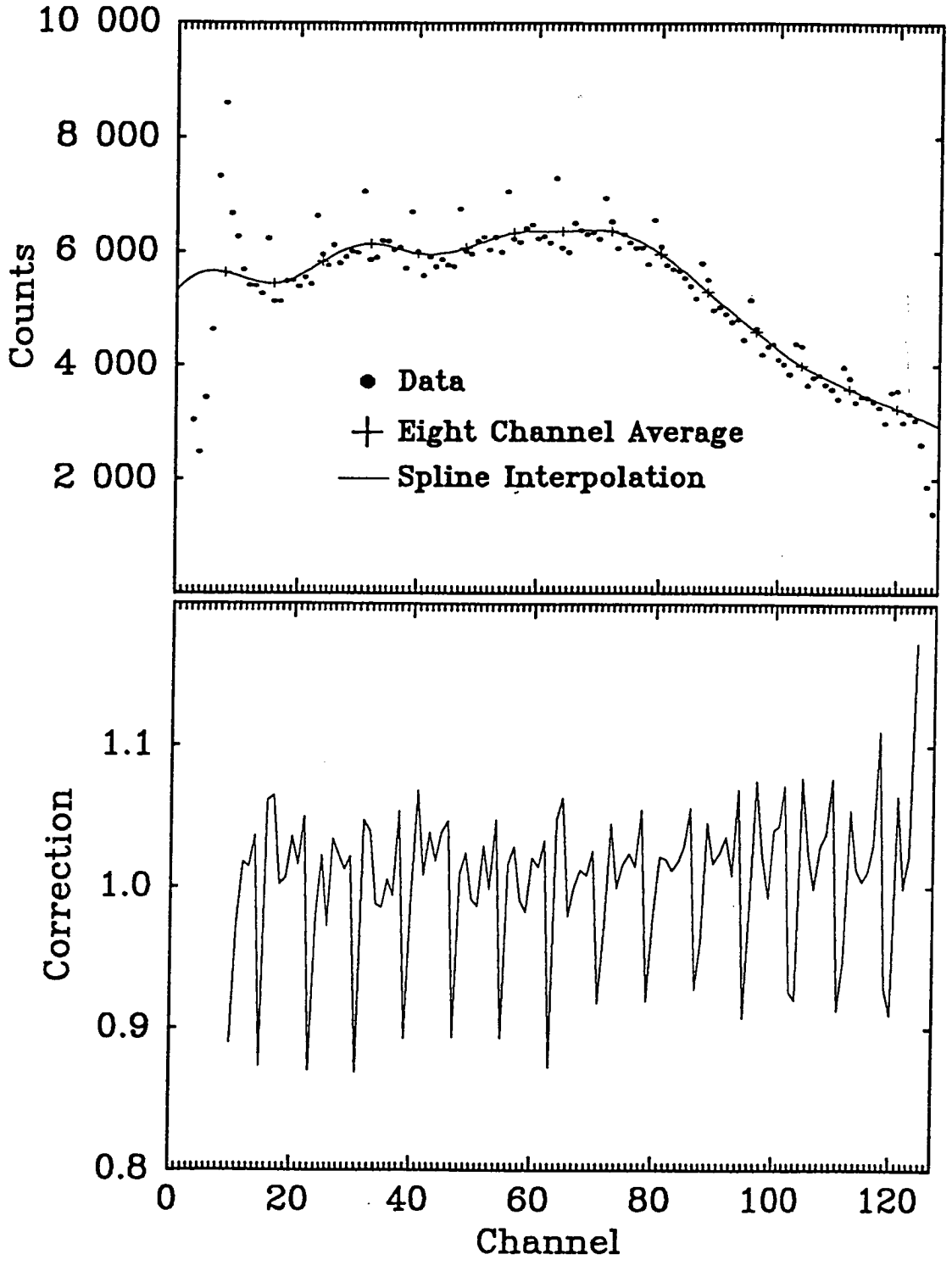

Fig 6.12 Illustrated is the procedure used to calculate the "Flat Field" calibration to the PHA data. In the first plot the dots are the original total number of counts observed from Sco X-1, GX 1+4, Sun and the GX 1+4 background. Note the unusual shape of the PHA spectrum below channel 5 and the drop in PHA sensitivity above channel 121.Also note the number of events in channel 127. The crosses represent the average counts over eight channels. The solid curve is the spline fit to these averages. The lower plot shows the actual flat field calibration which is the spline fit divided by the data. It is used as a multiplicative factor.

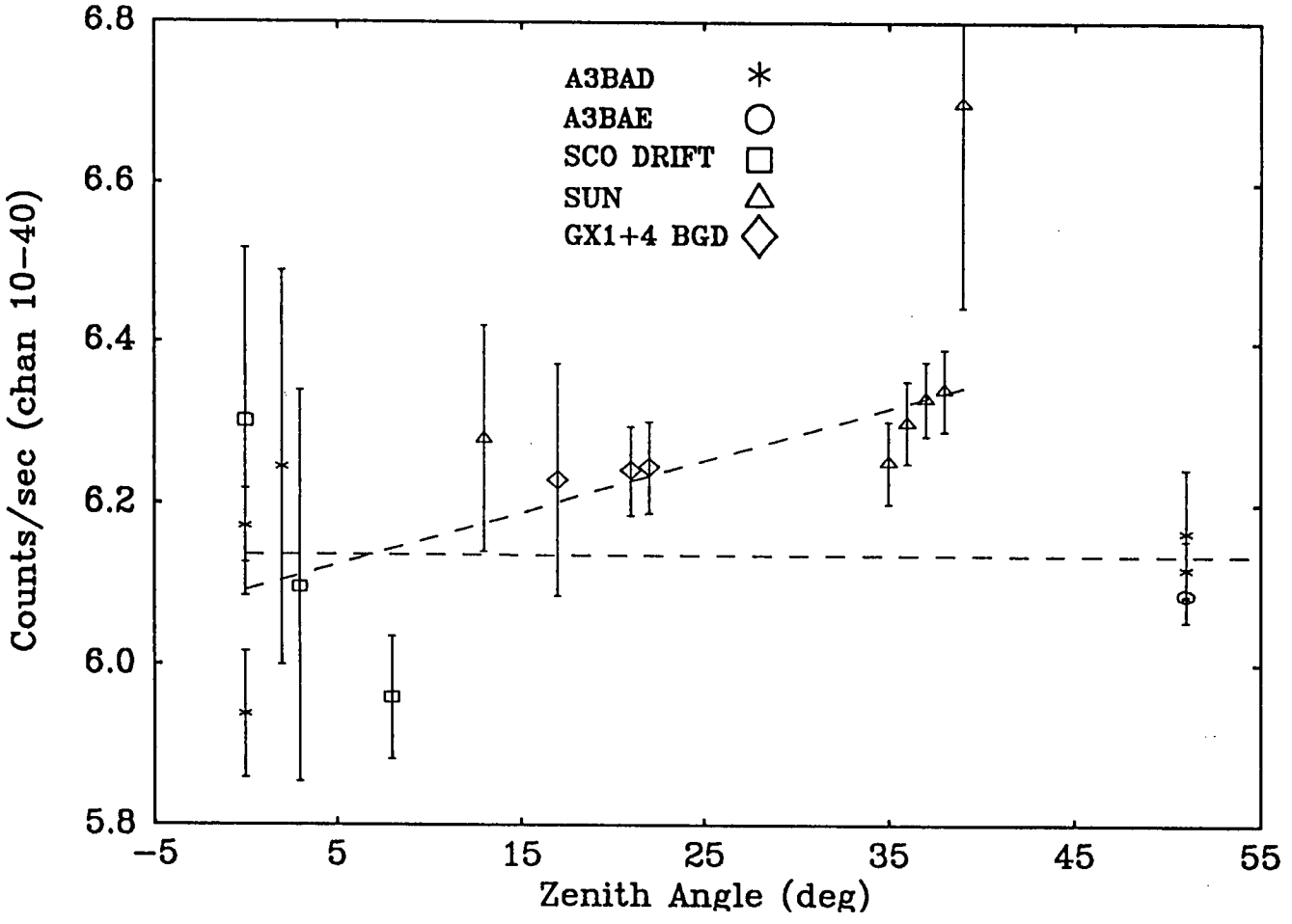

Fig 6.13 The variation in total (5 -114 keV) count rate versus zenith angle. Excepting the data near the Sun there is no significant trend with zenith.

The background data taken at a zenith distance of 51° had a lower count rate than the one taken in the direction of the sun. The variation in background with zenith angle can be described as either a steady rise to a maximum at about 40° (the sun is not a source) followed by a fall at 51° or a practically constant count rate with zenith angle (the sun is a source). Previous measurements and theoretical modeling (Costa et al. 1984 and references therein) show the γ-ray background increasing monotonically with zenith distance up to 110°. During the UTIC83 flight the background was observed to increase steadily between zenith angles 10° and 45° Above 45° the increase was less marked. It is thought that the intrinsic background variation was enhanced by a leaky veto system of the UT1 detector.

If the sun is considered a source, the background variation in zenith angle is slight. This would imply that the UT2 veto system was working efficiently. On the 20th November 1986 the sun was active as evidenced by the large soft (1.8Å and 0.5-4Å) X-ray and Hα flare that started at 8:58 UT (*Solar Geophysical Data comprehensive reports* No 513 Part II) approximately 3 1/2 hours after our solar observations. The solar observations were between 5:31 and 5:47 UT. There is also an indication of a soft X-ray increase starting during the solar pointing and lasting about an hour. It is thus reasonable to suspect that the sun was a X-ray source at the time of our observations.

No azimuth dependence in count rate was seen during the zen = 51° azimuth swing. The background used in all subsequent analysis is the sum of the two azimuth swings, the GX 1+4 background and the Sco X-1 drift scan background. The background is considered to be determined to about 1% accuracy. No zenith angle dependence correction was applied to the counting rates.

6.5 Results: Energy Spectra

Within the different data sections the frame pulse height counts were corrected frame by frame for overflows. The counts were then summed in time and the corrected background was subtracted. The excess pulse height counts were then "flat field" corrected. The resulting pulse height count rate spectra are shown in Figure 6.14

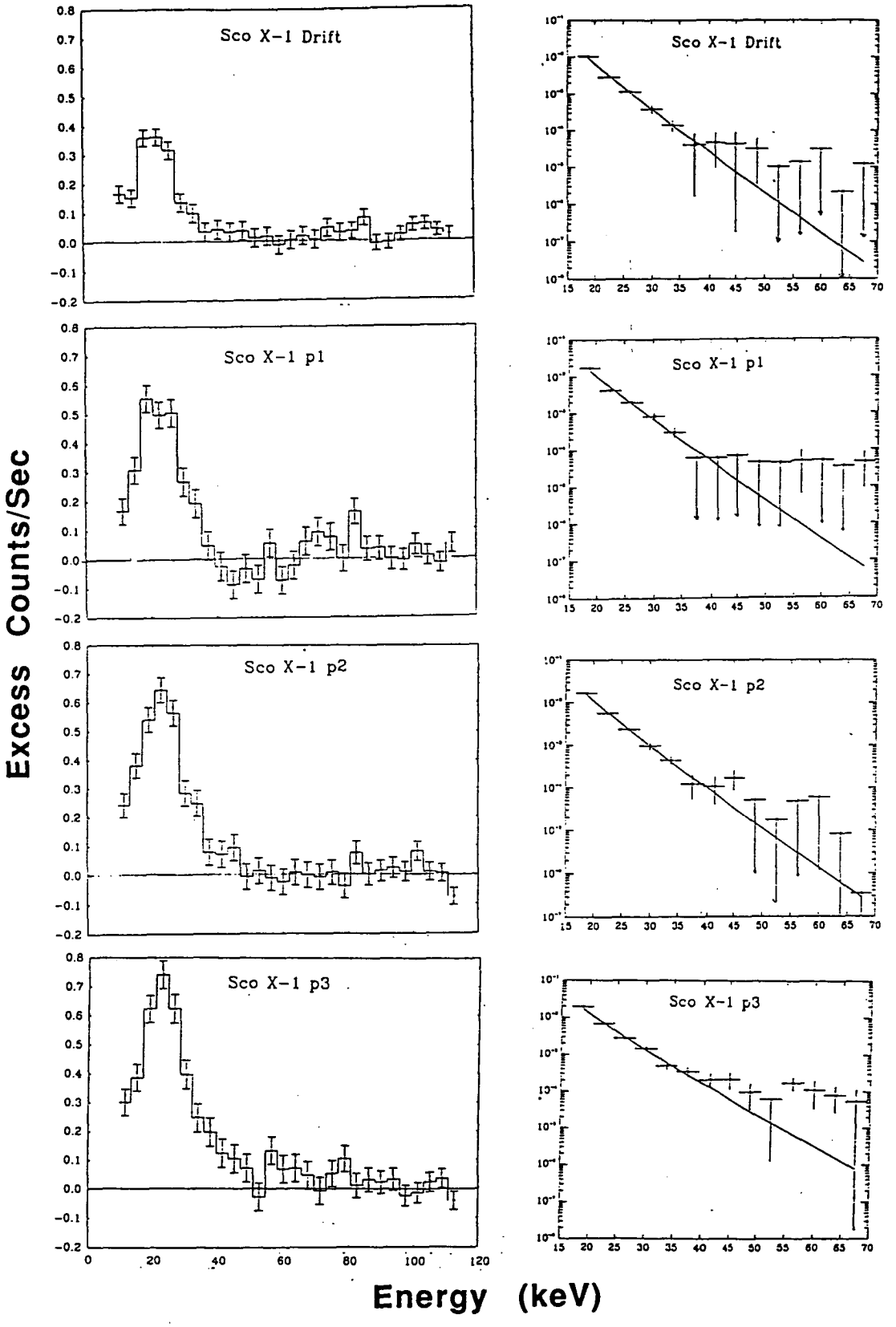

Fig 6.14 The background subtracted PHA spectra and deconvolved thermal bremsstrahlung (with energy dependent Gaunt factor) fits.

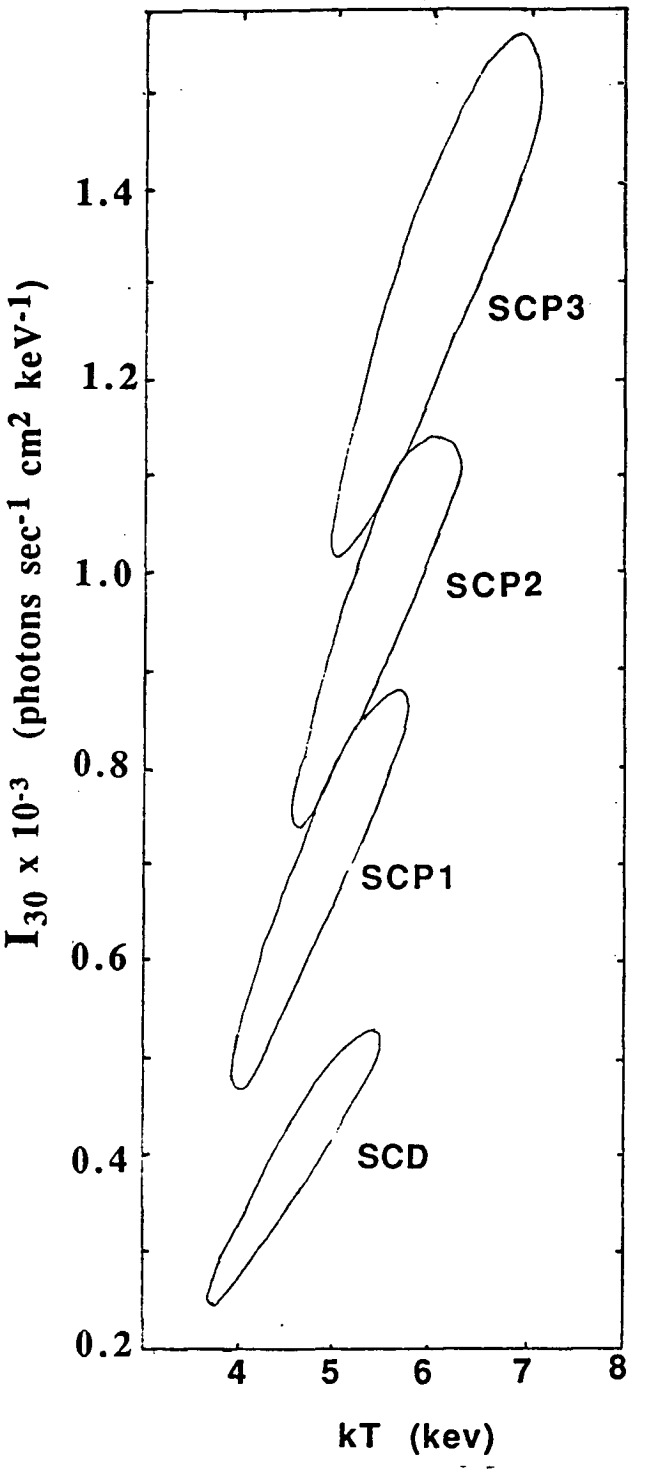

Fig 6.15 A Intensity-Temperature χ^2 contour map showing the 90% confidence regions for the four observations of Sco X-1. There is little or no overlap between adjacent observations showing that they are different at the 90% level. However there is no significant difference in the temperatures. The three pointed fits are not different at the 95% level.

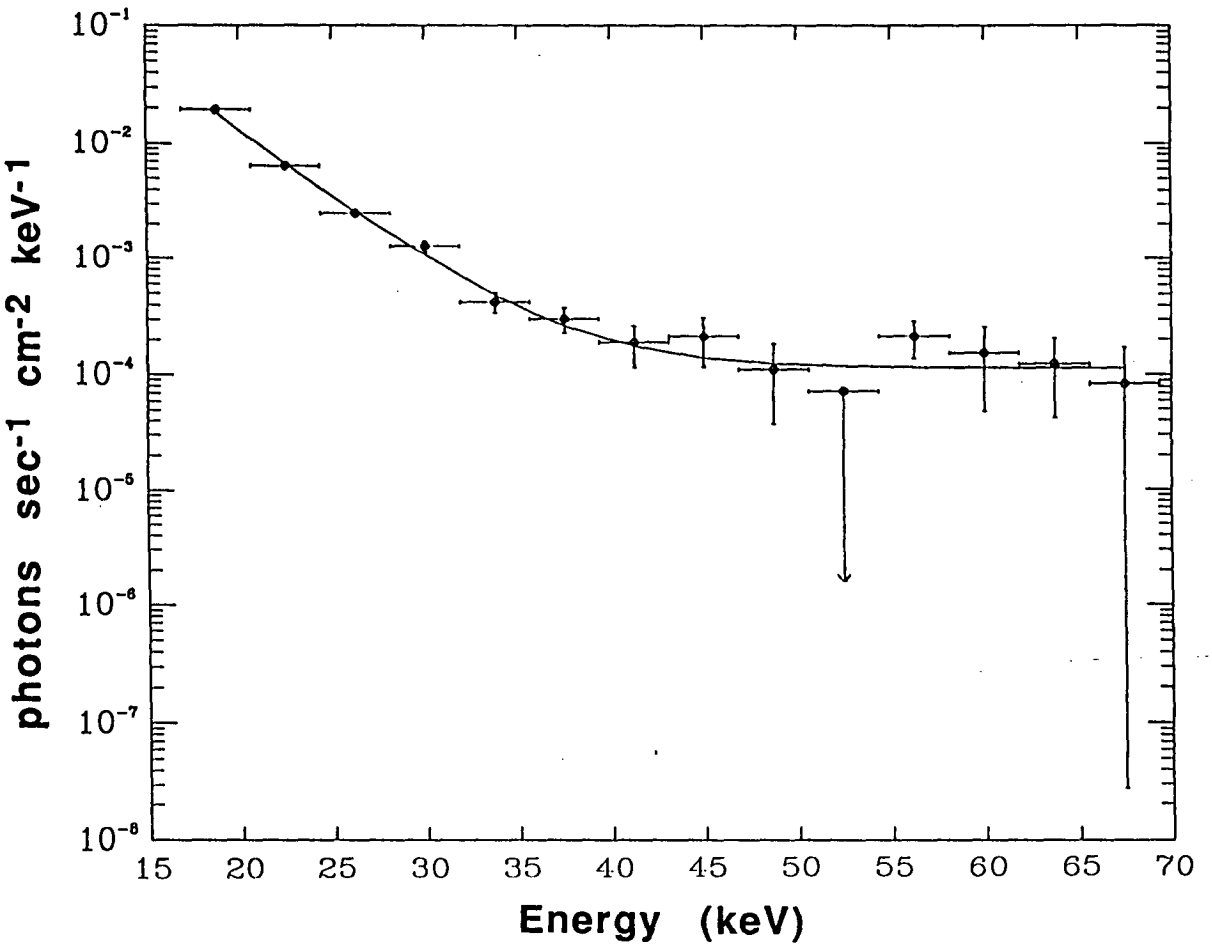

Fig 6.16 The deconvolved spectral fit to the SCP3 observation. The model used was a thermal bremsstrahlung (Gaunt factor included) and a power law tail.

TABLE 6.4

MODEL	FORMULA
Power Law	$A \left(\frac{E_0}{E} \right)^{\alpha}$
Exponential (Thermal Bremsstrahlung)	$A \exp\left[\frac{-(E - E_0)}{kT}\right]$
Exponential with Gaunt factor	$\beta = 0.37 \left(\frac{E_0}{E} \right)^{0.15}$ $A \left(\frac{E_0}{E} \right)^{1+\beta} \exp\left[\frac{-(E - E_0)}{kT}\right]$

A is the intensity photons s^{-1} cm^{-2} keV^{-1} at E_0
E_0 = 30keV

TABLE 6.5

	Power Law			Exponential			Exp + Gaunt Factor		
File	$I_{30}x10^{-4}$	a	χ^2_ν	$I_{30}x10^{-4}$	kT	χ^2_ν	$I_{30}x10^{-4}$	kT	χ^2_ν
SCD	4.05	6.75	0.438	3.69	3.49	0.653	3.80	4.50	0.001
SCP1	6.58	6.90	2.349	6.57	3.63	2.238	6.60	4.65	2.221
SCP2	9.51	6.12	0.482	9.62	4.06	0.602	9.69	5.38	0.535
SCP3	12.58	5.71	1.495	12.91	4.40	2.389	13.04	6.00	2.177

	Exp + Gaunt + Power Law				
File	$I_{30}x10^{-4}$	kT	$I_{50}x10^{-5}$	a $x10^{-5}$	χ^2_ν
SCD	3.24	4.21	2.46	-0.5	0.530
SCP1	6.60	4.65	<0.01	-0.03	2.714
SCP2	9.42	5.30	0.89	-6.0	0.641
SCP3	9.48	4.98	1.13	-1.0	1.210

Fits made over the energy range 16 – 70 keV with the data binned into 3.85 keV wide intervals. Intensities are in photons sec^{-1} cm^{-2} keV^{-1}.

File	$\overline{Zen}$	$\overline{Dis}$	Duration (Sec)	$I_{30}x10^{-4}$	kT
SCD	7.985	1.198	843	6.4 ±1.4	4.5 ±0.9
SCP1	17.735	0.955	295	10.0 ±3.0	4.6 ±0.8
SCP2	20.197	0.675	355	13.0 ±5.0	5.4 ±0.9
SCP3	21.822	0.672	299	9.5 ±4.0	5.1 ±1.1*

* From Exponential (Gaunt) + Power Law fit.

The error bars are based upon Poisson statistics. The distribution of the corrected frame counts were tested for normality using the K-S test. The distribution of the background counts were found to be consistent, at the 99% confidence level, with the normal distribution and hence the Poisson distribution. The backgrounds were inter-compared by treating one as a source and the others as backgrounds. The resulting differences and estimated 1 σ error bars are also consistent with a Poisson distribution.

Using the χ^2 minimization method these excess counts were fitted, over different energies ranges, with a variety of models namely; power law a thermal bremsstrahlung (exponential) with and without an energy dependent Gaunt factor. The Gaunt factor used is that of Mätzeler et al. (1978). The forms of these models are listed in Table 6.4.

It was found that the pulse heights below 16 keV could not be satisfactorily fitted, being always higher than the fit. Below 16 keV there are no celestial photons. Counts at these energies are either escape photons or the result of energy re-assignment caused by the finite resolution of the detector. An underestimation of either the escape fraction or energy resolution FWHM would explain the poor low energy fitting. The inclusion of these channels did not much affect the final fitted parameters but did markedly worsen the minimum reduced χ^2. All the spectral fit results presented do not include these channels. The fits were also restricted to below 70 keV as there was no significant excess in any of the PHA spectra above this energy.

The results of the spectral fits are summarized in Table 6.5 which lists the fitted parameters (the normalized intensity, power law index or the temperature) and also the minimum χ^2_ν of the fit. All the intensities are normalized at 30 keV. The temperature is expressed in terms of keV and is equal to kT where k is the Boltzmann constant (in keV) and T is the source temperature. Generally a thermal bremsstrahlung with Gaunt factor produced the best fits. These fits are displayed in Figure 6.14 along with the corresponding 2 parameter confidence interval maps in Figure 7.15

As the intensity at 30 keV increased from a low level during the drift scan of $I_{30} = 3.8 \times 10^{-4}$ photons cm^{-2} sec^{-1} keV^{-1} to a value of 1.3×10^{-3} photons cm^{2} sec^{-1} keV^{-1} during the SCP3 data section the best fit temperature

increases from 4.5 keV to 6.0 keV. Examining the 90% confidence regions for the fits shows there is little or no overlap. Thus adjacent spectra are significantly different at the 90% (but not at the 95%) confidence level. A constant temperature between 5. and 5.4 keV could satisfy all the data at the 90% confidence level. There is therefore no relationship between intensity and fitted temperature. During the observations the hardness ratio (≈20-23keV/23-33keV) remained approximately constant.

Immediately following a flare-like event the count rate increases and the PHA spectrum hardens (SCP3). A significant improvement in the fit to the SCP3 PHA spectrum can be obtained by adding a power law component to the thermal bremsstrahlung model (Figure 6.16). The best fit power law index is effectively zero ($\alpha \approx 10^{-5}$) and the temperature was 5 keV instead of 6 keV (without a power component). There is little or no improvement in the fit for any other data sections. The apparent trend of temperature versus intensity is broken when an power law component in addition to the thermal bremsstrahlung spectrum is used to model the PHA spectra.

6.6 Discussion

6.6.1 The "flare"

Between the SCP2 and SCP3 (4:56:30 - 4:58:00 UT) observations there is a flare-like event. Immediately obvious from the pulse height data (Figure 6.17) is the very soft nature of the flare.

After a search of the entire float data set, a second "flare" was found during a background observation at 1:27:56 - 1:28:06 UT. The main distinguishing feature of both events is a drop in the ratio of top tray counts to main detector counts. The characteristics of both events are:

1/ a rise in the counting rate in the single events from the main body of the detector.

2/ A rise in the number of frame overflows.

3/ No increase in the top tray double or single event rates.

4/ No increase in the rate of non-fluorescent double or bad events (PHA channel number >126)

5/ A small drop in the rate of double events from the main detector volume.

6/ A very soft energy spectrum with most of the excess counts below 20 keV

7/ No apparent increase in the veto cell count rates. However, these rates are only telemetered every 10 sec. At the times of the flares some of the vetorates are missing.

A detailed light curve and excess PHA spectrum for each 'Flare' is given in Figure 6.17.

Any large rise in the count rate will produce a rise in the overflow rate (2) and a decrease in the doubles rate (5) without an increase in the veto rate (7) or bad events (4). The "flare" is not apparent in the total event rate (34-37 events per frame).This suggests that the detector was near saturation. This is confirmed by the slight decrease in the number of main double events occurring at the time of each "flare". As discused in Section 6.4.1 (see Fig 6.10), at event rates above about 30 events per frame the FIFO buffer becomes full. As the event rate increases the only way to cram more events into a frame is to reduce the proportion of double events recorded. Both the very soft spectrum and lack of top tray counting rate increase are unusual.

At 20keV about 1 in 8 photons penetrate 3.1 gram/cm^2 of atmosphere while at 10 keV only a millionth of the incident flux reaches the detector. In the extreme at 5keV any incident flux is attenuated by $2x10^{-39}$. Even the gradual phase of solar flares which have a steep low energy spectrum (ratio 5keV to 20 keV flux of 10^5 Hudson 1979) would not result in any observable flux at the lowest energies. Some 20 keV could photons can reach the detector. The finite energy resolution (~3 keV FWHM at 20 keV) of the detector would smear out their energies to produce a roughly Gaussian distribution. This is not consistent with the observed PHA spectrum of either event.

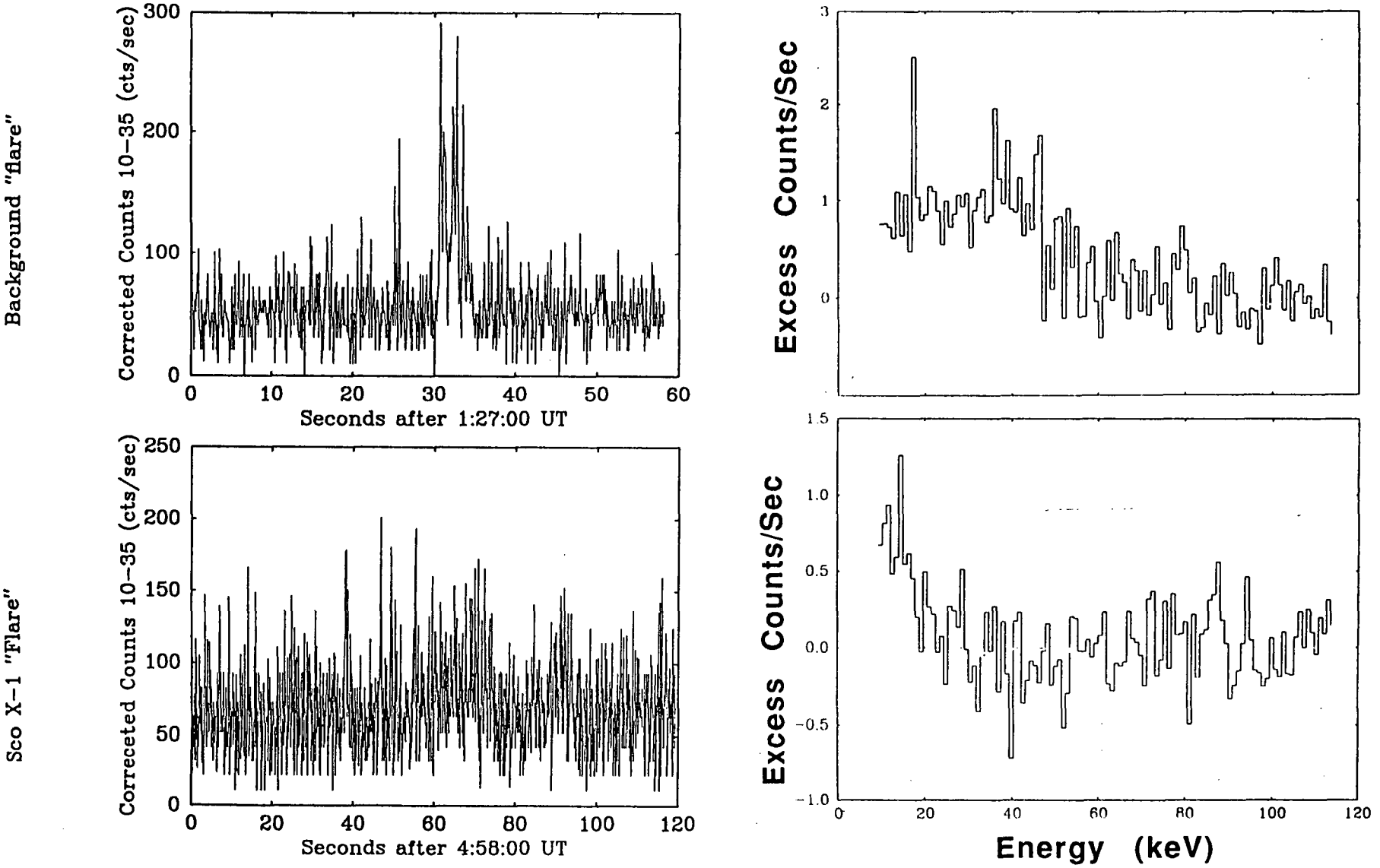

Fig 6.17 The light curves, corrected for overflows, for the two "flare" episodes and the corresponding excess PHA spectra. The average background rate was used for the "background flare" and the SCP2 PHA was used as the background for the "Sco X-1 flare".

On this basis the "flare" during the Sco X-1 pointed observation cannot be of celestial origin. The PHA spectrum of the background observation "flare" could conceivably be produced by a very soft X-ray astronomical source. The background "flare" is considered, because of the similarities between the two events, to be of the same origin as the "Sco X-1 flare". Particularly important is that both events show no increase in the top tray count rate concurrent with the increase in the main detector count rate.The "flare" counts must have been added before the X-ray FIFO buffer because the frame overflow rate increase. There are three general types of possible explanations. A local atmospheric source of X-rays, a veto system failure or some internal source of counts.

During the many balloon searches for weak γ ray bursts similar events were observed. A few have been confidently identified as γ-ray bursts (e.g. Nishimura et al. 1978). The majority were found to be local in origin. Cline et al. (1977), using two geographically separated balloon payloads found two populations of local events. One group were short microsecond to minute duration non-Poisson count rate excursions seen at only one site. The other set were longer (100sec) bursts seen by both payloads but delayed by 10sec. Both groups were tentatively identified with magnetospheric effects.

A widely observed magnetospheric effect that does give rise to X-ray bursts are auroral electron precipitation events. The observed X-ray spectra have a wide range of e-folding energies generally 15-60keV, but occasionally >150keV. Flux variations are seen on all time scales from milliseconds to minutes (Pilkington 1972; review). The X-rays from electron precipitation have similar time scales and energy spectra as the various anomalous X-ray bursts.

Electrons are accelerated, sometimes to relativistic energies, by downward pointing "V" shaped electric potentials. Then they interact with the upper atmosphere (90km) to produce bremsstrahlung X-rays which then penetrate to balloon altitudes (up to 10 g/cm^2), suffering both photoelectric absorption and Compton scattering. The Compton scattering diffuses the X-rays and modifies the spectrum. Monte Carlo simulations by Pilkington and Anger (1971) show that the spectrum softens (lower e-folding energies) with both vertical and horizontal distance from the initial precipitation. Collimated detectors therefore view a softer spectrum when the source is either outside or larger than the field of view. Combining both the effects of distance and restricted field of view e-folding energies as low as 15keV can be

achieved. Thus an electron precipitation event could give rise to the soft energy spectrum of the two "flare" like events observed during the 1986 flight as well as the TAS-X observation during the 1983 flight.

However, the X-rays could not enter the detector without increasing the top tray counting rate unless the top tray was not fully operational. This in highly improbable. If it was only partially operational it would give a low normal rate and a higher but still depressed "flare" rate.

The above is given as an example of the remoteness of any possible external source for the two flare like events. Finally, the ISAS detector on the same platform and also observing Sco X-1 did not record any flare like increase at the time of the Sco X-1 event (Ubertini private communication 1990).

Now let us consider a breakdown of the veto/shield system in response to hypothetical a X-ray source not within the field of view. Less than 20 keV photons could not penetrate the 1mm lead and 5mm steel shielding. At higher energies (>50keV) Compton scattering becomes important. It is possible that incoming high energy X-rays are Comptonized to produce a flux of <20keV X-rays within the detector volume. Any photo-electrons released from the walls would be stopped within the veto cells. Similarly 70% of 20 keV X-rays would be absorbed within the veto cell. At energies near 10 keV practically all (99.94%) incoming photons will be stopped near the walls. So any flare event should be accompanied by an increase in the veto rate.

A veto system failure would admit mainly fast charged particles which would give rise to high energy events. A failure of the veto system seems unlikely. The almost constant count rates with zenith angle shows that the veto-system was very efficient and operating correctly throughout the flight. However long term tests of the system were not carried out before the flight and so transient failure could have been overlooked.

No anomalies were seen in the house keeping data at the times of the "flares". A drop in the EHT voltage causes a very soft spectrum. After switching off the EHT the count rate slowly declines starting with the high energy channels. The process takes a few seconds. There is no indication of a drop in the EHT voltage (recorded every 1-2 sec). The constant rate of non-fluorescent doubles and bad events indicates that the operation of the detector did not change during the flares.

A noisy insulator or isolation capacitor could give rise to bursts of low channel counts. Such bursts have been noted during ground tests immediately after the detector is switched on. However, it is unusual that a breakdown only occurred for two short periods.

At present there is no firm conclusion on the cause for the two "flares". It seems that there is no external source of X-rays that can explain the events. At the time all indications are that the detector was working nominally. No long term tests were made of the detector and so transients could have escaped notice. These sort of tests will be carried out upon the resurrected detector.

6.6.2 The Hard Tail

Whatever the underlying cause of the flares the main concern is whether the Sco X-1 "flare" caused the hard tail excess seen immediately after-wards in the SCP3 observation. The background subtracted (overflow corrected) spectrum was examined minute by minute immediately before and after both flare events. There is no consistent changes for both events. Before and after the background event the 40-70 keV count rate remained constant and was not significantly different from the background while the 70-100keV background subtracted count rate changed from being negative to approximately zero. The count rate was about 2σ or $\approx 3\%$ below the expected background level. This behaviour contrasts with that near the Sco X-1 event. The 40-70 keV count rate increased, producing the hard tail within a minute of the "flare" while the 70-100keV count rate remained constant and not significantly different from the mean background level. The minute by minute background subtracted count rates are summarized in Table 6.6. Assuming that the two events are of the same type it seems that the increase in the 40-70 keV excess is due to Sco X-1.

The apparently negative flux between 40 and 70keV in the first pre-flare pointed (SCP1 in Figure 6.14) observation would suggest a problem with the background subtraction. But the negative background subtracted count rate is not significant. Using Poisson statistics it is only 1.5σ below the background and would amount to a 1% increase in the background. In contrast the Sco X-1 hard tail (40-70keV) in the SCP3 observation is 3.2 % (4.8σ) above the average background and ~4% above the SCP1 level. The background varies by less than 2.7%, at all energies, over the 0°-51° range of zenith angle. The zenith distance between the SCP1 and SCP3 observations is only two degrees and so any changes in background due to

its zenith angle dependence will be less than 0.25%. The hard tail cannot be due to uncertainty in the zenith dependence of the background.

TABLE 6.6

	40 – 70 keV		70 – 100 keV	
	SCO X-1	BGD	SCO X-1	BGD
	-0.50 ±1.12	-1.21 ±1.11	1.10 ±0.99	-2.40 ±0.95
	1.10 ±1.14	-0.26 ±1.13	2.37 ±1.00	-2.57 ±0.96
	0.99 ±1.14	-0.30 ±1.12	-1.36 ±0.97	-1.23 ±0.97
	0.95 ±1.13	0.18 ±1.12	0.64 ±0.98	-2.61 ±0.97
Flare →	2.58 ±1.13	-3.72 ±1.09	1.84 ±0.98	-0.05 ±0.98
	0.76 ±1.13	0.63 ±1.13	2.38 ±1.00	-0.11 ±0.98
	3.38 ±1.15	1.89 ±1.15	-0.51 ±0.98	0.05 ±0.99
	2.81 ±1.14	1.01 ±1.13	1.17 ±0.98	0.98 ±0.98

The variability of the 40-70keV background was investigated. The largest excursion in the backgrounds from the mean level found during a 5 minute (the SCP3 observation was 5 minutes long) integration was 1.8% (background rate is 77.78 cts/sec) which is consistent with Poisson statistics. For a 5 minute integration of the background the 1σ error is 0.5 cts/sec or 0.66% and 1.12 cts/sec or 1.49% for a 1 minute integration. So in a 5 minute integration a 3σ change in background amounts to 2% change in counting rate. Supposing a 1% error in the background determination for the Sco X-1 pointed observation exaggerates the variation in count rate between the SCP1 and SCP3 data sets and given that the background was underestimated by 1% then the 40-70keV excess tail represents a 2% or 3σ excursion from the true background while the SCP1 40-70keV flux would represent a -2% (-3σ) excursion. Thus the hard tail cannot easily be explained in terms of either of non-Poisson changes in the background or a reasonable error in background determination.

The correct approach to deciding the statistical validity of the hard tail is to consider whether it constitutes a significant change in the spectrum. The difference between the SCP3 and SCP1 observation (40-70keV) is 3.01 ± 0.76 cts/sec which represents 4σ change. The difference between the SCP2 and SCP1 observations is 1.23±0.73 cts/sec (2σ) over the 40 to 70keV range. Similarly the difference between the the SCP3 and SCP2 observation is 1.77 ± 0.73 cts/sec or 2.4σ. Overall there seems to be steady progression in the changes of the spectra of Sco X-1 from a low 40-70keV flux in SCP1 to slightly higher flux during SCP2 to the excess in SCP3. On the 1 minute timescale the change in count rate before as compared to just after the flare is 1.63 ± 1.6 cts/sec which is not significant. Between consecutive ~5 minute pointed observations of Sco X-1 there is a marginally significant change in the 40-70keV flux. Over the entire pointed observation (SCP1 compared to SCP3) there is a significant change. Thus it can be said that the hard tail represents a significant change in the spectrum and appeared over a timescale of ~10 minutes.

As a further test, the escape gated mode was used on the Sco X-1 pointed data See Figure 6.18 for the PHA spectra. During the flare there was no increase in the escape gated (i.e. doubles) count rate. There was an increase during the SCP3 observation. One scenario for the hard tail is that the flare was followed by a period of high energy pulses. It is unlikely that any spurious pulses would be pairs of events: one with an energy near 30 keV. Note also the gradual change from little or no excess in SCP1 to a slight excess in SCP2 to a significant excess in SCP3.

In summary the hard tail, represented by a flat power law, seen between 4:58 and 5:03 UT is not an effect of the anomalous flare event since the excess flux in the 40-70keV range is also seen in the escape gated mode. Also a comparison with a similar event during a background observation shows no similar hard excess afterwards. The Sco X-1 tail represents a 4.8 σ (3.2%) excess above the average background level. This is larger than any fluctuations seen in the background and much larger than any possible systematic error in estimating the background. The hard tail appeared on the fastest yet reported time scale i.e. ~10 minutes. In conjunction with the appearance of the hard tail was an increase in the flux level and the appearance of strong red noise in the power spectrum of Sco X-1

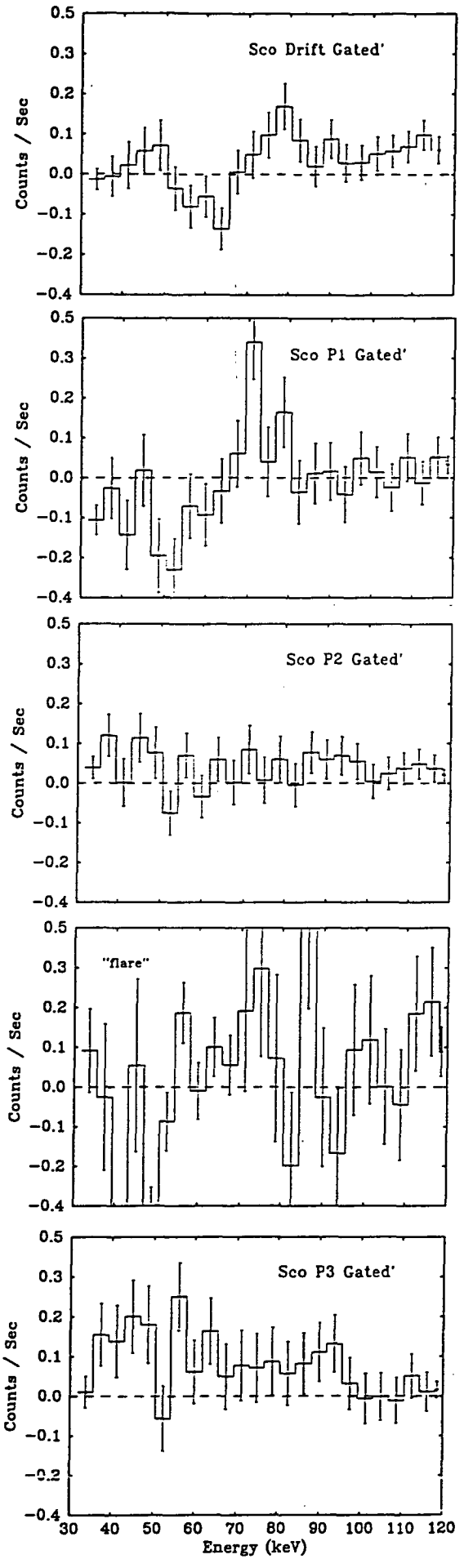

Fig 6.18 Gated mode PHA spectra showing the gradual appearance of the hard tail. There is little or no flux during the SCP1 observation while there is a slight excess during SCP2. The flare contains no gated mode counts. The SCP3 observation shows a definite excess. The background observations used are the same as used for the normal mode PHA spectra.

The temperatures determined for the Sco X-1 observations are similar to previous reported values. The intensity during the drift scan is amongst the lowest observed being comparable to the flux levels during the UTIC 1983 flight (Beurle et al. 1983) and Matsuoka (1972). The flux increases to an approximately average level during the pointed observation. The flat power law fit to the hard tail is similar to that found by Duldig et al. (1983). The present observation is therefore intermediate between the results of Haynes et al. 1972 (α=1.8, or kT=190 keV) and Greenhill et al 1979 (kT = 35 =± 5keV). An attempt to fit a extra thermal component to the data became unstable with the value of kT approaching infinity.

The hard tail is a highly variable and rare phenomenon; of the 32 separate hard X-ray observations surveyed there are only four other reported detections (Matsuoka 1972, Riegler et al. 1970, Greenhill et al. 1979 and Duldig et al. 1983). The upper limits set by Jain et al. (1984), Johnson et al. (1980) and Lewin et al. (1970) are a factor of three to ten below the flux levels observed here and by Greenhill et al. (1979), Riegler et al. (1970) and Duldig et al. (1983). This is a larger than the variations seen at lower energies. Flux changes of 100% have been seen during flares at energies below 30keV. Variability at 50keV on a timescale of 20 minutes have been reported by Duldig et al. (1979) and Matsuoka (1972). In the observations presented within this thesis the hard tail appeared on a time scale less than 10 minutes which is the fastest reported.

There have been reports of other sources displaying a hard tail. Of these Nova Oph (H1705-250), H1743-322, H1833-077 (Cooke et al. 1984), A0620-00 (Coe Engle and Quemby 1976) are soft X-ray transients while χ Per (Worrall et al. 1983) and GX339-4 are, respectively, a massive X-ray binary and a black hole candidate. Only A066-00, χ Per and GX339-4 have a two component spectra with the break at greater than 20keV. Cooke et al. could not find any trace of a hard tail from A066-00 at any phase of its 16 day cycle using the SAS data. This casts doubt upon earlier reports.

The soft transients and GX339-4 are considered similar to the Sco X-1 system; all being LMXB's powered by Roche lobe overflow. However, in Sco X-1 the mass donating star is evolved beyond the main sequence while the others are main sequence red dwarfs. This difference results in higher accretion rates and hence higher luminosity.

Two basic models have been proposed to explain hard X-ray tails. The models of Alme and Wilson (1973) and Zelodovich and Shakura (1969) consider spherical accretion onto a neutron star. Electrons in a hot shell surrounding a cooler atmosphere Compton scatter off the emerging photons distorting their spectrum above 10keV. The more detailed calculations of Alme and Wilson suggest that only low mass (<0.5 $M_\odot$) neutron stars at low accretion rates produce hard tails. This model seems untenable for Sco X-1 because of the high accretion rate required to produce the observed high luminosity. Also the hard tail has been seen during flaring episodes where the accretion rate is expected to be at its highest.

The other possible model is where a hard source is surrounded by a cooler corona. The thermal part of the final spectrum arises from Compton scattering of the emerging hard X-rays by the corona electrons while the hard tail is due to glimpses of the central source. A corona with $\tau>10$ is required to explain the width of the iron K line, the detailed shape of the thermal spectrum and to smear any beamed emission from the neutron star. The present observations require some mechanism for clearing the surrounding cloud on time scales of minutes. The other possible source of hard X-rays is the hot spot (Coe et al. 1980). Being near the edge of the accretion disk it could be uncovered more easily and rapidly. In this case there should be an orbital modulation in the appearances of the hard tail and further historical data. The phase plot of Duldig was extended to include the results presented in this thesis. No orbital modulation was apparent.

6.6.3 Intensity Temperature Relation

At energies below 20 keV there is a well documented (see Miyamoto and Matsuoka 1979 for a review) correlation between intensity and temperature. At higher energies this relation has not been observed (Matsuoka et al. 1972, Rothschild et al. 1980, Soong and Rothschild 1983, and Jain et al. 1984). An initial look at the thermal bremsstrahlung fit parameters (this thesis) suggest a positive I v kT relation. The trend is broken when an additional power law component is fitted to the hard tail of the SCP3 observation. Also the 90% confidence ranges for kT overlap and so all the Sco X-1 observations can be satisfied by a constant temperature between 5.0 and 5.4 keV. Thus there is no statistically significant trend. A similar situation is apparent in the results of Jain et al. (1984).

Beurle et al. (1983 in preprint version) after compiling many other observations suggested that there is a case for a steep inverse I-kT correlation. This is in the

opposite sense to the trend at lower energies. Such behaviour can be explained if the spectrum pivots about an intermediate energy. Such pivoting is a natural consequence of Compton scattering.

Figure 6.19 is a compilation of the available hard X-ray spectral observations of Sco X-1. It is in the form of an intensity-hardness diagram (HID). A similar diagram for low to medium energies is shown in Figure 3 of Priedhorsky et al. 1986). The value of Buselli et al. (1968) is affected by the presence of a hard tail. If the shift in derived kT, found when an additional power law tail is included in the spectral model (these results and Duldig et al), is applied the final value of kT is similar to the majority. This shift is applied in the diagram. For our results (AS86) and those of Duldig et al. (1983) the value of temperature used is that found when a hard tail component is included in the spectral analysis. The value of Agrawal et al. (1969) is really an upper limit because it is based upon the lack of any low energy counts and is not included. Figure 6.19 does include the individual measurements made by Matsuoka et al. (1972). Our observations (AS86) are located in the lower left hand corner of the plot. The error bars are those quoted by the authors or estimated from the data. The errors of some points could were not given in the literature and could not be reliably estimated. These are the most unreliable data in Figure 6.19.

There seems to be two branches; an almost vertical leg and a level leg reaching high intensities. This pattern is very similar to the two branched hardness-intensity diagrams found at medium (2-20keV) energies. If this similarity is true then the level branch of Figure 6.19 corresponds to the flaring branch while the vertical leg would correspond to the normal branch. However there are several uncertainties with this interpretation. Some observation (e.g. Duldig et al., Jain et al.) which fall in the vertical leg were apparently made while Sco X-1 was in the active state as evidenced by the rapid 10 second - to minute variability. Also the high kT values at high intensities may be affected by the spectral form used. To confirm this correspondence between the behaviour at medium and hard energies long term wide bandwidth X-ray observations of Sco X-1 are required.

If this interpretation is correct then Sco X-1 moved up the normal branch during the AS86 observations.

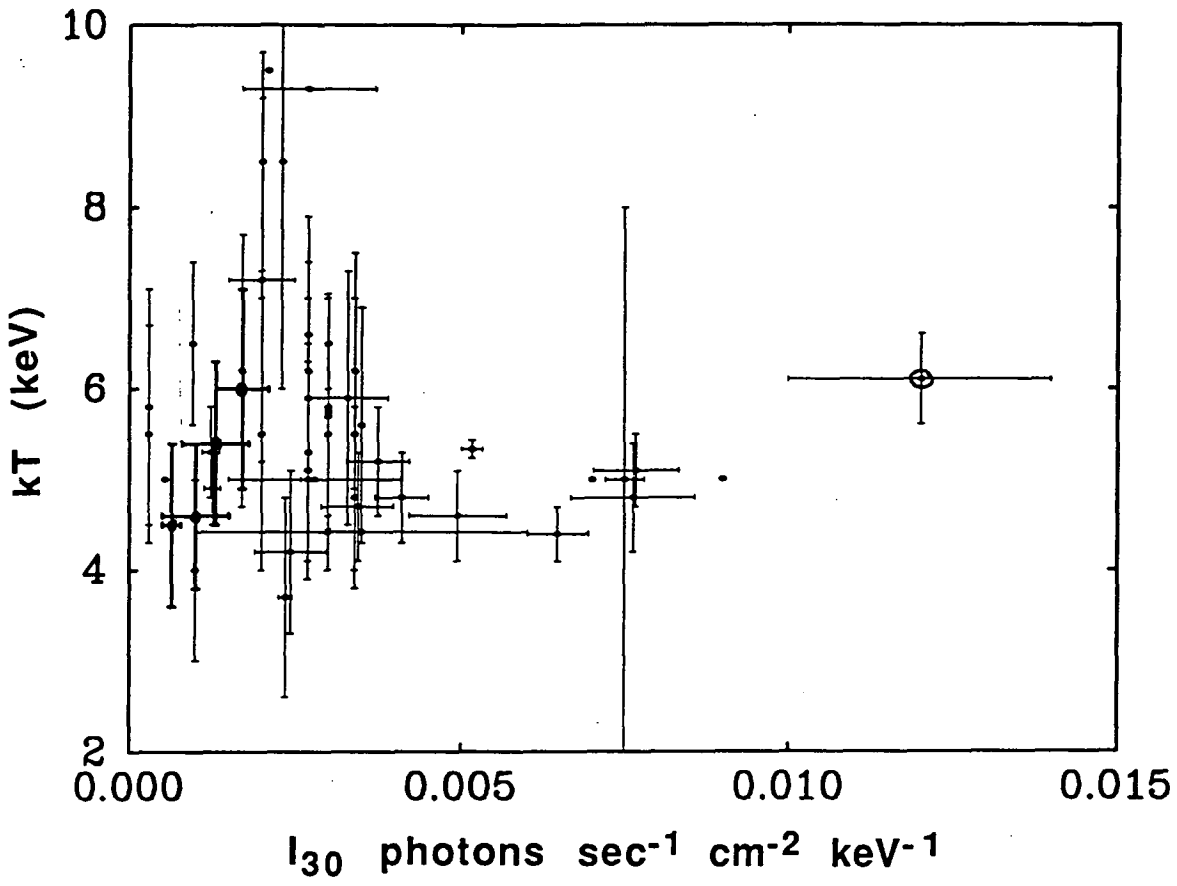

Fig 6.19 A plot of the historical data of temperature versus source intensity. The results presented within this thesis are the highlighted points in the lower left hand corner. The corrected point of Burselli et al. (1968) is circled and can be found to the extreme right. The 1 σ error bars are either those quoted by the authors or estimated. Errors for some points could not be determined. Data is taken from Johnson et al. (1980), Jain et al. (1973), Greenhill et al. (1979), Riegler et al. (1972), Peterson and Jacobson (1966), Duldig et al. (1983), Agrawal et al. (1971), Lewin Clark and Smith (1968), Overbeck and Tananbaum (1968), Lewin et al. (1970), Beurle et al. (1983), Matsuoka et al. (1972), Rothschild et al. (1980), Jain et al. (1970), Kasahara (1974), Damle et al. (1987).

6.6.4 Temporal Analysis

The possible detection of a 2.95 millisecond coherent periodicity is very important. It would provide direct evidence of a rapidly spinning neutron star, which is a requirement of the beat frequency model for the QPO. However, this detection relies upon the improvement in sensitivity gained by narrowing the frequency range searched. Without the reported period of Leahy (1987b) as a guide no significant period is found in the 1986 Sco X-1 data. Only a weak upper limit of about 8% rms can be set over the 100-500Hz range which is completely consistent with previous upper limits.

At energies below 20keV Sco X-1 and other LMXB's show a pattern of spectral and correlated QPO/red noise behaviour. Interpreting the high energy (>20keV) behaviour of Sco X-1 in terms of the "Z" source pattern (see Review sections 2.3.2 and 2.3.3 about QPO in general and section 2.42 about Sco X-1 in particular) relies upon two assumptions. Firstly that the intensity above and below 20keV are correlated and secondly that QPO/noise in both spectral regions are present and behave in the same manner. There seems to be correlation between the flux at high and low energies e.g. figure 3 of Soong and Rothschild (1983). However there are very few experiments that cover this energy range. The QPO and red noise have been noted as having a spectrum harder (larger percentage of flux at higher energies) spectrum than Sco X-1 in general (Priedhorsky et al. 1986). At present there has not been a detection of any QPO at high energies. This work (a preliminary report is given in Greenhill et al. 1990) and that of Damle et al. (1987) are the only searches so far undertaken.

The data presented here suggest a correlation between state and hard X-ray flux and and red noise behaviour. There was little (<1.8% 0-0.1Hz) red noise while Sco X-1 was faint while there is broad, strong (≈19% < 5Hz) red noise and moderate (2.7% <0.1Hz, 8% <1Hz) VLFN when Sco X-1 was bright. The excess noise (0-5Hz) detected during the SCP3 section of data is stronger than that seen during either the horizontal branch (Hasinger Priedhorsky and Middleditch 1989) or the flaring branch (Lewin, van Paradjis, van der Klis 1987 review). The LFN is comparable to that previously observed during the horizontal of flaring states.

The upper limits for any QPO, the red noise detections and the general flux changes are consistent with one of two interpretations in relation to the "Z" source pattern.

In the first case Sco X-1 is supposed to have made a rapid transition from the quiescent to the flaring state during the 20 minute pointed observation. Such transitions have been observed to occur within a few minutes (Priedhorsky et al. 1986). This scenario requires that any QPO's would have been changing rapidly in frequency and hence undetectable with the five minute integrations used. The <5Hz and <1Hz red noise components would correspond directly to similar components seen at lower energies. Comparing the strengths with previous reports suggest that both noise components have a hard spectrum up to 40 keV. Any 6Hz QPO which should have been visible while Sco X-1 was faint (drift scan) would need to be weak (<2.4%). This limit is well below the typical QPO intensity (4-6%) during the quiescent state. This discrepancy suggests that Sco X-1 was not in the lower part of the quiescent/normal branch and hence this scenario is untenable or that the QPO spectrum turns over at ≈20 keV. This behaviour is opposite to that implied for the red noise. This difference in spectra would imply different emission regions for the flaring branch QPO and red noise. This is contrary to the model of Lamb (1989). In this model (see review section 2.3.3) the normal and flaring branch QPO are caused by oscillations near the neutron star. The flaring branch red noise is supposed to be produced by the same oscillations becoming unstable and thus exciting a large range of frequencies.

The other possibility is that Sco X-1 made a transition along the normal branch to the horizontal branch. The 0-5Hz red noise would then correspond to a similar noise component that gave rise to the "2Hz" feature (Hasinger Priedhorsky and Middleditch 1989) and the 0-0.1 Hz and 0-1.0 Hz noise would be the LFN. Comparing our observed noise strengths with previous reported levels of the 2Hz feature (19% cf 4%) and LFN (2.4-8% cf 0.1%) during the horizontal branch strongly suggests that both noise components have a hard spectrum relative to the general Sco X-1 spectrum up to at least 40keV.

6.7 Conclusion

During the observations presented, Sco X-1 underwent a steady increase in brightness. The initial brightness, during the drift scan, is amongst the lowest reported. Mostly the spectrum could be well fitted by a thermal bremsstrahlung (with energy dependent Gaunt factor) with a temperature near 5keV. This is similar to previous measurements. However, in the last 5 minutes of the observations, when Sco X-1 was brightest, a hard (40-70 keV) X-ray tail was evident. Comparisons with observations in the previous 15 minutes suggest that the tail

appeared on a timescale of approximately 10 minutes. This is the fastest timescale reported for the appearance of a hard tail. The tail could be well represented by a flat power law. It represents an excess of 3% or 4.8 σ above the background. The excess representing the tail is larger than any fluctuation observed in the background and much greater than any systematic errors in the background determination. Gated mode observations also show the hard tail, thus ruling out any possible instrumental effect as the cause of the hard excess.

An apparent positive relationship between the intensity at 30 keV and the temperature is not significant at the 90% level. All the AS86 spectra are consistent with a constant temperature of 5.2±0.2 keV (90% confidence). A compilation of hard X-ray observations of Sco X-1 tentatively show a two branched hardness intensity diagram (HID) with the same form as that seen at lower energies. If the comparison between the two data sets (hard and medium energy HID) is valid then the position of the AS86 data on the hard X-ray HID suggests that Sco X-1 was moving along the normal branch.

In this case the observed strong red noise (0-0.1Hz 2.4%, 0-1.0Hz 8%, 0-5.0Hz 19%) when Sco X-1 was brightest, would correspond to the 2Hz feature and LFN seen by Hasinger, Priedhorsky and Middleditch (1989). A comparison of the observed noise strengths implies that the spectrum of the noise component is harder than the overall Sco X-1 spectrum up to 40 keV. The lack of any QPO's (upper limit <2.7%rms) can be explained if Sco X-1 was initially (drift scan) in the upper part of the normal branch where no medium energy QPO have been reported. If during the drift scan Sco X-1 was in the lower part of the normal/quiescent branch where <20 keV 6Hz QPO have always been observed, then the upper limit of <2.7%rms (90% confidence) suggests that either the 6Hz QPO were unusually weak or that the QPO spectrum turns over near 20 keV. If the latter is the case then this in combination with our observation of hard spectrum red noise would imply two separate emission regions for the QPO and red noise. This is at variance with the most widely accepted model for the origin of the QPO/red noise.

An alternative interpretation of our results is that Sco X-1 was making a transition from the quiescent/normal branch through the intermediate state to the active/flaring state. This case ignores the similarity of the I_{30}-kT diagram (Figure 6.19) with medium energy hardness intensity diagrams. The strong red noise observed during the AS86 flight would correspond directly to similar noise components seen at lower energies. The inferred energy spectrum of the noise remains harder than the

non-noise spectrum up to 40 keV. If the hard energy QPO/red noise behaves the same way as those at <20 keV, then no flaring branch QPO are expected when there is strong red noise present. In this scenario the SCP1 and SCP2 observations were made while Sco X-1 was in the intermediate state where the QPO frequency changes rapidly. Hence the QPO would not be detectable using the 5 minute integration of our observations and could not be detected using shorter integrations because of the lower sensitivity. The drift scan must correspond to the quiescent state. Here the upper limits of 2.7%rms to any 6Hz mode QPO strongly suggests that the spectrum of the QPO turns over near 20 keV which, as mentioned earlier, has serious consequences for current theories.

Also observed while Sco X-1 was bright was a possible 2.93, 3.4%rms periodic modulation. This could be the rotation period of the system's neutron star. However, caution is warranted since this detection relies upon the ability to restrict the frequency range searched by using the prior, Leahy (1987b), detection as a guide. Similar searches have failed to detect this period and so either the periodicity does not exist or the modulations is variable in strength. Obscuration by an overlying Compton scattering cloud could easily mask the pulsar signal. An outburst that cleared the cloud allowing both the hard tail and pulsar to be seen is possible. Outbursts of some sort are required to produce the radio frequency bursts and the two extended radio lobes. The detection of the pulsar spin period would be a major confirmation of the beat frequency models and would provide a means to refining these models.

Chapter 7

Optical Fast Photometry of Sco X-1

I know the stars
are wild as dust
and wait for no man's dicipline
but as they wheel
from sky to sky they rake
our lives with pins of light.

Leonard Cohenn
'Another Night with Telescope'

Twinkle, Twinkle little star,
How I wonder what you are,
Up above the world so high,
Like a diamond in the sky.

Jane Taylor
"Rhymes for the Nursery"

7.1 Introduction

Most early photometric observations of Sco X-1 (Petro et al.1981 and references therein) had insufficient time resolution to detect any QPO equivalent to those seen at X-ray wavelengths. They, however, established the bimodal behavior of Sco X-1. When Sco X-1 is brighter than m_b=12.7 it is found in an active, flaring state. The flares last of the order of minutes with the fastest timescale being 20 seconds. Also in the high state the optical and X-ray flux is generally well correlated. As Sco X-1 fades the optical/X-ray flux correlation becomes much weaker and the general timescale of flux variations becomes longer ($\gtrsim$1/2 hour).

It is when Sco X-1 is faintest, either between flares or in the quiescent state that the X-ray QPO's have been observed. The 6 Hz (generally 4-6%rms in amplitude) QPO are seen during the faintest part of the quiescent state while the 7-18Hz (6-10%rms) QPO's are seen during state transitions, and 11-20 Hz (5-10%rms) QPO are observed in the intensity dips between flares in the active state. In the upper part of the quiescent branch no QPO are observed. Recently a third spectral state has been reported (Hasinger, Priedhorsky and Middleditch 1989) .This state is characterized by constant hardness with decreasing intensity and a 2 Hz (4%rms) feature was found in the power spectrum. This is called the horizontal branch. During the quiescent state there is <2%rms VLFN (<1 Hz) but the red noise reaches up to 5.5%rms during flares in the active state. Variable strength X-ray, VLFN (<0.03 Hz) is evident in the power spectra of Kesterman et al. (1971).

Several early optical observations have been undertaken to search for coherent periodicities. As in similar X-ray searches no underlying periodicities have been found. Of these only two had sufficient time resolution to detect 6-20 Hz QPO's. Auto-correlation analysis by Frohlich (1973) indicated the the optical variations on time scales between 4 and 320 msec were consistent with white noise. The power spectra of Lampton, Bowyer and Harrington (1970) show an exponential decline in power out to about 100 Hz with no obvious sign of any broad features. Other optical searches (Feldman, Gribben and Plagemann 1970, Lasker and Hesser 1970, Robinson and Warner 1972) showed an exponential like decline of power with frequency reaching a base level by about 0.03 Hz. Frohlich (1972) gives a brief summary of the early optical period searches.

Several observers have noted transient periodicities. A 160 sec period was found following a flare by Gribben, Feldman and Plagemann (1970). A similar

periodicity was observed by Robinson and Warner (1972). The latter concluded that during flares the lowest frequency components died out first resulting in an apparent peak in the power spectrum when compared to the non-flare exponential spectrum. A 20 sec correlated X-ray/optical period lasting only 136 sec was found by Kesterman et al. (1970). This period could be related to the frequency break at 20 sec which corresponds to the shortest flare timescale. Frohlich (1973) found a ≅120 sec ,<1% amplitude, modulation that persisted from night to night. A similar period was noted by Lampton, Bowyer and Harrington (1970). This periodicity was rejected by these authors because the period was unstable. Similar long quasi-periods have been observed in several other LMXB. These are listed by Lewin, van Paradijs and van der Klis (1988). They are generally considered to be of a different origin from the high frequency (5-50 Hz) QPO's, being possibly related to the QPO seen in cataclysmic variables.

After the discovery of X-ray QPO several attempts were made to detect similar QPO's at optical wavelengths. None of the searches have been published except for a brief mention by Warner (1988) who found a 6 Hz feature that corresponded to the vibration frequency of the telescope used. Middleditch, Imamura and Steinman-Cameron (MIS1986), in a preprint, reported the discovery of excess optical red noise above that expected from atmospheric scintillation. Unfortunately the absolute size of the red noise excess was unknown because no standard star was observed. Also they reported a 12-18 Hz, 2% rms, broad feature in one observing run. However this run was at a high hour angle raising the suspicion of an atmospheric effect. These observations were made on May 21, June 4 and June 6 1985.

On the 12th and 13th March 1986, fast photometry was undertaken simultaneously with EXOSAT observations of Sco X-1 (Hasinger, Priedhorsky and Middleditch , HPM 1989)

The optical observations were carried out by Dr. I Tuohy at Siding Springs and Kym Hill, Dr. A.B. Giles , Dr. R.D. Watson and the author at Mt Canopus. The Siding Springs data was taken with the 2.4 Metre telescope at a time resolution of 2 millisec. The power spectra of the Siding Springs data showed no broad features at any time but showed steep low frequency noise below 4 Hz. This is entirely consistent with atmospheric scintillation. The Siding Springs data is marred by variable frosting upon the photometer window thus making any

comparison with the X-ray data or the determination of percentage limits for any QPO or red noise impossible.

7.2 Observations and Analysis

A single channel photometer (S20 response) was used on the Mt. Canopus 1 metre telescope. Observations were made in 'white light' with an integration time of 20 milliseconds through a 40" aperture. By using VNG signals we have absolute timing to within five milliseconds. An observing log with approximate (nearest minute) start and stop times and average sky subtracted count rates are given in Table 7.1. The light curve after sky subtraction and an approximate extinction correction is shown in Figure 7.1a. The average 'white' magnitude is 12.5 ± 0.1. This magnitude estimate cannot be used to establish the state of Sco X-1 because of the unknown difference between our "white" magnitude and the standard Cousins B magnitude and the uncertainties in the extinction correction.

Both the GSPC and ME detectors on EXOSAT were used to observe Sco X-1. Except on two occasions Sco X-1 was in the upper part of the quiescent branch. On one occasion Sco X-1 entered the horizontal branch. On the other occasion between 16 and 23 hours UT 13th March the source dipped into the lower part of the quiescent state and 6 Hz (1.3-1.6%rms) QPO were observed. Runs C and D overlap with this period while run B is during the transition between the upper and lower parts of the quiescent state. A plot, based upon figure 2 of HPM1989, showing the 1-17 KeV light curve is given in Figure 7.1b. As can be seen by comparison with Figure 7.1a the optical/X-ray correlation is not exact.

After editing to remove tracking errors contiguous 1024 point FFT's were performed upon each uninterrupted block of data. The power spectra were then averaged giving a single power spectrum for each observing run. Before fitting, the power spectra were binned into half Hertz intervals. The normalization used is that of Leahy et al. (1983) in which a single FFT of Poissonian (or normal) white noise has a flat power spectrum with a chi-squared distribution about a mean of two and with a variance of 4/NW where N is the number of transforms and W is the degree of frequency binning.

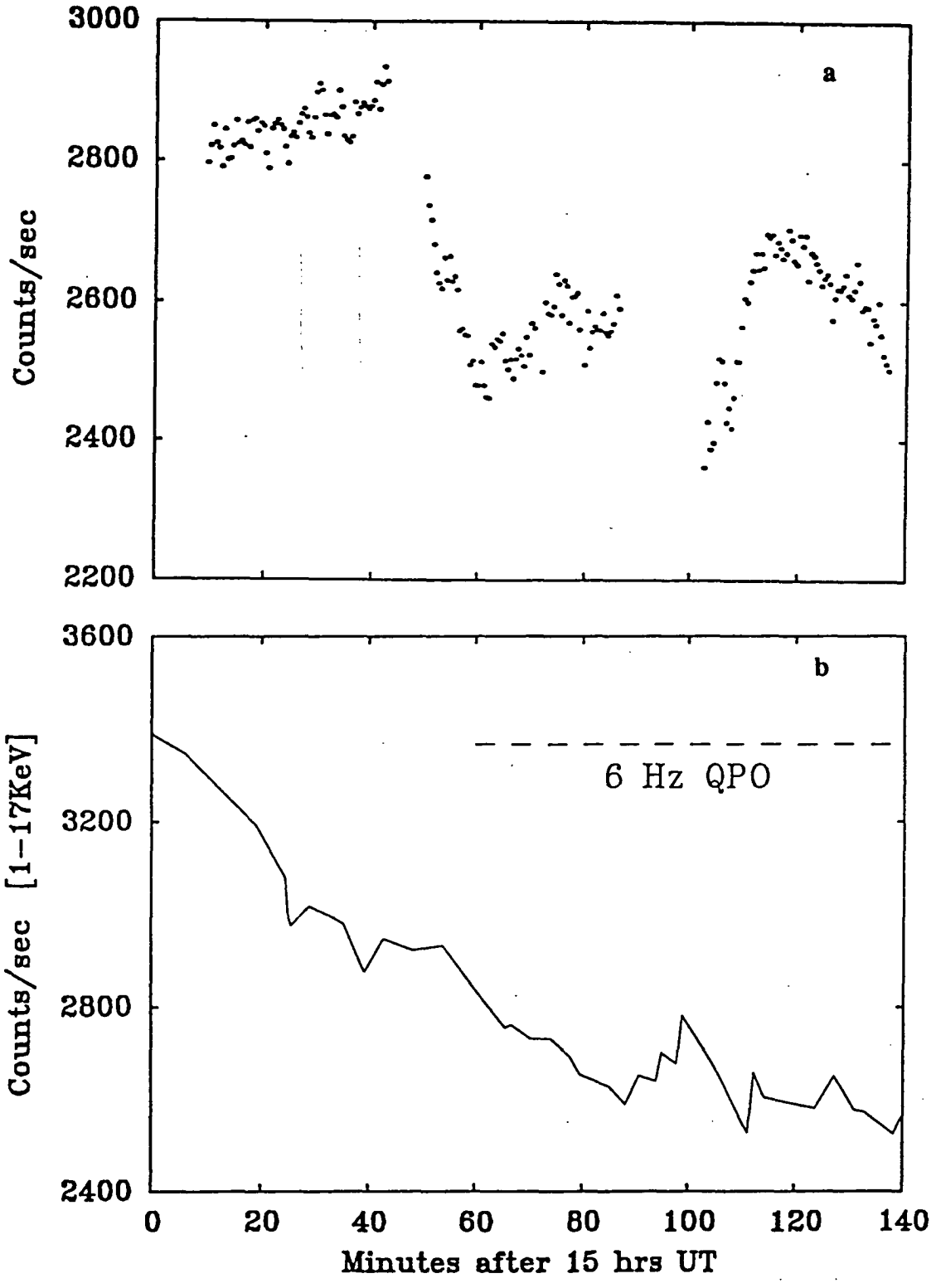

Figure 7.1 The X-ray, 1-17 keV, light curve is based upon figure 2 of Hasinger Priedhorsky and Middleditch (1989). The period when X-ray 6 Hz QPO were observed is marked. The optical "white" light curve has had the sky background subtracted and an approximate extinction correction applied. Each point is a 10 sec integration.

Table 7.1

Run	UT Time Start h m	UT Time End h m	N_{1024}	Total Cts/sec	Excess Cts/sec	A	B	χ^2_{48}	RED_t % rms	S/N	ZEN°
Sco X-1											
B	15 10	15 10	98	6349 ±2	1689 ±2	15.3 ±5.3	62 ±27	1.29	4.91±0.83	2.87	54.5
C1	15 50	16 11	62	6200 ±3	1675 ±3	9.6 ±2.1	32 ±9	1.27	3.93±0.41	3.08	49.3
C2	16 12	16 19	22	6283 ±5	1823 ±5						46.8
C3	16 20	16 26	21	6289 ±2	1823 ±5						44.4
C			105	6341 ±2	1741 ±2	11.4 ±2.0	37 ±8	0.38	4.24±0.36		
D	16 42	17 16	101	6463 ±2	2173 ±2	17.1 ±5.5	61 ±24	1.38	5.14±0.77	3.60	39.8
C+D			206	6401 ±1	1953 ±1	13.5 ±2.2	46 ±10	0.35	4.59±0.34		
All			304	6384 ±1	1868 ±1	13.9 ±2.3	50 ±10	0.30	4.66±0.38		

Run	UT Time Start h m	End h	N_{1024}	Total Cts/sec	Excess Cts/sec	A	B	χ^2_{48}	RED_t % rms	S/N	ZEN°
Comparison Stars											
A1	17 22	17 34	37	11071 ±4	6394 ±5	6.8 ±0.85	17 ±3	0.98	2.48±0.15	9.28	34.7
A2	17 35	17 49	39	11055 ±4	6935 ±5	7.4 ±0.67	12 ±2	1.29	2.59±0.11	9.27	33.0
A			76	11063 ±3	6916 ±3	7.1 ±0.56	14 ±2	0.68	2.53±0.10		
B	10 05	10 37	91	6517 ±2	6004 ±2	10.9 ±2.2	39 ±10	1.22	4.09±0.39	10.52	28.2
C	10 58	11 31	94	2014 ±1	1554 ±9	51. ±9.	78 ±16	1.29	15.91±1.36	4.90	27.6

Table 7.1

Sco X-1 and Star A were observed on the 13th March 1986 (JD 244 5407.1) and the comparison stars B and C on the 15th July 1987 (JD 244 699.9).The 1 sigma uncertainties are based upon the assumption that the χ^2 is approximately linear with respect to the parameters in the vicinity of the minimum.

Since the counting process is expected to be Poissonian the power spectra were fitted, (using the non-linear least squares method of Powell and Macdonald 1972) with an exponential of the form

$$P(f) = \frac{A}{B} \exp\left[- \frac{f}{B} \right] + \text{base} \qquad 7.1$$

The base noise level is fixed at 2.0. The constants A and B are the integral above the base level and the e-folding frequency respectively. The uncertainties quoted, in Table 7.1 are the standard errors. These should be a reasonable estimate of the 1 σ errors estimated because the residuals are approximately normally distributed and the exponential function is linear in its parameters.

Recalling Equation 3.32 the red noise rms percentage of the total count rate ($RED_T\%$), corresponding to A, is given by

$$RED_T\% = \sqrt{\frac{A}{I_{mean}}} \qquad 7.2$$

where I_{mean} is the average total (source + sky) counting rate per sec. To calculate the percentage of the source signal, I_{mean} is replaced by the the sky subtracted count rate. The correction for the dead time is small (<3% of $RED_T\%$) and so is not used. Also, the red noise is spread in frequency and so the binning correction is not applied to the values in Table 7.1. Also shown in Table 7.1 are the results for the nearby comparison stars.

The power spectrum of comparison Star A, observed on the same night as Sco X-1, drops toward the base level of two. For Sco X-1 the power is also decreasing but much more slowly (Figure 7.2a), with excess power above that of the standard star out to at least 25 Hz (Figure 7.2b). In Figure 7.2b the excess percentage noise is integrated over frequency and normalized with respect to the total count rate as per Equation 7.2.

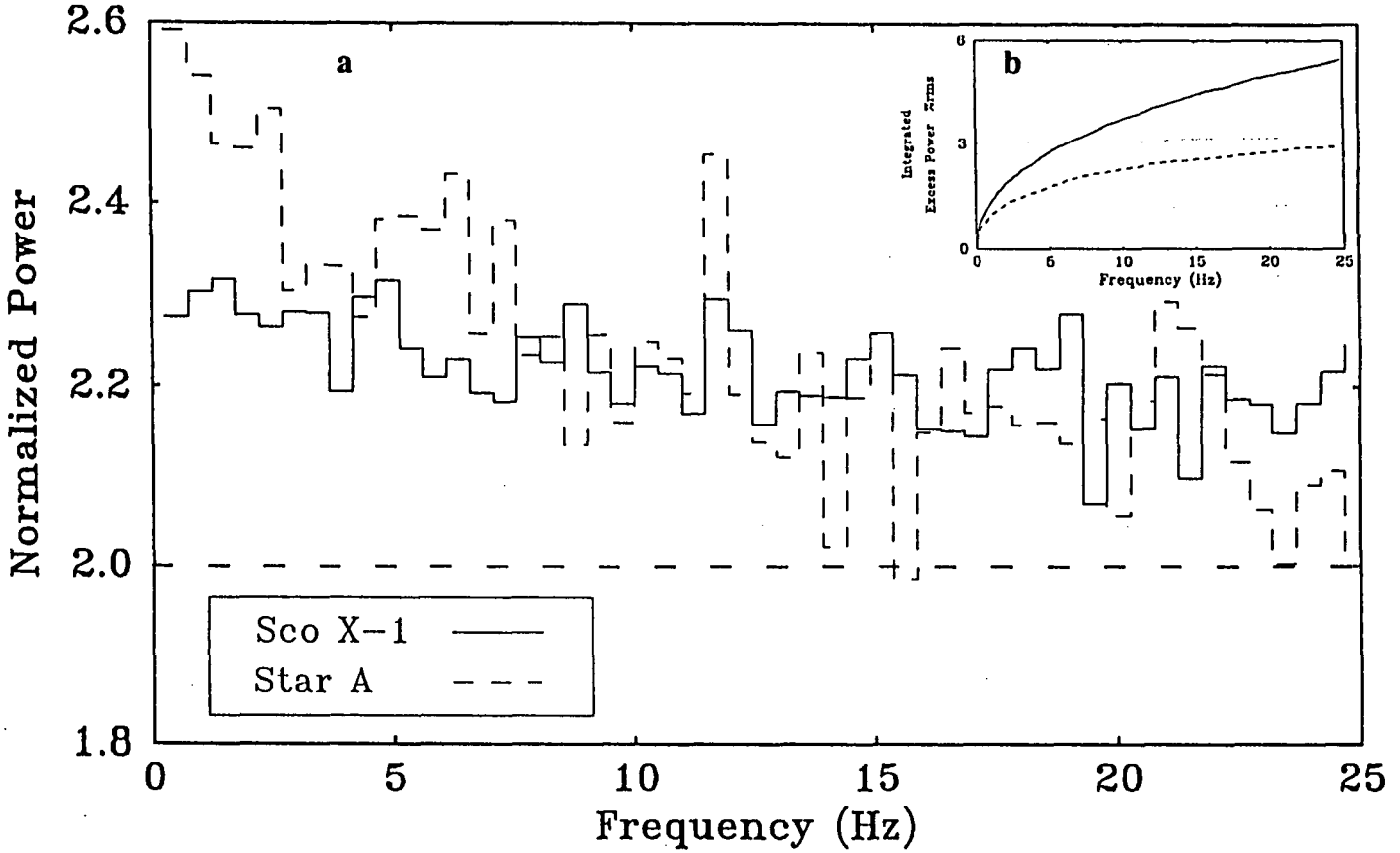

Figure 7.2 The average power spectra, normalized according to Leahy et al.. (1983), of Sco X-1 and the comparison Star A. The insert shows the integrated excess power above the expected Poisson noise level. This is normalized as an rms percentage of the total count rate.

The power due to atmospheric turbulence has been shown, both theoretically and observationally, to be independent of star brightness (Warner 1988 and references therein). This is true if all of the light from the star is included within the photometer aperture. If this is not the case, or the star is poorly centered, a brighter star will be more susceptible to seeing noise because scintillation will scatter more light out of the aperture. A fainter star's seeing disk would remain substantially within the aperture. Thus the red noise percentage obtained from the power spectrum of the Star A (brighter than Sco X-1) data will be an upper limit to any atmospheric contribution to the red noise observed from Sco X-1. The red noise from Star A is 2.5 ± 0.1 %rms which is well below the average for Sco X-1 of 4.7 ± 0.4%rms. Accordingly Sco X-1 apparently has intrinsic optical red noise of at least 2.1 ± 0.1 % rms over the 0-25 Hz range. In contrast data collected contemporaneously by Tuohy (1987 private communications) show no red noise above a few Hertz: a result consistent with purely atmospheric scintillation.

Compared to the 2·4 Metre data, the Mt. Canopus observations are expected to show a lower amount of atmospheric scintillation power because of scintillations $D^{-7/3}$ dependence upon telescope diameter (Young 1967). The difference in e-folding frequency between the Mt Canopus (50 Hz) and Siding Springs (~2Hz) power spectra can be explained in terms of the properties of atmospheric scintillation.

When plotted upon a log-log graph the power spectrum of scintillation shows two regions. Below a cut-off frequency , where the telescope aperture acts as a low pass filter, the power per Hertz is constant. Above the cut-off frequency the power per Hertz falls rapidly with peaks due to diffraction effects. A secondary mirror acts as a second aperture giving a second cut-off frequency approximately doubling the high frequency scintillation noise. The cut-off frequency is given by V_{wind}/D where V_{wind} is the wind velocity at ~10km height (where turbulence has the greatest impact upon seeing).

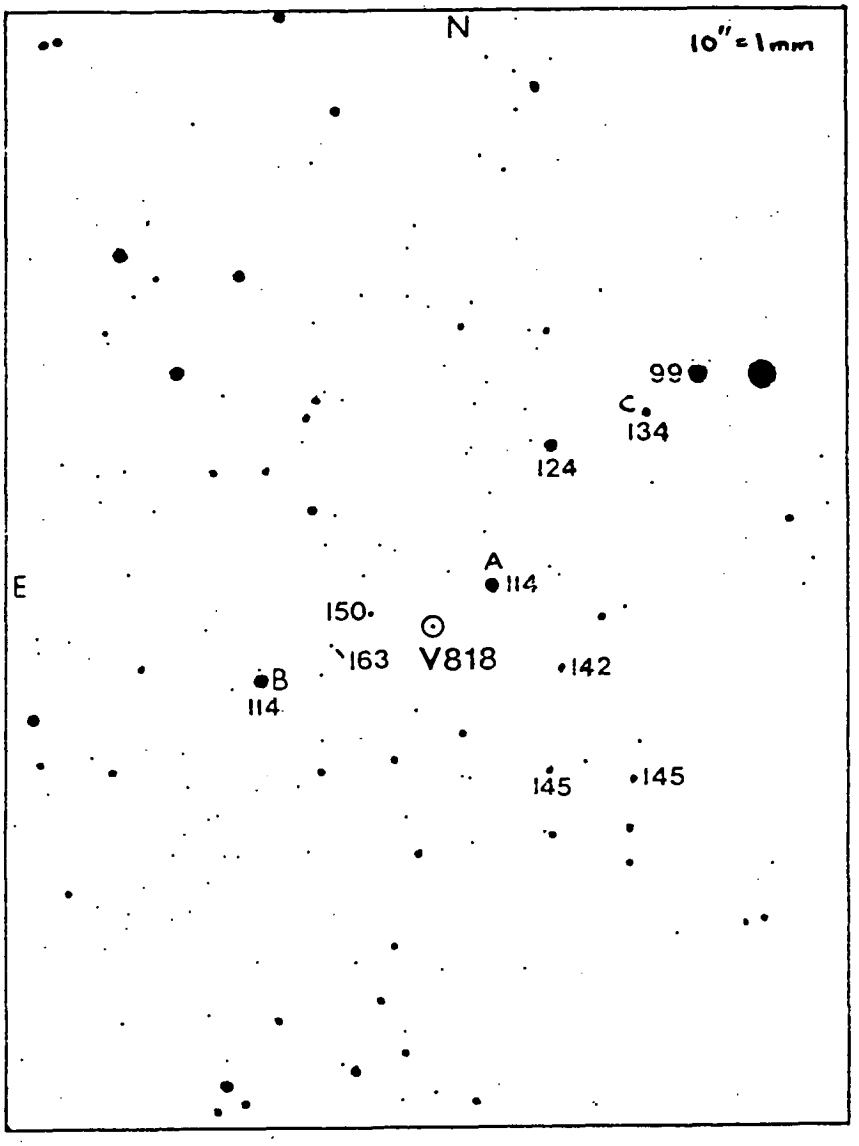

Figure 7.3 Finder chart based AASVO chart 387 identifying the comparison stars used. The magnitudes are visual and are given to the nearest 0.1 magnitude.

The high altitude wind would need to be a factor of twenty greater at Hobart to explain the higher cut-off frequency of the Mt Canopus data as compared to the Siding Springs data. A 50 Hz cut-off frequency on a 1 meter telescope requires a wind speed of 180 km/h. High altitude winds of this speed are quite common especially near the equinoxes when the jet streams tend to move south. The lower e-folding frequency seen for the brighter Star A, between runs C and D, suggests that atmospheric scintillation did not produce the extra red noise seen in the Mt. Canopus data. There also seems to be progression to lower e-folding frequency with increased signal to noise ratio (Sco X-1, Star A , 2.4 Meter data)

In order to investigate this possibility two other standard stars, identified in Figure 7.3 (Star B, C), were observed with two channels at 50 Hz on the night of 15th July 1987 using a 21" aperture. Sky conditions were similar to those prevailing on the 13th March 1986. However, both standards were observed at smaller zenith angles. Also the data collecting equipment was substantially different in form but not in function. The new observing system records data onto 20 Mbyte hard disk using a PDP 11/40 computer instead of a floppy disk using an LSI 11. This setup is a major improvement allowing more data to be collected and hence faster sampling rates (up to 5 KHz) to be used. At present no absolute start times are available with the new system. For further details see Hill (1988). The standard star data was processed in the same way as the original Sco X-1 observations. The results are also given in Table 7.1. The fainter (13.4 V mag), Star C, has a much higher red noise level compared with Star B (11.4 V mag) which is higher than that of the highest count rate comparison Star A (11.4 V mag) during the earlier observations. Clearly there is some instrumental effect producing an inverse relation between count rate and the measured red noise level. There is no similar relation between signal/noise and the red noise. This can be seen from the higher signal/noise obtained for Star B (a smaller aperture was used on a darker night) when compared to Star A or Sco X-1.

The origin of this count rate-red noise relation can plausibly be explained by the nature of the counting statistics. Previously it was assumed that the counts were basically Poisson distributed and so had a flat power spectrum with a mean of two. Actually the photomultiplier counts consist of three components: two Poisson distributed time variable sources (star and sky) and the dark count. At count rates greater than 20 counts/sample the star and sky counts will be very nearly normally distributed. The dark count is non-Poisson. Cosmic rays produce large pulses at a rate of approximately one per minute per square centimeter at sea level (Thorn-EMI

photomultiplier technical report). These pulses can be followed by a series of after pulses which are caused by either ionization within the residual gas in the photomultiplier or by ringing in the amplifiers. Natural radioactivity within the window also produces extra counts. Finally the actual photo-emission process is slightly non-Poisson (Prescott 1966).

The dark count frequency histogram was formed from two sections of dark count data taken on the night 12-13th March (Figure 7.4a). According to Walker (1987) the dark count rate has a double exponential distribution as seems to be the case in Figure 7.4b. Because of the short length of the dark data set (4096 samples) no reliable fit could be made to the longer term exponential.

For each run where a successful fit to the power spectrum was obtained a frequency/count-rate or probability distribution (frequency histogram) was formed (e.g. Figure 7.5). All the probability distributions show a high count rate tail that is unaccounted for by a Poisson distribution. The high counts of the dark count easily explain the high count rate tail. Thus, the fraction of counts above the Poisson 3 sigma level ($N_{3\sigma}$) should be a good measure of the contribution of the dark count to overall count rate. Then if the red noise is due to the dark count, the red noise level should be related to the number of counts in the non-poisson tail ($N_{3\sigma}$).

The number of bins above 3 sigma ($N_{3\sigma}$) is calculated using the mean and sigma for a Poisson distribution. These $N_{3\sigma}$ values are then converted to a rms percentage and plotted against the red noise percentage for both the three comparison stars and Sco X-1 in Figure 7.7. There is an approximately linear relation between the two variables. Sco X-1 is only marginally above the general trend indicating that any intrinsic red noise makes only a small contribution to its signal.

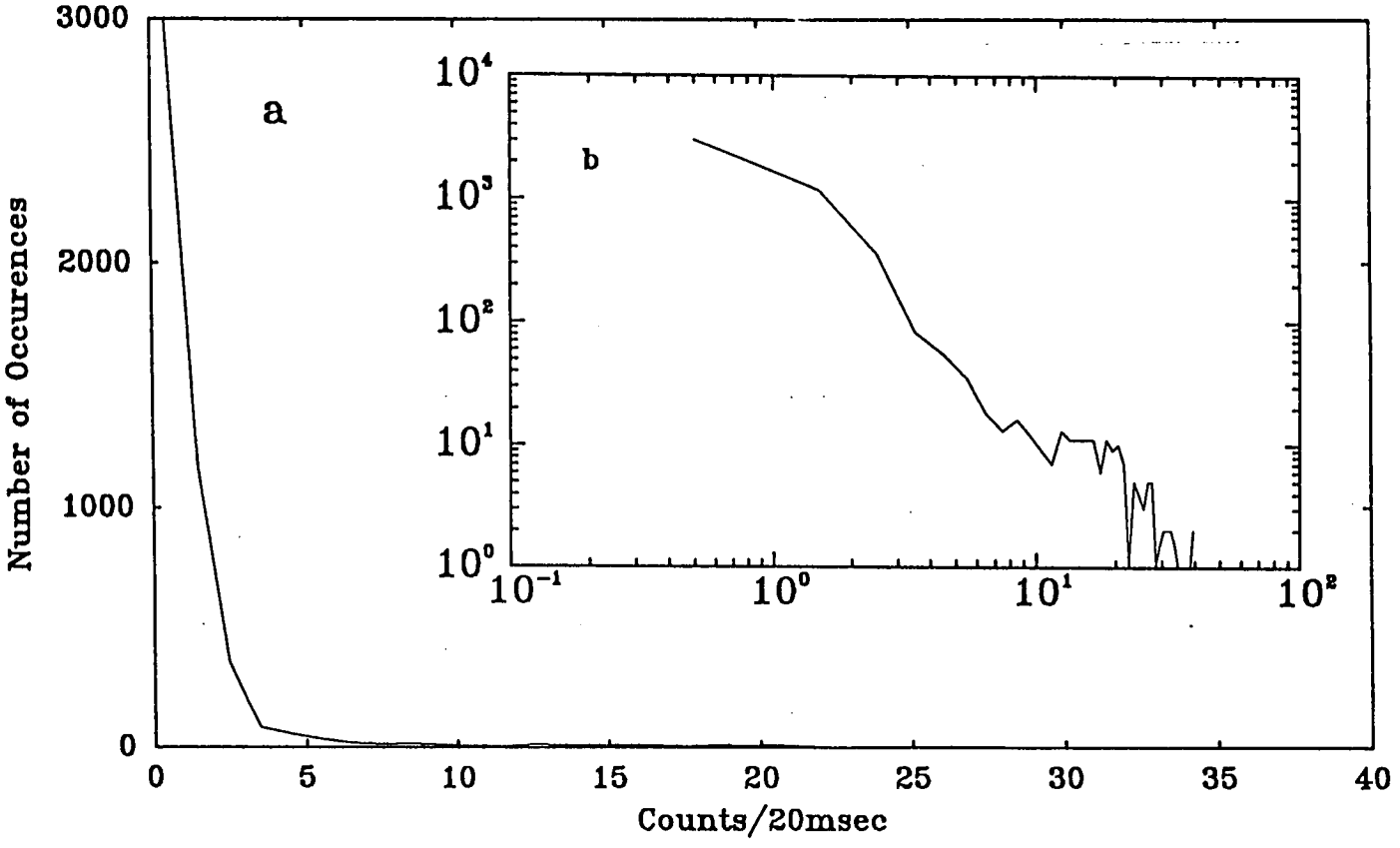

Figure 7.4 The dark count frequency verses count-rate histogram.

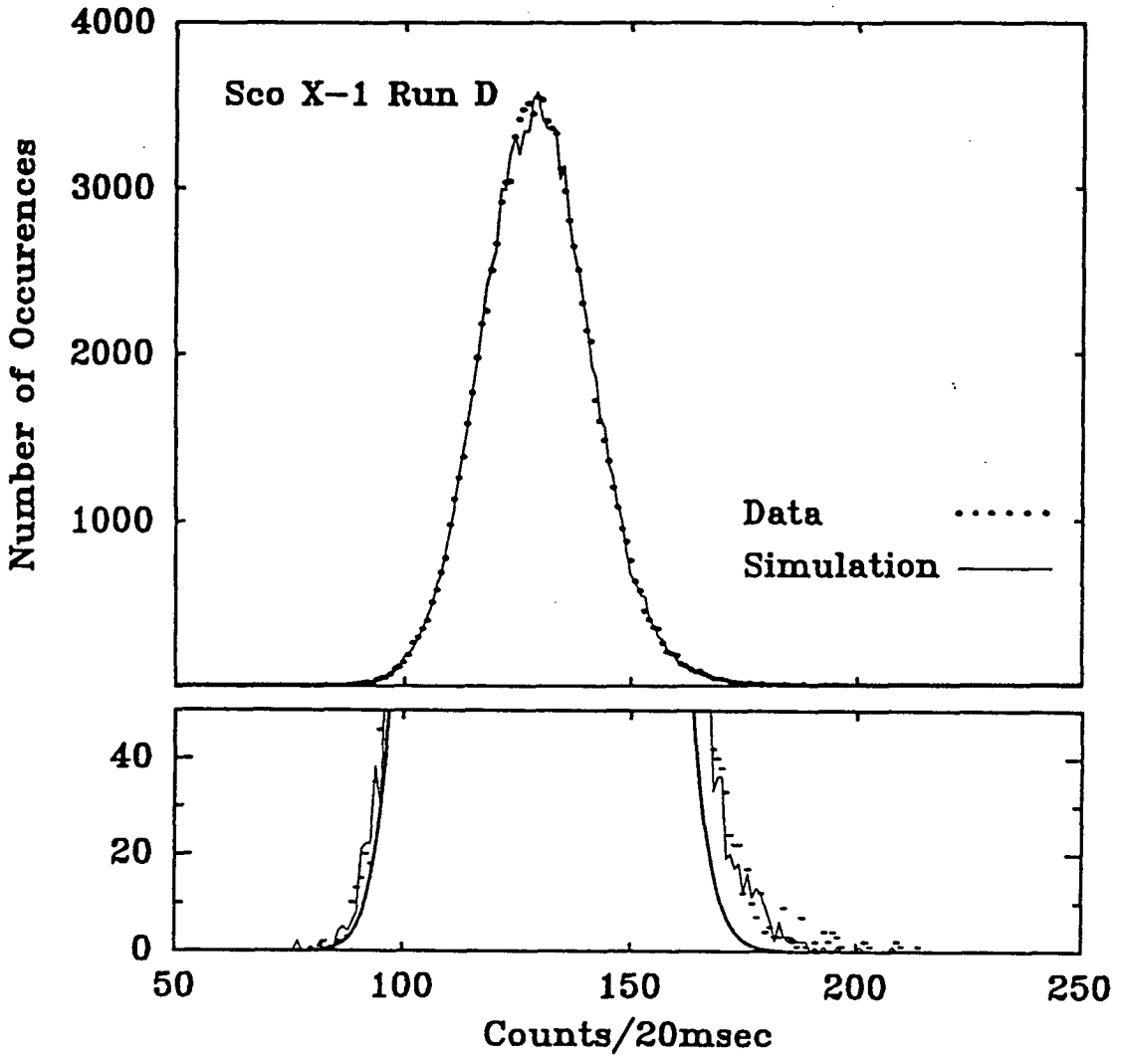

Figure 7.5 The frequency count-rate histogram for Sco X-1 run D. Both the simulated and actual histograms are shown. The lower panel shows the extended high count-rate tail as compared to the expected Poisson distribution (thick solid curve).

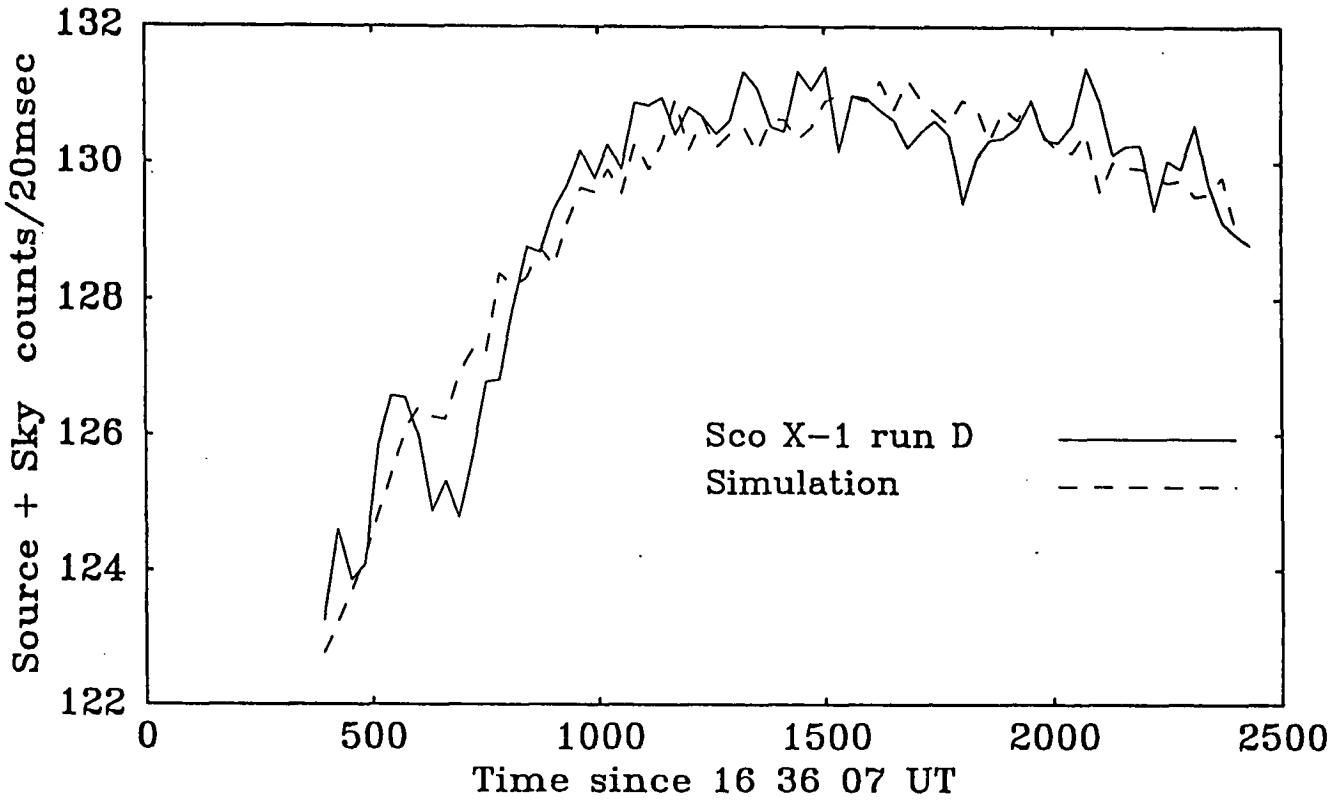

Figure 7.6 A comparison between the simulated and actual total count rate light curve for Sco X-1 run D.

7.2.1 Simulations

A series Monte Carlo simulations were performed to elucidate the counting statistics-noise characteristics. In the first set of simulations the counts generated consisted of two components: a constant mean Poisson distributed deviate and a count following a smoothed (in the high counts/bin region) version of the dark count distribution.

The rejection method (Press et al. 1986) was used to generate the dark count random deviates. Unfortunately no suitable comparison function could be found for the dark count probability distribution. Instead all numbers between zero and one were generated out of which only those below the dark count distribution were accepted. Since this is very inefficient and so only one Monte Carlo simulation of the combined dark and constant sky count (set at 10 cts/20 msec) was made. To this were added different constant Poissonian source count simulations.

All the resulting simulation power spectra showed a sharp low frequency (red) exponential drop off and an excess white noise component. The excess white noise level slowly approached the nominal white noise level of two with increasing count rate. A plot (Figure 7.8) of each component versus excess high counts ($N_{3\sigma}$) showed a linear relation as did the real data.

The exponential component was clearly associated with the dark count since it decreased rapidly in amplitude and area with increasing count rate and does not exist for the Poisson distributed star counts alone. It is unlike the slow exponential decline (e-folding frequency >5 Hz) of the actual optical data. It is not a true representation of the actual red noise. It is suspected that the large number ($\approx 10^8$) of unaccepted deviates started to show up the long period of the random number generator used. This exponential 'spike' does not show up in the second series of simulations, however it does illustrate well the decreasing influence of the non-poisson dark count with increasing count rate.

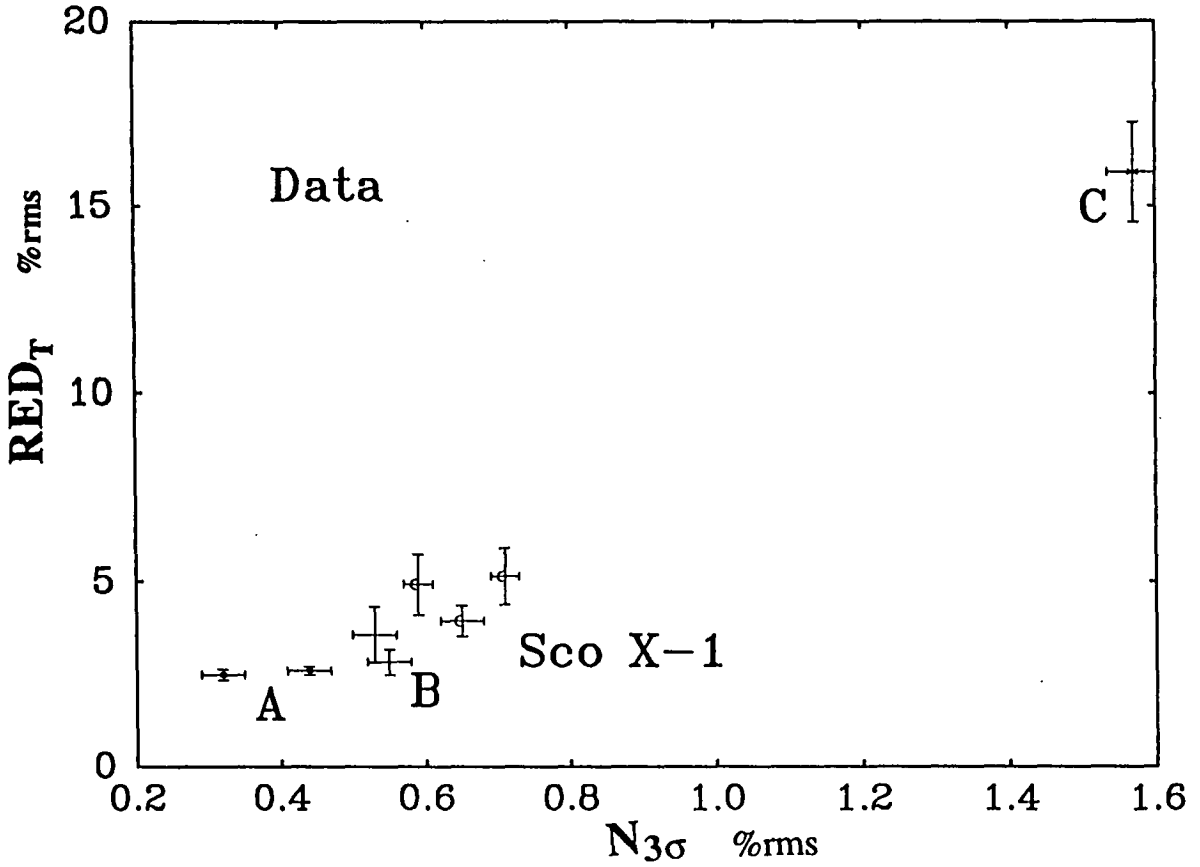

Fig 7.7 Plot of red noise versus percentage of counts above the Poisson 3 σ level. The uncertainties are Poisson 1σ errors.

It is apparent from the above simulation that the previously measured values of red noise consists of two components: that due to the counting statistics and that due to the source or atmospheric scintillation. An attempt was made to fit the data's power spectra with an exponential along with a flat base level. Due to the poor signal/noise and the small frequency range (20 -25 Hz say) of any flat part in the power spectra no sensible fits could be found. In order to get the base levels and to more accurately model the data another set of simulations were undertaken.

In these Monte Carlo modelings the signal was considered to consist of three components; the star's light, sky background and the photomultiplier's dark count. Poisson statistics were used for both the star and sky count simulations. The dark count was generated by randomly choosing a value from the dark count data taken on the night. The sky and star-sky count rates were fitted with a polynomial using the F-test (at α=0.05) used to discriminate against unwarranted terms. These fits where then used as a time variable mean for the Poisson deviates representing the star and sky brightness. For each simulation a power spectrum and probability distribution was formed. A comparison between simulated and real light curves and probability distributions are shown in Figures 7.6 and 7.5 respectively. All simulations produced similar quality of agreement with their respective original light curves.

7.2.2 Simulation Results

A simulation without any dark count contribution yielded a flat power spectrum with a level of two. Thus the excess white noise seen in the simulations and the data originates from the dark count. All simulated power spectra were flat. The average over 0-25 Hz gives the level of the excess white noise. As a validity check these base levels were compared to the average over the 20-25 Hz range of the data's power spectra. Generally the two levels are in close agreement. In the case of a disagreement of more than 0.01 between the two levels both were used in subsequent fits. The uncertainty of the simulation's base level is about 0.01 as judged from a couple of duplicate simulations, the spread of base values and their differences with high frequency levels of the data. This translates into an approximately 0.1% change in the final red noise percentages. In order to obtain a better estimate of the uncertainties a large number of simulations would need to be made.

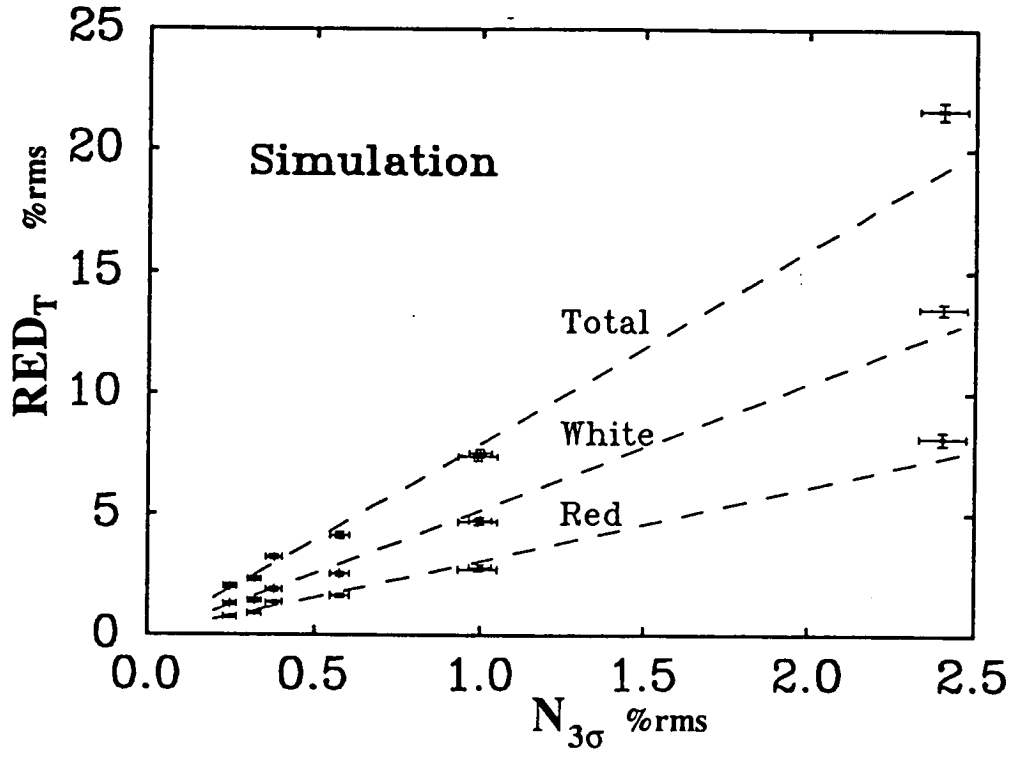

Figure 7.8 The variation in the white and red components of the simulated power spectra are illustrated as a function of count rate. The count rates range from 10 cts/bin (lower left points) to 250 cts/bin (right hand points)

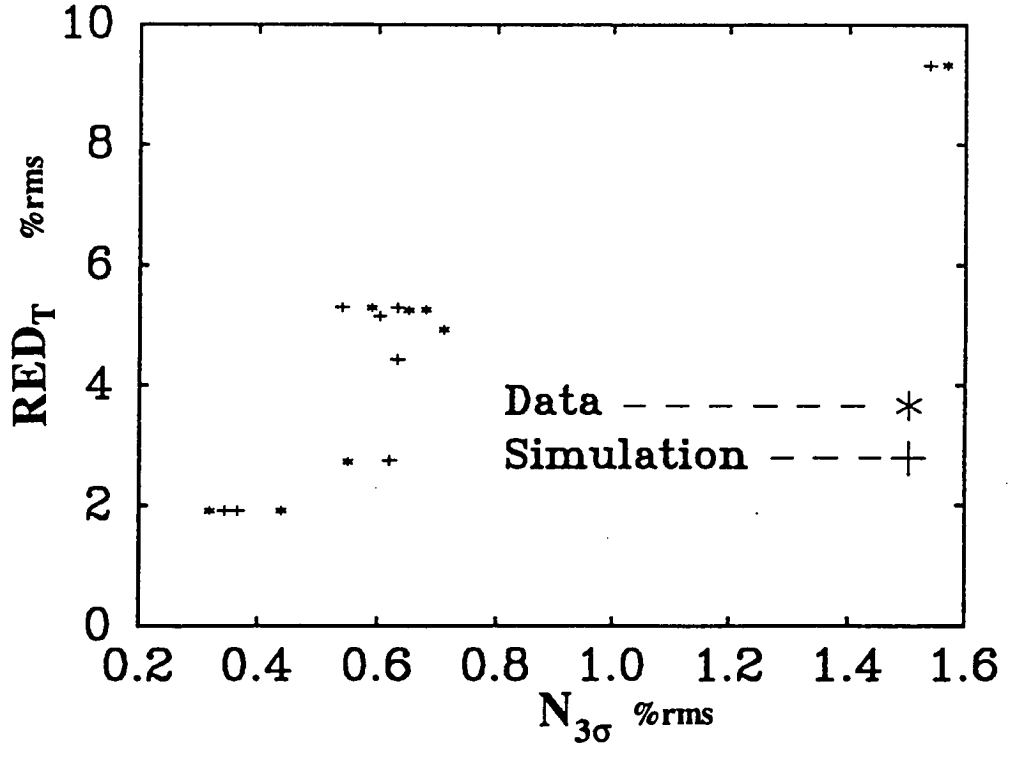

Figure 7.9 A comparison of the simulations with the data in terms of the variation of the excess white noise against the fraction high count rate events.

Table 7.2

Run	Base	A	B	RED_T	White	$N_{3\sigma}$	RED_S	QPO
Sco X-1								
B	2.18	0.52±0.19	3.6±2.0	0.90±0.15	2.66	0.59	1.76 ±0.41	1.44
	2.20	0.33±0.15	2.4±1.3	0.72±0.15	2.81		1.40 ±0.32	
C1	2.17	1.0 ±0.24	5.2±1.7	1.27±0.14	2.62	0.65	2.44 ±0.27	1.55
	2.20	0.65±0.17	3.7±1.4	1.02±0.13	2.84		1.95 ±0.23	
C	2.17	1.20±0.20	6.9±2.0	1.38±0.11	2.59	0.67	2.58 ±0.27	1.52
	2.20	0.65±0.17	4.1±1.4	1.01±0.13	2.81		1.90 ±0.23	
D	2.21	0.38±0.27	3.3±3.7	0.77±0.24	2.85	0.71	1.31 ±0.41	1.25
C+D								1.22
All								1.01
Comparison Stars								
A1	2.12	2.21±0.39	7.6±2.0	1.41±0.12	0.74	0.32	1.81 ±0.14	
	2.10	2.76±0.43	9.2±2.2	1.58±0.12	0.67		1.99 ±0.14	
A2	2.14	3.05±0.39	5.4 0.9	1.66±0.10	1.78	0.44	2.08 ±0.14	
	2.10	3.95±0.44	6.8±1.1	1.89±0.10	1.50		2.40 ±0.14	
B	2.18	0.69±0.19	4.7±1.6	1.03±0.13	2.63	0.55	1.09 ±0.14	
C	2.54	0.78±0.19	4.5±1.3	1.97±0.23	8.19	1.57	2.26 ±0.27	

Table 7.2. The errors are calculated in the same manner as those of Table 1. The values of WHITE, $N_{3\sigma}$ and RED_T are %rms of the total count rate while RED_S and the QPO limits are expressed as an rms percentage of the source flux.

The simulated base levels were then used as a fixed parameter in the fitting of the data's power spectra. The resulting fitted area and e-folding frequency (A,B), red noise, white noise and the total count percentages are listed in Table 7.2. A plot of the excess white noise versus excess high counts ($N_{3\sigma}$) is plotted in Figure 7.9 for both the real and simulated data.

Star A shows slightly higher amounts of red noise (%rms of total counts) when compared to Sco X-1. This is a consequence of some of the light from Star A being spilled outside the aperture, increasing the effects of scintillation. The final values of source percentage red noise show no significant trend with respect to count rate, zenith angle or excess high counts. There is no significant difference between the red noise, as a fraction of source counts, of Sco X-1 (average 1.88±0.37%) and that of Star A (1.94±0.10%). Using the above figures a 2σ upper limit of 2.6% rms can be set on the existence of any excess intrinsic optical red noise from Sco X-1.

7.2.3 QPO Upper Limits

After removing the best fit function (exponential + base) from each run's power spectrum, the residuals were tested with the sign, runs and Kolmogorov-Smirnov (K-S) test. Also used was the peak test of Mereghetti et al. (1987). Since 6 Hz QPO's were observed by EXOSAT the search was restricted to the 2-10 Hz frequency range. In none of the individual runs were any peaks detected at the 95% confidence level using the sign, runs or K-S tests.

The power spectra of runs C and D were summed and averaged. Also a grand average power spectrum was formed for the entire data set. Both these spectra were searched using the K-S test; without detection. The peak test detected peaks at the 95% confidence level in run B (8 ,Hz, 0.24Hz FWFM) and in run C (4.8Hz, 1.9Hz FWFM). As a check the peak and K-S tests were applied to the power spectra of the comparison star data. The peak test detected signals, again at the 95% confidence level. The K-S detected no peaks. It thus seems that the peak test is not totally reliable and any detections should be treated with suspicion.

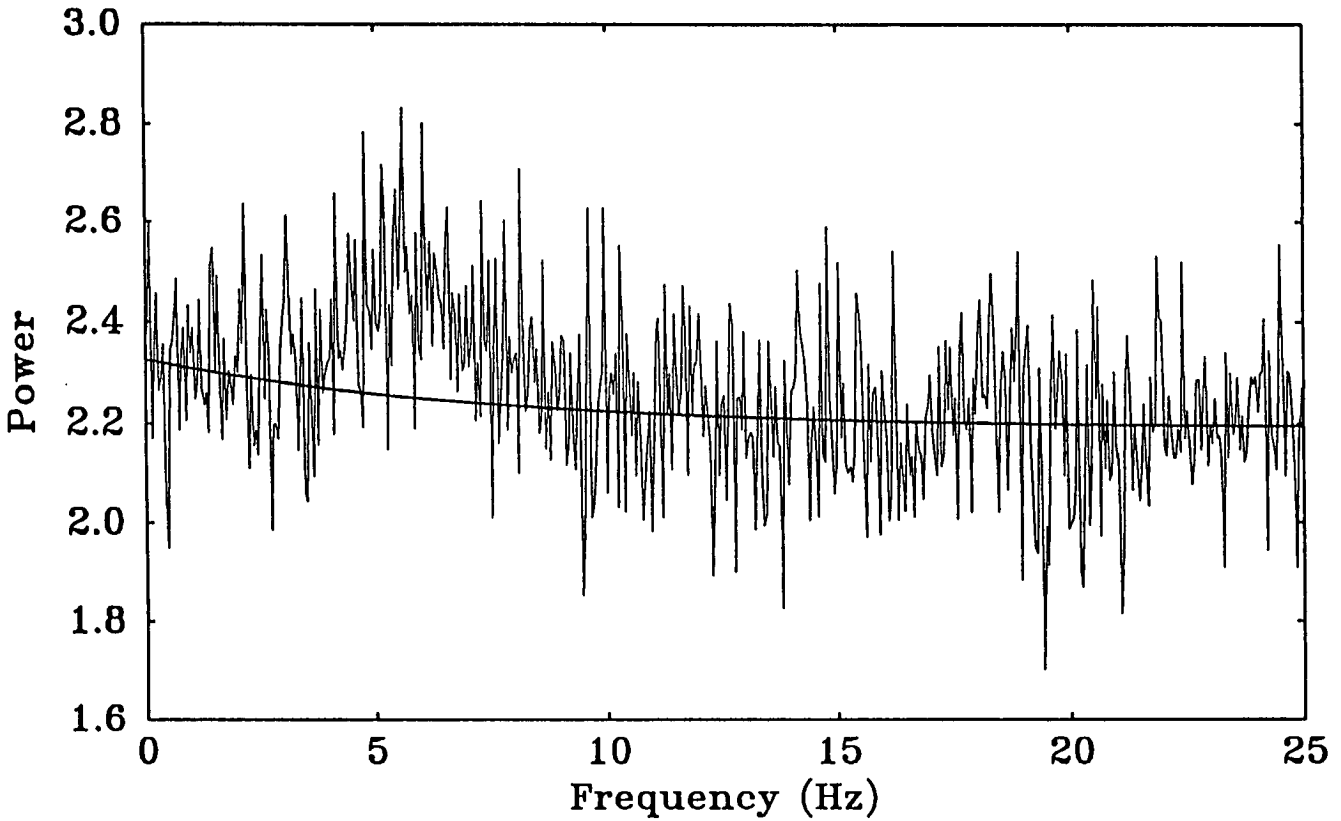

Figure 7.10 A test peak of area 1.22% rms of the source flux, 1 Hz FWHM and central frequency 6 Hz is added to the combined power spectrum of Sco X-1 run D.

The setting of percentage upper limits was undertaken in two stages. Lorentzian peaks of different centroid frequency and area were added to the best fit's residuals. The FWHM of the test peak was set at 1.0 Hz, which is typical of quiescent branch X-ray QPO's. The centroid frequencies were set half way between adjacent Fourier frequencies at ≈1/2 Hz intervals between 2 and 8 Hz. The K-S test was then applied repeatedly forming a probability map in frequency and peak area. Over the frequency range 4 to 10 Hz the K-S test was always failed at the 95% confidence level whenever the test peak exceeded about 1%rms of the source signal. Other tests showed that the statistical tests were more sensitive to broader features.

This procedure does not give the final upper limit because the fitting of the power spectra partially compensates for any peak. The above ≈1% limit was used as guide for the next series of tests. A series of Lorentzian peaks with centroid frequency f_c = 5.981445 Hz and FWHM 1.0 Hz and variable area were added to the original power spectra. Again note that the test frequency is half way between two Fourier frequencies. The resulting test power spectra were then fitted in the same manner as the original power spectra. The procedure was stopped when the K-S test was just failed at the 95% confidence level. This peak area was converted to a percentage of the source count rate using Equation 7.2 and listed in Table 7.2. Since the test frequencies used were between Fourier frequencies these upper limits are the most conservative possible.

The residuals, at these limits, were tested using the peak test of Mereghetti et al. (1987). In all cases the test peak was detected at the 95% confidence level indicating that the peak test is at least as sensitive as the K-S test. An example of a just detectable (using the K-S test) peak is given in Figure 7.10.

7.2.4 Variation Function Analysis

A simple to implement method of looking for any aperiodic variability is the variation function as described by Maejima et al. (1984). The variability coefficient, η, which measures the normalized excess variance above that expected for Poisson statistics, is given by

$$\eta = \frac{\left[V(t_b) - X(t_b) \right]^{\frac{1}{2}}}{X(t_b) - Y(t_b)} \qquad 7.3$$

Here $V(t_b)$ is the variance when the data are binned with a width of t_b. The mean total (source + background) counts $X(t_b)$ in the numerator represents the variance due to Poisson statistics alone. Thus the numerator is the excess variability on a time scale of t_b. This is normalized to the background subtracted source counts: $Y(t_b)$ being the background count rate on t_b timescale.

The variability function is related to the auto-correlation function and hence the Fourier power spectrum. It is expected to become zero when there is no intrinsic time variation and show generally larger values at smaller values of t_b in the presence of any variation. In fact, it shows a $\eta \propto t_b^{-1/2}$ form when the variability is white.

Since the variation function assumes a stationary process, the star + sky and sky counts were detrended. The detrending function was found with a least squares polynomial fit. The highest useful term was determined using the F-test (Bevington 1969) upon the χ^2 values of each fit. The same polynomials as used in the simulations were employed. In the case of the earlier Sco X-1 runs the sky was only measured for several short periods. The fitted trend (linear) was used for $Y(t_b)$ while the source + sky was detrended separately. In the case of the standard star (B,C) data a straight forward subtraction was used for the normalization.

The variation functions (VF) of the Sco X-1 and standard star data reveal an intrinsic variation in all cases (Figures 7.11 and 7.12). At time scales less than a second the variability is proportional to $t_b^{-0.3}$ for both Sco X-1 and the comparison stars implying the presence of the same non-white variability. This variability can be reasonably attributed to atmospheric scintillation. At longer time scales the VF for the comparison stars continues to decrease (index -0.3) till a constant, approximately zero , level is reached. In contrast Sco X-1 shows approximately constant ($\approx$1.5%rms) variability on all time scales greater than a few seconds. Similar amplitude variability has been well documented (Petro et al. (1981) and references therein).

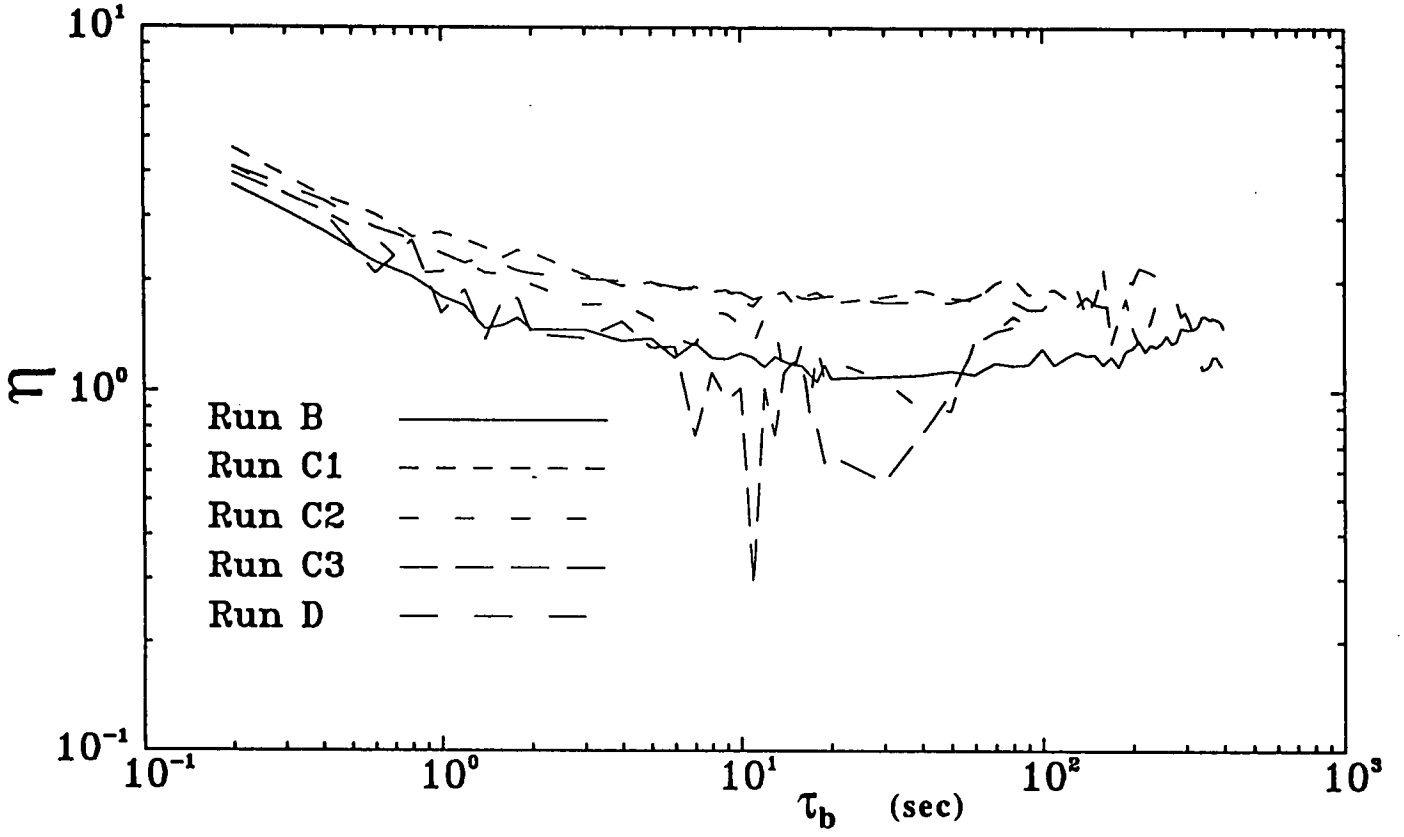

Figure 7.11 The variation function of the individual Sco X-1 runs.

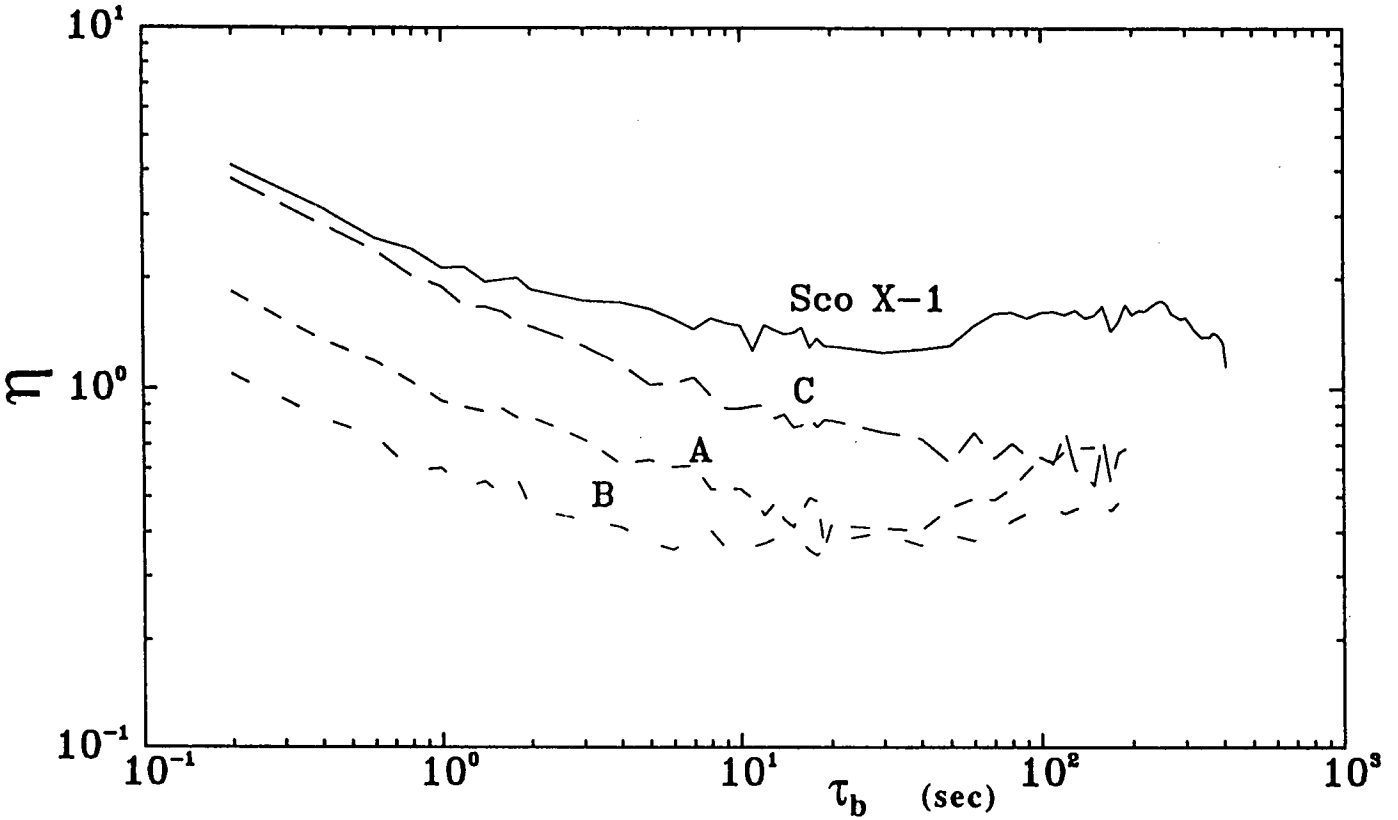

Figure 7.12 The average variation function of Sco X-1 compared to the variability of the standard stars.

The comparison star variability shows a general trend, of lower variability with higher signal to noise ratio. Sco X-1 also follows the same trend once again showing that it has no intrinsic red noise above that due to atmospheric scintillation. The relationship between S/N and the VF is not surprising given the similar form of the two variables i.e. (dropping the t_b subscript)

$$\eta = \frac{[V\text{-}X]^{1/2}}{X\text{-}Y}$$

$$\frac{\text{Signal}}{\text{Noise}} = \frac{(X\text{-}Y)}{X^{1/2}} \qquad 7.4$$

If there is little or no intrinsic variability there should be a one to one inverse relation between the two variables. When this trend is accounted for any variability intrinsic to Sco X-1 is of the order of 1.5% being strongest at scales greater than a few seconds.

7.3 Discussion

The Mt. Canopus data show no sign of any optical QPO. Upper limits of ≈1.4%rms are set for individual runs. The upper limit set for the time when X-ray QPO were observed (i.e. runs C and D) is 1.22% rms of the source flux.This is below the 1.3-1.6% rms amplitude QPO seen at X-ray wavelengths during runs C and D (HPM1989). If any optical QPO existed at the time, they must have had a strength less than that observed at X-ray energies.This lack of any optical QPO's can be explained if the X-ray flux is subject to the same 10 - 20 sec reprocessing smearing as the optical flares (Petro et al. 1981). In the case of the optical/X-ray flares the optical flare amplitude is about half that seen in their X-ray (<20 KeV) counterparts. Scaling this amplitude reduction to the shorter time-scale of the 6 Hz QPO any optical QPO should be suppressed by a factor of ≈100 relative to the X-ray QPO. Such a reduction would place any optical QPO's well below our detection threshold. The red noise is not affected by the reprocessing smearing because it is not a coherent signal.

This is in contrast to the earlier (1985), observation by MIS1986 of ≈15 Hz optical QPO during one run. At X-ray wavelengths 15 Hz QPO's are associated with the flaring state when Sco X-1 is also optically bright. The magnitude estimates given by MIS1986 suggest that Sco X-1 was faint and hence in the quiescent state. Thus this observation of ≈15 Hz QPO would be in marked contrast to the previous

behaviour of Sco X-1. The run during which optical QPO were claimed was when Sco X-1 was low in the sky. Under these conditions any periodic tracking error, or telescope vibration would be enhanced by the larger seeing disk. This is particularly true when a small aperture (in this case 9") is used upon a relatively bright star. Given these uncertainties about their origin these reported optical QPO's will not be considered further.

The initial calculation of the red noise levels from Sco X-1 and the comparison stars assumed that the power spectra could be fitted with an exponential and a base power level of two. However, the non-Poisson dark count raised the base level above the Poisson level of two. When this effect was taken into account, with the aid of simulations, a 2σ, 2.6%rms upper limit can be set upon any intrinsic optical red noise over the 0-25 Hz range. This is in agreement with the observations of Tuohy (1987) who found no power excess above that expected from atmospheric scintillation. An estimate of $\leq$1.5% excess variability on all time scales from 0.2 to 4000 sec (5 Hz to 0.25 mHz) can be made using a variation function. Simultaneous X-ray observations (HPM 1986) showed 1.3 - 1.6%rms VLFN which is lower than the upper limits set for any optical red noise.

Being of a lower frequency LFN will be less affected than QPO by any reprocessing smearing. A 0.1 Hz signal will be reduced by a factor of two. Also since it is not a coherent (or partially coherent) signal, any initial red noise will, when smeared, appear as red noise but with a broader frequency range.

The MIS1986 observations of optical red noise during a quiescent state is not incompatible with the X-ray behavior of Sco X-1. In the upper part of the X-ray quiescent branch LFN and no QPO's is the norm. If Sco X-1 was in such a state the results of MIS1986 and those presented here can be fitted within the general "Z" source picture of the X-ray/optical/QPO behavior of Sco X-1.

7.4 Conclusions

The results presented here correspond to when Sco X-1 underwent a transition between the upper and the lower parts of the quiescent state. At optical wavelengths there was little (<2.6% rms) red noise in the 0-25 Hz range and no (upper limit 1.2% 95% confidence) optical QPO's. The lack of any optical QPO's coincident with the 6 Hz QPO detected by EXOSAT can be understood if they are subject to the same 10 to 20 sec smearing as the optical flares. The low amount

of red noise is entirely consistent with the low red noise levels seen at X-ray wavelengths. A comparison with the observations of MIS1986 strongly suggest that Sco X-1 also displays variable strength optical red noise. In terms of the " Z source " behavior pattern the data of MIS1986 would correspond to the upper part of the quiescent/normal branch where, at X-ray (<20KeV) wavelengths Sco X-1 shows LFN but no QPO. Hence it appears that the X-ray LFN and the optical red noise are related and dependent upon the state of Sco X-1.

To confirm this postulated correlation between the optical and X-ray noise characteristics further simultaneous high speed optical and X-ray observations are required. The optical observations must include standard star observations to determine the contribution of atmospheric scintillation. In these regards the observations presented here are a first step.

Chapter 8

GX 1+4 : 1986 Observations

'Twas brillig, and the slithy toves
Did gyre and gimble in the wobe:
All minsy were the borogoves,
and the mome raths outgrabe.'

Lewis Carroll
"Through The Looking Glass"

8.1 Introduction

The X-ray pulsar GX 1+4 was observed between 5:48:30 and 6:03:00 UT, during the 26th November 1986 flight. During this period the source transited, passing nearly overhead, resulting in a virtually constant line of sight atmospheric depth of 3.1 grm cm^{-2}. The determination of the pointing solution was undertaken by Dr. D.P. Sharma. The platform azimuth was found using data from the A.I.T. 3-axis magnetometer and a sighting of the sun using the rotation modulation collimator. When compared to the UT 3 axis magnetometer data a 1.75° offset was found. This offset appeared to be constant during the sun, GX 1+4 and GX 1+4 background observations. This offset was applied to the UT 3 axis magnetometer azimuth and the zenith was provided by the shaft encoder upon the detector. The azimuth and zenith angles were corrected for the effects of the platform tilting. No tilt correction was applied to the magnetometer output. Using this pointing solution it was found that the detector was generally pointed to within 0.15° of the position of GX 1+4. Since the source was almost overhead, any azimuth error has very little affect upon the final calculated collimator efficiency. The pointing stability was better than 0.1°.

Excess flux was detected over the entire ≈20 to 114 keV energy range. As with the Sco X-1 data both the background and source data were corrected for frame overflows and the A/D bin width variations. Also the background used was the same i.e. the average of two swings in azimuth (0°and 51° zenith angle), 2 minutes of data just before the Sco X-1 drift scan, a pointed/slew observation near the sun and a pointed observation of a source free region 4° away from GX 1+4. As discussed in Chapter 6 there is little or no variation in background count rate with zenith angle.

8.2 Results

8.2.1 Pulse Period

The χ^2 method was used to search for the ~2 min X-Ray pulsation period. At each trial period the data are phase folded and a value of reduced χ^2 calculated assuming a constant signal. When the trial period matches the underlying period the phase folded light curve has the largest amplitude and so the χ^2 is a maximum. Periods ranging from 200 to 3800 frames (19-319 sec) were tested. Spurious peaks can

arise in the Q method when the number of bins is a whole integer fraction of the tested period. When this happens some bins have very few or no samples. To guard against this possibility several different χ^2 searches were made using a different number of phase bins per period on each occasion. In all cases, Figure 8.1 being an example, several periods were found i.e. strong χ^2 peaks at 112, 224 and 336 sec and weaker peaks at 56 and 168 seconds. By an extrapolation of previously published, period measurements a period of the order of 100 seconds was expected. The aspect information showed no coherent oscillations at any frequency.

In the case of a sinusoid signal the resulting χ^2 peak should be a sinc function. (Leahy 1987a). To find the best estimate of the true period the 112 sec χ^2 peak could be fitted with a sinc function, however the 224 sec peak is highly asymmetric and no reliable fit could be made. Instead, the χ^2 peaks were fitted with a Gaussian. The base level was fixed at 1.0. This is the expected noise level of the reduced χ^2 values if the data is Poisson distributed. The noise level was found to be near 1.0 when overflow corrected counts were used in the period search. For uncorrected counts the base χ^2 noise level was 0.8. Both the 112 and 224 second peaks were fitted for each different period search (number of bins per period changed in each search) for two different energy ranges (channel 10-80, and 80-121 i.e. 9.4-75 keV and 75-114 keV). The average period was about 1153 frames. There was considerable scatter in the individual period estimates.

In order to check this estimate and to set one sigma limits upon the period two simulations were undertaken. In the first Monte Carlo simulation, the original (10-121 channel) data was randomized by adding a Gaussian deviate with a standard deviation equal to the square root of the mean count rate. A Gaussian deviate is an adequate representation of the Poisson distribution when the count rate is greater than 20 counts/bin, which is the case for the 10-121 channel data (21.26 counts/frame). The χ^2 period search was applied to each set of randomized data and the 112 sec peak fitted with a Gaussian. The resulting distribution of the simulated counts is not Poissonian. Adding a Gaussian deviate to the original data distribution creates a distribution with a larger spread than the original Poisson distribution. The effect upon the χ^2 periodogram is to raise the noise level. Instead of fitting a Gaussian with a fixed base level the χ^2 peaks were fitted for both the Gaussian peak and base level. From 1068 simulations the best period was found to be 1155.5 frames.(See Figure 8.2).

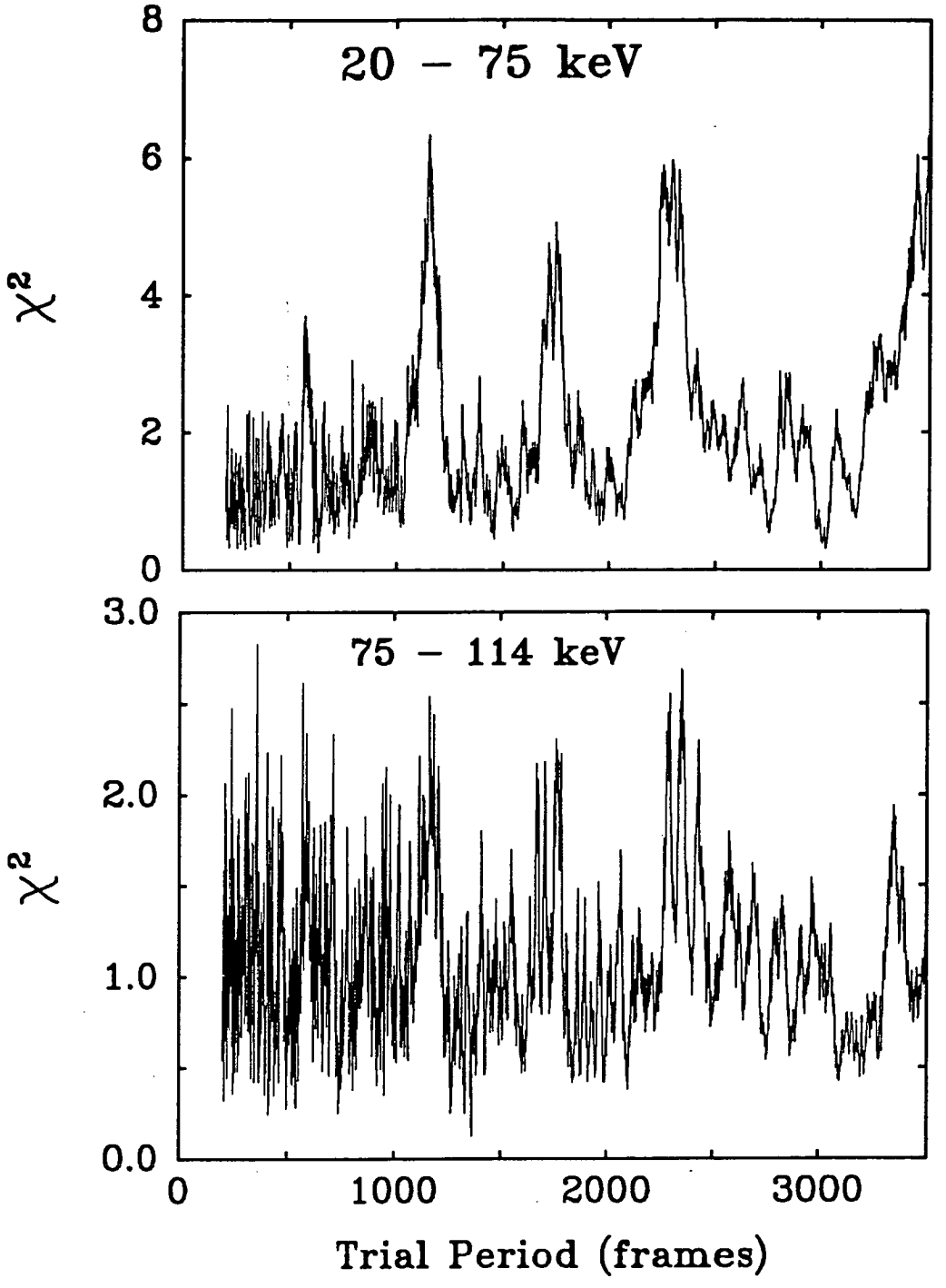

Figure 8.1 The χ^2 periodograms over the low (<75keV) and high (>75keV) energy ranges. There are approximately 10 frames per second. Strong peaks are seen at ≈ 112, 224,386 sec. Weaker peaks at 56 and 168 sec are visible in the 20-75 keV periodogram.

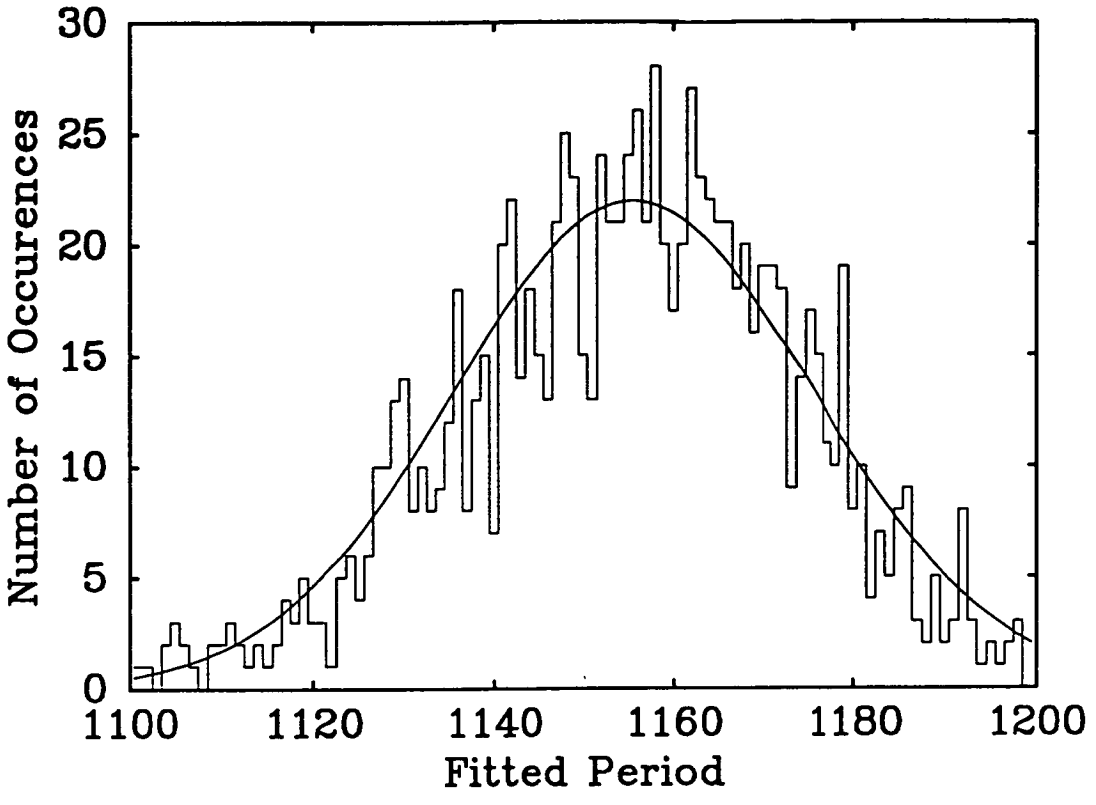

Figure 8.2 The frequency distribution of simulated periods. The smooth curve is a Gaussian with a peak at 1155.5 frames and σ = 11 frames.

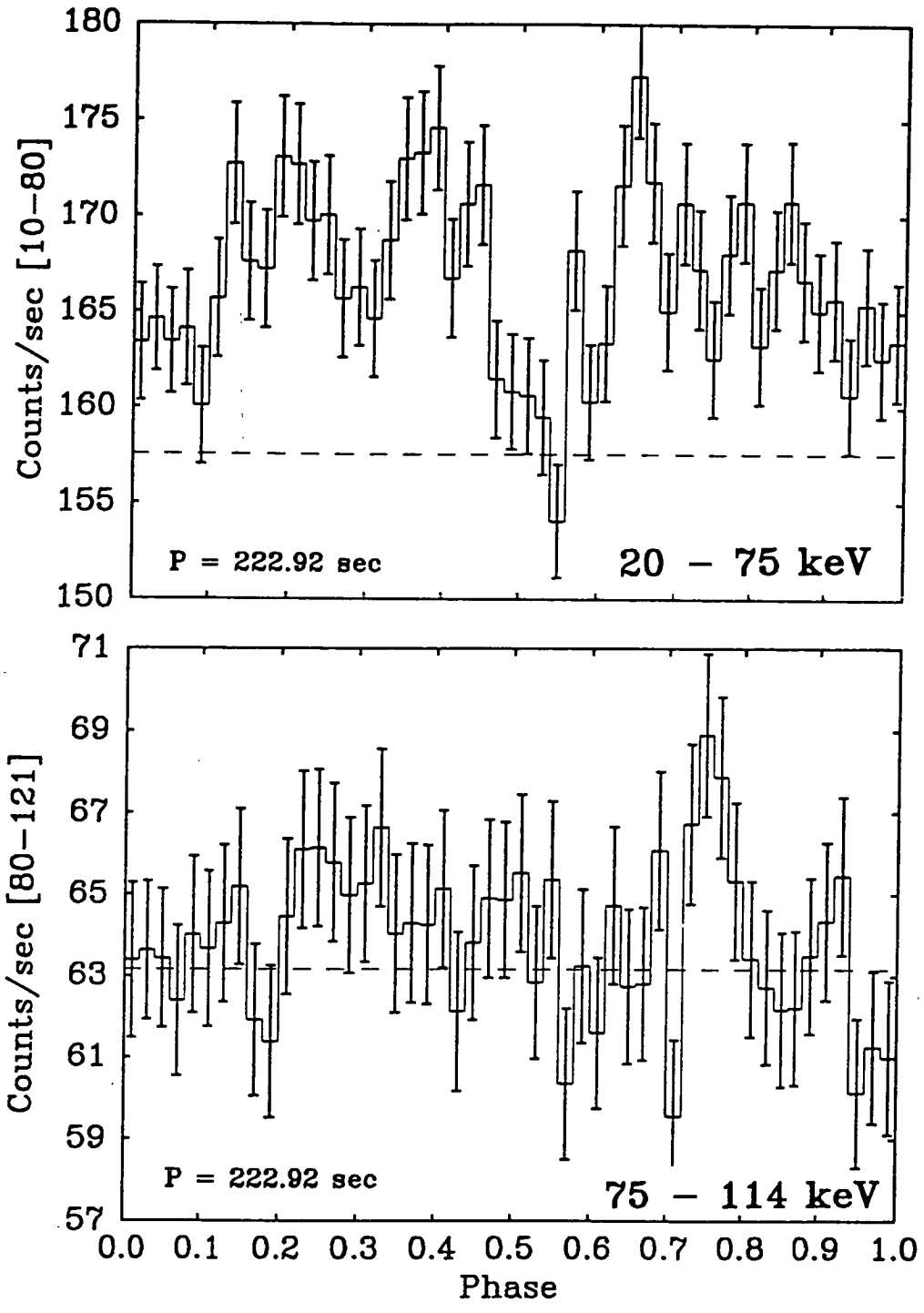

Fig 8.3 The pulse profiles at double the best period with 50 bins per cycle. These data used to test for differences between alternate 112 sec pulses.i.e. between the first and second halves of these phase diagrams.

To find the one sigma uncertainty of the estimated period a separate set of simulations were performed. The original data was first phase folded with the above period (1155.5 frames) using 100 bins per period. Using a 5 point running average, the resulting pulse profile was smoothed and used to generate a simulated set of data. Each data set (551), was searched for the underlying period and the resulting χ^2 peak was fitted with a Gaussian and a fixed base level of one. Since the deviates were from a single Gaussian distribution the noise level of the χ^2 values were the expected level. The one sigma error was found to be ± 13 frames.

As noted in relation to the millisecond timing analysis of the Sco X-1 data, the frame period is slightly variable (± 0.06 msec). This variability is not significant when compared to the 112 sec pulse period of GX 1+4. By comparing the UT clock with a frame counter the average frame period during the GX 1+4 observations was found to be 96.559 ± 0.003 milliseconds. When this frame period is used the best GX 1+4 period is 111.6 ± 1.35 seconds. This is slightly shorter, and with greater error limits than the earlier period estimate of 111.8 ± 1.0 (Greenhill et al. 1989). This previous estimate was based upon only 50 simulations.

8.2.2 Odd/Even Pulse Differences

There is no general agreement on whether the true period of GX 1+4 is ~2 minutes or ~4 minutes. Some authors (e.g. Strickman et al. 1980, Kendziorra et al. 1982) have claimed a significant difference between alternate pulses when a 4 minute period is used.

Our data cover eight complete cycles of the 111.6 sec period. To test any differences between odd and even pulses the data were phase folded (50 bins/period) at twice the 111.6 second period. The two halves (<0.5 phase, >0.5 phase) of the resulting pulse profile were compared (see Figure 8.3). There is a barely significant (2.5σ) difference in mean counting rate of the odd and even peaks. Using the hardness ratio based upon the 10-80 channel (20 to 75 keV) and 80-121 channel (75 - 114 keV) counts no significant difference in hardness was found between alternate pulses. The χ^2 and Kolmogorov - Smirnov tests for two distributions were applied to the double period pulse profile in three different energy bands (10-80, 80-121, 10-121 channel). No significant (95% confidence)

difference was found between the two halves of the 223 sec folded light curve. These two statistical tests will be failed if there is a significant difference in either the total counting rate or shape of the two pulse profiles.

Since no evidence was found for a difference between the odd and even pulses, and for comparison with the majority of published light curves the 111.6 sec period was adopted in all subsequent analysis.

8.2.3 Phase Folding

The frame by frame overflow corrected counts were phase folded over different energy ranges using the best fit period of 111.6 seconds. Data below channel 10 and above channel 121 were not used because difficulties in determining the detectors response. At the low energy end problems arise through a combination of noise and the A/D converter's cyclic variation in bin width. Above channel 122 the effect of the upper limit discriminator system caused the response to fall rapidly and this could not be reliably fitted with the flat field calibration curve.

Initially phase folding was performed on data from consecutive 20 channel (18.75 keV) wide energy ranges. This range is similar to the FWHM resolution of the detector. Figure 8.4 shows these pulse profiles. Immediately obvious is the change in pulse profile above 85 keV (channel 90). At lower energies the pulse profile is broad with an indication of a central notch of width ≈0.2 in phase. No modulation, and very little or no excess counts are seen in the energy range 65 to 84 keV (channel 70 to 90). At the highest energies the profile is a sharp spike at the same phase and with the same width as the lower energy notch. The position of the notch/spike feature near phase 0.5 is purely fortuitous. In all phase folds the starting time was chosen to be 5:48:30 UT, i.e. when GX 1+4 was first fully in the field of view.

The energy ranges of the pulse profiles in Figure 8.4 should be rearranged. X-rays below about 20 keV are absorbed by the atmosphere. Between channel 10 and 20 (9.4 and 18.75keV i.e. one channel is 30/32= 0.9375 keV wide and the zero energy point is at channel zero) the counts are the result of either escape or transfer from adjacent (higher) energies caused by resolution smearing. Escape photons will primarily due to incident photons 30 keV higher in energy i.e. the range 39.4 to 49 keV. At 20 keV the detector FWHM energy resolution is 8.3 keV (≈9 keV channels). Thus counts due to energy smearing will have originally had energies

between 19 and 30 keV. Since the 19-30 keV count rate is higher than the 39 to 49 keV count rate energy smearing could dominate the low energy flux. Since the origin of these low energy (channel 10-20) counts is ambiguous they will be not incorporated into any further phase folds. Escape gating creates a natural energy boundary. Between about channel 20 (18.75keV) and 39.4keV(channel 42) the counts are primarily, directly from the source. Above about 39.4 energy losses due to photon escape becomes important. Another energy boundary is set where the broad pulse appears to disappear. This occurs at about channel 70 (65.6 keV). The high energy spike seems to appear above about channel 90 (84 keV). After phase folding the data over various energy ranges up to channel 126 it was found that the high energy spike disappeared above about channel 110 (103 keV). The implied energy width of the spike is smaller than the detector resolution (~18keV at 94keV). In order to ensure that all spike photons are included in the phase fold the energy range 84.4 to 114 keV (90-121 channel) is used. Channels 122 to 126 (inclusive) are not used in the phase folding because of the poorly calibrated A/D response. Channel 127 contains saturation events and so is not used. Using the gated mode counts, phase folding can be extended up to over 140keV. Between 120 keV and 141keV (channel 128 and 150) there is no modulation apparent. However the detector sensitivity, particularly in escape gated mode, is low at these energies. Given the above considerations, Figure 8.5 illustrates the changes in pulse profiles with energy.

Several tests were performed by Dr. D.P Sharma, to assess the reality of the high energy spike. It appears when either half of the data is phase folded. When folded at double the period two narrow peaks separated by 0.5 phase are seen. Possibly the most convincing evidence for the reality of the high energy narrow pulse is presented in Figure 8.6. This figure, produced by the author, shows a 10 second running mean of the 75-114 keV (80-121 channel) data. Individual high energy pulses can be discerned. Out of the eight possible pulses, six are definitely high while none are low. Also clearly seen in Figure 8.6 is the double peaked nature of the lower energy pulse profile. The double peaked pulse profile naturally explains the periods found at 86 and 168 second periods found using the χ^2 period search.

Overall the pulse profiles are of two types; a broad double peak at energies <75 keV and a single, narrow peak at > 75 keV. These two profiles are shown in Figure 8.7.

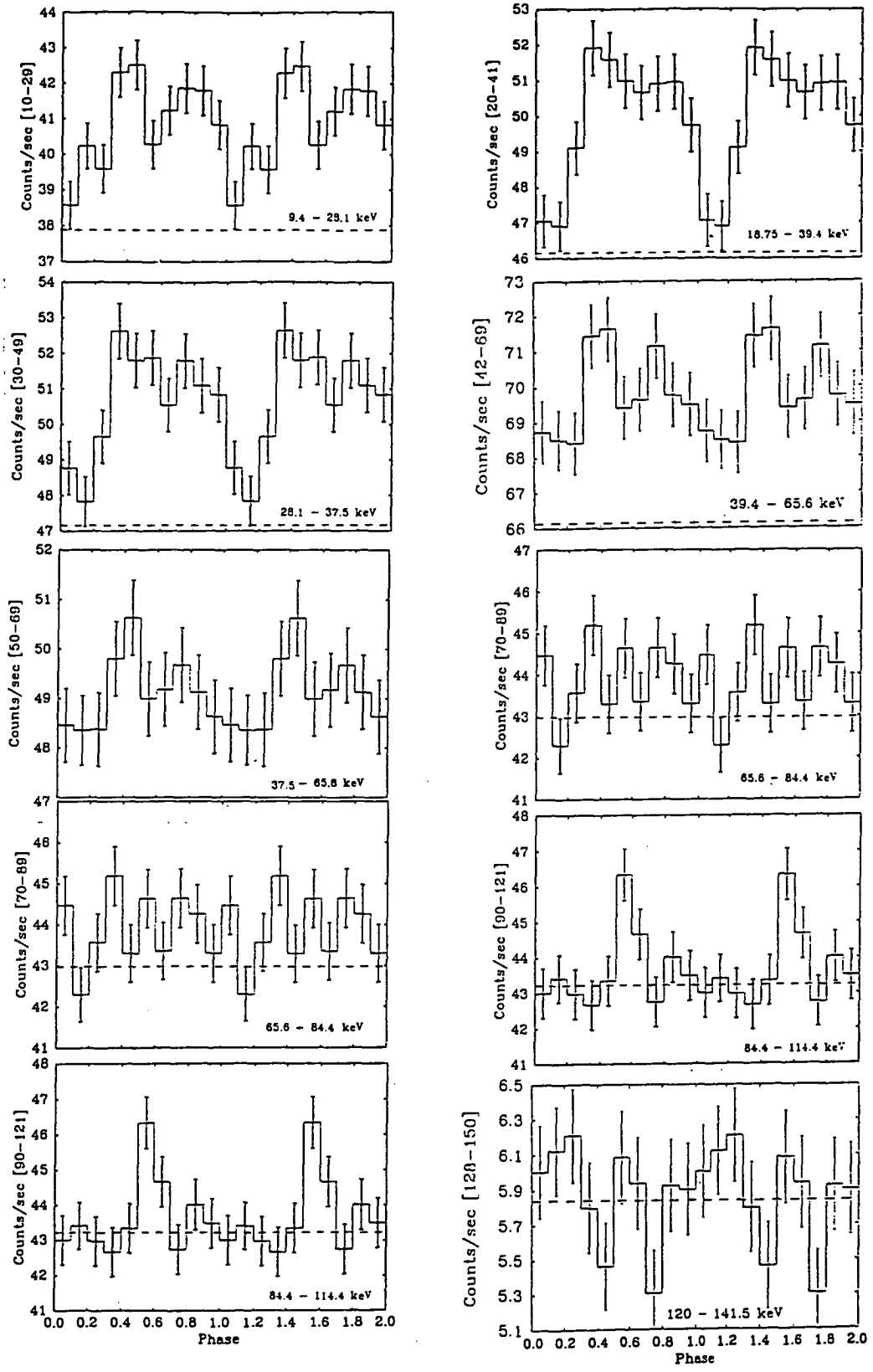

Figure 8.4 (LEFT) Phase diagrams (10 bins/period) at approximately 19keV wide intervals , showing the changes in pulse profile with energy.

Figure 8.5 (RIGHT) Phase diagrams over re-arranged energy windows to show the characteristic changes in pulse shape with energy. The counts have been corrected for frame overflows.

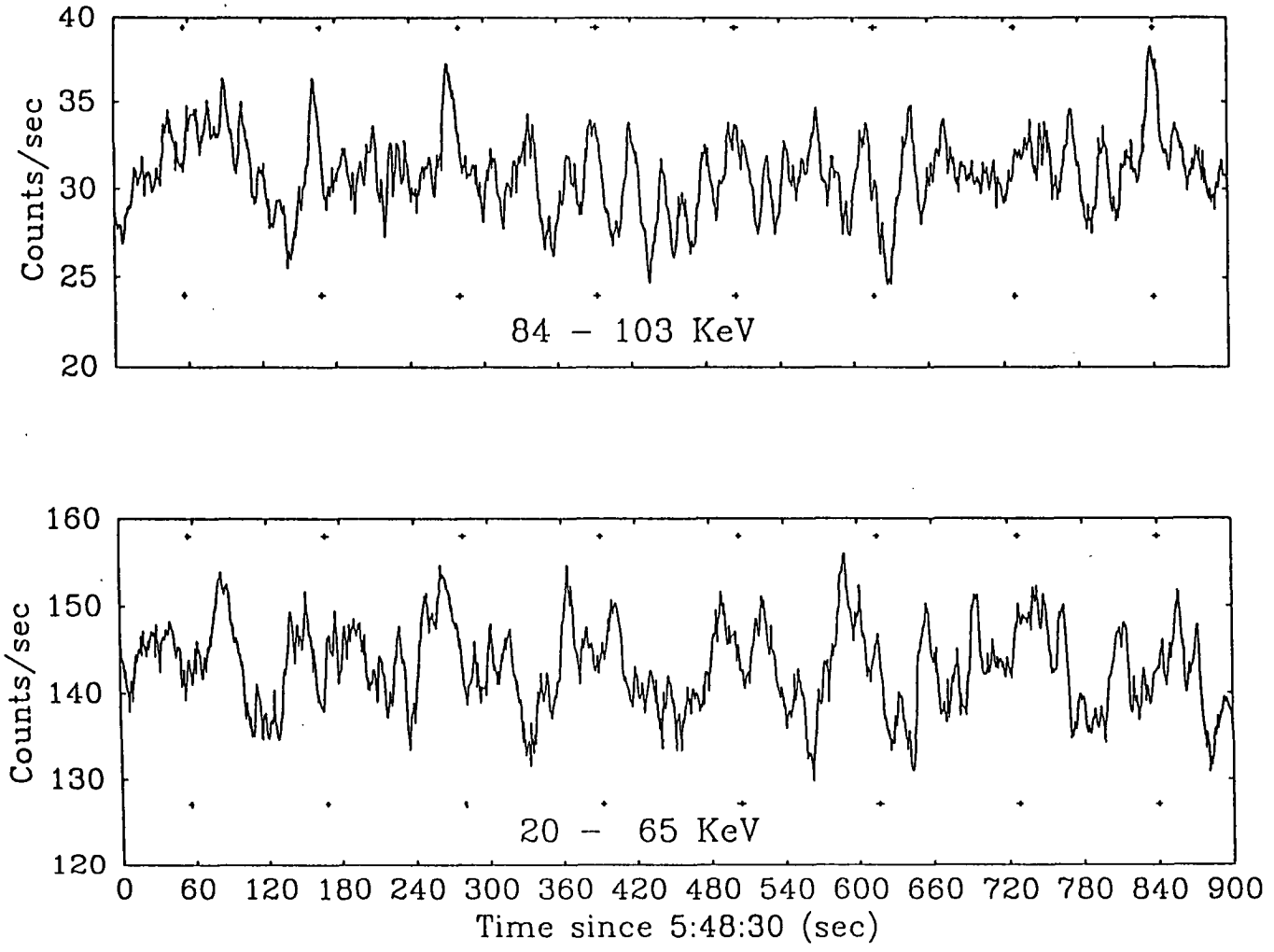

Fig 8.6 Smoothed light curves of GX 1+4 in the low (<75keV) and high (>75keV) energy ranges between 5:48:30 and 6:03:30 UT. No collimator correction has been applied. However, the transmission was almost constant, at better than 90%, between 60 and 840 sec. The crosses mark the position of phase 0.5 in the phase diagrams.

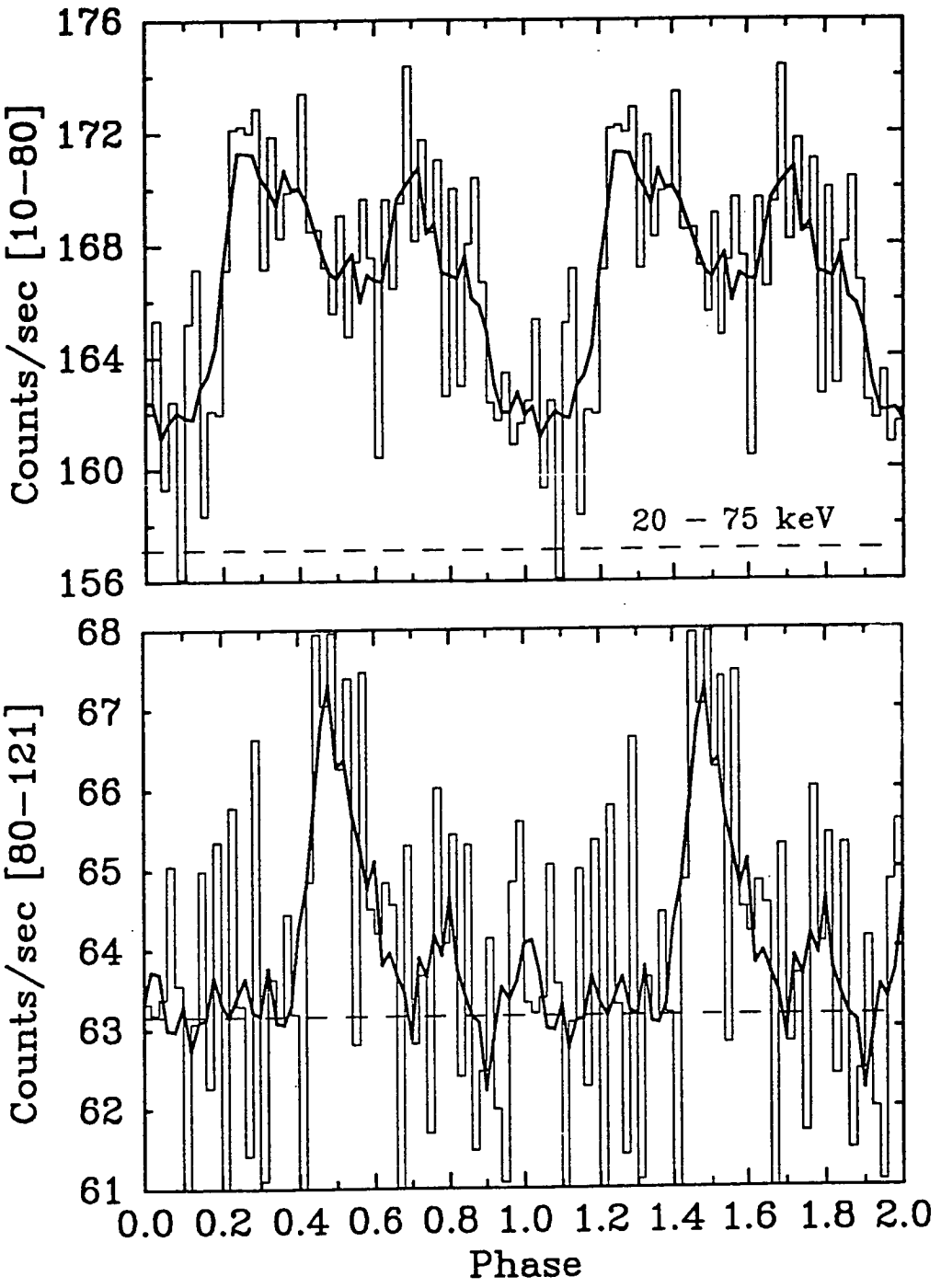

Figure 8.8 Pulse profiles on the same scale and over the same energy range as Figure 8.7 but with 50 bins/period. The continuous curves are the smoothed (0.1 phase running mean) are the smoothed pulse profiles. The notch/spike are about 0.4 phase in width.

The apparent ≈0.2 phase width of the notch and spike may be due to the binning employed. To better define the width of the notch/spike the 10-70 channel and the 90-121 channel data were folded with 50 bins per period. In Figure 8.8 the dark line represents a running weighted 5 point (0.1 phase) phase smoothing of the phase binned counts. The width of both the spike and notch is about 0.4 in phase (FWHM~0.2 in phase ≡ 72°).

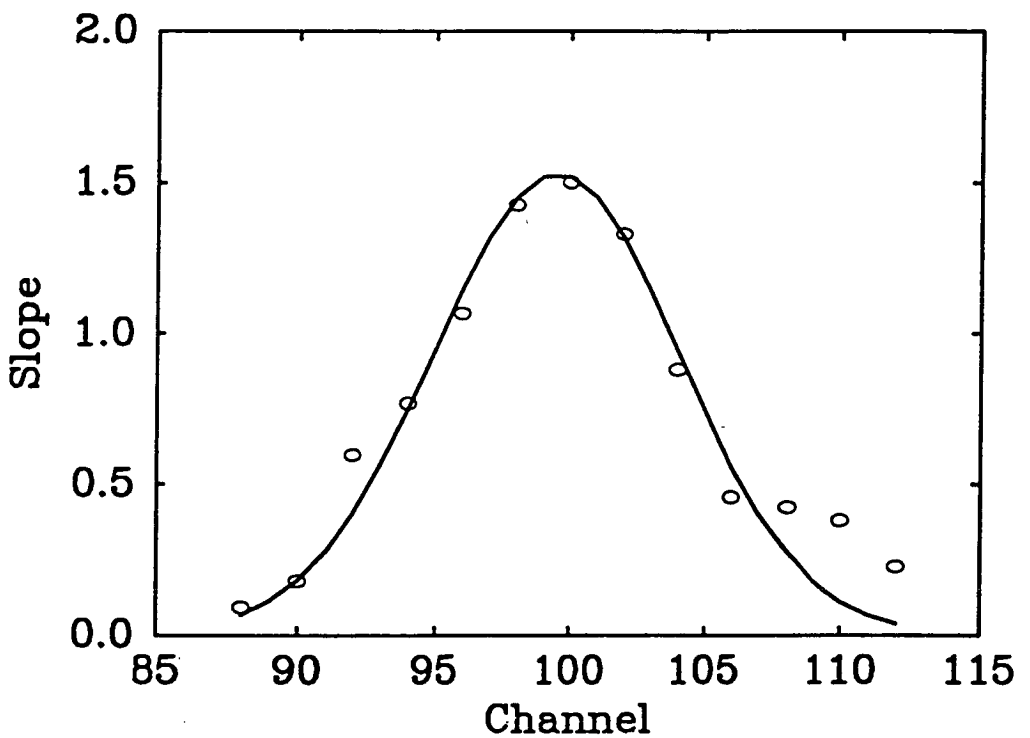

Figure 8.9 The reconstructed energy spectrum of the high energy spike. The slope is in arbitrary units. The smooth curve is a Gaussian with peak at channel 100 (94keV) and FWHM of 12 channels (11.25keV).

To find the central energy and energy extent of the high energy spike the data was phase folded over different energy ranges between 75 and 114 keV (80-121 channel). The lower limit of the energy range was progressively increased from 75 to 108 keV (channel 80 - 115). The average height, over the phase range 0.4-0.6, above background was used as the measure of the pulse strength. The resulting plot of low energy boundary versus spike strength is the integral of the pulse spectrum. The integral curve was smoothed and the gradients measured. The resulting recovered spectrum is shown in Figure 8.9. The recovered spectrum is consistent with a Gaussian peak with a FWHM of ≈10keV and a central energy of 94keV. The uncertainty in energy width is not known but could well be 2 keV. The energy width is smaller than the expected detector energy resolution (18keV at 94 keV). The energy resolution may not strictly follow the $\sqrt{E}$ dependence because of the energy dependence of the interaction region. At lower energies most photons interact in the top tray of the detector. Here the energy resolution could be worse than the bulk of the detector where the 94 keV photons of the pulse would interact.

The fractional pulsed flux (fpf) (Kendziorra et al. 1982) being the ratio of the pulsed flux to the total flux is

$$fpf = (C_i - n_{bin} * C_{min}) / (C_i - n_{bin} * C_{bgd}) \qquad 8.1$$

was calculated for each energy range of Figure 8.5. This fpf is half the fractional pulse amplitude given by (Cmax - Cmin)/ Cmean. The fpf (42 ± 15%) was less in the 40.3 to 65.6 keV range than in the ≈20 to 39.3 keV range (72±14%). Over the ≈20–75 keV range the pulsed fraction is 50±10%. The high energy spike, whose peak is 4σ above the background is 100% modulated.

The notch at phase 0.5 appears to increase in depth with energy. The depth is measured relative to the maximum count rate which occurs in the 0.3 phase peak. This depth can be expressed as a fractional modulation of the total flux. In the lowest energy range (≈20 to 39 keV) the notch is not significant, representing a 35±23% modulation...In the 39.4-65.6 keV range the notch depth increases to 61±40% of the total flux. This increase is not significant. Over the ≈20 to 75 keV range the notch represents a 55 ± 21% reduction in flux as compared to the maximum flux at phase 0.3.

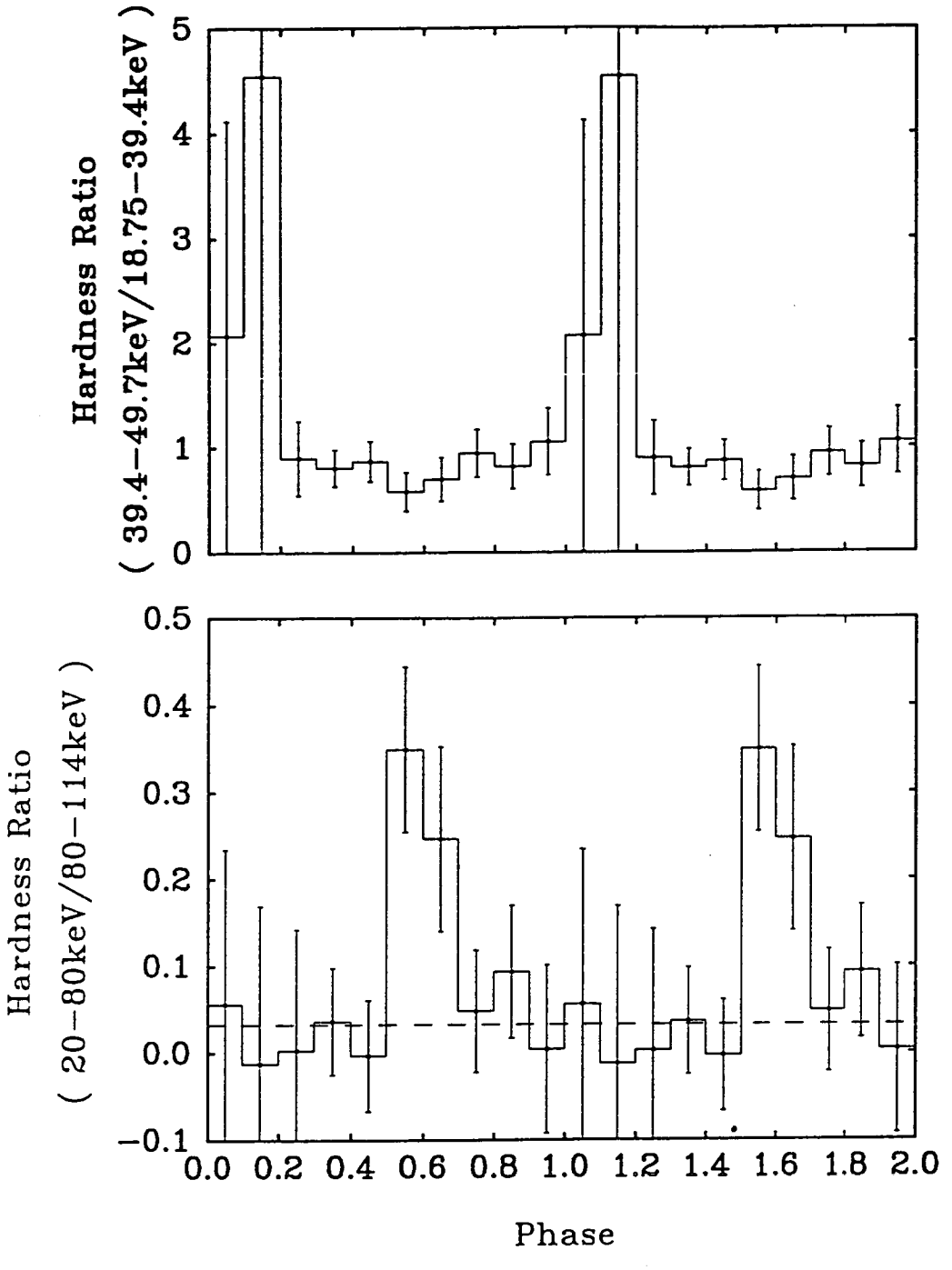

Figure 8.10 Hardness ratio phase diagrams from the data presented in Figure 5 (top two panels) and Figure 7. The background count rate has been subtracted and the counts corrected for frame overflows. The error bars are based upon Poisson statistics.

The changing fractional modulation and the increase in the depth of the notch with energy suggest changes in the energy spectrum with phase. The ratio of the 39-49/20-39 keV counts as well as the hardness ratio 39-69/20-39 keV show (Figure 8.10) that GX 1+4 has a much harder spectrum between pulses and that the notch is the softest phase range. However when the hardness ratio 75-114/20-75 keV counts is used the notch/spike is the hardest phase range, again emphasizing the remarkable change in the spectrum of GX 1+4 above about 80 keV.

8.2.4 General Spectroscopy

The overall, all phases, excess count rate pulse height spectrum is given in Figure 8.11. This spectrum was fitted with several models; a thermal bremsstrahlung with the Gaunt factor (Mätzler 1978), a power law and a combination of a power law and emission or absorption line. Initially the spectrum was fitted over the 17 to 115 keV range. Below 17 keV the fitted spectrum underestimated the flux. This is probably due to an underestimation in the escape fraction or resolution. Including data below 17 keV did not greatly affect the final fitted parameters. In all cases the normalization energy used was 30 keV. The intensity at 30 keV was $5.5 \pm 0.4 \times 10^{-4}$ photons sec^{-1} cm^{-2} keV^{-1} for both the power law and thermal bremsstrahlung models. The power law index was $\alpha = -1.7 \pm 0.3$ and temperature $kT = 104 \pm 20$ keV. The uncertainties are the 90% confidence levels. There was little difference in the value of the reduced chi-squared ($\chi^2_{23} = 1.4 : 23$ dof) between the power law and thermal bremsstrahlung models. Examination of the overall power law fit of Figure 8.11 (lower panel) shows that above about 80 keV there is little flux except between 105 and 110 keV. This excess is probably associated with the narrow pulse seen in the phase folded data. The high energy flux may represent an additional component in the spectrum of GX 1+4. In order to find the spectrum without this component the energy range was restricted to 17-88keV and the 0-1.0 phase PHA spectrum refitted. The final power law and thermal bremsstrahlung models were barely different. This suggests that the ≈105 keV excess is not significant. The results these fits are given in Table 8.1.

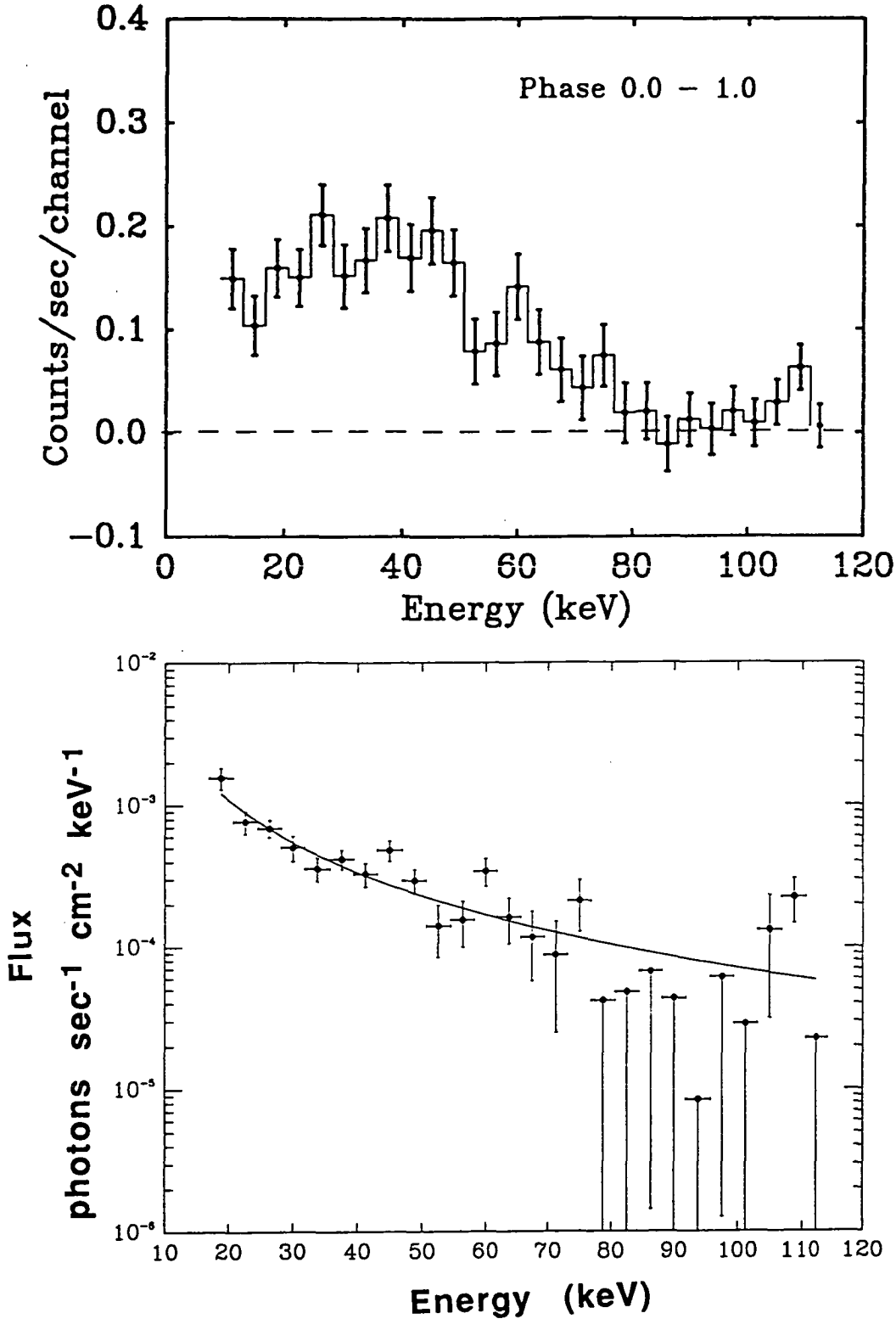

Figure 8.11 The overall (0.0-1.0 phase) pulse height (overflow corrected) spectrum and the power law fit to the corresponding flux spectrum. The data has been binned into 4 channel averages.

TABLE 8.1

17 - 115 keV (4 channel bins)						
Phase Range	I_{30} x10^{-4}	α	χ^2_{23}	I_{30} x10^{-4}	kT (keV)	χ^2_{23}
0.0-1.0	5.5	1.7	1.437	5.5	114.	1.40
0.6-0.4	5.4	1.8	2.019	5.5	83.	1.945
0.2-0.4	8.1	1.9	1.099	8.2	72.	1.050
0.4-0.5	4.6	0.8	0.811	------	------	-------
0.4-0.6	5.1	1.1	1.050	5.1	Huge	1.050
0.6-0.8	7.0	2.2	1.716	7.1	53.	1.684
0.8-0.2	3.2	1.6	1.770	3.2	141.	1.755
17 - 88 keV (4 channel bins)						
Phase Range	I_{30} x10^{-4}	α	χ^2_{16}	I_{30} x10^{-4}	kT (keV)	χ^2_{16}
0.0-1.0	5.5	1.7	1.656	5.5	108.	1.594
0.6-0.4	5.3	1.7	2.105	5.4	102.	2.048
0.2-0.4	7.8	1.7	0.634	7.8	123.	0.627
0.4-0.5	5.9	1.5	0.624	5.9	187.	0.625
0.4-0.6	5.8	1.6	0.922	5.8	154.	0.913
0.6-0.8	6.9	2.1	1.565	7.0	58.	1.550
0.8-0.2	3.2	1.5	1.851	3.3	131.	1.823

Power law and thermal bremsstrahlung fits to 4 channel PHA data over two energy ranges.

In addition to a power law continuum both an emission line near 100 keV and an absorption line near 85 keV were used as models for the phase averaged PHA spectrum. To improve the signal to noise ratio the data PHA (17-114keV) was first binned up to form 8 channel averages. The procedure was then to fix the central energy of the line and fit for all other parameters. The central energy was then

changed. The best fit central energy was considered found when the reduced chi-squared was minimum. The initial guesses for the power law continuum parameters were those found in using only a power law model. No emission line model could be found for the 0-1 phase PHA spectra. Two possible absorption line models were found to be consistent with the all phases PHA spectrum : a narrow (~1keV wide) very deep line or a shallower broader line (see Figure 8.12). In both cases the continuum parameters were practically unchanged as compared to the power law only model. The final absorption line parameters are summarized below in Table 8.2. The line intensity is the depth (I_{line}) below the continuum level at the central energy. The reduced χ^2 value for the power law model fitted to the same data points (i.e. 8 channels binned together from 17 to 115 keV) is χ^2_{11} = 1.638. Using the F-test and the tables in Bevington (1969) there is a significant (95% confidence) improvement when the 0-1 phase PHA spectrum is fitted with a power law and wide absorption line rather than simply a power law.

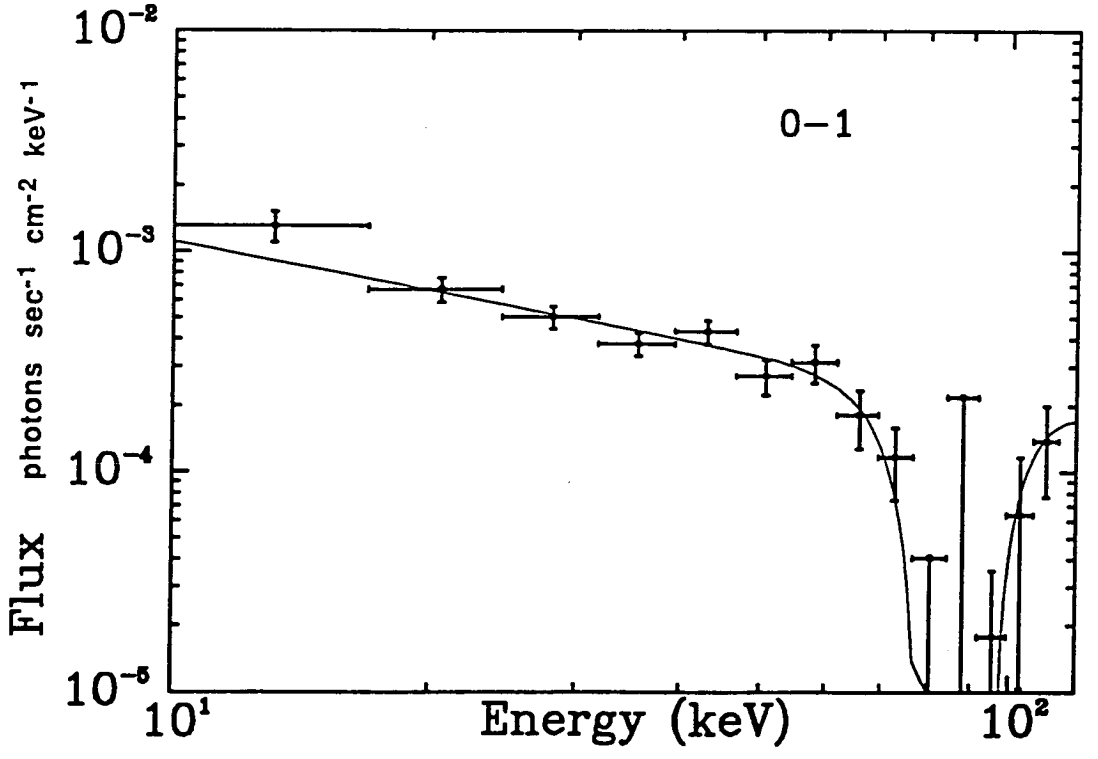

Fig 8.12 Power law + broad absorption line model for the overall flux spectrum. The central energy is 86keV.

Table 8.2

Model	I_{30}	α	E_{Line}	I_{Line}	FWHM	dof	χ^2_ν
Emission Line	5.8*	-1.7*	97*	0.	0.6	11	1.57
Narrow Absorption Line	5.8*	-1.7*	86*	11.2	1	11	1.39
Wide Absorption Line	4.9	-1.7	86*	3.0	30	9	1.02

* Fixed Parameters. I_{30} and I_{line} are in units of photons $cm^{-2}sec^{-1}keV^{-1} \times 10^{-4}$, the line energy ($E_{Line}$) and the line FWHM are in keV.

8.2.5 Pulse Phase Spectroscopy

The data were split into five, 0.2 wide, phase ranges and the excess count rate spectrum fitted with both power law and thermal bremsstrahlung (with Gaunt factor) models. In terms of the reduced χ^2 values, a choice between the power law and thermal bremsstrahlung models could not be made at any phase, but the power law model produced the more reasonable fits. It was found that including the highest energy data (>80 keV) caused the thermal bremsstrahlung fit to the 0.4-0.6 phase to become unstable i.e. the temperature approached infinity. Clearly the high energy data points of the narrow pulse do not fit an exponential spectrum. In this phase range a power law could be fitted. Restricting the energy range to below 80 keV yielded reasonable thermal bremsstrahlung and power law fits at all phases. Over the restricted energy range the power law index was steeper. Except for the 0.4-0.5 and 0.4-0.6 phase ranges the change was small. See Table 8.1. Over the spike/notch (0.4-0.6) phase range the derived continuum spectrum is severely affected by the positive flux at higher energies. This suggests that there is an additional, high energy component in the spectrum.

When the full energy range (17-115 keV) is used to fit the data, the best fit spectral indices and temperatures indicate that GX 1+4 has a harder spectrum between pulses and during the notch/spike (Table 8.1) i.e. when GX 1+4 is fainter. However when the energy range is restricted to below 88 keV the notch/spike range the power indices indicate a much softer spectrum. This situation is confirmed by the hardness ratio plots of Figure 8.10. The 20-80kev/80-114keV ratio shows that

GX 1+4 is hardest at the notch/spike phase while the 39-50keV/19-39keV ratio shows the 0.4-0.6 phase range as the softest of the pulse.

The 90% confidence regions for the 17-114keV power law fits are shown in Figure 8.13. The considerable overlap in the 90% confidence regions for the different phase range fits indicate that there is no significant change in either the intensity or power law index over the 0.2-0.8 phase range. This phase range could be fitted (90% confidence) by a single spectrum with $I_{30} \approx 5 \times 10^{-4}$ photons $cm^{-2} sec^{-1} keV^{-1}$ and $\alpha \approx -1.8$ which is the point in the middle of the region of overlap. The 0.8-0.2 phase range (between pulses) is significantly fainter than the rest of the pulse. However, there is no significant (90%) difference in the derived spectral index. A spectral index between 1.8 and 2.6 could satisfactorily (90% confidence) fit the PHA spectrum of GX 1+4 at all phases.

The pulse height spectrum and corresponding power law fit for the notch/spike phase (0.5-0.6) region is shown in Figure 8.14. To improve the fit either an emission line at about 100 keV with a steeper power law or an absorption line near 70 keV with a flatter power law could be used. A fit of all parameters involved in a power law and line model was attempted. The fitting procedure did not converge indicating that the statistics were insufficient, with so few degrees of freedom.

The strategy used to obtain a fit, was to fix the central energy of the line and fit all other parameters, i.e. power law index, intensity at 30 keV, line intensity and line width. The only phase range which gave an emission line fit was 0.4-0.6 or 0.4-0.5. The best emission line fit (0.4-0.5) was obtained with E_{line}= 97 keV, $I_{line} = 1.2 \times 10^{-3}$ photons cm^{-2} sec^{-1} keV^{-1} above the continuum level at 97keV,width (FWHM) =7.2 keV $I_{30} = 6 \times 10^{-4}$ photons $cm^{-2} sec^{-1} keV^{-1}$, and α=-2.0 and χ^2_9=0.577 (cf. power law fit to the same data with χ^2_{11}=1.327, 11 dof). See Figure 8.15. Using the F-test upon the reduced chi-squared values the emission line model (+power law) represents a significant (95% confidence) improvement over the simple power law the fit to the notch /spike spectrum.

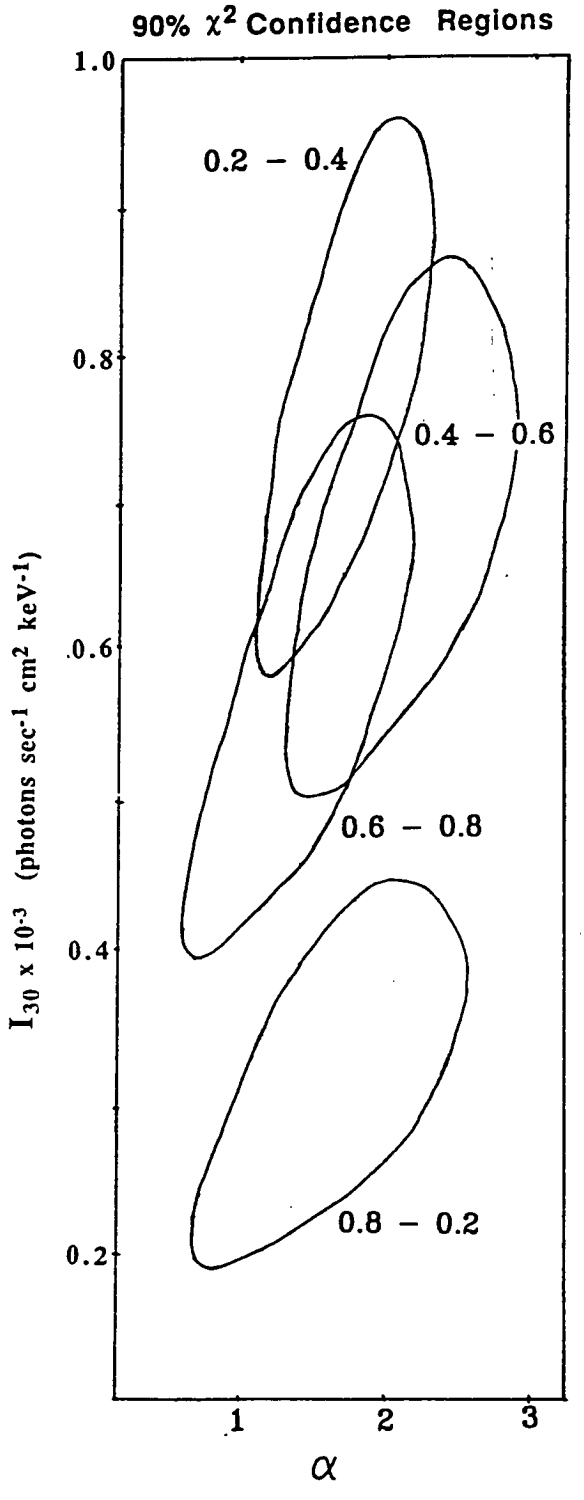

Fig 8.13 The 90% χ^2 confidence regions for the individual power law fits to consecutive 0.2 phase intervals. There is no significant change in spectral index with phase.

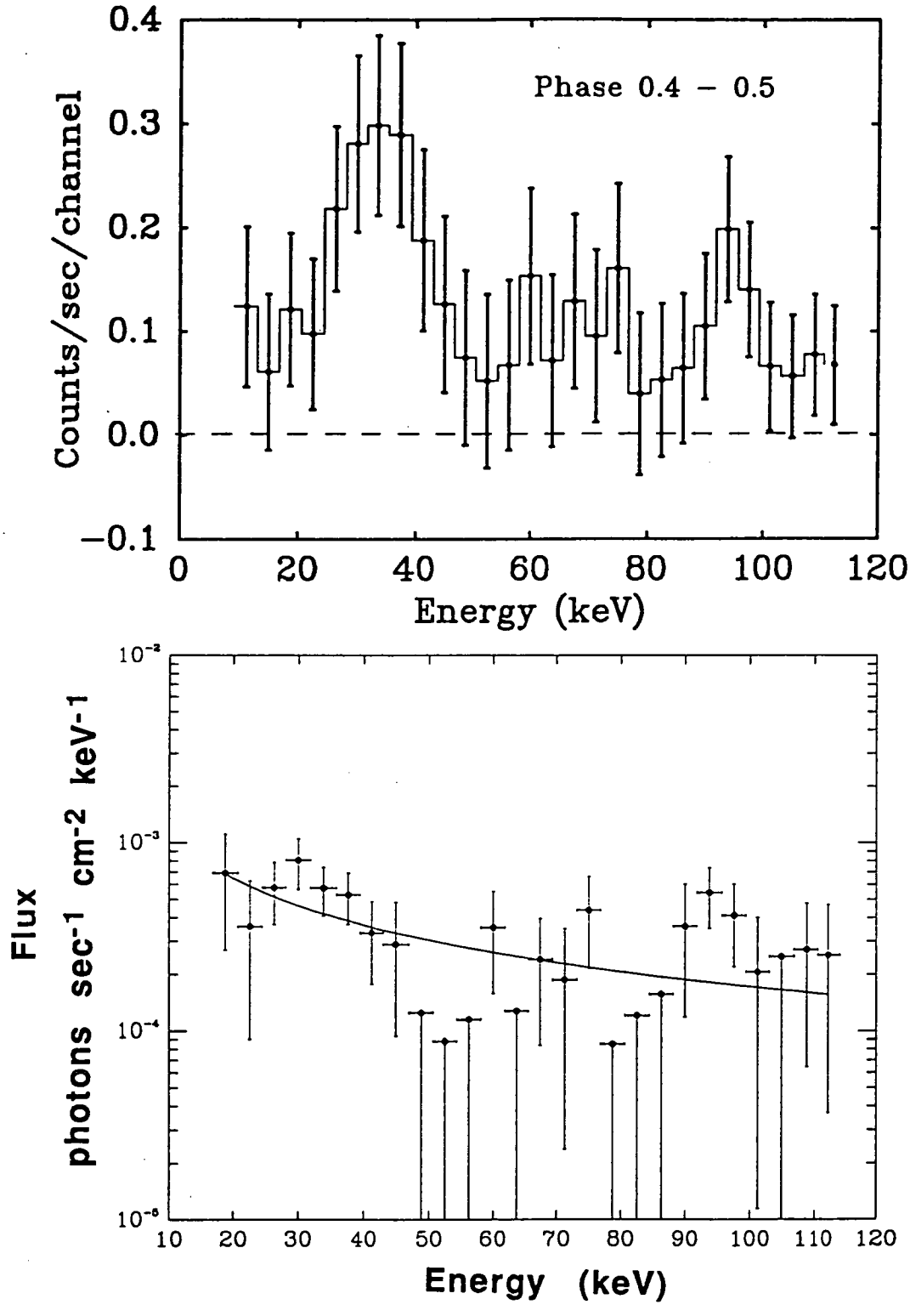

Fig 8.14 Pulse height and flux spectra for the 0.4-0.5 (spike/notch) phase interval. The best fit power law is also shown.

At all phases, except 0.4-0.6 an absorption line did not fit the data with the best fit line intensities being practically zero ($\approx 10^{-10}$). In the phase range 0.4-0.6 the best fit absorption line with E_{Line} =86 keV was extremely thin (10^{-12} keV) and deep $I_{Line} = 2.6 \times 10^{-3}$ photons $cm^{-2} sec^{-1} keV^{-1}$ and the reduced chi-squared value for 11 dof was $\chi^2_{11} = 1.528$. This does not represent an improvement upon the power law model fit or the power law plus emission line model. The extreme narrowness of the best fit line is physically untenable.

In varying the line energy the above procedure naturally leads to the determination of the confidence region for the central energy. It was found that the data could be fitted with an emission line with central energy (E_{line}) greater than 80 keV, i.e. the spectrum could just as well be fitted by a narrow line near 97 keV or as the wing of a more intense, broader feature at higher energy. A similar situation exists for the absorption line model; the 90% confidence interval allows either a broader shallow line or a narrow deep line.

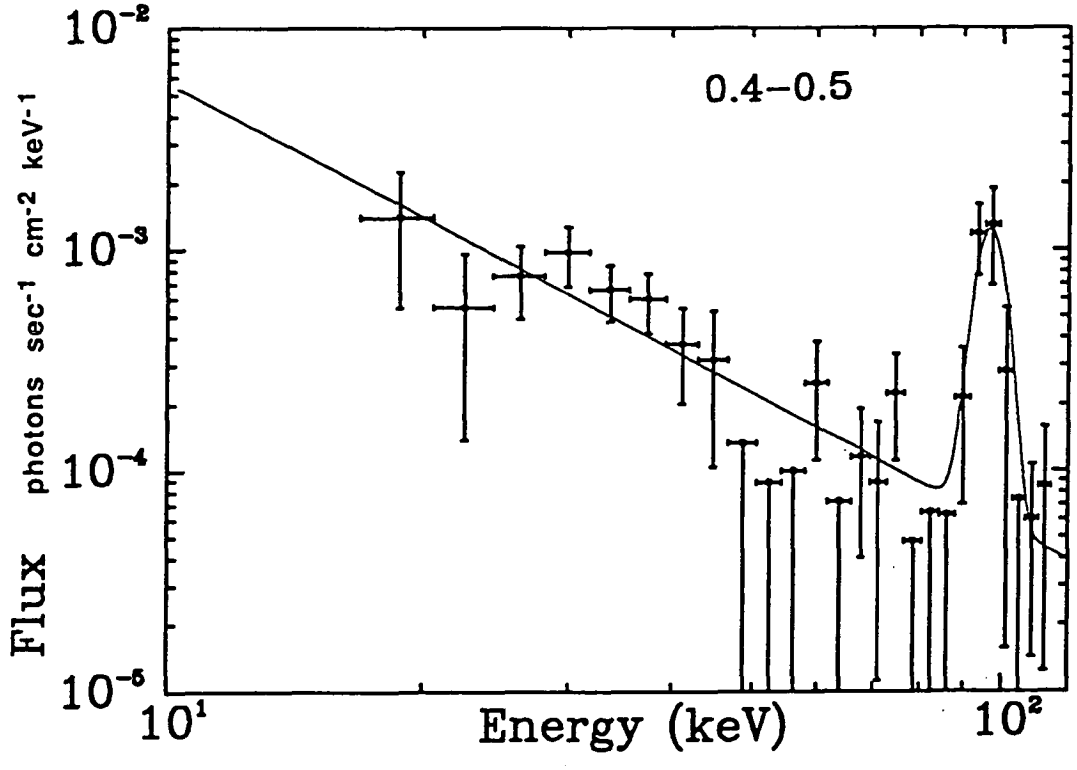

Figure 8.15 Power law + emission line model for the 0.4-0.5 phase interval flux data. The central energy is at 97keV.

8.3 Discussion

During the AS86 observations the 20-60keV luminosity was $\approx 3 \times 10^{37}$erg s^{-1}, assuming a source distance at 10kpc. If the low energy spectrum has a shape similar to that observed by GINGA (Dotani et al. 1989) and there is no flux above 200 keV then the calculated total luminosity was $\approx 3 \times 10^{37}$erg s^{-1}. An extension of AS86 spectrum to lower energies gives a flux approximately 10 times larger than the March 1987 GINGA observations. Since then further GINGA observations show a factor of 10 increase in luminosity during 1987/1988 (Sakao et al. 1990). However, other observations show that the luminosity has not increased steadily. The MIR-HEXE observations in Oct 1987 and Sept 1988 reported by Mony et al. (1989) suggest that the luminosity was similar to our Nov 1986 observation. The Birmingham group using the TTM telescope on MIR have failed to detect GX 1+4 on recent occasions in 1987 and 1988. Cook et al. as quoted by McClintock and Leventhal (1989) set upper limits lower than our flux in April 1988. All these measurements are about $\approx 1/3$ of the average 1970's luminosity and much greater ≥ 20 times) than the upper limits set using EXOSAT during the 1983-1985 period. During this off period GX 1+4 was about a factor ≈ 50 times fainter than the minimum luminosity measured during the 1970's (Hall and Develaar 1983, Mukai 1987). This corresponds to a brightness of $\leq 0.015 \times 10^{37}$erg s^{-1}.

The spectrum is also harder than measured during the 1970's as evidenced by the AS86 data and the MIR-HEXE data presented by Mony et al. (1989).

Also, during the faint state the pulse period behaviour changed from steady spin up to steady spin down. There are two possible sequences of pulse period changes. In the more radical history the pulse period rapidly increased in 1980 - 1983 and then decreased at $\approx -6 \times 10^{-8}$s/s until the end of 1986. This conclusion, reached by (Greenhill et al. 1989) relied upon two low significance balloon (Jayanthi et al. (1987) and Damle et al. (1987) observations and an initial period determination from the MIR-HEXE observations made in 1988 (Kendziorra private communication) and also our AS86 observations. Alternatively, the pulse period could have changed slowly and smoothly from spin up to spin down. This scenario is consistent with the shortest of the possible periods of Jayanthi et al. (1987), the re-evaluated period determination of Leahy (1988) using the data of Damle et al. It is also consistent with the period presented here at the 1σ level. It is not consistent with the period determination of Manchanda et al. (1987). More

recently between 1986 and 1990 the spin down rate has slowed to $\approx 4.4 \times 10^{-8}$s/s (Sunyaev et al. 1990).

Two possible models have been proposed to explain the low state of GX 1+4. Manchanda (1988) proposed that GX 1+4 underwent a 'nova' like eruption that smothered the X-ray source. Very large amounts of attenuation are required to suppress the flux up to energies greater than 20keV. The obscuration began to clear in early 1986. This model is untenable because the measured (see Sakao et al. for a tabulation of GINGA observations) low energy absorption is little different from the 1970's despite the flux being $\approx 1/3$ lower than the 1970's. Also the absorption is greater when GX 1+4 was brighter (Sakao et al., 1990).

More probably the mass transfer process changed, greatly reducing the accretion rate. High/low states, of shorter duration, have been noted in several low mass X-ray binaries, and cataclysmic variables. A disk will form in the GX 1+4 system because of the low wind velocity of a red giant (10km s^{-1}) is well below the upper limit set for disk formation (see Equation 2.21). According to the Gosh and Lamb (1979) disk accretion torque theory, a decrease in accretion rate is accompanied by the expansion of the pulsar's magnetosphere. A point can be reached where the magnetosphere radius is greater than the co-rotation radius and the centrifugal forces eject the incoming material. Accretion is virtually stopped. This is the "propeller" mechanism.

The luminosity, during the early 80's, could have dropped sufficiently so that the "propeller" mechanism became operative (Equation 2.13 in Section 2.5.4). The neutron star spins down in the absence of accretion torques. Taking the EXOSAT limits as the maximum possible luminosity and using Equation 2.13 the propeller effect would start if the magnetic moment was $\mu \leq 24$. Most accretion would be stopped and the disk would be disrupted by the stirring action of the magnetic field (Wang and Robertson, 1985). Spin down would also start. The spin down timescale is highly uncertain (see review by Henrichs, 1983). It is estimated by Wang and Robertson as being

$$t_s = 3\times10^6 \eta^{-1/2} \left(\frac{\beta}{\zeta} \right)^{3/4} P^{-3/4} \dot{M}_{12}^{-3/4} M^{3/4} R_6^{1/2} B_{12}^{-1/2} \qquad 8.2$$

Here the period (P) is in seconds, the accretion rate is in units of $10^{-12}M\odot$ the mass (M) is in solar units, the radius R is in units of 10^6cm and the surface magnetic field B is in units of 10^{12}G. The constants η which measures the fraction of matter passing through the magnetospheric boundary, is ≈ 1, $\zeta \approx 0.5$ (a boundary layer density enhancement factor) and β (a measure of the plasma rotation speed relative to the co-rotation velocity caused by the twisting of the magnetic field) can be significantly smaller than unity. Assuming $\eta=1$, $\beta=1$, $\zeta=0.5$, $\dot{M}=1$, $R_6=1$, $M=1.4M\odot$ and P=110 sec and $B=10^{13}$G the spin down timescale is estimated as 6.6×10^4yr or $P/\dot{P} \approx 1.5\times10^{-5}yr^{-1}(5\times10^{-11}S/S)$. This is much slower than the observed rate between 1986 and the present. But is consistent with the almost constant period if GX 1+4 made a gradual change from spin-up to spin-down during 1980-86.

According to the Gosh and Lamb theory the spin rate change is quite sensitive to luminosity i.e. $\propto L$. While the modified Gosh and Lamb theory of Wang (1987) suggests the spin down rate is $\propto L^{3/7}$. In either case the major drop in luminosity during 1980-1985 should have been accompanied by an interval of little or no pulse period change. This is in accord with the scenario that GX 1+4 made a smooth transition between spin up and spin down. During the 1986-1990 brightening the pulse period derivative should have varied in step with the luminosity. Although factor of 10 changes in the luminosity of GX 1+4 have occurred since 1986 there has been no corresponding changes in spin down rate as can be seen from the almost straight line connecting post 1986 period determinations (Figure 2.3). Such luminosity independent spin down has not been previously observed and is hard to explain in terms of present theories. However, these theories provide the only framework for understanding of pulsar torques and have been successful in the past.

In order to explain both the 1970's spin up and the present spin down the Wang (1987) modification of the Gosh and Lamb accretion torque theory requires that GX 1+4 is a fast rotator with a large magnetic moment $\mu_{30}=50$ G cm^3 (Dotani et al. 1989) which corresponds to a very strong surface magnetic field strength of $\approx 10^{14}$G . Such a high magnetic field strength was rejected by Dotani et al., on three grounds. The first being that at such high field strengths e^+ e^- pair production should occur and so distort the high energy spectrum of GX 1+4. This situation may not be so far fetched given the suggestion that GX 1+4 is the galactic centre 511keV source (McClintock and Leventhal 1990). The second objection was based

upon the relation between cut-off energy and cyclotron energy of Harding et al. (1984). The cut-off energy of GX 1+4 was found by White, Swank and Holt (1983) (WSH83) to be 10 keV. However, these authors noted that the cut-off was barely discernable in the nearly flat spectrum. Also higher energy, ≈30keV cutoff energies have been reported (Ricketts et al. 1982). The theoretical cut-off energy, magnetic field strength relation is really one of spectral hardness and magnetic field strength. The hard energy spectrum of GX 1+4 is taken by Frontera and Fiume (1989), using the model of Harding et al. (1984) as indicating a strong magnetic field of $\approx 2 \times 10^{13}$G. The third objection is that radio pulsar spin down trends imply a neutron star magnetic field of $\lesssim 2 \times 10^{12}$G. Recent arguments (Kundt 1985, Wijers, Burm, Verbunt 1989) suggest that magnetic field decay is not indefinite but may level off. Also, the field strengths required to explain the observed cyclotron lines range from 0.6×10^{12}G for X2259+586 to possibly $\approx 7 \times 10^{12}$G for Vela X-1 (Kendziorra et al. 1989). Previously, the presence of highly magnetic neutron stats in the old binaries was explained by the recent formation of the neutron star by accretion induced collapse (AIC) of an old white dwarf (Wijers, Burm and Verbunt 1989). Only under a limited set of circumstances is AIC possible without disrupting the low mass binary during the accompanying supernova explosion.

Given the current debate about magnetic field decay and the lack of any need on evolutionary grounds for AIC to explain the strongly magnetic pulsars of Her X-1 and 4U1626-67 (Verbunt et al. 1990), it is unreasonable to reject a high magnetic field on the grounds of the radio pulsar data.

In order to avoid the need for a very strong magnetic field Dotani et al. (1989) proposed that the accretion mechanism changed from Roche Lobe overflow to wind capture via a retrograde disk. The propeller mechanism and its stirring of the accretion disk could provide a means to allow a major change in the overall structure of the accretion disk. Maybe providing a trigger mechanism for a switch from prograde to retrograde rotation. In the retrograde disk case Dotani et al. calculated that the required magnetic moment was $\mu_{30}=11$ G cm^3 (B=2.2×10^{13}G). This figure they also rejected as being too strong. The above counter arguments still hold.

There are also other indicators that a field of this strength exists for GX 1+4 system. As mentioned earlier the hardness of the GX 1+4 spectrum suggests a field of $\approx 2 \times 10^{13}$G. Similarly the increase in pulsed fractional modulation with energy implied a strong magnetic field (Frontera and Fiume 1989). Such a

prediction is borne out by the recent discovery of a cyclotron like emission feature in the spectrum of Vela X-1 (Kendziorra et al. 1989). The pulse profiles of Vela X-1 are similar to those presented in this thesis. The spectrum of GX 1+4 was modelled using magnetic Comptonization by Bolt et al. (1976). They derived a magnetic cyclotron resonance energy of near 250keV as did Beurle at al (1983). Similar modelling of the Her X-1 spectrum predicted a cyclotron line energy of 100keV. This is approximately a factor of two to three greater than the actual cyclotron energy. Naively applying a similar rescaling of this model to GX 1+4 would imply a cyclotron energy of about 100keV. This would then match the possible absorption/emission feature seen in our high energy data.

Within our spectra there is no evidence for an emission feature near ≈40keV as reported by Maurer et al. (1982). The initial detection of this feature depended upon the source model used for the spectrum. Its reality was supported by its being variable in strength with pulse phase. Alternatively the feature could be regarded as absorption near 30keV. No second harmonic was found. A similar peak was found by Beurle et al. (1983). When Mony et al. (1989) fitted a thermal bremsstrahlung model to their MIR-HEXE data they found a broad 40-70keV excess. This excess was removed when the physically more appropriate Comptonization model of Sunyaev and Titarchuck (1980) was applied. This suggests that the spectral feature observed near 40keV could have been an artifact of the simple spectral models used. Thus there is no strong evidence of any cyclotron features below about 60keV in previous X-ray observations.

Any interpretation of the AS86 observation of GX 1+4 must explain several key features.

1: The appearance of a wide double peaked pulse profile in which the central notch possibly increases in relative depth with energy.

2: The pulse is very weak or non-existent in the energy range 65-84keV.

3: At energies between 85-104keV there is a narrow spike which occurs at the same phase as the low energy notch.

4: Any model should also consider the pulse shape seen in GINGA observations. Here, at lower energies (≤20keV) a notch much narrower than the notch observed during the AS86 flight.

5: The overall spectrum is a hard power law or thermal bremsstrahlung with a lack of flux between 70-85keV. When the high energy pulse data is included the spectrum is hardest at the notch/spike phases. However, below 75keV these phases are the softest of the pulse.

6: The PHA spectrum of the notch/spike phase range is better fitted by a two component model i.e. a power law continuum with an additional emission line at 97 keV with width ≈7keV.

The Dotani et al. (1989) field estimate of μ_{30}=11 (E_{cyc}=250keV) provides a starting point from which a comparison between the AS86 data and the two photon model of Kirk, Nagel and Storey (1989), (hereafter KNS), can be made. This model applies to energies up to about half the cyclotron energy. Assuming a mass of 1.4M⊙ for the neutron star, L_E =1.8x10^{38}erg/s and using a total luminosity of ≈3x10^{37}erg/s for the current observations then Kirk's (1985) model will apply if the angular size of the accretion column(s), Ω, satisfies

$$\pi/9 < \Omega < 2\pi/3 \qquad 8.3$$

This is within the range of sizes considered reasonable (Kirk 1985).

The KNS model predicts a double-humped, wide pulse profile in which the central notch widens and decreases in relative depth as the cyclotron frequency is approached. At about 1/2 - 1/3 E_{cyc} the pulse becomes single peaked. These pulse profiles are very similar to those of other models such as Nagel (1981), Harding et al. (1984). Both these earlier models assume that thermal bremsstrahlung is the dominant emission mechanism. The two photon emission process has been shown (Kirk and Melrose 1986) to be much more efficient than thermal bremsstrahlung emission. So for the same luminosity the slab thickness required is smaller with the two photon emission model. The slab thus has a wider opening angle. In this regard the KNS model predicts a wide pulse without requiring a column geometry.To produce the observed double peaked pulse profiles requires that the angle between our line of sight and the magnetic axis (θ) is small.

In the KNS model the transition from double to single peaked pulse profiles occurs at 1/3-1/2ω_{cyc}. If the observed appearance of a single peaked pulse at ~94keV is taken as this transition then the implied cyclotron energy is 190 - 280 keV. This

range of field strengths is in accord with the field strength estimated by Dotani et al. from the spin up/down history of GX 1+4 (E_{cyc}=250keV or μ_{30}=11).

A direct comparison can be made between the high energy pulse profile (Figure 8.7b) and the expected angular emission of the KNS model (figure 2 and 3 of KNS) . To make the comparison the maximum of the high energy spike will be considered to correspond to θ=0 (i.e. looking straight down the field lines). Each 0.1 phase bin spans 36° of the pulsar beam. Taking the centre of the 0.5-0.6 phase bin (bin1) as θ=0 then bin 2 spans the angle range 13° to 49° while bin 3 spans 49° - 85° and so on. Figure 8.16a is a reproduction of figure 2c of KNS. This figure shows the angular dependence of the X-ray emission from a τ = 5 slab when the cyclotron energy is 50 keV, at energies of 2.5, 5, 10 and 20 keV (top to bottom). The τ=5 case gives the narrowest notch at low (GINGA) energies. If these energies are rescaled to Ecyc=250 keV then the curves give the angular dependence of the X-ray emission at energies of 12.5 keV (cf. harder GINGA energy band observations), 25 keV (figure 8.5a top panel), 50 keV (figure 8.5b) and 100 keV (Figure 8.5d). Using this rescaling the KNS model predicts that Bin 2 (13°-49°) of the 100 keV pulse profile should be factor ≈2/3 of that in bin 1. The observed high energy spike (figure 8.7b, lower panel) drops in intensity more rapidly than this. In order to have the model pulse profile match the AS86 observations the intensity in bin2 must be reduced by a further factor of ≈2. Dr. M. Storey proposed that resonant scattering above the surface of the neutron star can provide a means to produce a narrow pulse within the frame-work of the KNS model.

To explain this scenario it must be recalled (Section 2.5.8 and 2.5.9, Trümper 1982) that in the presence of a strong magnetic field the angular dependence of the absorption co-efficients near resonance are different for the two polarizations. This is a consequence of vacuum polarization. In the classical (Zheleznyakov 1970) and approximate quantum (Melrose and Zheleznyakov 1981) cases the absorption of the extraordinary mode (x) is a maximum and the ordinary (o) mode is a minimum at θ=0. Only the extraordinary mode photons have a strong resonance at the cyclotron frequency (Ventura 1979).

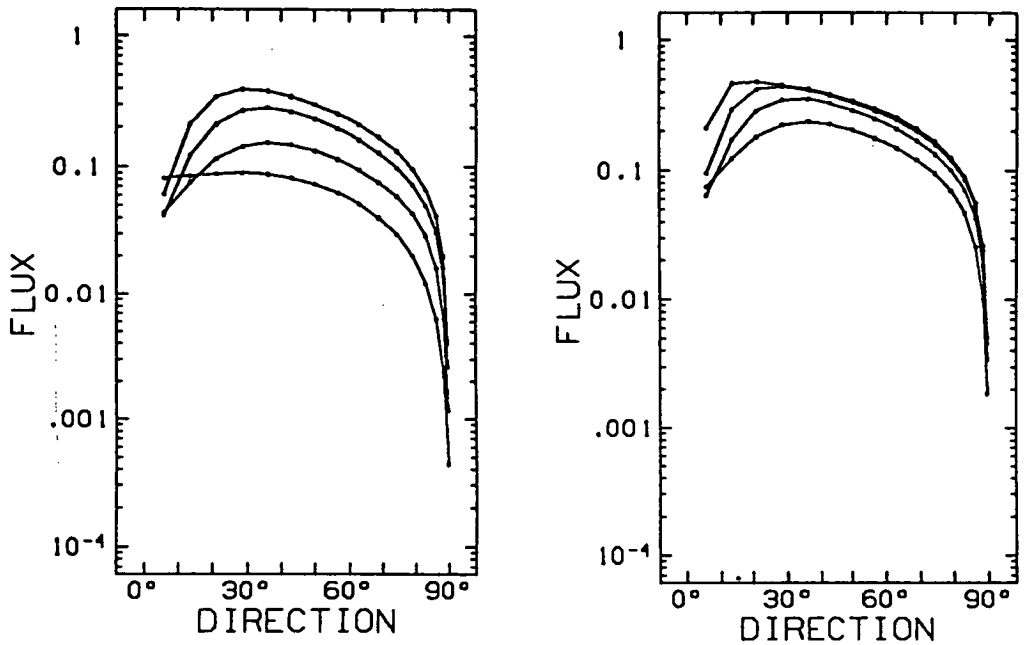

Fig 8.16 (a) The calculated angular dependence of the emission for E_{cyc}=50keV, τ=5 and temperature of 10 keV (Figure 2c of KNS). (b) The calculated angular dependence of the emission for E_{cyc}=100keV, τ=5 and temperature of 20 keV (Figure 3c of KNS). In both cases the curves are for energies of 2.5, 5, 10, and 20 keV (top to bottom).

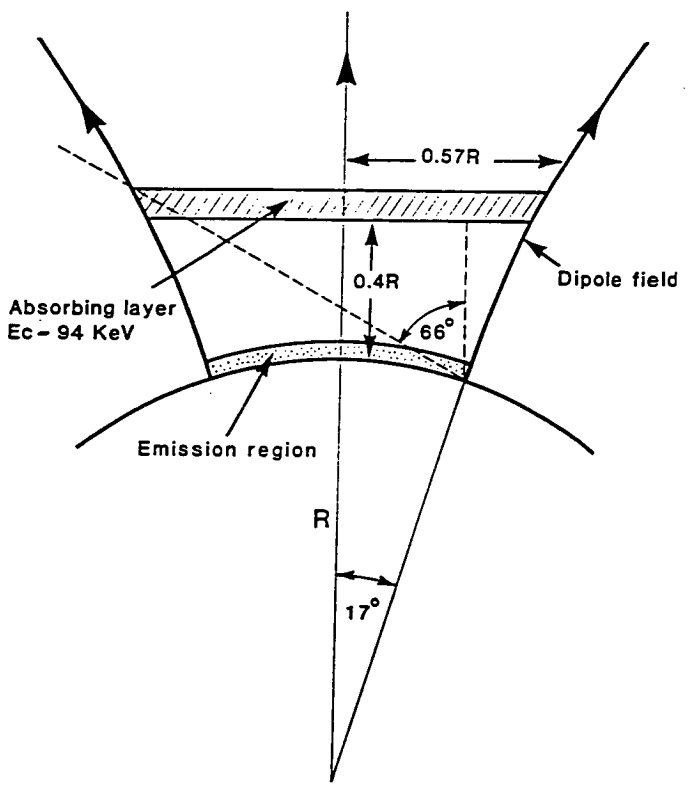

Fig 8.17 Diagram showing the geometry of the accretion column. Resonant absorption occurs at different energies for different heights above the surface of the neutron star. For an energy of 94 keV (the energy of the high energy pulse) resonant absorption will occur at a height of 0.4 neutron star radii above the surface. Absorption will extend to viewing angles of 40°. Diagram by Dr. M. Storey.

The x-mode absorption would need to extend out to θ=40° in order to produce the observed reduction in flux in the second bin. Hence, because of the combination of x-mode absorption at moderate angles and lower o-mode absorption at lower angles the high energy pulse is expected to be primarily o-mode emission. Moving away from the surface the local magnetic field and hence the cyclotron frequency drops. The accretion column is not cylindrical but follows the dipole geometry of the magnetic field. Therefore above the surface of the neutron star resonant absorption will take place at a lower energy and over a wider opening angle than near the surface. Figure 8.17 illustrates the resonant absorption geometry. Given a surface field of 2.2×10^{13}G (E_{cyc}=250 keV), the required absorbing layer, with a local cyclotron frequency corresponding to 97keV, would need to be at a height, D=0.4R (R is the neutron star radius), above the neutron star's surface. At this height the 40° opening angle implies that the polar cap is 0.34R in radius. Resonant absorption would also modify the emission pattern at lower energies. The effects would extend over a wider phase range, i.e. making the central notch deeper and wider than predicted by the KNS model. However, resonant absorption should be weaker higher in the accretion column because the density of the infalling material will be lower, higher in the accretion column. Hence resonant absorption may have little effect upon the lower energy pulse profiles.

Hardness Ratios

The two photon model also predicts that the central notch will have a harder spectrum than the surrounding peaks. For frequencies well below the cyclotron frequency ($<1/2\omega_{cyc}$) the two photon emission probabilities for the x and o modes (w^x, w^o) of the KNS model simplify to:

$$W^x \propto \frac{16}{15}\sin^2\theta\left[\frac{4}{Y^3} - \frac{2}{Y^2} + \frac{2}{Y} - 4\right] + \frac{16}{15}\cos^2\theta\left[\frac{3}{Y} - 4\right] \qquad 8.4$$

$$W^o \propto \sin^2\theta\left[\frac{32}{3Y}\right] + \left[\frac{3}{Y} - 4\right] \qquad 8.5$$

Here $y=\omega/\omega_{cyc}$ and θ is the angle between the viewing direction and the magnetic axis. In the limit where $\theta \rightarrow 0$, the above equations reduce to:

$$W = W^x = W^o \propto \left[\frac{3}{Y} - 4\right] \qquad 8.6$$

In the other limit ($\theta \rightarrow 90°$) the emission probabilities become

$$W^o \propto \frac{32}{2Y} + \frac{16}{15}\left[\frac{3}{Y} - 4\right]$$

$$W^x \propto \frac{16}{15}\left[\frac{4}{Y^3} - \frac{2}{Y^2} + \frac{2}{Y} - 4\right] \qquad 8.7$$

When $\theta=90°$ the X-rays do not intercept the accretion column and at $\theta=0°$, the radiation is dominated by o-mode radiation and will be similarly absorbed at all energies below the surface cyclotron energy. Thus at these two angles, resonant absorption will not affect the calculation of the hardness ratio.

Near $\theta=0$ the x and o mode emission intensities are about equal. At the two central energies used to form the hardness ratio plot of Figure 8.10b the hardness ratios at $\theta=0°$, 90° are given as

$$W(\theta=0°,\omega=94keV)/W(\theta=0°,\omega=47keV) = 0.33$$

$$W^T = W^x + W^o$$

$$W(\theta=90°,\omega=94keV)/W(\theta=90°,\omega=47keV) = 0.15$$

These estimates are remarkably close to the observed hardness ratios, (Figure 8.10b).

This analysis can be extended to lower energies i.e. at energies between 20 and 75keV. The spectral windows between 39-49keV and 18.75-39keV were used to form the hardness ratio plot of Figure 8.10a. The calculated hardness ratios at $\theta=0°$ and 90° are 0.55 and 0.29 respectively. These ratios are not compatible with the observations. In fact, at lower energies the central notch is apparently the softest portion of the pulse rather than the hardest as predicted by KNS. This is related to the behaviour of the depth of the central notch. In the AS86 observations the depth appears to increase with energy which results in a softer spectrum contrary to the expectations of the KNS model.

In this scheme the low energy notch seen by GINGA cannot also be due to resonant absorption as suggested by Dotani et al. (1989). If resonant absorption were operative over the range 1.2-90keV then a notch would be expected at all energies, which is contrary to the pulse profile of Figure 8.4a in the 19-39 keV range. There are two other linked objections to the Dotani et al. absorption model. They assume a cylindrical geometry for the accretion column which is a poor approximation to the dipole field structure. Their calculated optical depth of $\tau_x=10^4$ is excessive and can only produce a narrow notch when a cylindrical column geometry is used. If, as predicted by both classical and approximate quantum theory there is any angular dependence in the optical depth then such a high optical depth would imply substantial absorption out to large angles especially within a dipole geometry. Hence no pulse would be seen (Storey private communication 1990). The only way out of this contradiction with observations is to assume that the absorption stops suddenly at the edge of the accretion column.

Alternatively the high energy spike can be interpreted as the result of either a resonant absorption line at about 84keV or an emission line at near 94 keV. This implies a magnetic field of either $7.2\text{x}10^{12}$G or $8.1\text{x}10^{12}$G respectively. A magnetic field with $\omega\hbar$=100keV was one of the specific cases considered by KNS. The t=5 case presented in figure 3c of KNS is reproduced as Figure 8.16b. However, these pulse profiles are calculated for a plasma temperature of 20 keV which may be too high for GX 1+4. As in other cases considered by KNS the notch seen at low energies is expected to gradually widen and reduce in depth with increasing energy. At lower slab optical depths, corresponding to lower accretion rates, the resulting KNS pulse profiles are wider. The moderate optical depth (τ=5) case produces profiles closest in shape to those observed by GINGA and during the AS86 flight. The GINGA dip is ≈1/2 the depth of the maximum count rate over the 1.2-18.4 keV energy range. To reproduce such a narrow notch the line of sight must pass close (θ=10°:τ=5) to the magnetic axis. The expected total width of notch is about 25° at 5keV and ≈40° at 10keV (τ=5). See Figure 8.16b which is a reproduction of Figure 3c of KNS. The GINGA notch is about 40° wide in both the 1.2-6.9keV and 6.9-18.4keV windows as can be seen from figure 1 of Dotani et al. (1989) . Extending this analysis to 20keV the notch is expected to be slightly shallower (≈1/3 of the maximum) and wider (≈50°). Between 18.75 and 39.4keV the AS86 data (Figure 8.5) the notch is practically non-existent and at higher energies it is ≈70° wide.

A direct comparison is made between the KNS (no resonant absorption above the neutron star surface) and the observed depth of the notch is made in Table 8.3. The depth of the notch relative to the maximum count rate has been measured from the published GINGA X-ray light curves (Dotani et al 1989, and Makishima et al. 1988) and from Figure 8.5. The predicted ratio of the notch for bin 1 ($\theta<\pm18°$) as compared to bin2 ($18°<\theta<54°$) is measured from figure 2c and 3c of KNS (Figure 8.16). The predicted flux is taken as the average of the fluxes at the beginning, middle and end of each phase bin. The KNS model provides a reasonable match when E_{cyc} is assumed to be 94 keV ($B=2.2\times10^{13}$ G).

Table 8.3

Data			KNS fig 2c		KNS fig 3c	
Energy		Notch/Peak	E_{cyc} 94keV	E_{cyc} 250keV	94keV	250keV
2.5	GINGA	0.5	-	-	0.73	-
5.5	"	0.32	0.30	-	0.32	0.73
13.5	"	0.32	0.41	-	0.34	0.42
29	AS86	0.81	0.76	0.32	-	0.34
52	"	0.62	-	0.5	-	0.48
94	"	-	-	1	-	-

As an alternative to the E_{cyc}=250 keV scenario, the author proposes that the cyclotron energy is either 86 keV (the absorption line fit to the phase averaged spectrum) or near 94-97 keV (the high energy peak). In this case the GINGA notch is due to anisotropic scattering of the KNS model while the notch above 40keV is either the low energy wing of a cyclotron line at 86 keV or resonant absorption above the surface of the neutron star. The lack of a notch near 30 keV (Figure 8.5 top panel) is explained as the transition from double peaked to single peaked pulse profile at $\approx1/2\ E_{cyc}$ as in the KNS model.

Ventura (1979) shows that the resonance can have effects far from the cyclotron frequency. Mittra et al. (1990) invoke resonant absorption to explain the steep

spectrum of Her X-1. Near the resonance at 84keV the absorption extends over a large angle making pulsations difficult to detect.

Only the x-mode scattering cross-section is strongly resonant and decreases with θ while the o-mode coefficient is approximately constant but increases strongly with angle (Ventura 1979). Just above resonance the x-mode will still be heavily absorbed while the o-mode can escape only along the field lines. The limited energy range of the high energy spike can be explained by the power law drop off in the spectrum and the lowering of the detector sensitivity at high energies.

A variation on this scheme is if the 94-97keV pulse represents a cyclotron emission feature. Here the notch in the pulse profiles which is apparent in our data above 40keV would be caused by resonant absorption above the neutron stars surface. As the surface is approached the local cyclotron frequency increases and the central notch widens. Near the surface just below resonance most of the outgoing radiation is absorbed and so no pulse is detectable. Again the high energy pulse is o-mode radiation escaping along the field lines.

8.4 Conclusion

Our period determination of 111.6±1.35 sec is consistent with a gradual change in pulse period behaviour in the "dark ages" of the early 1980's. The accretion rate could well have fallen below the critical level turning GX 1+4 off, via the propellor mechanism. Such an off state could provide the means to switch from spin up to spin down behaviour. All variations (particularly in the retrograde disk) of the Gosh and Lamb accretion torque theory are sensitive to the source luminosity. GX 1+4 has shown a general spin down rate while varying significantly in luminosity. However, large short term variations in the spin down rate are possible given the sparsity of the observation. In this regard GX 1+4 provides a valuable test of the present theory.

A broad approximately symmetrical pulse is seen between 20 and 40keV. At higher energies a narrow notch appears within the maximum of the pulse. The pulse disappears between 70 and 90 keV. Between ≈90 and ≈104keV a narrow (0.2 - 0.4 phase) wide spike is observed at the same phase as the lower energy notch. This change suggests either a cyclotron feature or the transition from complex (double humped) pulse profile to a single peaked profile as expected from several models.

The spectrum observed in 1986 was both fainter and harder than that seen during the 1970's. Spectral fitting using the χ^2 minimization method shows no statistically significant changes in power law index or temperature with phase. However, below 70keV the spectrum varies smoothly with phase being softest at the phase of the notch/spike. The spectrum at the notch/spike phase can best be fitted by a power law with an addition cyclotron emission line. The overall (0-1) phase range spectrum can be best fitted by a model with a power law and an additional cyclotron absorption line. The best fit absorption line is at 86keV while in emission the line centre is at 97keV (cf 94 kev for the central energy of the high energy pulse profile). Both the notch/spike emission line and the overall phase absorption line models are a significant (95% confidence) improvement (in the χ^2 sense) in the representation of the data when compared to a simple power law model.

A hybrid KNS/resonant scattering model with the cyclotron energy being either 86keV or 97keV can explain qualitatively both the GINGA and AS86 data. In this scenario the low energy dip is the result of the absorption within the emitting region as per the KNS model. As the energy increases the dip widens and slowly disappears till is is barely detectable (e.g. Figure 8.5). Above 40keV resonant absorption begins to cause a notch in the pulse profile which eventually widens sufficiently to reduce the pulse to undetectable levels. The high energy spike then represents mainly o-mode radiation either at or just above resonance. Quantitatively the model is moderately successful. The KNS model using figure 8.16 (=fig 2c and 3c of KNS) yield relative notch depths similar to those observed by GINGA and during the AS86 flight.

Taking the cyclotron energy as being either 86 or 97keV then the surface magnetic field of GX 1+4 would be 7.2×10^{12}G or 8.1×10^{12}G and the line of sight would pass within about 10° of the magnetic axis. These magnetic field strengths are consistent with the retrograde disk model if the total luminosity of GX 1+4 is lower than estimated by Dotani et al. (1989).

Outstanding questions remain which can only be resolved by further high energy observations. It is crucial to the hybrid model presented here that the deepening of the notch with energy be firmly established. Also important is whether or not the cyclotron energy is near 90keV. In this regard high sensitivity observations are required to ascertain which spectral model is correct. (absorption/emission line) and how the spectrum varies with phase. If the high energy spike is truly limited in

energy this would strengthen the case for identifying it with a cyclotron emission line. This then leads to the question: what is the pulse shape above the high energy spike? Knowing the magnetic field strength, would also constrain present accretion torque theories.

Chapter 9

Conclusions

I don't pretend to understand the universe.
Its are great deal bigger than I am.

Thomas Carlyle

I can live with doubt and uncertainty. I think it's much more interesting to live not knowing, than to have answers which might be wrong.

Richard Feynman

Conclusions are usually consolidated guesses.

Henry Haskins

9. Conclusion

Results from two hard X-ray detectors flown in 1983 and 1986 are presented. Both detectors were large area xenon filled proportional counters which used both passive and active background rejection techniques. The 1986 detector used a six sided veto system which greatly reduced background counting rate. Also used in post flight analysis was the method of escape gating. This method was shown to produce an improvement in the signal to noise ratio when applied to the hard spectrum source GX 1+4. The problems associated with the redistribution of photon energies were found to be intrinsic to the method necessitating the formation of a hybrid normal/gated spectrum. Such a spectrum is presented for GX 1+4. This is the first escape gated spectrum of an astronomical source that the author is aware of.

In relation to the 1983 flight the effects of platform tilts are examined. These are shown to have a significant effect on positions derived using sun sensor and magnetometer navigation sensors. The position errors are generally of the order of the tilt. They cannot be ignored in crowded fields or when accurate fluxes are required.

The background during the 1983 flight was found to vary with zenith and azimuth angle. The size of the variations were greater at lower energies. In azimuth the background varied sinusoidally being highest toward the west. The zenith variation in background counting rate was more complicated. The count rate increased with zenith angle to about 45° where there is some evidence for a leveling in the trend. At zenith angles less than ten degrees there is evidence that the background below 20keV is constant or increases towards lower zenith distances. The variation in zenith (>10°) can be explained in terms of a leaky veto system and the known zenith dependence of atmospheric X-rays. The east/west anisotropy can also be explained by veto inefficiencies.

During the 1983 balloon flight four source regions were observed Sco X-1, SS433, MR2251-178 and the SMC. Upper limits set for the hard X-ray flux of SS433 are consistent with a power law spectrum with α=-2. This is the spectral index predicted by Begelman et al. (1980) as a result of beam interactions with the surrounding medium. MR2251-178 was not detected. The upper limits provide no useful constraints upon the spectrum and so there is no additional information about the origin of the diffuse X-ray background. SMC X-1 was not successfully

observed because of a combination of an azimuth offset and platform tilting. Also observed was a source of uncertain origin. This source is dubbed TAS X. There is no known X-ray source near the estimated position ($\alpha=22^h\ 52^m$ $\delta=-17^\circ\ 47'$ epoch 1983.3) of TAS X. The spectrum has an excess of counts below 20keV which cannot be explained by fluorescent escape or resolution smearing. Ignoring all counts below 20keV the inferred spectrum is very soft with a power law index of 2.9±0.7. Its properties are similar to the soft X-ray transients, several of which are now considered black hole candidates. Other possible, more local, origins are considered. Soft spectrum electron precipitation events have wide angular extents which is contrary to the point like nature of TAS X. The low energy counts could be produced by noise within the detector. The discriminators levels were very close to the noise threshold and so small gain changes can result in large changes in the low energy count rate. The excess flux at low energies is partially accounted for by a change in the zenith dependence in the background at angle $<10^\circ$. If the zenith angle corrected count rates below 15 keV are considered to be products of noise and background uncertainty then there is no need for a source to explain TAS X.

Results from three observations of Sco X-1 are reported. During the 1983 flight Sco X-1 was detected at a significance of only ~2.5σ. This was a consequence of a combination of a high low energy background rate, an azimuth offset, high line of sight atmospheric absorption and Sco X-1 being fainter than average. These results are consistent with those presented by Beurle et al. (1983), which were made during the same flight. Since Sco X-1 was faint it was probably in its quiescent state. In March 1986, simultaneously with EXOSAT observations, fast photometry was obtained using the Mt. Canopus 1 meter telescope. The EXOSAT data showed that Sco X-1 made a transition from the lower to the upper part of the quiescent (normal) branch. No optical QPO's were detected even at times when 6 Hz QPO were observed by EXOSAT. This non detection can be explained by the same reprocessing smearing seen during simultaneous X-ray /optical flares. No optical 0-25 Hz, red noise (<2.6 rms) was observed. This is consistent with the low levels of X-ray (<20keV) red noise seen during the quiescent/normal branch. A comparison with previous fast photometry suggests that the levels of X-ray and optical red noise are correlated. Further simultaneous X-ray and fast photometric monitoring are needed to confirm this relationship.

Sco X-1 was successfully observed during the November 1986 flight. A search was conducted for both QPO, red noise and regular pulsations. The coherent 2.9

millisec period of Leahy et al. (1987b) is tentatively confirmed. This detection depends upon being able to limit the frequency range searched to that near a known signal. However time constraints prevented a full analysis. No (<2.8%rms 95% confidence) QPO were observed. The QPO upper limits are consistent with Sco X-1 being away from the flaring branch. During the the observation Sco X-1 made a transition from a faint to bright state. This transition was accompanied by two changes. Strong (≈19%rms) 0-5Hz low frequency noise appeared. Also ≈8% 0-1Hz noise was observed. The spectrum changed within 10 minutes from a standard exponential with KT =4-5 keV to a similar spectrum with a hard flat power law tail extending to ≳70keV. This hard tail is detected at the 4 σ level. Throughout the flight no other similar count rate excursion was found. The hard tail is larger than any uncertainties in the background rate. It is not an instrumental effect because it is clearly evident in the escape gated mode without any coincident rise in the non-fluorescent doubles rate. Overall the most likely explanation is that the observed hard tail is intrinsic to Sco X-1.

The other source observed in 1986 was GX 1+4. Only eight complete cycles were seen. Using superposed epoch analysis the pulse period was found to be 111.6±1.35 sec. This period is consistent with a gradual change in pulse period from steady spin up to steady spin down over the 1980-1986 interval. This change in pulse behaviour occurred at a time when GX 1+4 was very faint. It is suggested that the luminosity may have dropped below the critical level at which the propeller mechanism becomes operative. In this case accretion would have been effectively cut off. At the time of the 1986 flight GX 1+4 was both fainter and had a harder energy spectrum than during the 1970's.

The pulse profile between 20 and 70 keV consisted of a broad pulse with a central notch of phase width ~0.2 . The depth of the notch seems to increase with energy. Between 65 and 85 keV no pulse is evident. Above about 85 keV the pulse profile is completely different consisting of a narrow spike. The phase and width of the spike is the same as the notch seen at lower energies. This radical change in pulse profile suggests a cyclotron resonance. Pulse phase spectroscopy supports either a wide absorption line near 86 keV or a narrow emission line near 97 keV. The implied surface magnetic field is either 7.2×10^{12} G (86 keV) or 8.1×10^{12} G (97keV).

Assuming that the resonant frequency is near 86 or 97keV the present data can be explained in terms of a hybrid model in which the GINGA notch is explained in terms of the two photon emission model of Kirk, Nagel and Storey (1987), while the higher energy 1986 flight data is thought to be due to resonant cyclotron absorption above the neutron star's surface. Beaming would occur at or just above the cyclotron frequency thus explaining the high energy spike. The centre of the pulsar beam must pass within about 10° of the line of sight. Given the uncertainties in the total luminosity a magnetic field strength near $8x10^{12}$ G is compatible with the retrograde disk model proposed by Dotani et al. (1989) to explain the spin up/down behaviour of GX 1+4.

References.

Achterberg A., Blandford R.D., Goldrich D. (1983), Nature **304** 607.

Agrawal P.C., Biswas S., Iyengar V.S., Kurte P.K., Machanda R.K. and Sreekantan B.V. (1969), Nature **224** 51.

Agrawal P.C., Biswas S., Gokhale G.S., Iyengar V.S., Kunte P.K., Manchanda R.K. and Sreekantan B.V. (1971) Astrophys. Spa. Sci. **10** 500.

Ali Alphar M. (1986), Mon. Not. Roy. Astro. Soc. **223** 469.

Alme M.L. and Wilson J.R. (1973) Astrophys. J. **186** 1015.

Alphar M. A. and Shaham J. (1985), Nature **316** 239.

Ambruster C.A., Sciortino S and Golub L. (1987), Astrophys. J. (Supp.) **65** 273.

Andrew B.H. and Purton C.R. (1968), Nature **218** 855.

Angel J.R.P., Kestenbaum H. and Novick R. (1971), Astrophys. J. (Lett.) **169** L57.

Angellini L. (1989), 23 rd ESALAB Symp: "Two Topics in X-Ray Astronomy." Vol **1** 81.

Angellini L., Stella L. and Parmar A.N (1989) Astrophys. J. **346** 906.

Awaki H., Koyama K., Kunieda. H. and Tawara Y. (1990), Nature **346** 544.

Becker R.H, Bolt E.A, Holt S.S., Pravdo S.H., Rothschild R.E., Serlemitsos P.J. and Swank J.H. (1976) Astrophys. J. (Lett.) **207** L167.

Begelman M.C, Sarazin C.L, Hatchett S.P., McKee C.F.and Arons J., (1980) Astrophys. J. **238** 722.

Begelman M.C. and Rees M.J. (1984), Mon. Not. Roy. Astro. Soc. **206** 209.

Bell A.R. (1990) Nature **345** 138.

Beurle K., Bewick A., Engel A.R., Harper P.K.S., Quemby J.J., Spooner N.J.C., Fenton A.G., Fenton K.B., Giles A.B., Greenhill J.G., Warren D.M. and Martin I.M. (1983), Adv. Space. Res. **3** 43.

Bevington P.R. (1969), "Data Reduction and Error Analysis for the Physical Sciences" McGraw Hill, New York.

Blanford R.D and Ress M.J. (1974) Mon. Not. Roy. Astro. Soc. **169** 395.

Blisset R.J. and Cruise A.M. (1979) Mon. Not. Roy. Astro. Soc. **186** 45.

Boldt E.A., Holt S.S. and Serlemitsos P.J. (1971), Astrophys. J. (Lett.) **164** L9.

Boldt E.A., Holt S.S., Rothschild R.E. and Serlemitsos P.J. (1976) Astron. Astrophys. **50** 161.

Boyton P.E., Deeter J.E, Lamb F.K. and Zylstra G. (1986) **307** 545.

Börner G., Hayakawa S., Nagase F. and Anzer U. (1987), Astron. Astrophys. **182** 63.

Bradt H.V., Braes L.L.E., Forman W., Hesser J.E., Hitner W.A., Hjellming R., Kellogg E., Kunkel W.E., Miley G.K., Moore G., Pel J.W., Thomas J., Van den Bout P., Wade C. and Warner B. (1975), Astrophys. J. **197** 443.

Bradt H.V.D. and McClintock J.E. (1983), Ann. Rev. Astron. Astrophys. **21** 13.

Brainard J. and Lamb F.K. (1987) Astrophys.J. (Lett.) **317** L33.

Brazier K.T.S., Carraminan A., Chadwick P.M., Dipper N.A., Lincoln E.W., Mannings V.G., McComb T.J.L., Orford K.J., Rayner S.M. and Turver K.E. (1990), Astron. Astrophys. **232** 383.

Buccheri R., Ozel M.E. and Sacco B. (1987), Astron. Astrophys. **175** 353.

Buselli G., Clancy M.C., Davidson P.J.N., Edwards P.J., McCracken K.G. and Thomas R.M. (1968), Nature **291** 1124.

Canizares C.R., Clark G.W., Li F.K., Murthy G.T., Bardas D., Sprott G.F., Spencer J.H, Mook D.E., Hiltner W.A., Moffett T.J., Grupsmith G., VandenBout P.A., Golson J.C., Irving C., Frohlich A. and van Grederen A.M. (1975) Astrophys J. **197** 457.

Canizares C.R., McClintock J.E. and Grindlay J.E. (1979), Astrophys. J. **234** 556.

Chapline G. Jr. and Stevens J. (1973) Astrophys. J. **184** 1041.

Charles P.A. 23 rd ESALAB Symp: "Two Topics in X-Ray Astronomy." Vol **1** 129.

Chester T.J. (1979), Astrophys. J. **227** 569.

Chodil G., Mark H., Rodrigues R., Seward F.D., Swift C.D., Turiel I., Hiltner W.A, Wallerston G. and Mamery E.J. (1968), Astrophys. J. **154** 645.

Clark G.W., Woo J.W., Nagase F., Makishima K. and Sakao T. (1990), Astrophys. J. **353** 274.

Cline T.L., Desai U.D., Schnidt W.K.H. and Teegarden B.J. (1977), Nature **266** 694.

Coe M.J., Engel A.R. and Quemby J.J. (1976), Nature **259** 544.

Coe M.J., Dennis B.R., Dolan J.F., Crannel C.J., Manrer G.S., Frost K.J., Orwig L.E., Grof W. and Price K.M. (1980), Astrophys. J. **237** 148.

Coe M.J., Engel A.R., Evans A.J. and Quemby J.J. (1981), Astrophys. J. **243** 155.

Collmar W. and Gruber D.E (1989) 23 rd ESALAB Symp: "Two Topics in X-Ray Astronomy." Vol **1** 353.

Collura A., Maggio A, Sciortinos, Vaiana G.S. and Rosner R. (1987) Astrophys. J. **315** 340.

Cooke B.A., Levine M., Lang F.L., Primini F.A and Lewin W.H.G (1984) Astrophys. J. **285** 258.

Cooke D.J. (1971), Ph.D. Thesis, Univ. Tasmania.

Costa E, Massaro E., Salvati M. and Appoloni A. (1984) Astophys. Spa. Sci. **100** 165.

Cowie, L.L. (1989), 23rd ESALAB Symp: "Two Topics in X-ray Astronomy". Vol **2** 707.

Cowley A.P. and Crampton D. (1975), Astrophys. J. (Lett.) **201**. L65.

Cowley A.P., Hutchings J.B. and Crampton D. (1988) Astrophys. J. **333** 906.

Crampton D. and Cowley W.P. (1975), Astrophys. J. **197** 467.

Crampton.D., Cowley A.P., Hutchings J.B. and Kaat.C. (1976), Astrophys. J., **207** 907.

Cutler E.P, Dennis B.R. and Dolan J.F. (1986) Astrophys. J. **300** 551.

Damle S.V., Kunte P.K., Leahy D.A., Naranan S., Sreekantan, B.V. and Veukatesan D. (1987), Adv. Spa. Res. **8** 415.

Damle S.V., Kunte P.K., Leahy D.A., Naranan S., Sreekantan B.V. and Venkatesan D. (1989), 23rd ESALAB Sym. "Two Topics in X-ray Astronomy" Vol **1** 377.

Davidsen A., Malina R. and Bowyer S. (1977) Astrophys. J. **211** 866.

De Jager O.C., Swanepoel J.W.H. and Raubenheimer B.C. (1989), Astron. Astrophys. **221** 180.

Deeming T.J. (1975), Astrophys. Space Sci. **36** 137.

Deeter J.E. (1983), Astrophys. J. **281** 483.

Dennis B.R., Beall J.H., Cutler E.P., Crannell C.J., Dolan J.F., Frost K.J. and Orwig L.E. (1980a), Astrophys. J. (Lett.) **236** L49.

Dieters S.W.B., Greenhill J.G, Sharma D.P., Sood R.K., Waldron L., Story M.C. (1991), Adv. Spa. Res. **11** 35

Dolan J.F. (1972), Astrophys. Spa. Sci. **17** 472.

Dolan J.F., Crannell C.J., Dennis B.R. and Orwig L.E. (1987), Astrophys. J. **322** 324.

Dotani T., Kii T., Nagase F., Mukishima K., Ohashi T., Sokao T., Koyama K. and Touhy I.R. (1989), Pub. Astron. Soc. Jap. **41** 427.

Doty J.P, Hoffman J.A. and Lewin W.H.G. (1981), Astrophys. J. **243** 257.

Duffett-Smith P. (1979), "Practical Astronomy with you Calculator ", Cambridge University Press. Cambridge.

Duldig M.L., Emery M.W, Fenton A.G, Fenton K.B., Greenhill J.G. and Thomas R.M. (1977), Proc. Astron. Soc. Aust. **3** 117.

Duldig M.L. (1981), Ph.D. Thesis. University of Tasmania.

Duldig M.L., Greenhill J.G., Fenton K.B., Thomas R.M. and Watts D.J. (1983), Astrophys. Space Sci. **95** 137.

Dworetsky M.M. (1983), Mon. Not. Roy. Astro. Soc. **203** 917.

Edelson R.A. and Krolik J.H. (1988), Astrophys. J. **333** 646.

Edwards - Chesley S. (1975), Astrophys. J. **196** 103.

Elsner R.F., Weisskopf M.C., Apparoo M.V., Darro W, Ramsey B.D., Williams A.C, Grindlay J.E. and Sutherland P.G. (1985), Astrophys. J. **297** 288.

Evans W.D., Bellan R.D., Conner J.P., Strong J.B., Hiltner W A. and Kunkel W.E. (1970), Astrophys. J. (Lett.), **162** L115.

Fegan D.J. (1990), 21st Inter. Cosmic Ray Conf. Proc. **Vol 11** 23.

Feldman P.A., Gribben J.R and Plagemann S.H. (1970), Nature **226** 432.

Felten J.E. and Rees M.J. (1972), Astron. Astrophys. **17** 226.

Fernie J.D. (1989), Pub. Astron. Soc. Pac. **101** 225.

Ferraz Mello S. (1981), Astron. J. **86** 619.

Fishman G.J. (1981), Astrophys. Spa. Sci. **75** 125.

Fomalont E.B., Geldzuhter B.J., Hjelling R.M. and Wade C.M., (1983), Astrophys. J. **275** 802.

Fontera F. and Dal Fiume D. (1989), 23 rd ESALAB Symp: "Two Topics Of X-Ray Astronomy." Vol **1** 57.

Forman W., Giacconi R., Jones C., Schreier E. and Tanabaum H. (1974), Astrophys. J.(Lett.) **193** L67.

Forman W., Jones C. and Tannenbaum H. (1976), Astrophys. J. **208** 849.

Fortner B., Lamb F.K. and Miller G.S. (1989), Nature **342** 775.

Frank J., King A.R. and Raine D.J. (1985), "Accretion Power in Astrophysics", Cambridge University Press. Cambridge.

Frank J., King A.R. and Lasota J.P. (1987), Astron. Astrophys. **178** 137.

Friedman H., Fritz G., Henry H.C., Hollinger J.P., Meekins J.F. and Sadeh D. (1969), Nature **221** 345.

Frohlich A. (1973), Mon. Not. Roy. Astro. Soc. **165** 313.

Fullerton A. W., (1985), "The Study of Variable Stars with Small Telescopes" Ed: Percy J. R., Cambridge Uni. Press. Cambridge.

Geldzahler B.J., Fomalont E.B., Hilldrup K. and Cory B.E. (1981), Astron. J. **86** 1036.

Geldzahler B.J. and Fomalont E.B. (1986), Astrophys. J. **311** 805.

Geldzahler B.J. and Hertz P. (1987), Astrophys. J. **322** 342.

Geldzahler B.J., Fomalont E.B. and Cohen N.L. (1989), Proc. 23rd ESLAB Symp: "Two Topics in X-Ray Astronomy" Vol **1** 415.

Giacconi R., Gursky H., Pablini F. and Rossi B. (1962), Phys. Rev. Lett. **9** 439.

Giles A.B. (1985), "Mirrabooka: An Australian Wide-Bandwidth X-Ray Astronomy Satellite" Payload & Operations.

Glass I.S. and Feast M.W. (1973), Nature **345** 39

Gosh P. and Lamb F.K. (1979), Astrophys. J. **234** 296.

Gotthelf E., Halpren J., Szentgyorgyi A., Becker R. and Helfand D. IAU Circ. 4635.

Gottlieb E.W., Wright E.L. and Liller W. (1975), Astrophys. J. (Lett.), **195** L33.

Gray D.F. and Desikachary K. (1973), Astrophys. J. **181** 523.

Greenhill J.G., Coe M.J., Bell-Burnell S.J., Strong K.T. and Carpenter G.F. (1979a), Mon. Not. Roy. Astr. Soc. **189** 563.

Greenhill J.G., Duldig M.L., Emery M.W., Fenton A.G, Fenton K.B., Thomas R.M. and Watts D.J. (1979b), Proc. Astron. Soc. Aust. **3** 349.

Greenhill J.G., Fenton A.G., Fenton K.B., Thomas R.M., Duldig M.L., Emery M.W., Cooke D.J., Phillips J., Watts D.J., Hudson R.M. and Middleton E. (1979c), 16th Int. Cosmic Ray Conf., Kyoto **11** 8.

Greenhill J.G., Giles A.B., Sharma D.P., Dieters S., Sood R.K., Thomas J.A., Waldron L., Manchanda R.K., Carli R., Hammer P., Kemdziorra E., Staubert R., Bazzano A., Ubertini P. and La Padula C. (1989), Astron. Astrophys. **208** L1.

Greenhill J.G., Sharma D.P., Dieters S.W.B., Fenton K.B., Sood R.K. and Waldron L. (1990a), Proc. 21st Internat. Comic Ray Conf., Adelaide, OG-1.2.2.

Greenhill J.G., Giles A.B., Salmon G.L., Sharma D.P. and Dieters S.W.B. (1990b), Accepted by Advances Spa. Sci.

Gribbin J.R., Feldman P.A. and Plageman S.H. (1970), Nature **225** 1123.

Groth E.J. (1975), Astrophys. J. (Supp.), **29** 285.

Gursky H., Giacconi H., Gorenstein P., Waters J.P., Oda M., Bradt H., Garnire G. and Sreekantan B.V. (1966), Astrophys. J. **146** 310.

Hall R. and Davelaar J. (1983), IAU Circ. 3872.

Halpren J.P. (1984), Astrophys. J. **281** 90.

Harding A., Mészàros P., Kirk J.G. and Galloway D.J. (1984), Astrophys. J. **278** 369.

Harwitt M. (1988), "Astrophysical Concepts" pp.105-109, pp.239-245 2nd Ed Springer-Verlag, New York.

Hasinger G. and van der Klis M. (1987), IAU Circ. 4489.

Hasinger G. and van der Klis M. (1989), Astron. and Astrophys. **225** 79.

Hasinger G., Priedhorsky W.C. and Middileditch J. (1989), Astrophys. J. **337** 843 (HPM 1989).

Hawkins F.J., Mason K.O. and Sanford P.W. (1973), Nature **241** 109.

Hayakawa S. (1981) Spac. Sci. Rev. **29** 211.

Haymes R.C., Ellis D.V. and Fishman G.J. (1968), J. Geophys. Res. **73** 867.

Haymes R.C., Harden F.R., Johnson W.N. and Prichard H.M. (1972), Astrophys. J. (Lett.) **172** L47.

Henrichs H.F. (1983), p363. "Accretion Driven Stellar X-ray Sources" Eds: Lewin W.H.G., Heuval E.P.J van den. Cambridge Uni. Press. New York.

Hill K.M. (1989), Ph.D. Thesis. University of Tasmania.

Hjellming R.M. and Wade C.M. (1971), Astrophys. J. (Lett.) **164** L1.

Hjellming R.M (1988), "Galactic and Extragalactic Radio Astronomy" 2nd Ed. Eds: Verschuur C.L., Kellermann K.I. Springer-Verlag. Berlin.

Hocking W.K. (1989), p59. Computers in Physics Jan/Feb.

Hoffmeister S., Richter G., Wenzel W., Dunlop S. (Translator), (1985), "Variable Stars" Springer-Verlag. Berlin.

Horne J H. and Baliumas S L (1986), Astrophys. J. **302** 757.

Hoyng P. (1976), Astron. and Astrophys. J. **47** 449.

Hudson H.S. (1979), p.115 "Particle Acceleration Mechanisums in Astrophysics" Eds: Arons J., McKee C.M. and Max C., Amm. Inst. Phys., New York.

Hurewicz W. (1975), pp.65-69 "Lectures On Ordinary Differential Equations". MIT Press, Cambridge.

Hutchings J.B. (1982), "Galactic X-ray Sources" Eds: Sanford P.W., Laskarides P., Sulton J. John Wiley & Sons. Chichester.

Illarionov A.F. and Syunyaev R.A. (1972), Soviet Astron. **16** 45.

Ilovaisky S.A., Chevalier C., White N.E., Mason K.O., Sanford P.W., Delvaille J.P. and Schnopper H.W. (1980), Mon. Not. Roy. Astro. Soc. **191** 81.

Imamura J.I., Steinman-Cameron T.Y, and Middileditch J. (1987), Astrophys. J. (Lett.) **314** L11.

Isern J., Hernanz M., Canal R., Laby J. and Mochkovitch R. (1987), Astron. Astrophys. (Lett.) **172** L23.

Jain A., Hasinger G., Pietsch W., Proctor R., Reppin C., Trümper J., Voges W., Kendziorra E. and Staubert R. (1984), Astron. Astrophys. **140** 179.

Jain A.K., Jayanthi U.B., Kasturirangan K. and Rau U.R. (1973), Astrophys. Spa. Sci. **21** 107.

Jayanthi U., Jablouski F. and Braga J. (1987), Astrophys. Spa. Sci. **137** 233.

Johnson-Neil W., Kurfess J.D., Bleach R.D. (1976), Astrophys. Spac. Sci. **42** 35.

Johnson-Neil W., Kurfess J.D., Maurer G.S. and Strickman M.S. (1980), Astrophys. J. **238** 982.

Joss P.C. and Rappaport S.A. (1984), Ann. Rev. Astron. Astrophys. **22** 537.

Kasahara I. (1974), Astrophys. and Spa. Sci. **29** 191.

Kendziorra E., Staubert R., Reppin C., Pietsch W., Voges W., Trümper J. (1982), p205. "Galactic X-ray Sources" . Eds: Sandford P.W., Laskarides P., Sulton J. John Wiley & Sons. Chichester.

Kendziorra E., Mony B., Maisack M., Staubert R., Döbereiner S., Englhauser J., Pietsch W., Reppen C., Trümper J., Efremov V., Kaniovsky S., Kuznetsov A. and Sunyaev R. (1989), 23rd ESALAB Symp: "Two Topics in X-Ray Astronomy" Vol **1** 467.

Kestermbaum H., Angel J.R.P., Novick R. and Cocke W.J., (1971), Astrophys. J. (Lett.) **169** L49.

Kii T., Hayakawa S., Nagase F., Ikegami I. and Kawai N. (1986), Pub. Astron. Soc. Jap. **38** 751.

Kirk J.G. (1985), Astron. and Astrophys. **142** 430.

Kirk J.G. and Trümper J.E. (1983), "Accretion Driven Stellar X-Ray Sources" Eds: Lewin W.H.G. and van den Heuval E.P.J. Cambridge Uni Press, London.

Kirk J.G., Nagel W. and Storey M.C. (1986), Astron. and Astrophys. **169** 259.

Kitamoto S. (1989), 23rd ESALAB Sym. "Two Topics in X-Ray Astronomy" Vol **1** 231.

Knoll G.F. (1979), "Radiation Detection and measurement" John Wiley & Sons, New York.

Knude J. (1987), Astron. Astrophys. **171** 289.

Koo J-W.G. and Haymes R.C. (1980), Astrophys. J. (Lett.) **239** L57.

Koyama K., Inoue H., Tanaka Y., Awaki H., Takano S., Ohashi T. and Matsuoka M. (1989), Pub. Astro. Soc. Jap. **41** 731.

Kraus U., Herold H., Maile T., Nollert H.-P., Rebetzky A., Ruder H. and Wolf K. (1989), Astron. Astrophys. **223** 246.

Kreminsky W. and Priedhorsky W.C. (1978), Pub. Astron. Soc. Pac. **90** 434.

Kreysig E. (1979), "Advanced Engineering Mathematics" 4th ed. John Wiley &Sons, New York.

Kundt W. and Gopal-Krishna (1984), Astron. Astrophys. **136** 167.

Kundt W. (1985), p263 "The Evolution of Galactic X-Ray Binaries". Eds: Truemper, J., Lewin W.H.G., Brinkman W. and D. Reidel , Dordrecht.

Kuo S.S.(1972), pp.116-124 "Computer Application of Numerical Methods" Addison Wesley, Phillipines.

Kurtz D.W. (1985), Mon. Not. Roy. Astro. Soc. **213** 773.

Kylafis N.D. and Klimis G.S. (1987), Astrophys. J. **323** 678.

La Sala J. and Thorstensen J.R. (1985), Astron. J. **90** 2077.

Lamb F.K., Shibazaki N., Shaham J. and Alpha M.A. (1985), Nature **317** 681.

Lamb F.K. (1986), p151 "The Evolution of Galactic X-Ray Binaries", Eds: Truemper, J, Lewin W.H.G., Brinkman W. and D.Reidel, Dordrecht.

Lamb F.K. (1989), 23rd ESALAB Symp:"Two Topics in X-Ray Astronomy" Vol **1** 215.

Lamb P. and Sanford P.W. (1979), Mon. Not. Roy. Astro. Soc. **188** 555.

Lampton M., Bowyer C.S. and Harrington S. (1970), Astrophys. J. **162** 181.

Lampton M., Margon B. and Bowyer S. (1976), Astrophys. J. **208** 177.

Lang K.R. (1980), pp.46-48, "Astrophysical Formulae" 2nd Ed., Springer-Verlag, Berlin.

Langemeir A., Hasinger G., Sztajo M., Trümper J. and Pietch W. (1985), IAU Circ. 4147.

Langer S.H. and Rappaport S. (1982), Astrophys. J. **257** 753.

Laros J.G. and Singer S. (1976), Astrophys. J. **205** 550.

Lasker B. and Hesser J. (1970), Bull. Amm Astron. Soc. **2** 198.

Leahy D.A., Elsner R.F. and Weisskopf W.C. (1983), Astrophys. J. **272** 256.

Leahy D.A. (1987a), Astron. Astrophys. RN **180** 275.

Leahy D.A. (1987b), IAU Circ. 4485.

Leahy D.A., Darbro W., Elsner R.F., Weisskopt M.C., Sutherland P.G., Kahn S. and Grindlay J.E. (1983), Astrophys. J. **260** 160.

Levine A.M., Lang F.L., Lewin W.H.G, Primini F.A., Dobson C.A., Doty J.P., Hoffman J.A., Howe S.K., Scheepmaker A., Wheaton W.A., Matteson J.J., Baity W.A., Gruber D.E., Knight F.K., Nolan P.L., Pelling R.M., Rothschild R.E. and Patterson L.E. (1984), Astrophys. J. (Supp.) **54** 581.

Lewin W.H.G., Clark G.W. and Smith W.B. (1968), Astrophys. J. (Lett.) **152** L55.

Lewin W.H.G., van Paradijs J. and van der Klis M. (1988), Space Sci. Rev. **46** 273.

Lewin W.H.G., McClintock J.E., Ryckman S.G., Glass I. and Smith W.B. (1970), Astrophys. J. **162** L109.

Lewin W.H.G and Joss P.C. (1988).p41 "Accretion Driven X-ray Binaries".Eds: Lewin W.H.G., Heuval E.P.J van den. Cambridge Uni. Press. New York.

Lewin W.H.G., Ricker G.R. and McClintock J.E. (1971), Astrophys. J. (Lett.) **169** L17.

Li F., Clark G. and Market T. (1978), Nature **272** 723.

Ling J.C., Mahoney W.A., Willet J.B. and Jacobson A.S. (1979), Astrophys. J.**231** 896.

Lomb N.R. (1976), Astrophys. Spa. Sci. **39** 447.

Maejima Y., Makishima K., Matsuoka M., Ogawara Y. and Oda M. (1984), Astrophys. J. **285** 712.

Makino F. (1989), IAU Circ. 4855.

Makishima K., Oshashi T., Sakao T., Dotani T., Inoue H., Koyama K., Makino F., Mitsuda K., Nagase F., Thomas H.D., Turner M.J.L., Kii T. and Tawara Y. (1988), Nature **333** 746.

Manchanda R.K. (1972), J. Geophys. Res. **77** 4254.

Manchanda R.K., Agrawal P. and Rao A. (1987), Proc. 20th Inter. Cosmic Ray Conf. **1** 99.

Manchanda R.K. (1988), Astrophys. Spa. Sci. **150** 31.

Manchanda R.K. (1989), IAU Circ. 4871.

Marachi L., Teves A and van der Heuval E P J (1977), Astrophys. J. **216** 819.

Margon B. (1984), Ann. Rev. Astron. Astrophys. **22** 507.

Mark H., Price R.E., Rodrigues R. and Steward F.D. (1969), Astrophys. J. (Lett.) **156** L67.

Market T.H., Winkler P.F., Laird F.N., Clark G.W., Hearn D.R., Sprott G.F., Li F.K., Bradt H.V., Lewin W.H.G. and Scnopper H.W. (1979), Astrophys. J. (Supp.) **39** 573.

Mason K.O., Charles P.A., White N.E., Culhane J.L., Sandford P.W. and Strong K.T. (1976), Mon. Not. Roy. Astro. Soc. **177** 513.

Matsuda T., Inoue M. and Sawada K. (1987), Mon. Not. Roy. Astro. Soc. **226** 785.

Matsuoka M., Fujii M., Miyamoto S., Nishimura J., Oda M., Ogawara Y., Hayakawa S., Kasahara I., Makino F., Tanaka Y., Agrawal P.G. and Sreekantan B.V. (1972), Astrophys. Spa. Sci. **18** 472.

Maurer G.S., Johnson-Niel W., Kurfess J.D. and Strickman M.S.(1982), Astrophys. J. **254** 271.

Mätzeler K., Bai T., Crannell C.J. and Frost K.J. (1978), Astrophys. J. **223** 1058.

McClintock J.E. and Leventhal M. (1990), Astrophys. J. **346** 143.

Melrose D.B. and Zheleznyakov V.V. (1981), Astron. Astrophys. **95** 86.

Mereghetti S. and Grindlay J.E. (1987), Astrophys. J. **312** 727.

Mészàros P. (1984), Spa. Sci. Rev. **38** 325.

Middleditch J., Mason K.O., Nelson J. and White N. (1981), Astrophys. J. **244** 1001.

Middleditch J. and Cordova F.A. (1982), Astrophys. J. **255** 585.

Middleditch J. and Kristian J. (1984), Astrophys. J. **279** 157.

Middleditch J. and Priedhorsky W.C. (1986), Astrophys. J. **306** 230.

Middleditch J., Imamura J.N. and Steinman - Cameron T. Y. (1986), Preprint.

Mihara T., Makishima K., Ohashi T., Sakao T., Tashiro M., Nagase F., Tanaka Y., Kitamoto S., Miyamoto S., Deeter J.E. and Boynton P.E. (1990), Nature **346** 250.

Milgrom M. (1976), Astrophys. J. **208** 191.

Milgrom M. and Katz J. I. (1976), Astrophys. J. **205** 545.

Mitra A.K. (1989), Astron. Astrophys. (Lett.) **219** L1.

Mitsuda K., Inoue H., Koyama K., Makishima K., Matsuoka M., Ogawara Y., Shibazaki N., Suzuki K., Tanaka Y. and Hirano T. (1984), Pub. Astro. Soc. Jap. **36** 741.

Mitsuda K. and Tanakay Y. (1985), "The Evoloution of Galactic X-ray Sources" Eds: Lewin W.H.G. and van den Heuval E.P.J. D. Reidel, Dordrecht.

Mitsuda K. (1989), 23rd ESLAB Symp: "Two Topics in X-Ray Astronomy" Vol **1** 197.

Miyamoto S. and Matsuoka M. (1977), Spa. Sci. Rev. **20** 687.

Miyamoto S. (1978), Astron. Astrophys. **63** 69.

Miyamoto S. and Kitamoto S. (1989), Nature **342** 773.

Mony B., Kendiziorra E., Maisack M., Staubert R., Döbereiner S., Englhauser J., Pietsch W., Reppin C., Trümper J., Efremov V., Kaniovsky V Kuznetsov A. and Sunyaev R (1989), 23rd ESALAB Symp: "Two Topics in X-ray Astronomy" Vol **1** 541.

Mook D.E., Messina R.J., Hiltner W.A., Belliam R., Conner J., Evans W.D., Strong I., Blanco V.M., Hesser J.E., Kunkel W.E., Lasker B.M., Golson J.C., Pel J., Stokes N.R., Osawa K., Ichimura K., Tomita K. (1975), Astrophys. J. **197** 425.

Mukai K. (1987), Private Communication.

Murakami T. (1989), 23rd ESALAB Sym. "Two Topics in X-ray Astronomy" Vol **1 173.**

Nagase F. (1989), 23rd ESALAB Sym. "Two Topics in X-ray Astronomy" Vol **1** 45.

Nagase F. (1989), Pub. Astron. Soc. Jap **41** 1.

Nagel W. (1981), Astrophys. J. **251** 278.

Neugebauer G., Oke J.B., Becklin E. and Garmire G. (1969), Astrophys. J **155** 1.

Nishimura J., Fujii M., Tawara M., Oda M., Ogawara Y., Yamagami Y., Miyamoto S., Kajiwara M., Murakami M., Yoshimori M., Nakagawa M. and Sakurai T. (1978), Nature **272** 337.

Nishimura J., Kona Y. and Ohta S. (1984), "Attitude Control Systems for Balloon Borne Telescope by using a Reaction Wheel", internal report Institute of Space and Astronomical Science". Japan.

Nolan P.L., Gruber D.E., Knight F.K., Matteson J.L., Petterson L.E., Levine A.M., Lewin W.H.G. and Primini F.A. (1982), Astrophys. J. **262** 727.

Nousek J.A. and Shue D.R. (1989), Astrophys. J. **242** 1207.

Ogawara Y., Matsuoka M., Miyaamoto S., Muranaka N., Nishimura J. and Oda M. (1976), Astrophys. Spa. Sci. **42** 211.

Overbeck J.W. and Tananbaum H.D. (1968), Astrophys. J. **153** 899.

Paradijs J. van and Lewin W.H.G. (1986), p187 "The Evolution of Galactic X-ray Binaries" Eds: Truemper J., Lewin W.H.G, Brinkman W. D. Reidel Dordrecht.

Parsignault D.R. and Grindlay J.E. (1978), Astrophys. J. **225** 970.

Pedersen H., Lulo J., Inone H., Koyama K., Kukishima K., Matsuoka M., Mitsuda K., Murakami T., Oda M., Ogawara Y., Oshashi T., Shibazaki N., Tunaka Y., Hayakawa S., Kunieda H., Makino F., Masai K., Nagase F., Tawarai Y., Miyamoto S., Tsunemi H., Yamashita K., Kondo I., Jernigan J.G., van Paradijs J., Beardsley A., Cominski L., Doty J. and Lewin W.H.G. (1982), Astrophys. J. **263** 325.

Pennix W. (1989), 23 rd ESALAB Symp: "Two Topics in X-Ray Astronomy." Vol **1** 185.

Pennix W., Lewin W.H.G., Mitsuda K., van der Klis M., van Paradijs J., Zijlstra A.A. (1990), Mon. Not. Roy. Astro. Soc. **243** 114.

Peterson L.E. and Jacobson A.S. (1966), Astrophys. J. **145** 963.

Petro L.D., Bradt H.V., Kelly R.L., Horne K. and Gomer R. (1981), Astrophys J. (Lett.) **251** L1.

Pilkington G.R. and Anger C.D (1971), Planet. Spa. Sci **19** 1069.

Pilkington G.R. (1972), "Earths Magnetospheric Processes" D.Reidel Holland Dordrecht.

Ponman T. (1981), Mon. Not. Roy. Astro. Soc. **196** 583.

Pomman T. (1982), Mon. Not. Roy. Astro. Soc. **201** 769.

Powell D.R. and Macdonald J.R. (1972), p148. The Computer Journal **15** #2.

Pravdo S.H., White N.E., Bolt E.A., Holt S.S., Serlemitsos P.J., Swank J.H., Symkowiak A.E., Toughy I. and Gamire G. (1979), Astrophys. J. **231** 912.

Prescott J.R. (1966), Nuc. Inst. & Meth. **39** 173.

Press W.H. and Schechter P. (1974), Astrophys. J. **193** 437.

Press W.H., Flannery B.P., Tenkolsky, S.A. and Vetterling, W.T. (1986), "Numerical Recipes" Cambridge Uni. Press Cambridge.

Press W.H. and Teukolsky S.A. (1988), p77 "Computers in Physics". Nov/Dec.

Press W.H. and Rybicki G.B. (1989), Astrophys. J. **338** 277.

Priedhorsky W.C. and Holt, S.S. (1981), Spa. Sci. Rev **45** 291.

Priedhorsky W. (1986), Astrophys. J. (Lett.) **306** L97.

Priedhorsky W., Hasinger G., Lewin W.H.G, Middleditch J., Parmar A., Stella L. and White N. (1986), Astrophys. J. (Lett.) **306** L91.

Priedhorsky W.C. and Holt S.S. (1987), Astrophys. J. **312** 743.

Prothero R.J. (1987a), "Phasographs and Circular Statistics" p91 of VHE Gamma Ray Astronomy. Eds: Turver K.E. D Reidel: Dordretch. (Rappatour paper at 20th Int. Cosmic Ray Conf. Moscow)

Prothero R.J. (1987b), Proc. Astron. Soc. Aust. **7** 167.

Prothero R.J. and Hocking W.K. (1988), Astro. Lett. and Com. **27** 237.

Ranpach M. and Michell W. (1977), Computing Report 10, Flinders Institute of Atmospheric and Marine Sciences.

Ray A. and Kluzniak W. (1990), Nature **344** 415.

Ricker G.R., Clarke G.W., Doxsey R.E., Dower R.G., Jernigan J.R., Delvaille J.P., McAlpine G.M. and Hjellming R.M. (1978), Nature **271** 35.

Ricketts M.J., Hall R., Page C.G., Witford C.H. and Pounds K.A. (1982), Mon. Not. Roy. Astron. Soc. **201** 759.

Riegler, G.R. Boldt E. and Serlemitsos P. (1970), Nature **226** 1041.

Robinson E.L. and Warner B. (1972), Mon. Not. Roy. Astro. Soc. **157** 85.

Rosner R., Golub L. and Varana A.S. (1985), Ann. Rev. Astron. Astrophys. **23** 413.

Rothschild R.E., Gruber D.E., Knight F.K., Nolan P.L., Seong Y., Levine A.M., Primiki F.A., Wheaton W.A., Lewin W.H.G. (1980), Nature **286** 786.

Ryan J.M., Jennings M.C., Radwin M.D., Zych A.D. and White R.S. (1979), J. Geophys. Res. **84** 5279.

Sakao T., Kohmura Y., Makishima K., Oshashi T., Dotani T., Kii T., Makiko F., Nagase F., Takeshima T. and Turner M.J.L. (1990), Mon. Not. Roy. Astron. Soc. **246** L11.

Sandage A.R., Osmer P., Giacconi R., Gorenstein P., Gursky H., Waters J., Bradt H., Garmire G., Sreekantan B.V., Oda M., Osawa K. and Jugakn J. (1966), Astrophys. J. (Lett.) **146** 316.

Scargle J.D. (1981), Astrophys. J. (Supp.) **45** 1.

Scargle J.D. (1982), Astrophys. J. **263** 835.

Scargle J.D. (1989), Astrophys. J. **343** 874.

Schultz N.S., Hasinger G. and Trümper J. (1989), Astron. Astrophys. **225** 48.

Schwarzenberg-Czerny A. (1989), Mon. Not. Roy. Astro. Soc. **241** 153.

Secmat H. (1971), "Introduction to Atomic and Nuclear Physics", 4th Ed., Chapman and Hall, London.

Shaham J. (1986), Astrophys. J. **310**, 780.

Shakura N.I. and Sunyaev R.A.(1974), Astron. Astrophys. **24** 337.

Sharma D.P., Dieters S.W.B., Emery M.W., Fenton K.B., Giles A.B., Greenhill J.G., Sprent A., Warren D.M. (1987), Proc. 20th Inernat. Cosmic Ray Conf., Moscow. OG 9 1-3.

Shibazaki, N. (1989), 23rd ESALAB Symp: "Two Topics in X-ray Astronomy", Vol **1** 237.

Simonetti J.M., Cordes J.M. and Heechen D.S. (1985), Astrophys. J. **296** 46.

Skinner G.K. and TTM/KVANT team (1990), IAU Circ. 4879.

Smith A. and Turner M.J.L. (1981), Nuc. Inst. & Meth. **189** 511.

Smith A. and Turner M.J.L. (1982), IEEE Trans. on Nuc. Sci. **29(1)** 146.

Soong Y. and Rothschild, R.E. (1983), Astrophys. J. **274** 327.

Soong Y., Gruber D.E, Pet*erson L.E. and Rothschild R.E. (1990), Astrophys. J. **348** 641.

Spooner N.J.C., Engle A.R., Leake J.W., Quemby J.J. and Sanford D.W. (1986), Nuc. Inst. and Meth. **A248** 533.

Sprent T. (1986), p91. Proc 21st Aust. Survey Conf.(Adelaide).

Steiman-Cameron T., Imamura , Middleditch J., Kristan J. (1990), Astrophys. J. **359** 197.

Stein J.A. and Lewin W.H.G. (1967), J. Geophys. Res. **72** 383.

Stella L., White N.E. and Rosner R. (1986), Astrophys. J. **308** 699.

Stellingwerf R.F. (1978), Astrophys. J. **224** 953.

Stollman G.M., Hasinger G., Lewin W.H.G., van der Klis M. and van Paradijs J. (1987), Mon. Not. Roy. Astro. Soc. **227** 7.

Storey M.C. (1986), Ph.D. Thesis, University of Sydney.

Strickman M.S., Johnson-Neil W. and Kurfess J.D. (1980), Astrophys. J. (Lett.) **240** L21.

Strickman M.S., Kurfess J.D. and Johnson-Neil W. (1982), Astrophys. J. (Lett.) **253** L23.

Sunyaev R.A. and Titarchuck L.G. (1980), Astron. Astrophys. **86** 121.

Sunyaev R.A., GRANT team (1990), IAU Circ., 5104.

Sutherland P.G., Weisskopf M.C. and Kahn S.M. (1978), Astrophys. J. **219** 1029.

Suzuki K., Matsuoka M., Inoue H., Mitsuda K., Ohashi T., Tanaka Y., Hirano T. and Miyamoto S. (1984), Pub. Astro. Soc. Jap. **36** 761.

Swingler D.N. (1989), Astron. J. **97** 280.

Tanaka Y. (1989), 23rd ESALAB Symp: "Two Topics in X-ray Astronomy", Vol **1** 3.

Tennant A.F. (1987), Mon. Not. Roy. Astro. Soc. **226** 963.

Tennant A.F. (1988), Mon. Not. Roy. Astro. Soc. **230** 403.

Terrell N.J. (1972), Astrophys. J. (Lett.) **174** L35.

Theinhardt J., Burk R., Kendziorra E. and Stanbert R. (1984), Nuc. Inst. & Meth. Phys. Res. **221** 288.

Thomas R.M., Duldig M.L. and Greenhill J.G. (1977), Nature **267** 332.

Trümper J., Pietsch W., Reppin C., Voges W., Staubert R. and Kendzioora E. (1978), Astrophys. J. (Lett.) **219** L105.

Trümper J. (1982), p231 "Galactic X-ray Sources" Eds: Sanford P.W., Laskerides P., Sulton J. John Wiley & Sons. Chichester.

Tuoghy I. (1987) Private Communication.

Ubertini P., Bazzano A., Boccaccini L., Mastropietro M., La Padula C.A., Patriarca R. and Polcaro, V.F. (1981), Spa. Sci. Inst. **5** 237.

Vacca W.D., Sztajino M., Lewin W.H.G., Trümper J., van Paradijs J. and Smith A. (1987), Astron. Astrophys. **172** 143.

van der Klis M., Jansen F., van Paradijs J., Lewin W.H.G., van den Heuvel E.P.J., Trümper J.E. and Sztajno M. (1985), Nature **316** 225.

van der Klis M. (1987) Exosat Preprint 81.

van der Klis M. (1989), 23rd ESALAB Symp: "Two Topics in X-ray Astronomy" Vol **1** 203.

van der Klis M. (1989), Ann. Rev. Astron. Astrophys. **27** 517.

van der Klis M., Stella L., White N., Jansen F.and Parmar A.N. (1987a), Astrophys. J. **316** 411.

van der Klis M., Hasinger G., Stella L., Langmeir A.and van Paradijs J. (1987b), Astrophys. J. (Lett.) **319** L13.

Velnsamy T., Pramesh Rao A. and Sakumar S. (1985), Mon. Not. Roy. Astro. Soc. **213** 735.

Velnsamy T. and Subrahmanya C.R. (1989), Mon. Not. Roy. Astro. Soc. **239** 281.

Ventura J. (1979), Phys. Rev. D. **19** 1684.

Verbunt F., Wijers R.A.M.J. and Burm, H.M.G. (1990), Astron. Astrophys. **234** 198.

Vrtilek S.D., Pennix W., Raymond J.C. and Verbunt, F. (1989), Proc. of 23rd ESALAB Symp: "Two Topic in X-ray Astronomy" Vol **1** 671.

Wade C.M. and Hjellming R.M. (1971), Astrophys. J. **170** 523.

Walker G. (1987), pp.223-228. "Astronomical Observations", Cambridge University Press, Cambridge.

Walpole R.E. and Myers, R.H. (1978), "Probability and Statistics for Engineers and Scientists". 2nd Ed. Collier Macmillian, London.

Wang J.C.L., Wasserman I.M. and Salpeter E.E. (1989), Astrophys. J. **338** 343.

Wang J.M. and Robertson J.A. (1985), Astron. Astrophys. **151** 361.

Wang Y.M. and Frank J. (1981), Astron. Astrophys. **93** 255.

Wang Y.M. (1987), Astron. Atrophys. **183** 257.

Wang Y.M. and Schlickeiser R. (1987), Astrophys. J. **313** 200.

Warner B. and Robinson E.L. (1972), Mon. Not. Roy. Astro. Soc. **159** 101.

Warner B. (1988), "High Speed Astronomical Photometry". Cambridge University Press, Cambridge.

Warren D.M. (1980), Honours Thesis, University of Tasmania.

Warwick R.S., Koyama K., Inoue H., Takano S., Awaki H. and Hoshi R. (1989), Pub. Astro. Soc. Jap. **41** 739.

Wasserman I. (1990), Nature **346** 222.

Watts D.J. and Thomas R.M. (1979),Astrophys. Space Sci. **64** 213.

Watts D.J. (1983), Ph.D. Thesis, University of Tasmania.

Weisskopf M.C., Kahn S.M. and Sutherland P.G. (1975), Astrophys. J. (Lett.) **199** L147.

Wheaton Wm. A. Doty J.P., Primini F.A., Cooke B.A., Dobson C.A., Goldman A., Hecht M., Hoffman J.A., Howe S.K., Scheepmaker A., Tsiang E.Y., Lewin W.H.G., Matterson J.L., Gruber D.E., Baity W.A., Rothschild R., Knight F.K., Nolan P. and Peterson L.E. (1979), Nature **282** 240.

White N.E.and Mason K.O., Sanford P.W., Ilovaisky S.A. and Chevalier C. (1976), Mon. Not. Roy. Astron. Soc. **176** 91.

White N.E., Swank J.H. and Holt, S.S. (1983), Astrophys. J. **270** 711.

White N.E. and Mason K.O. (1984), Space Sci Res **40** 167.

White N.E., Peacock A. and Taylor B.G. (1985), Astrophys. J. **296** 475.

White N.E (1989) EXOSAT preprint 105.

Whiteoak P.A., Mezies J.W. Feast M.W. (1983), IAU Circ. 3885.

Whiteoak P. and Menzies J (1984), IAU Circ. 3919.

Wijers R.A.M.J., van Paradijs J. and Lewin, W.H.G. (1987), Mon. Not. Roy. Astro. Soc. **228** 17.

Wijers R., Burm H. and Verbunt, F. (1989), 23rd ESALAB Symp: "Two Topics in X-ray Astronomy" Vol **1** 677.

Willis A.J., Wilson R., van den Bout P., Sanner F., Black J., Davis R.J., Dupree A.K., Gursky H., Hartman L., Raymond J., Matilsky T., Burger M, De Loore C., van Dessel E.J., Whitelock P., Menzies J., Meikle W.P.S., Joseph R.D., Sanford P., Pollard G. and Sandford M.C.W. (1980), Astrophys. J. **237** 596.

Wilson C.K. and Rothchild, R.E. (1983), Astrophys. J. **274** 717.

Wood K.S., Meekins J.F., Yentis D.J., Smathers H.W., McNutt D.P., Bleach R.D., Byram E.T., Chubb T.A., Friedman H., Meidav M. (1984), Astrophys. J. (Supp.) **56** 507.

Wood K.S., Hertz P., Norris J.P., Vaughan B.A., Michelson P.F., Mitsuda K. and Dotami T. (1989), 23rd ESALAB Symp:, "Two Topics in X-ray Astronomy" Vol. **1** 689.

Worrall D.M., Knight F.K., Nolan P.L., Rothschild R.E, Levine A.M., Primini F.A., Lewin W.H.G. (1981), Astrophys. J. (Lett.) **247** L31.

Wright E.L., Gottlieb E.W. and Lillier W (1975), Astrophys. J. **200** 177.

Young, A.T. (1967), Astron. J. **72** 747.

Zel'dovitch Ya. B. Shakura N.I. (1969) Soviet Astron. **13** 175.

Zheleznyakov, V.V. (1970), "Radio Emission of the Sun and Planets", Pergamon, Oxford.